Roma Tre

Fisica

CORSO DI DOTTORATO DI RICERCA IN

XXXVIII

CICLO DEL CORSO DI DOTTORATO

Microdosimetric approaches for optimizing proton therapy and targeted radionuclide therapy

---

Lucrezia Bianchi

Nome e Cognome del dottorando — Firma

Dr. Andrea Fabbri

Docente Guida/Tutor — Firma

Prof. Giorgio Matt

Coordinatore — Firma

ROMA TRE UNIVERSITY

DOCTORAL THESIS

Microdosimetric approaches for optimizing proton therapy and targeted radionuclide therapy

---

Author:
Lucrezia BIANCHI

Supervisor:
Dr. Andrea FABBRI

Co-supervisor:
Dr. Claudio VERONA
Dr. Andrea ATTILI

A thesis submitted in fulfillment of the requirements for the degree of Doctor of Philosophy

in the

Department of Mathematics and Physics
Ph.D Programe in Physics, Cycle XXXVIII

"Nothing in life is to be feared; it is only to be understood. Now is the time to understand more, so that we may fear less."

Maria Skłodowska-Curie

Abstract

Hadron therapy and targeted radionuclide therapy have emerged as advanced clinical approaches for cancer treatment. Their main goal is to increase radiation doses to tumors while minimizing toxicity to healthy tissues. Proper characterization of radiation quality is thus crucial to ensure safe and effective tumor treatment. For this reason, microdosimetry has been employed. It helps to better understand the relationship between energy deposition and biological effects. It also identifies suitable quantities for characterizing and quantifying radiation quality. In spite of its potential, more technological and methodological improvements are needed for clinical use. Both the development of reliable solid-state microdosimeters suitable for clinical beams and the definition of biological models that connect physical quantities to therapeutic outcomes remain crucial elements in the research field.

Within this context, this PhD work contributes to the microdosimetric characterization of radiation using a combined experimental and modeling approach, also supporting improved understanding of biological effects and more effective quality assurance strategies.

Integrating experimental and Monte Carlo modeling approaches, the first part of the research concerns the DIODE (Diamond Integrated devices fOr haDronthErapy) project. This work presents the development and experimental characterization of DIODE, an innovative detection system based on single-crystal synthetic diamond designed to perform simultaneous dosimetric and microdosimetric measurements in clinical hadron therapy beams. Tests conducted at the Proton Therapy Center in Trento with a 70 MeV proton beam confirmed the device's excellent linearity with dose and its ability to accurately estimate Linear Energy Transfer (LET) and Relative Biological Effectiveness (RBE) variations. The measured RBE values, ranging between 1.1 and 1.8, are consistent with literature data and Monte Carlo simulations.

One of the key aspects of this project concerns the characterization of the so-called "border effect", a typical challenge for solid-state microdosimeters linked to incomplete charge collection at the edges of the sensitive volume. Through IBIC (Ion Beam Induced Charge) analysis and Geant4 simulations, it has been quantified that this effect can cause significant variations in microdosimetric quantities, up to 40% for $\bar{y}_F$ and 20% for $\bar{y}_D$. Therefore, understanding and mitigating this phenomenon is essential to ensure the accuracy of clinical measurements. Overall, the DIODE system is an advanced and reliable tool for real-time beam quality assessment and optimization of biologically based treatment plans in modern ion therapy.

At the same time, the SEGNAR (Synergic Effects of Gold Nanorods and Radiopharmaceuticals) project analyzed the biological efficacy of ^{99m}Tc conjugated to gold nanorods (AuNRs). Through Geant4-DNA simulations and the Monte Carlo temporal - Microdosimetric Kinetic Model (MCt-MKM), it was demonstrated that the dose enhancement due to the presence of gold is minimal (6-7 orders of magnitude lower than the radionuclide alone). However, the study of the synergistic effect of the ^{99m}Tc-AuNR system revealed that the co-localization of multiple sources for AuNR leads to a dose enhancement, making the dose distribution extremely heterogeneous. Despite the increase in local dose, the synergistic effect is limited by the low dose rate (6-hour half-life of ^{99m}Tc), which allows cellular repair mechanisms to actively intervene during irradiation, reducing the formation of sublethal lesions. The study demonstrates that the fundamental role of gold nanorods lies in their function as carriers capable of positioning the radionuclide as close as possible to the cell nucleus to exploit the high LET of Auger electrons and maximize DNA damage.

Finally, this thesis presents a new standard for quality assurance for proton therapy by reducing uncertainties in radiobiological calculations performed by the Treatment Planning Systems (TPS) and improving their robustness. New innovative perspectives in theranostics are introduced as a result of the combined usage of ^{99m}Tc and nanoparticles that could be further converted and used with other toxic radiopharmaceuticals using specially designed nanomaterials.

Keywords: Microdosimetry, Hadron therapy, Diamond detectors, Monte Carlo simulations, Targeted radionuclide therapy, Quality assurance, Theranostics.

Contents

List of Figures

List of Tables

Acronyms

AE	**A**uger **E**lectron
AuNP	**G**old **N**anoparticle
AuNR	**G**old **N**anorod
CCE	**C**harge **C**ollection **E**fficiency
CDF	**C**umulative **D**istribution **F**unction
CE	**C**onversion **E**lectron
CNAO	**N**ational **C**enter for **O**ncological **H**adrontherapy
CSP	**C**harge **S**ensitive **P**reamplifier
CVD	**C**hemical **V**apor **D**eposition
DER	**D**ose **E**nhancement **R**atio
DIODE	**D**iamond **I**ntegrated device f**O**r **H**a**D**ronth**E**rapy
DNA	**D**eoxyribonucleic **A**cid
Dos	**D**osimeter
DSB	**D**ouble-**S**trand **B**reak
EC	**E**lectron **C**apture
EDX	**E**nergy **D**ispersive **X**-ray spectroscopy
EPR	**E**nhanced **P**ermeability and **R**etention
FESEM	**F**ield **E**mission **S**canning **E**lectron **M**icroscopy
GEM	**G**as **E**lectron **M**ultiplier
Gy	**G**ray
HSG	**H**uman **S**alivary **G**land
IBIC	**I**on **B**eam **I**nduced **C**harge
IC	**I**nternal **C**onversion
ICRP	**I**nternational **C**ommission on **R**adiological **P**rotection
ICRU	**I**nternational **C**ommission on **R**adiation **U**nits and Measurements
IT	**I**someric **T**ransition
LEM	**L**ocal **E**ffect **M**odel
LET	**L**inear **E**nergy **T**ransfer
LLN	**L**aw of **L**arge **N**umbers
LQM	**L**inear-**Q**uadratic **M**odel
LSPR	**L**ocalized **S**urface **P**lasmon **R**esonance
MCA	**M**ulti-**C**hannel **A**nalyzer
MCTS	**M**onte **C**arlo **T**rack **S**tructure
MCt-MKM	**M**onte **C**arlo temporal-**M**icrodosimetric **K**inetic **M**odel
MKM	**M**icrodosimetric **K**inetic **M**odel
NIR	**N**ear-**I**nfrared

PDFs	**P**robability **D**ensity **F**unctions
PET	**P**ositron **E**mission **T**omography
PTT	**P**hotothermal **T**herapy
RBE	**R**elative **B**iological **E**ffectiveness
RNG	**R**andom **N**umber **G**enerator
ROS	**R**eactive **O**xygen **S**pecies
SEGNAR	**S**ynergic **E**ffects of **G**old **N**anorods **A**nd **R**adiopharmaceuticals
SEM	**S**canning **E**lectron **M**icroscopy
SOBP	**S**pread-**O**ut **B**ragg **P**eak
SOI	**S**ilicon-**O**n-**I**nsulator
SPECT	**S**ingle-**P**hoton **E**mitting **C**omputed **T**omography
SSB	**S**ingle-**S**trand **B**reak
SV	**S**ensitive **V**olume
TDRA	**T**heory of **D**ual **R**adiation **A**ction
TEPC	**T**issue-**E**quivalent **P**roportional **C**ounter
TPS	**T**reatment **P**lanning **S**ystem
TRT	**T**argeted **R**adionuclide **T**herapy
μ**Dos**	**M**icrodosimeter

General introduction

Every year, a considerable amount of morbidity and mortality worldwide is caused by cancer, posing a major threat to public health. To treat malignant tumors, various treatments are employed, such as surgery, radiation therapy, or chemotherapy. Recently, advanced treatment techniques, such as hadron therapy and targeted radionuclide therapy, have been implemented.

Their primary goal is to increase the radiation dose delivered to tumors while minimizing toxicity to healthy tissues. The proper characterization of radiation quality is therefore a key element to ensure safe and effective cancer treatments. Because the energy deposition pattern at micrometer and sub-micrometer levels explains the variation in biological effects caused by the same absorbed dose from different radiation qualities, conventional dosimetry has severe limitations.

The absorbed dose alone, therefore, cannot properly represent the radiation's biological effectiveness. Conventional dosimetric quantities provide an average description of energy deposition in tissues but fail to describe the stochastic nature of interactions at the cellular and subcellular scales, where the most significant biological damage occurs.

For this reason, microdosimetry was developed to investigate energy deposition events within volumes comparable to the size of critical biological structures. Through dedicated radiobiological models, microdosimetry can be directly related to biological effects, enabling a better understanding of the mechanisms underlying radiation-induced damage.

Additionally, it supports the development of more accurate radiobiological models and reliable predictions of treatment planning and outcomes. Despite its potential, more technological and methodological improvements are still needed for clinical use.

Thus, both the development of reliable solid-state microdosimeters suitable for clinical beams and the definition of biological models that connect physical quantities to therapeutic outcomes in a solid way remain crucial elements in the research field.

The work carried out during this PhD fits within the described framework, contributing to the microdosimetric characterization of radiation through a combined experimental and modeling approach whose aim is to optimize the analysis of biological effects, supporting effective quality assurance strategies. Among the specific objectives of this thesis are:

- Characterization of a new portable diamond-based detector designed to simultaneously perform dosimetric and microdosimetric measurements of ion beams.

- Modeling of the border effect in diamond-based microdosimeters and its impact on microdosimetric measurements in proton therapy.
- Study of radiobiological effects of ^{99m}Tc in targeted radionuclide therapy, and the possible enhancement and synergistic effects of a theranostic system based on gold nanoparticles and ^{99m}Tc-radiopharmaceutical.

The research activities related to the first two objectives were achieved in the DIODE (Diamond Integrated device fOr HaDronthErapy) project. The detectors were manufactured by the research group at Tor Vergata University in Rome, and their characterization was carried out in collaboration with Dr. Claudio Verona. I contributed to the experimental campaign carried out at the Trento Proton Therapy Center (TIFPA) facility for the characterization of the device using clinical proton beams and analyzed the experimental data, including the Monte Carlo simulations required for a systematic comparison with the measurements. To analyze the impact of the border effect under typical proton therapy conditions, I collaborated with Dr. Gabriele Parisi. Starting from the experimental data collecting at the Surrey Ion Beam Center, we developed a model to describe this effect. I then applied the border effect to experimental and simulated data to quantify its impact on microdosimetric quantities.

The activities related to the last objective are part of the SEGNAR (Synergic Effects of Gold Nanorods And Radiopharmaceuticals) project, carried out in collaboration with Dr. Andrea Attili, and were entirely based on my simulation work. I studied the radiobiological impact of ^{99m}Tc and estimated the cell surviving fraction using the Monte Carlo temporal - Microdosimetric Kinetic Model (MCt-MKM). This original reformulation of the MKM takes into account the temporal structure of irradiation. Since the half-life of ^{99m}Tc is on the order of hours, the resulting irradiation is protracted over time. Then I quantified how the cell repair mechanisms of sublethal damage, which act on time scales of minutes, occur during irradiation itself. I also studied the possible dose enhancement induced by AuNRs, as well as a possible synergistic effect between ^{99m}Tc and AuNRs. By analyzing the radiobiological effect as a function of the coordination number in the ^{99m}Tc-AuNR system, I studied how biological effects are modulated by the spatial dose distribution, ranging from a homogeneous pattern (low coordination numbers) to an extremely heterogeneous distribution (high coordination numbers).

This thesis is structured as follows:

Chapter 1 presents the study through a clear overview of the physical and biological foundations of the work. Different topics are introduced, such as radioactive decay and radiation–matter interactions, and then move to key radiobiological concepts, such as DNA damage and RBE. Moreover, the content of this chapter provides an accurate overview of the current state of the art of radionuclide therapy—focusing on Auger electrons and ^{99m}Tc as well as recent developments in proton therapy.

Chapter 2 addresses microdosimetric quantities and related radiobiological models. It describes microdosimetry detectors, with a focus on solid-state detectors.

Chapter 3 deals with the computational tools employed throughout this work. The Monte Carlo method, with distinctions between "condensed-history" and "track-structure" approaches, is fundamental part of this overview. This chapter also focuses on the Geant4 toolkit and its Geant4-DNA extension for nanometric-scale simulations to characterize particle interactions in liquid water, which will be discussed in the ensuing chapters.

Chapter 4 examines the results of the DIODE project. In particular, the experimental characterization of a novel diamond-based detector capable of performing both dosimetric and microdosimetric measurements of clinical proton beams will be described. The central sections focus on the investigation and modeling of the border effect, an electric-field distortion that influences microdosimetric measurements. In conclusion, the chapter reports the experimental characterization (with IBIC technique), the corresponding Monte Carlo simulations, and evaluations of radiation quality as well as RBE in clinical proton beams.

Chapter 5 explores the potential of theranostic systems. It presents a Monte Carlo study on the radiotherapy enhancement effect resulting from the combined use of gold nanoparticles and radiopharmaceuticals. The chapter details the modeling of nanoparticle geometry, along with the calculation of radial dose profiles and the application of MCt-MKM to estimate the radiobiological effects of ^{99m}Tc and the possible synergistic effects of gold nanorods - ^{99m}Tc systems.

Chapter 1

Literature review

Radiotherapy is a type of treatment that uses ionizing radiation to kill cancer cells and is particularly used in the treatment of various forms of cancer. The fundamental principle of all radiation therapies is to cause maximum damage to cancerous tissue by delivering a sufficiently high absorbed dose, while minimizing unnecessary exposure and toxicity to healthy organs and tissue [126].

The choice of cancer treatment depends on the type of cancer, its location, the presence of metastasis and patient health factors. Radiotherapy with high-energy photons or electron beams represents at present approximately 50% of treatments of malignant tumours at least in the initial part of their treatment [75]. When the irradiating beams are made of charged particles (protons and other ions, such as carbon), radiation therapy is called hadron therapy. This treatment may offer advantages for certain tumors where precision is critical, especially for tumors near sensitive areas or critical organs. By sparing healthy tissue, hadron therapy has the potential to reduce the risk of side effects and improve patient outcomes with respect to photon or electron beams.

Despite significant treatment advancements, once the cancer has metastasized, 10-year survival rates remain poor [42][93]. For these reasons, alternative therapeutic strategies able to reduce the risk of cancer recurrence must be explored.

Targeted radionuclide therapy (TRT) has seen a recent growth in interest from a clinical perspective. This treatment utilizes radiopharmaceuticals to deliver radiation directly to cancer cells while sparing healthy tissues. Radiopharmaceutical selection is a critical component in the design of TRT, as each radionuclide exhibits distinct properties. TRT incorporates alpha-particle, beta-particle, or or radionuclides emitting Auger electrons to deliver a therapeutic dose of ionizing radiation to the intended target.

A significant challenge in radiopharmaceutical development is identifying matched pair radionuclides for diagnostic and therapeutic applications. Theranostics is an emerging medical approach that incorporates paired radiopharmaceuticals to selectively diagnose ("diagnostics") and treat ("therapeutics") various types of disease [40]. Theranostic radiopharmaceuticals consist of a radionuclide tethered to a vector (antibody, peptide, small molecule, etc.) that binds to a target [236]. A positron

or gamma-emitting radionuclide can be incorporated for diagnostic imaging with positron emission tomography (PET) or single-photon emitting computed tomography (SPECT) to provide a visual representation of the radiopharmaceutical distribution in vivo and help identify specific sites of disease [236].

To further enhance therapeutic efficacy and overcome radioresistance, research is increasingly focusing on radiosensitizers. Nanomaterials, particularly Gold Nanoparticles (AuNPs), are being investigated for their ability to act as dose enhancers, amplifying the generation of secondary particles and reactive oxygen species within the tumor cells.

In this chapter, the fundamental physical and biological principles relevant to this thesis are reviewed. Sections 1.1 and Sections 1.2 introduce the general mechanisms of radioactive decay and nuclear isomeric transitions, with a specific focus on Auger electron emission, and outline the interactions of ionizing radiation with matter, distinguishing between photons, electrons, and heavy charged particles. Section 1.3 covers the essential radiobiological principles, including DNA damage mechanisms, the Linear-Quadratic Model (LQM), Relative Biological Effectiveness (RBE), and the distinction between direct and indirect radiation effects. Section 1.4 discusses the principles of Targeted Radionuclide Therapy (TRT), highlighting the therapeutic potential of various β^- and Auger electron emitters, including ^{99m}Tc. Section 1.5 provides an overview of heavy ion and proton therapy, emphasizing the physical advantages of the Bragg peak and beam delivery techniques. Finally, Section 1.6 explores the role of nanotechnology in radiation therapy, focusing on gold nanoparticles (AuNPs) as radiosensitizers to enhance secondary electron production and oxidative stress in tumor cells.

1.1 Radioactive decay

Radioactive decay is a fundamental phenomenon in nuclear physics. It describes how unstable nuclei (radionuclides) transform into more stable configurations by emitting radiation. This transformation can occur in different ways, such as alpha, beta, or gamma decay. The occurrence of these decay processes is directly linked to nuclear instability. Unstable nuclei are mostly caused by either an unfavorable nucleon configuration or an excess of energy. In the first case, the imbalance between protons and neutrons leads to β decay, α decay. In the second case, the excess energy is released through γ emission or internal conversion. In both situations, the nucleus moves towards a lower-energy, more stable state. Nuclei close to the neutron–proton line of stability are generally stable, while those with too many protons or neutrons, or with excess internal energy, undergo radioactive decay to reach a more favorable configuration.
The amount of a radionuclide in a sample refers to the *activity* of the sample. In the SI unit system, it is expressed in Becquerel (Bq) - the number of disintegrations per second. The activity A i.e., the rate of decay, is directly proportional to the number of

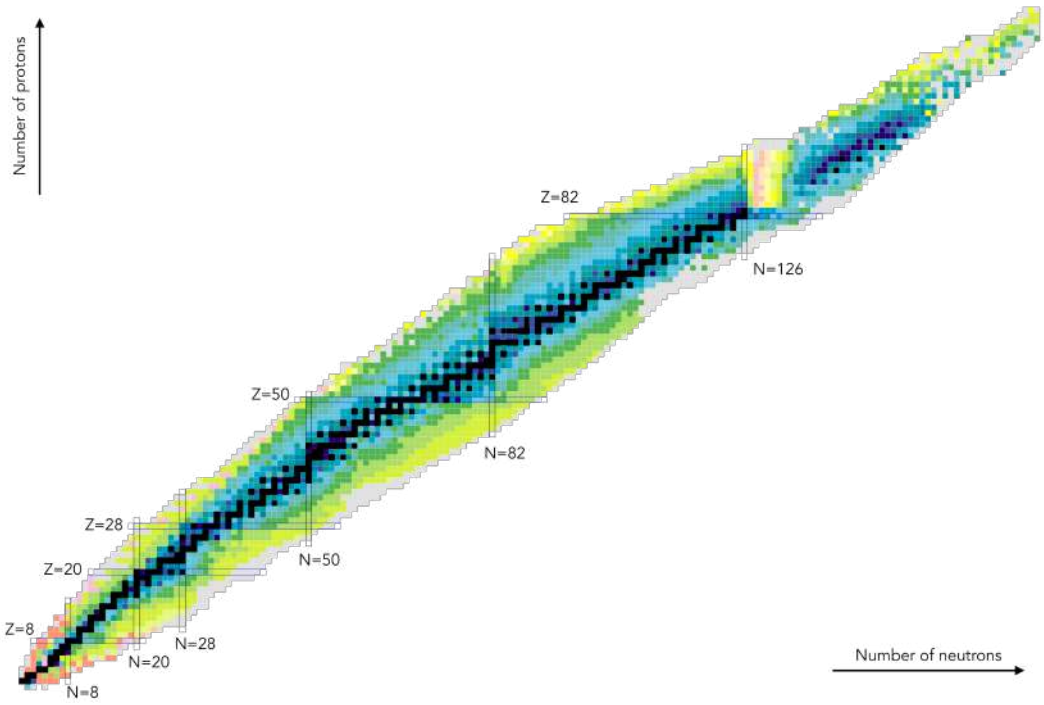

FIGURE 1.1: Chart of Nuclides illustrating the "valley of stability" and the distribution of isotopes as a function of the number of protons (Z) and neutrons (N) [195]

atoms N of nuclide present:

$$A(t) = -\frac{dN}{dt} = \lambda N(t) \tag{1.1}$$

where λ is the decay constant - the probability per second that the emission takes place), in units of s^{-1} [17]. The average time that an atom can be expected to exist before its nucleus decays is given by:

$$\tau = \frac{1}{t}. \tag{1.2}$$

This time represents the source degradation by a factor of e and can be transformed into the *half life* $t_{1/2}$ of the radionuclide:

$$t_{1/2} = \frac{ln(2)}{\lambda} \tag{1.3}$$

i.e., the time during which the activity decreases to half its original value. Integrating the 1.1, it brings to the exponential law of radioactive decay:

$$N(t) = N_0 e^{-\frac{ln(2)}{t_{1/2}}t} = N_0 e^{-\lambda t} \tag{1.4}$$

where N(t) is the number of undecayed atoms at time t and N_0 is the number of atoms at $t = 0$.

As seen above, there are different types of radioactive decay. Beta decay has three

modes of decay [216]:

- β^- **decay**: Nuclei with an excess of neutrons undergo this mechanism of disintegration. An electron (e^-) and an electron antineutrino ($\bar{\nu}_e$) are released when a neutron (n) is converted into a proton (p). The transformation can be written as follows, where X (Y) is the parent (daughter) nucleus:

$$^{A}_{Z}X \rightarrow ^{A}_{Z+1}Y + e^- + \bar{\nu}_e. \tag{1.5}$$

- β^+ **decay**: Proton-rich radioactive nuclei emit positrons (e+) and electron neutrinos ($\bar{\nu}_e$) after converting a proton into a neutron:

$$^{A}_{Z}X \rightarrow ^{A}_{Z-1}Y + e^+ + \nu_e. \tag{1.6}$$

- **Electron capture (EC)**: This decay mode is prevalent in proton-rich nuclei, similar to β^+ decay. An electron from an inner shell orbital is captured by a nucleus, which also converts a proton into a neutron and ejects an electron neutrino. The transformation is expressed as:

$$^{A}_{Z}X + e^- \rightarrow ^{A}_{Z-1}Y + \nu_e. \tag{1.7}$$

1.1.1 Nuclear isomeric transition decay

α decay and β decay modes can produce a daughter nucleus in an excited state without using all the decay energy available. This state has a long half-life (more than 5 ns [272]) and is called *metastable state*. The daughter nucleus will then transition to its ground state through two possible mechanisms. It may emit the excitation energy in the form of one or more γ photons in a decay process referred to as γ *decay*, or it may transfer the excitation energy to one of its associated atomic orbital electrons (usually a K-shell electron) in a process called *internal conversion*. In this case, an atomic electron (called internal conversion electron or CE) is ejected from one of the atomic shells, leaving a vacancy in that shell. The decay energy for IC is given by:

$$Q_{\mathrm{IC}} = Q_\gamma - I_i = E_{\mathrm{CE}} + E_{\mathrm{RN}} \tag{1.8}$$

where I_i is the ionization potential, or the energy required to extract the electron from the atomic shell, and Q_γ is the energy difference between two excited nuclear states, which is equivalent to the energy of a γ photon in a γ decay. The kinetic energy of the CE is represented by E_{CE}, while the kinetic energy of the recoil nucleus is represented by E_{RN}, which is significantly less than E_{CE} [216]. CE have a defined energy spectrum and are therefore mono-energetic.

Furthermore, the removal of orbital electrons by EC or IC creates vacancies in the atomic shells and leaves the atom in an excited state. The ensuing atomic relaxation can take place through radiative and non-radiative transitions. In the first case, X-rays with characteristic energies are emitted as the outer shell electrons fill the vacancies in

the inner shells. The energy of the X-ray is equal to the energy difference between the atomic shells involved in the transition. On the other hand, non-radiative transitions are related to the Auger effect, in which an outer atomic electron, known as an Auger electron (AE), is emitted instead of a photon as a result of the rearrangement of the atomic electrons to fill the vacancy in an inner shell.

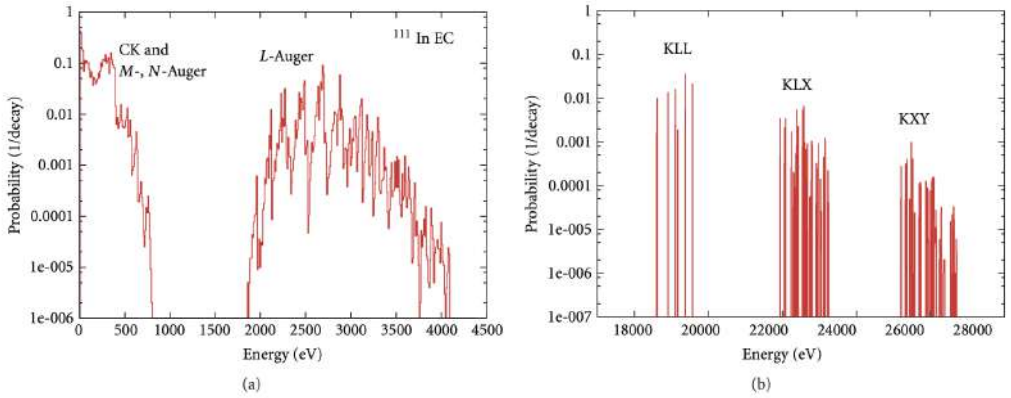

FIGURE 1.2: Auger spectrum of ^{111}In [17].

An example of a radionuclide with a discrete energy spectrum, (^{111}In), is shown in Figure 1.2. The CE emitted by ^{111}In is shown in Figure 1.2(a). Furthermore, the atom is left in an excited state when orbital electrons are removed via electron capture (EC) or internal conversion (IC), creating vacancies in the atomic shells. Both radiative and non-radiative transitions contribute to the subsequent atomic relaxation. In the first situation, outer shell electrons fill the vacancies in the inner shells, emitting X-rays with characteristic energies. The energy difference between the atomic shells involved in the transition represents the energy of the X-ray. Conversely, non-radiative transitions are associated with the Auger effect, where the rearranging of atomic electrons to fill the vacancy in an inner shell results in the emission of an outer atomic electron, known as an Auger electron, rather than a photon. AEs are released at discrete energies, similar to CE (see 1.2). An electron in an outer shell Y transitions to the vacancy in an inner shell X, and an electron is ejected from the outer shell Z in an AE process indicated XYZ. For example, an electron is referred to as a KL_1L_2 Auger electron if X is the K-shell, Y is the L1 sub-shell, and Z is the L_2 sub-shell [17]. The energy of the AE is therefore expressed as follows:

$$E_{\mathrm{AE}}(XYZ) = I_X - I_Y - I_Z \tag{1.9}$$

where I_X,I_Y, I_Z represent the ionization potentials of the atomic shells involved in the transition. The relaxation of an atom through radiative and non-radiative transitions is shown in Figure 1.3.

Moreover, there exist two types of transition: the Coster-Kronig effect and the super Coster-Kronig effect [216]. The first is referred to as transition energy, which originates from two sub-shells of a given atomic shell and is transferred to an electron in another

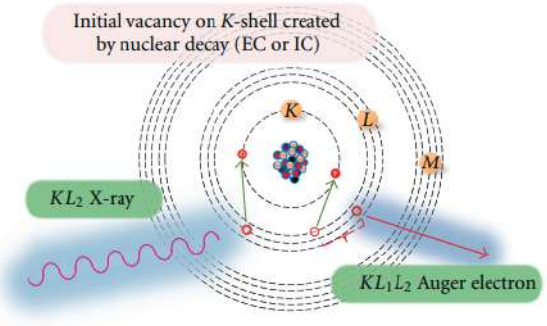

FIGURE 1.3: Schematic illustration of the relaxation of a K-shell vacancy created by nuclear decay (EC or IC). Image by Lee et al [17], licensed under CC BY 3.0.

shell. The second is referred to as transition energy, which originates from two subshells of a given atomic shell, and the energy is transferred to an electron in the same shell. Furthermore, AEs have low kinetic energy, ranging from a few eV to several tens of keV. As a result, AEs deposits all of their energy across extremely limited ranges in water, ranging from several hundreds of micrometers to a fraction of a nanometer [144].

1.2 Ionizing radiation interactions

1.2.1 Photons

Photoelectric effect

An electromagnetic process known as the photoelectric effect occurs when a photon interacts with an orbital electron, giving the electron all of its energy. After that, the electron will be released from the atom as a photoelectron. Its kinetic energy is equal to:

$$E_K = h\nu - E_B \tag{1.10}$$

where $h\nu$ is the incident photon energy and E_B is the binding energy of the ejected photoelectron. In this interaction, the photon is not re-emitted. Along with the photoelectron, an ionized atom with a vacancy in one of its bonded shells is also produced by the interaction. By rearranging electrons from other atomic shells or capturing a free electron from the medium, this vacuum is quickly filled. As a result, one or more distinctive X-ray photons might also be produced. However, photoelectric absorption usually reabsorbs these X-rays at the initial site. In some fraction of the cases, the emission of an Auger electron may substitute the characteristic X-ray in carrying away the atomic excitation energy [152]. For low-energy photons, the photoelectric process is the most common mechanism of interaction. Additionally, the process is enhanced for absorber materials with a high atomic number Z.

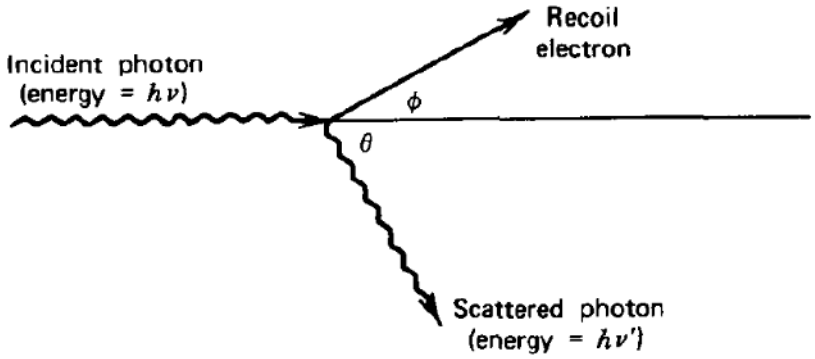

FIGURE 1.4: Schematic representation of the Compton scattering process [152].

Compton effect

The incident gamma-ray photon and an electron in the absorbing material interact through the Compton scattering process. For gamma-ray energies characteristic of radioisotope sources, it is frequently the main interaction mechanism. When Compton scattering occurs, the incoming gamma-ray photon is redirected at an angle θ relative to its initial path. The electron, which is considered to be initially at rest, receives some of the energy from the photon (recoil electron). The energy delivered to the electron can range from zero to a significant portion of the gamma-ray energy because all possible angles of scattering are available. The number of electrons available as scattering targets determines the probability of Compton scattering per atom of the absorber, which rises linearly with Z.

Pair production

Pair production can occur when gamma-ray energy reaches twice the rest-mass energy of an electron (1.02 MeV). This process is limited to high-energy gamma rays due to the low probability of interaction until the energy reaches several MeV. During the interaction, the gamma-ray photon disappears and is replaced by an electron-positron pair. The surplus energy of the photon (>1.02 MeV) is shared by the positron and electron as kinetic energy. Two annihilation photons are typically created as secondary products of the interaction because the positron will annihilate after slowing down in the absorbing medium. The probability cross section of pair production per nucleus has no straightforward expression, but its magnitude approximately varies as the square of the absorber atomic number Z [152].

Rayleigh scattering

Coherent or Rayleigh scattering occurs when a photon coherently interacts with every electron of the atom, without transferring any energy and so without exciting or ionizing the atom. As a result, the photon scatters with a change in direction but no change in energy. This interaction is more likely in high-Z materials and at

low photon energy. As photon energy rises, the photon deflection angle likewise decreases [152].

1.2.2 Electrons

Understanding and taking into account the features of their interactions is crucial since electrons are the most common secondary particle species created as charged hadrons move through matter. They can excite and ionize atoms similarly to charged hadrons since they are negatively charged particles. However, electrons can be deflected by interacting with the Coulomb force around the atom because they are far lighter than hadrons. To preserve the system's momentum, a photon is released as a result of this deflection (Bremsstrahlung process).

1.2.3 Protons and heavy ions

Stopping power and linear energy transfer (LET)

The linear stopping power (S) of a charged particle (or secondary charged particle created by primary radiation) in a medium is defined as the expected energy loss (dE) per unit path length (dx) traversed in that material [215]:

$$S = \frac{dE}{dx}. \tag{1.11}$$

The SI unit is J/m; it can also be written as eV/m or MeV/cm. The stopping power combines the total effect of three processes [76] [152]:

$$-\frac{dE}{dx} = S_e + S_r + S_n \tag{1.12}$$

S_e is the electronic (or collision) stopping power, caused by charged particle interactions with atomic orbital electrons that result in ionization or excitation; S_r is the radiative stopping power, caused by bremsstrahlung photon emission in the electric field of atomic nuclei or atomic electrons; and S_n is the nuclear stopping power, caused by elastic Coulomb interactions with atomic nuclei. For charged particles heavier than electrons and positrons, the radiative term (due to bremsstrahlung production) may be negligible, with the nuclear component dominating just before the particle reaches rest. The Bethe theory [215] is the most widely applied approximation for estimating the stopping power of charged particles. In particular, the classical expression that describes the specific energy loss, known as the Bethe-Bloch formula, is expressed as [152]:

$$-\frac{dE}{dx} = \frac{4\pi e^4 z^2}{m_0 \nu^2} NZ \left[ln \frac{2m_0 \nu^2}{I} - ln\left(1 - \frac{\nu^2}{c^2}\right) - \frac{\nu^2}{c^2} \right], \tag{1.13}$$

where ν and ze are the velocity and charge of the primary particle, N and Z are the number density and atomic number of the absorber atoms. m_0 is the electron rest mass, and the parameter I represents the average excitation and ionization potential of the absorber. Another quantity widely used in medical physics is the linear energy

transfer (LET). It describes the energy transferred to the medium per unit distance as a particle passes through matter. The LET of a particle is determined by its charge, electron density in the medium, and energy. This definition refers to unrestricted linear energy transmission as the electronic component of stopping power [152]. The restricted linear energy transfer (L_Δ) is the amount of energy lost through only electronic collisions (S_e), which transfer energy below a threshold Δ to electrons as it passes through matter, as shown in Eq. 1.14:

$$L_\Delta = \text{LET}_{\text{restricted}} = \frac{dE_\Delta}{dx} \tag{1.14}$$

where $\frac{dE_\Delta}{dx}$ is the rate of energy loss through electronic interactions with respect to distance through the medium, excluding secondary (delta) electrons whose kinetic energy exceeds Δ. Restricted LET describes the energy transfer to the medium in close proximity to the particle path, as energetic secondary or delta electrons may travel a long distance before depositing energy. By limiting the energy transfer to secondary electrons to a threshold Δ, they are allowed to escape the region of interest, essentially considering their energy deposition events as distinct from those along the track of the primary radiation. This is why the concept of LET is introduced to calculate the energy transferred to a localized region of interest. LET is expressed in keV/μm in SI units.

The Bragg peak

Charged particles, such as ions, exhibit an exponential increase in energy near the limit of their range, followed by a quick decrease. This is known as the Bragg peak [76][152]. The v^2 term in the Bethe-Bloch equation (1.14) causes the Bragg peak, resulting in a rapid increase in stopping power as the particle slows down [76][239]. Particles in a medium interact randomly with atoms [196]. At the Bragg peak, not all particles in a beam experience the same amount and type of interactions, resulting in a tiny spread of energies. As a result, the Bragg peak will subsequently broaden, a phenomenon known as *straggling* [76]. This mechanism is more noticeable in lighter ions like protons and at greater energies, as the more energetic the particle, the deeper it penetrates the material.

Elastic and inelastic nuclear scattering

Protons and heavy ions can interact with atomic nuclei numerous times as they move through a substance [76]. Elastic scattering causes particles to change trajectory. The scattering angle of a particle depends on its mass and the atomic number of the target material. Particles with smaller masses have higher scattering angles when traveling through the same medium. Protons scatter more laterally than heavier ions like carbon [101]. Unlike elastic nuclear scattering, the inelastic nuclear interaction generates secondary particles (other than electrons), which are important to consider when calculating the RBE. This process occurs when a hadron overcomes the Coulomb barrier and interacts directly with the nucleus, resulting in an energy transfer. This

interaction has the possibility of significantly changing the energy and direction of the hadron, as well as elevating the nucleus to an excited state. To move to a stable state, particles are ejected from the nucleus, including recoil protons, neutrons, photons, and alpha particles. Secondary particles (fragments) from the first interaction can lead to additional tertiary fragments [76][285]. These products are generally of higher LET than the incident particle, causing significant biological damage.

1.3 Fundamental quantities in radiobiology

The effects of radiation on matter, including living matter, depend on the characteristics of the radiation field and on the interactions between radiation and matter, as described by the relevant interaction quantities. When matter is exposed to ionizing radiation, it is the stochastic quantity that plays an important role. As stated in ICRU 36 report [14], the *energy deposit* ε_i is the energy deposited in a single interaction, i:

$$\varepsilon_i = T_{in} - T_{out} + Q_{\Delta m} \tag{1.15}$$

where T_{in} is the energy of the incident ionizing[1] particle (exclusive of rest mass), T_{out} is the sum of the energies of all ionizing particles leaving the interaction (exclusive of rest mass), $Q_{\Delta m}$ is the change in the rest energies of the nucleus and of all particles involved in the interactions. It relates to changes such as those occurring in nuclear reactions and pair (electron-positron) production. Q gets a positive sign in case of a decrease in rest energy and a negative sign in case of an increase in rest energy. ε_i can be considered as the energy deposited at the point of interaction, which is called the *transfer point*, i.e., the location where an ionizing particle loses kinetic energy.

The energy imparted, ε, to the matter in a given volume is the sum of all energy deposits in the volume:

$$\varepsilon = \sum_i \varepsilon_i \tag{1.16}$$

where the summation is performed over all energy deposits, ε_i, in that volume. For the determination of ε, is necessary to specify a volume and a time interval. If the energy imparted to the matter in a given volume is due to a single event, it is equal to the sum of the energy deposits in the volume associated with the event. If the *energy imparted* to the matter in a given volume is due to several events, it is equal to the sum of the individual energies imparted to the matter due to each event.

The mean energy imparted, ε, to the matter in a given volume equals the radiant energy, R_{in}, the sum of the kinetic energies of all those charged and uncharged ionizing particles which enter the volume minus the radiant energy, R_{out}, of all those charged and uncharged ionizing particles which leave the volume, plus the sum, $\sum Q$, of all changes of the rest energy of nuclei and elementary particles which occur in the volume:

$$\bar{\varepsilon} = R_{in} - R_{out} + \sum Q \tag{1.17}$$

[1] In accordance with ICRU Report 33, ionizing particles are taken to be charged or uncharged particles capable of ionization in the primary or secondary interactions.

An ionizing particle may enter and leave the volume without interacting in it. In this case, it does not contribute to ε since its kinetic energy on entering the volumes equals that on leaving it: $R_{in} = R_{out}$. The concept of mean energy imparted is shown in Figure 1.5:

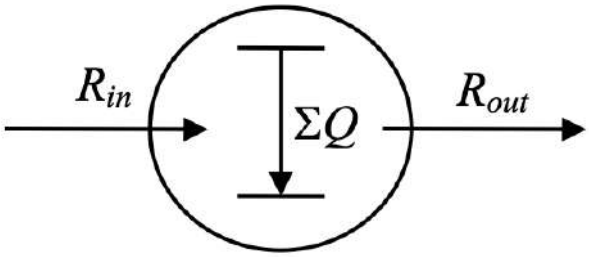

FIGURE 1.5: Schematic illustration of the mean energy imparted [33].

The specific energy imparted, z, is the quotient of ε and m, where ε is the energy imparted to matter of mass m:

$$z = \frac{\varepsilon}{m} \tag{1.18}$$

The specific energy imparted is, just as ε , a stochastic quantity. The value of z due to the irradiation of mass m cannot be predicted. In repeated measurements under given conditions, it will fluctuate statistically according to a probability distribution resulting from statistical fluctuations in both the number and the type of basic processes.

To avoid dealing with stochastic quantities in energy deposition, it is possible to define [231] the absorbed dose, D, as the differential quotient of dε and dm, where ε is the mean energy imparted to matter of mass dm:

$$D = \frac{d\bar{\varepsilon}}{dm} \text{ or } D = \lim_{m \to 0} \frac{\bar{\varepsilon}}{m} \tag{1.19}$$

The SI unit is Gray (1 Gy = 1 J/kg).

Absorbed dose results from a two-step limiting process. First, the mean energy imparted is determined, which in principle involves repeated exposures of a finite mass to a given irradiation condition and averaging the results to estimate a mean value. This mean value is proportional to the mean absorbed dose in the finite mass.

To obtain the absorbed dose, a second limiting process is performed, which consists of reducing the size and mass of the exposed volume toward zero. This limiting process is reflected by the differentials in the formal definition. These considerations underline the distinction between the specific energy z and the absorbed dose D: the specific energy is a stochastic quantity associated with a finite mass, whereas the absorbed dose is a non-stochastic quantity defined at a point. Since z fluctuates in both space and time, it is not possible to define a gradient or rate for it. In contrast, the absorbed dose represents the expectation value of energy imparted per unit mass of an infinitesimal volume (the condition m$\to$0 implying V$\to$0, not the density $\rho \to$0). It is defined at every point of an irradiated medium and provides a way to describe

spatial and temporal distributions of energy deposition. The differences and similarities between z and D can be further illustrated by Figure 1.6 in which ε/m is plotted as function of the irradiated mass m.

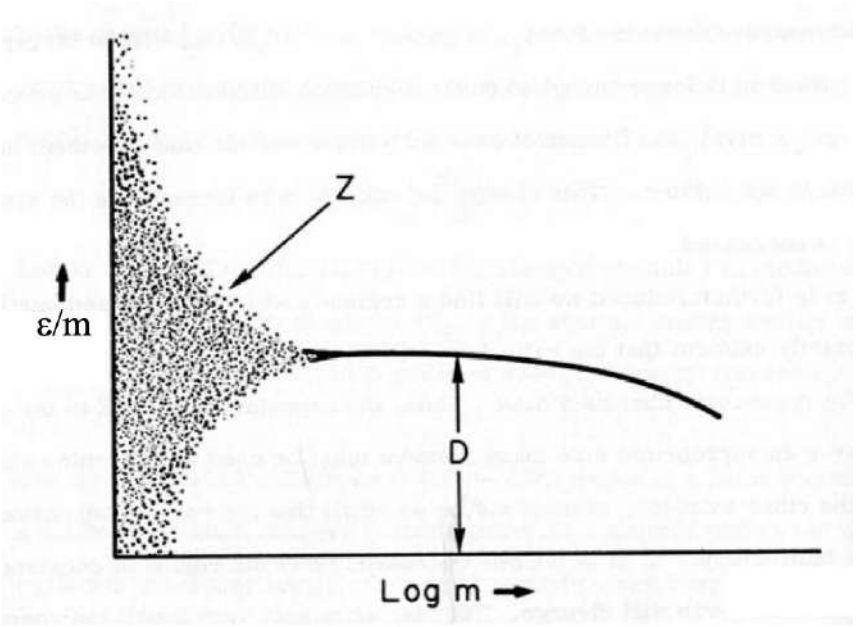

FIGURE 1.6: Ratio of ε/m as a function of the mass m exposed to a beam of ionizing radiation. The horizontal line indicates the region where the absorbed dose can be determined in a single measurement. The shaded area represents the region in which statistical fluctuations are significant [33].

Going from a large mass down to a smaller mass ε/m will increase a little due to an increase in fluence of charged particles in the mass element caused by less attenuation of the primary beam. As m is further reduced, we will find a region in which the charge particle fluence is sufficiently uniform that z will be constant. It is in this region that the ratio $\varepsilon/m = z$ represents the absorbed dose.

In the extreme case of very small values of m, the energy deposition is caused by a few interactions. The ratio ε/m will strongly diverge because the energy deposition is determined by whether or not a charged particle will interact within m. Consequently, ε will be zero for many mass elements and very large for others. These fluctuations occur because charged particles lose energy in discrete steps.

This view shows that the interactions and energy deposition from ionizing radiation are not uniform on microscopic scales.

In many situations, absorbed dose is therefore totally inadequate to describe radiation action in biological or other material because the mechanisms and effects are dominated by the inhomogeneous microscopic properties, especially at cellular and sub-cellular dimensions. At the same absorbed dose, different types of radiation can produce different biological effects depending on the spatial distribution of energy-deposition events along their path. Low-LET radiation (such as X-rays, γ-rays, and medium to high-energy electrons) deposits energy sparsely along its tracks, generally inducing less severe biological effects per unit dose. Instead, high LET radiation (such

as alpha particles, protons, neutrons, and low-energy electrons) generates very dense energy deposits, increasing the probability of complex and difficult to repair damage at the cellular level (Figure 1.7).

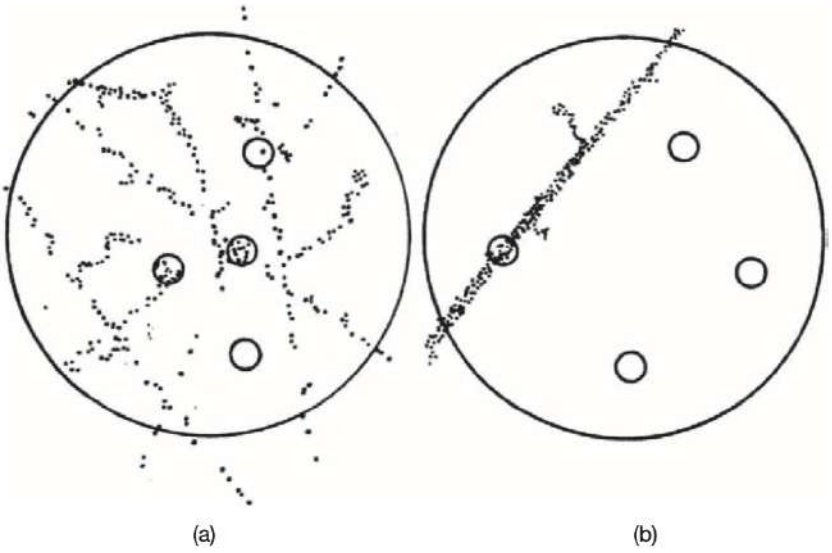

FIGURE 1.7: Comparison of ionization density in a cellular medium: sparsely ionizing low-LET radiation (X-rays) (a) and densely ionizing high-LET radiation (neutrons) (b) [136].

1.3.1 Relative Biological Effectiveness (RBE)

To quantify the responses of living matter to different types of radiation, the concept of relative biological effectiveness (RBE) is introduced. The RBE is the ratio of the absorbed dose of reference radiation (usually 250 keV X-rays) to the absorbed dose of the specific radiation, which produces the same biological effect (typically a 10% survival level is considered):

$$\mathrm{RBE} = \frac{D_{\mathrm{ref}}}{D_R} \tag{1.20}$$

where D_{ref} is a dose from a reference radiation field and D_R is the dose from the radiation field under test required to produce the same specific biologic effect. RBE varies with several factors, including LET, radiation dose, fractionation, dose rate, biological system, endpoint measured, and radiation quality.

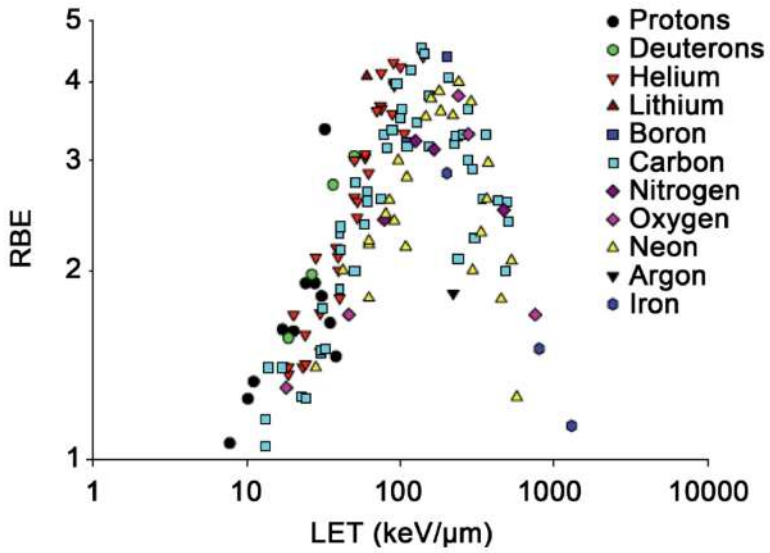

FIGURE 1.8: Relationship between RBE and LET for a multitude of heavy charged ions from protons to iron [257].

A high LET correlates with a high RBE, as more ionization events within short distances result in a higher probability of causing DNA damage, which is difficult for the cell to repair. As shown in Figure 1.8 RBE rises with LET until it reaches a maximum value of 3-8 (depending on the level of cell kill) at LET = 200 keV/m, after which it decreases due to energy overkill.

1.3.2 Biological effects of ionizing radiation

At the microscopic level, incoming rays or particles can interact with orbital electrons in cellular atoms and molecules, leading to excitation or ionization. Excitation transfers enough energy to an orbital electron to displace it further away from the nucleus, however it does not have enough energy to leave the atomic shell. Ionizing radiations promote electron ejection in biological material, resulting in the generation of energetic secondary particles (electrons). These secondary particles can migrate away from their source and release energy into the surrounding medium through interactions with other atoms and molecules. Biological damage induced by ionizing radiation arises from either direct or indirect action of radiation as shown in Figure 1.9.

Direct effect occurs when ionizing radiation interacts directly with critical target molecules within the cell, such as DNA, lipids, and proteins. This interaction causes ionization or excitation, initiating a chain of events that alters the structure of biomolecules. This mechanism is the predominant mode of action of high LET radiation, such as alpha particles and neutrons, and is responsible for approximately two-thirds of total biological damage. DNA has long been considered the most critical target in direct action because, unlike other macromolecules, it is present in a single copy in the nucleus, and its unrepaired damage can be fatal to cells [16].

Indirect effect occurs when radiation interacts with water molecules, which make

up most of the cell. This reaction, called water radiolysis, generates highly energetic and reactive species, particularly free radicals known as Reactive Oxygen Species (ROS). ROS, together with reactive nitrogen species (RNS), are extremely reactive and damage cellular macromolecules and cell structure. Indirect effect is the dominant contribution for low LET radiation (such as X-rays, gamma rays, and beta particles), and is responsible for about two-thirds of the total damage induced by these radiations [215]. Oxygen acts as a radiosensitizer in this process [16].

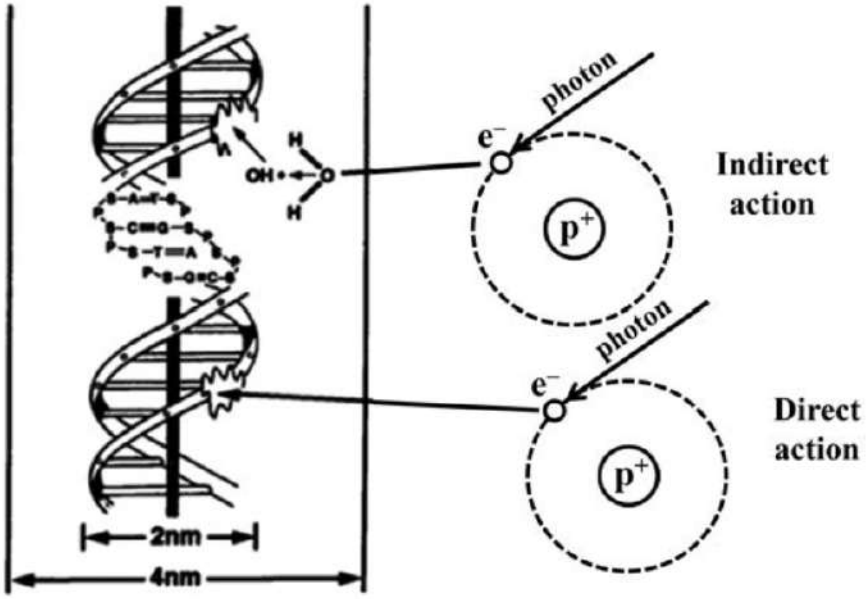

FIGURE 1.9: Comparison between direct and indirect damage to DNA induced by ionizing radiation [17].

Both direct and indirect interactions with DNA can result in a variety of lesions. They can be divided into two groups: **base damage** and **strand breakage**. The structural changes to the DNA base pairs that comprise the genetic code, such as the attachment of an OH molecule to the base or its total removal, are referred to as base damage. Damage to the sugar-phosphate backbone that disrupts the DNA helix structure is referred as a "strand break". These are further divided into single-strand breaks (SSBs), which damage only one strand, and double-strand breaks (DSBs), which damage opposite strands in close proximity. DSBs typically occur with separations of less than ten base pairs and can result in the complete separation of the DNA molecule. A cell exposed to 1 Gy of X-rays usually produces 103 damaged bases and SSBs, while the yield of DSBs is about 30–40 per Gray [276].

One of the fundamental indicators of the radiobiological effect of irradiation is the cell Surviving Fraction (SF), that is to say, the percentage of irradiated cells in a sample that survive a given absorbed dose while maintaining their reproductive integrity (remaining clonogenic cells). Cell survival curves, which relate the SF to the absorbed dose, are particularly useful to predict cell survival and cell killing probabilities.

1.3.3 Linear-Quadratic Model (LQM)

The linear-quadratic model is an alternative to describe the dose-response relationship between ionizing radiation exposure and stochastic effects. In particular, it describes the effects that radiation has on cell survival probability. According to the model, the survival fraction after irradiation can be calculated as [37]:

$$SF(D) = e^{-\alpha D - G\beta D^2} \tag{1.21}$$

where G represents the Lea-Catcheside factor [159],[158] a time-dependent factor, whose effect is to reduce β for protracted irradiations. α (Gy^{-1}) and β (Gy^{-2}) are radiobiological parameters. The linear component α is dominant at low doses and is associated with the production of double-strand DNA breaks and lethal single-radiation-track damage [36][116][184]. The quadratic term, β, models the probability of misrepair events and becomes dominant at higher doses, generating the characteristic "shoulder" of the survival curve. Double-strand breaks can be repaired within an exponentially distributed random time; however, if another break occurs nearby before repair is completed, misrepair may happen. This probability increases quadratically with dose [116][184].

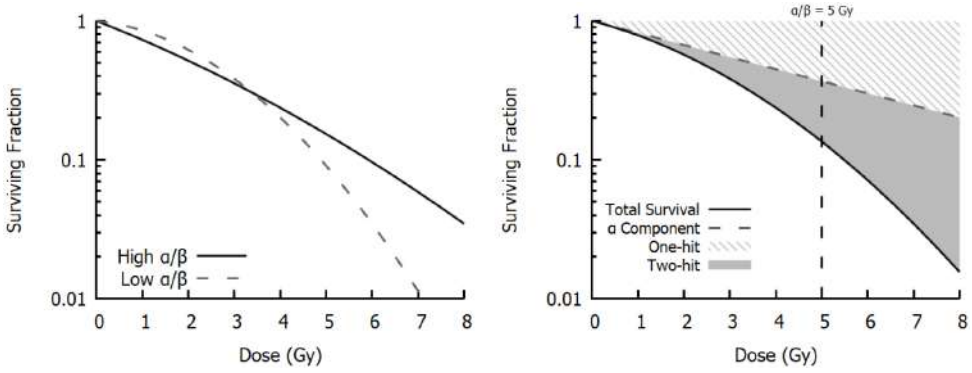

FIGURE 1.10: Examples of LQ survival fraction (SF) curves. **Left:** SF for cell lines with high and low α/β ratios; high α/β lines show an almost linear response, while low α/β lines display pronounced curvature. **Right:** Separation into one- and two-hit kinetics; at low doses, cell killing is dominated by single-hit events, whereas multi-hit mechanisms become more relevant at higher doses [184].

The α/β ratio is important for determining the radiosensitivity of a cell (the ratio of damage to repair rate). Cells with a higher α/β ratio show greater radiosensitivity and a more linear response curve. Cells with a low α/β ratio are less radiosensitive and exhibit greater curvature in the cell response curve, as shown in Figure 1.10.

1.4 Principles of radionuclide therapy

Targeted Radionuclide Therapy (TRT) involves the systemic or selective local-regional administration of radioactive atoms that target specific areas associated with the lesion. In this therapy, the goal is to deliver the radioactive isotope in the form of a radiopharmaceutical, coupling it to an appropriate molecular complex (carrier) that acts as a delivery vehicle. The radiopharmaceutical exploits a specific physiological or biochemical mechanism of the lesion to accumulate in malignant cells. This is obtained by binding to targets that are expressed only or over-expressed in the tumour cells [99].

The success of TRT depends on the choice of the appropriate radionuclide. This assessment must consider physical properties, such as the type of emission and half-life, which ideally should be in the order of a few days to ensure effective treatment cycles. Chemical properties, which determine the feasibility of its binding to the carrier molecule, must also be considered. Finally, the effectiveness of the treatment is linked to the size of the lesion, since the range (radius of action) of the emitted radiation must be adequate to effectively hit the target.

The most commonly used therapeutic radionuclides include β^-emitters (such as ^{131}I, ^{177}Lu, and ^{90}Y) [247]. These are the best choice in most cases due to their electron range (from a few millimeters to a few centimeters). However, α emitters and AEs emitters are increasingly being used for millimeter and submillimeter ranges [7].

TRT is a safe and effective approach with minimal toxicity compared to other systemic options such as chemotherapy and biological therapy. In addition, most clinical radionuclides emit detectable gamma photons, which allows non-invasive visualization of the biodistribution of the therapeutic agent using nuclear medicine imaging techniques, a crucial property in the theranostic approach [247]. While β^- emitters are effective for irradiating large tumors due to their long range, they are less suitable for micrometastases or minimal residual disease and have the disadvantage of increasing toxicity to surrounding healthy tissue. For the eradication of isolated tumor cells and micrometastases, radionuclides that emit AEs or α particles are considered more appropriate [81][112]. Auger electrons are high LET radiation that release their energy over an extremely short range, in the order of nanometers. The therapeutic effectiveness of AEs lies in their ability to induce extensive and difficult-to-repair DNA fragmentation [38]. To maximize the cytotoxic effect, the AE emitter must be in proximity to the nuclear DNA. In fact, the dose absorbed in the cell nucleus can be 94 times higher if irradiation with ^{99m}Tc occurs in the nucleus than when it occurs on the cell membrane [34]. An ideal radionuclide for AE therapy should have [256]:

- Electrons emitted with energies below 40 keV;
- A photon-to-electron emission ratio (p/e) below 2;
- A biological half-life between 30 minutes and 10 days;

- The ability to be efficiently incorporated into a selective carrier molecule that binds to nuclear DNA [263].

In the next section, the physical parameters of some β^- and AE emitters employed or currently under investigation for TRT applications are explained. The radionuclides examined were chosen based on previous studies indicating their therapeutic potential.

1.4.1 β^- emitters

^{131}I

Iodine-131 (^{131}I) is a medium-energy β^- emitter with a half-life of 8.02 days. The β^- particles have a maximum energy of 807 keV and an average energy of 182 keV, with a maximum range of 3.6 mm in water [140]. ^{131}I decays to excited levels of ^{131}Xe, including the metastable state ^{131m}Xe, emitting high-energy γ rays primarily at 364 keV (81.7%), 637 keV (7.2%), and 723 keV (1.8%). These γ emissions allow imaging via scintigraphy or SPECT, though with low spatial resolution, and contribute little to tumor dose while increasing exposure to the patient and medical staff. ^{131}I can be produced in nuclear reactors via ^{235}U fission or by neutron irradiation of TeO_2 (^{130}Te) through the ^{130}Te(n,γ)^{131}Te and ^{130}Te(n,γ)^{131m}Te reactions. ^{131}Te and ^{131m}Te decay to ^{131}I with half-lives of 25 min and 30 h, respectively [151]. For theranostic applications, the combined use of ^{124}I and ^{131}I is considered more effective. ^{131}I has been successfully used in the diagnosis and treatment of thyroid cancer, as well as non-malignant thyroid disorders such as hyperthyroidism. Other therapeutic applications include targeted radionuclide therapy (TRT) of non-Hodgkin lymphoma (NHL) with ^{131}I-tositumomab (Bexxar) and treatment of neuroendocrine tumors with ^{131}I-metaiodobenzylguanidine (^{131}I-MIBG) [99].

^{90}Y

Yttrium-90 (^{90}Y) is a high-energy β^- emitter with a half-life of 64.1 h (2.67 d), decaying to ^{90}Zr. Its β^- particles have a maximum energy of 2.28 MeV and a range of up to 11.8 mm in water [140]. Unlike ^{131}I, ^{90}Y emits negligible γ radiation; thus, a theranostic pair is typically formed with ^{111}In for SPECT imaging, although post-therapy ^{90}Y Bremsstrahlung or PET imaging is also feasible due to the low positron emission (3×10^{-5} per β decay) [281][246]. ^{90}Y is commonly obtained from a ^{90}Sr/^{90}Y generator, with ^{90}Sr produced by ^{235}U fission. ^{90}Y radiopharmaceuticals have been successfully applied in targeted radionuclide therapy (TRT). Clinical examples include ^{90}Y-ibritumomab tiuxetan (Zevalin) for consolidation therapy of non-Hodgkin lymphoma (NHL) [189], peptide receptor radionuclide therapy (PRRT) with ^{90}Y-DOTATATE and ^{90}Y-DOTATOC for metastatic neuroendocrine tumors [271][226], and ^{90}Y-labeled PSMA–617 for metastatic castration-resistant prostate cancer [224]. Additionally, ^{90}Y is widely used in radioembolization to treat primary and metastatic liver tumors [234].

^{177}Lu

Lutetium-177 (^{177}Lu) is a medium-energy β^- emitter with a half-life of 6.647 d. It emits β^- particles with a maximum energy of 497 keV and a range of 1.9 mm in water [140]. In addition, ^{177}Lu emits γ photons at 208 keV (11%) and 113 keV (6.4%), suitable for quantitative imaging before and during treatment. ^{177}Lu can be produced in nuclear reactors via two routes [62]: (i) direct production by neutron irradiation of ^{176}Lu targets (^{176}Lu(n,γ)^{177}Lu), and (ii) indirect production via ^{176}Yb(n,γ)^{177}Yb $\beta^- \rightarrow ^{177}$Lu, which requires chemical separation from ^{176}Yb. Therapeutic applications of ^{177}Lu are similar to those of ^{90}Y. For example, in the treatment of metastatic neuroendocrine tumors, ^{177}Lu has largely replaced ^{90}Y due to comparable efficacy with lower toxicity [99]. Clinical applications include ^{177}Lu-DOTATATE for advanced, progressive somatostatin-receptor–positive midgut neuroendocrine tumors [252], ^{177}Lu-PSMA-617 for metastatic castration-resistant prostate cancer showing high response rates and pain reduction, and ^{177}Lu-lilotomab satetraxetan (Betalutin), currently under investigation for B-cell non-Hodgkin lymphoma (NHL) [154].

^{161}Tb

Terbium-161 (^{161}Tb) has emerged as a potential alternative to ^{177}Lu for targeted radionuclide therapy. It has a half-life of 6.906 d and emits β^- particles with a maximum energy of 593 keV. In contrast to ^{177}Lu, ^{161}Tb emits a substantially higher number of very low-energy Auger electrons (AE) and low-energy conversion electrons (CE), mainly below 40 keV. These high-LET electrons enhance the local dose deposition within $\sim$30 μm of the decay site, increasing tumor irradiation without additional renal toxicity [118]. ^{161}Tb also emits photons at 75 keV (10.2%), allowing post-therapy SPECT imaging similarly to ^{177}Lu. Moreover, ^{161}Tb fits into a theranostic framework, as isotopic terbium companions can serve for pre-therapy imaging, whereas ^{177}Lu lacks an optimal diagnostic match [191][287]. Because ^{161}Tb and ^{177}Lu are both radiolanthanides, they share comparable chemical properties and can be radiolabeled using similar methods [161][192]. No-carrier-added ^{161}Tb can be produced in clinically relevant amounts via the ^{160}Gd(n,γ)^{161}Gd $\beta^- \rightarrow ^{161}$Tb reaction [161][102]. Experimental data, including cell survival assays and mouse xenograft studies, have demonstrated the superiority of ^{161}Tb over ^{177}Lu [105][192][193]. Additionally, theoretical dosimetry indicates that ^{161}Tb may outperform ^{177}Lu in very small tumors [264].

1.4.2 AE emitters

^{125}I

Iodine-125 (^{125}I) has a half-life of 59.4 d and decays to stable ^{125}Te by electron capture. Its decay emits conversion electrons (3.7–35.5 keV), Auger electrons (23 eV–30.3 keV), and low-energy γ rays (average $\sim$25 keV). While the photon emissions are useful in low–dose-rate brachytherapy with permanent ^{125}I seeds, they

Radionuclide	^{131}I	^{90}Y	^{177}Lu	^{161}Tb
Half-life (day)	8.02	2.67	6.647	6.906
β^- mean energy (keV)	182	932.9	133.3	154.3
Daughter nucleus	^{131}Xe (stable)	^{90}Zr (stable)	^{177}Hf (stable)	^{161}Dy (stable)
CE intensity per decay	6.46%	0.01%	15.47%	142%
CE energy per decay (keV)	9.57	0.2	13.52	39.28
CE energy range (keV)	45.6–602.4	1742.7	6.2–206.3	3.3–98.3
AE intensity per decay	69.75%	0.13%	111.65%	1096.4%
AE energy per decay (keV)	0.41	0.0007	1.13	8.94
AE energy range (keV)	0.026–32.9	0.022–1.8	0.01–61.7	0.018–50.9
Total energy/decay (keV)	574.5	933.1	183.0	238.9

TABLE 1.1: Properties of some β^- emitters [223].

represent a drawback for TRT and are not suitable for imaging. Large-scale production of ^{125}I is achievable through neutron irradiation of enriched gaseous ^{124}Xe via the ^{124}Xe(n,γ)^{125}Xe $\beta^- \rightarrow ^{125}$I reaction [151]. ^{125}I is the most extensively studied Auger emitter, and has been central to investigating the dependence of AE cytotoxicity on subcellular localization, particularly DNA incorporation. Its therapeutic potential has been demonstrated in several tumor models using ^{125}I-iododeoxyuridine (^{125}IUdR), a thymidine analogue that integrates into DNA [28]. Although some ^{125}I-labeled agents have advanced to phase II clinical trials [149], the use of ^{125}I in TRT remains experimental. The long half-life of ^{125}I, among other practical limitations, complicates its clinical implementation [104].

^{119}Sb

Antimony-119 (^{119}Sb) has a half-life of 38.19 h (1.59 d) and decays to stable ^{119}Sn by electron capture. Its suitability for the treatment of small tumors and micrometastases has been highlighted in several studies [22], and its combination with ^{117}Sb ($T_{1/2}$ = 2.8 h) has been proposed to enable SPECT-based 3D dosimetry[258][259].

Two main production routes have been proposed to obtain ^{119}Sb in clinically relevant amounts: (i) direct cyclotron production via proton irradiation of enriched ^{119}Sn through the ^{119}Sn(p,n)^{119}Sb reaction [259]; (ii) indirect production using a ^{119m}Te/^{119}Sb generator [20], in which the parent nuclide ^{119m}Te ($T_{1/2}$ = 4.7 d) is produced by high-energy proton irradiation of natural Sb targets via the ^{121}Sb(p,3n)^{119m}Te and ^{123}Sb(p,5n)^{119m}Te reactions, and subsequently decays to ^{119}Sb by electron capture. The generator-based route may yield ^{119}Sb in quantities 10–100 times greater than the direct route, while also ensuring longer availability of the isotope—an essential factor for the development of ^{119}Sb radiopharmaceuticals [20].

^{103m}Rh

Rhodium-103m (^{103m}Rh) has a half-life of 56.1 min and decays to stable ^{103}Rh via isomeric transition, emitting predominantly conversion and Auger electrons, with very low photon yield. Each decay produces roughly 30 times more low-energy (< 40 keV) electrons than photons [139]. Although the potential of ^{103m}Rh for treating small tumors was recognized early [22], large-scale production remains challenging;

however, its short half-life does not preclude use when administered locally (e.g., intratumorally or intracavitarily). ^{103m}Rh can be obtained from generator systems based on its parents ^{103}Ru ($T_{1/2}$ = 39.21 d) or ^{103}Pd ($T_{1/2}$ = 16.99 d). Therapeutic quantities may be produced through: (a) fission production of ^{103}Ru via ^{235}U(n,f); (b) neutron capture on enriched ^{102}Ru; (c) neutron activation of enriched ^{102}Pd to yield ^{103}Pd; (d) proton or deuteron irradiation of ^{103}Rh via the ^{103}Rh(p,n)^{103}Pd and ^{103}Rh(d,2n)^{103}Pd reactions [250]. Solution-based generators using either ^{103}Ru or ^{103}Pd have been demonstrated [250]. The ^{103}Ru route, however, presents drawbacks due to β^- and γ emissions from the parent nuclide, which complicate shielding and risk compromising the dosimetric advantages of ^{103m}Rh if contamination occurs. Nonetheless, progress has been made in purifying ^{103}Ru from irradiated thorium targets [177], and advances in ^{103}Pd/^{103m}Rh generators have also been reported. A solid-phase generator based on neutron-activated ^{102}Pd was shown to yield high-specific-activity ^{103m}Rh suitable for preclinical studies, although current efficiencies remain insufficient for clinical use [139].

^{99m}Tc

Although ^{99m}Tc is widely known as an imaging agent, its potential as a therapeutic agent has only recently been explored. ^{99m}Tc decays to ^{99}Tc by isomeric transition (IT), followed by internal conversion (IC) and subsequent electron emission (10%), or by gamma photon emission (90%). ^{99m}Tc emits Auger electrons with energies ranging from approximately 0.9 keV to 15.4 keV, producing 4 Auger electrons and 1.1 internal conversion electrons per decay. The range of AEs emitted by ^{99m}Tc varies from 2.05 nm to 251 μm. Coster-Kroning (CK) MMX electrons (average energy 116 eV, range 6 nm) and CK NNX electrons (average energy 33 eV, range 2 nm) are among the most interesting for TRT [115]. ^{99m}Tc has a physical half-life of 6 hours. A short half-life is advantageous for achieving higher absorbed doses per unit of time [263]. For example, in 2 hours, ^{99m}Tc undergoes 206 decays, a significantly higher number than ^{123}I (100 decays in 2 hours, $T_{1/2}$=13 hours) or ^{125}I (1 decay in 2 hours, $T_{1/2}$=60 days). Furthermore, the wide availability of ^{99m}Tc via in situ generators and its low cost represent an important advantage over other radioisotopes. Being a radiometal, antibodies labeled with ^{99m}Tc tend to remain trapped inside the target cell for longer periods after internalization, a crucial factor for TRT with AEs [103]. The emission of gamma at 140.511 keV makes this radioisotope an ideal candidate for in vivo imaging, allowing therapy monitoring and follow-up using the same radiotracer. Its radiobiological efficacy is comparable to other Auger electron emitters, thus it is maximum when the decay occurs close to the DNA [127]. Monte Carlo simulations estimated that ^{99m}Tc AEs induce 1.27 single-strand breaks (SSBs) per localized decay at the DNA base by direct effect (compared to 2.58 for ^{123}I and 0.95 for ^{67}Ga). Double-strand breaks (dsb) caused by ^{99m}Tc have been estimated at 0.11 per decay by direct effect and 0.68 per decay by indirect effect [92]. Despite its advantages, ^{99m}Tc has limitations, particularly a low AE yield: it emits less than 1% AE per decay, which is much lower than ^{125}I (3.7%–19.9%), ^{123}I, and ^{201}Tl. For this reason, and in order to

develop more selective and stable carrier molecules, further studies are needed to better define their dosimetric implications and radiobiological efficacy.

TABLE 1.2: Properties of Some Auger-Electron-Emitters [58][223].

Radionuclide	^{103m}Rh	^{119}Sb	^{125}I	^{99m}Tc
Half-life (day)	0.039	1.591	59.4	0.25
Type of decay (%)	IT (100%)	EC (100%)	EC (100%)	IT (100%)
Daughter nucleus	^{103}Rh (stable)	^{119}Sn (stable)	^{125}Te (stable)	^{99}Tc (unstable)
CE (intensity per decay)	99.06%	83.97%	94.47%	110%
CE (energy per decay, keV)	34.97	16.97	7.28	15.4
CE energy range (keV)	16.56-39.76	19.4-23.9	3.7-35.5	100-140
AE (intensity per decay)	587.94%	2368%	2300%	400%
AE (energy per decay, keV)	2.72	8.86	11.96	0.9
AE energy range (keV)	0.034-22.28	0.011-27.9	0.023-30.3	0.2-17.8
Total energy per decay (keV)	39.34	48.97	61.74	142.6

1.5 Heavy ion and proton therapy

External beam radiation therapy is a fundamental modality in the treatment of cancer, but the primary goal of this therapeutic modality remains the delivery of the maximum dose to the target region while minimizing irradiation of surrounding healthy tissue. In this context, the use of high-energy protons and hadrons represents a significant innovation as it provides highly conformal dose distributions, sparing surrounding healthy tissues thanks to the physical properties of the Bragg peak.

The main advantage of accelerated ions (protons and heavy ions) over conventional photon and electron therapy lies in their unique depth dose distribution profile. These charged particles deposit most of their kinetic energy at the end of their path, as previously discussed in section 1.2.3.

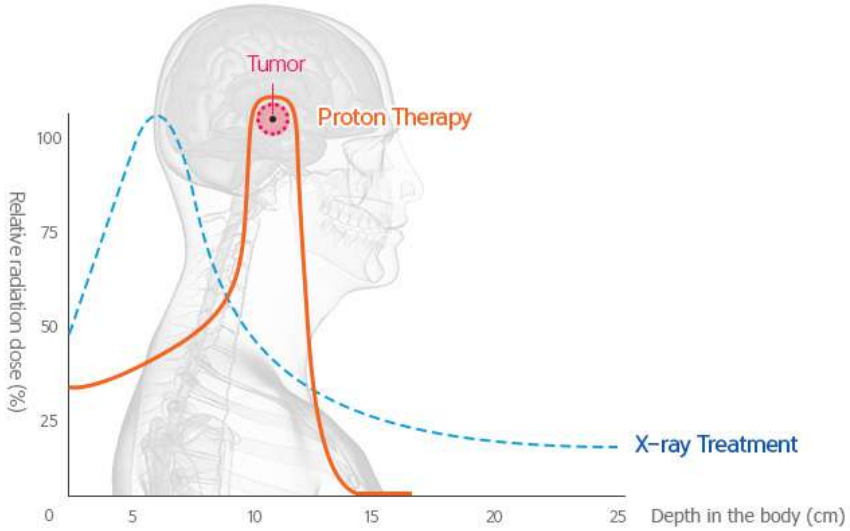

FIGURE 1.11: Dose distribution of a proton beam (Bragg peak) compared to X-ray treatments. Retrieved from `http://www.samsunghospital.com/home/proton/en/whatIsProtonTherapy/principle.do`

The depth of the Bragg peak can be precisely controlled by varying the energy of the incident particle, making protons and heavy ions particularly suitable for treating deep-seated tumors (see Figure 1.11). The combination of several Bragg peaks can also be used to increase the dosage in the tumor volume by using different converging beams.

Another advantage of protons is that the primary radiation field does not give any dose after the Bragg peak, although some dose is still deposited by secondary particles and target fragmentation. This has a particular advantage over X-rays since it spares sensitive structures possibly located beyond the tumor volume, such as the brainstem or bladder, which may be located close to the tumor volume. Collimated proton and heavy ion beams also undergo less scattering than photon or electron beams, allowing for a higher degree of dose conformity. Moreover, heavy ions have a higher LET compared to photons. This LET rises sharply near the end of the particle range, giving charged particles such as protons and heavier ions a higher RBE compared to photon and electron therapy. These features makes heavy ions suitable for the treatment of radioresistant tumors.
The initial proposal to use accelerated ions or protons for therapeutic purposes dates back to 1946 by Wilson [277]. The first clinical use of protons took place in 1954 [78]. Thanks to continuous advances in accelerator technologies, such as synchrotrons and cyclotrons, the availability of facilities for proton and heavy ion therapy has increased significantly. As of 2023, there are 125 facilities in total, of which 110 are proton facilities, and 15 are carbon therapy facilities [74].

To deliver a uniform dose to the treatment volume, there are two methods: passive scattering and active scanning (raster-scanned) delivery [178].

The traditional passive delivery method in hadron therapy, based on a spread-out Bragg peak (SOBP), proves to be a reliable approach providing solid dose distribution as it is less sensitive to uncertainties in the beam range [59][277]. Although it offers less flexibility in shaping the dose for complex target geometries, this method relies on physical devices such as collimators and patient-specific boluses, which increase the unwanted dose outside the target caused by scattering and secondary neutron production [61].

On the contrary, active delivery techniques such as pencil beam scanning can overcome many of the limitations described above by steering magnetically a narrow beam across the tumor, "painting" the dose. This kind of approach allows higher conformality and reduces dose to healthy tissues, avoiding patient-specific compensators [204][167]. Moreover, active scanning is more sensitive to organ motion and range uncertainties and requires more precise control when it comes to energy switching between layers, making the system more technically complex [204]. Overall, while passive delivery is still widely used for simpler treatments, active scanning is preferred for complex tumor geometries where sparing of critical organs is essential.

1.6 Gold nanoparticles as radiosensitizers

As already seen, radiotherapy has limitations, including toxic side effects due to dose heterogeneity and prolonged exposure to healthy tissues. In addition, the development of radio-resistance by cancer cells may require higher doses of radiation, increasing the risk of damaging or killing normal cells and tissues [194]. To address these challenges, numerous strategies have emerged, including the use of radiosensitizers, defined as chemical or biological compounds capable of increasing the effective dose of radiation therapy in cancer cells [186][163][248].

In this context, the development of nanotechnology has opened up new potential therapeutic strategies. Nanomaterials containing elements with high atomic numbers (Z), such as bismuth (Z=83)[113], gold (Z=79)[170][153][288], tungsten (Z=74)[280], and others, are commonly used as dose enhancers. Among these, gold nanoparticles (AuNP) are considered ideal radiosensitizers due to their high X-ray absorption and unique physicochemical properties. While originally developed for conventional photon-based radiotherapy, the potential of AuNPs has recently been highlighted in Proton Therapy (PT). Due to their high atomic number and favorable biological properties, AuNPs act as radiosensitizers by amplifying the generation of secondary electrons and reactive oxygen species (ROS) upon proton irradiation. This amplification enhances DNA damage specifically within tumor cells while preserving the advantages of the Bragg peak, which minimizes damage to healthy tissues [43].

1.6.1 Physicochemical properties and targeting strategies

Gold nanoparticles have numerous advantages that make them suitable for biomedical and therapeutic applications. Their high atomic number (Z=79) provides a strong mass-energy absorption coefficient, which, for keV photon energies, can be approximately 100 times greater than that of soft tissues [248]. Additionally, AuNPs are generally bio-compatible and characterized by low toxicity, especially when compared to traditional therapeutic agents such as cisplatin. However, concerns regarding their long-term accumulation in the reticuloendothelial system (RES)—organs like the liver and spleen—remain a challenge, with accumulation influenced heavily by size and surface chemistry [289].

To function effectively, AuNPs must reach the tumor site in sufficient quantities. Particle size is a critical determinant of pharmacokinetics; nanoparticles smaller than 6 nm are rapidly cleared by the kidneys, whereas larger ones are typically captured by the RES [171][197]. Nanoparticles smaller than 100 nm can accumulate effectively in tumor tissues by exploiting the Enhanced Permeability and Retention (EPR) effect [50]. The optimal size varies depending on the therapy; while spherical AuNPs of 50 nm have shown high enhancement in photon radiotherapy in vitro [51], Monte Carlo simulations for Proton Therapy suggest that particles around 30 nm may strike the optimal balance for maximizing the Dose Enhancement Ratio (DER) near DNA targets [176].

However, passive accumulation via EPR is often insufficient. Upon entering biological fluids, AuNPs acquire a "protein corona" that can alter their biological

identity, immune recognition, and distribution [44]. Consequently, modern strategies employ active targeting, where the large surface-to-volume ratio of AuNPs is utilized to functionalize them with ligands such as antibodies, peptides, or folate [50]. This approach not only improves tumor specificity but also enhances internalization into cancer cells, which is vital for therapeutic efficacy in PT [43]. Recent advances also include Green Synthesis methods, which use natural products like plant extracts to reduce toxic chemicals and enhance bio-compatibility [235].

1.6.2 AuNPs radiosensitization mechanisms

The radiosensitizing effect of AuNPs is not a singular event but a complex cascade involving physical, chemical, and biological phases. It arises fundamentally from the difference in mass–energy absorption coefficients between the nanoparticles and soft tissues. In conventional radiotherapy, the interaction is dominated by the photoelectric effect. Incident photons are absorbed by bound electrons in the inner shell (K, L, or M shells) of the gold atom, ejecting these energized electrons. The photoelectric effect is strongly dependent on both the energy of the photon and the binding energy of the electrons in the atom. Since AuNPs have a high atomic number (Z=79), their cross section for X-rays is proportionally very high (approximately between Z^3 and Z^5).

When a photon is absorbed, the electron vacancy created in the gold atom is filled by electrons from the outer layers through the Auger effect (see section 1.1.1). This process releases low-energy photons (fluorescence) and a cascade of secondary electrons (such as Auger electrons). These low-energy electrons have a range of several microns and are capable of causing highly localized ionization events, thus increasing the radiation dose deposited in sub-cellular volume.

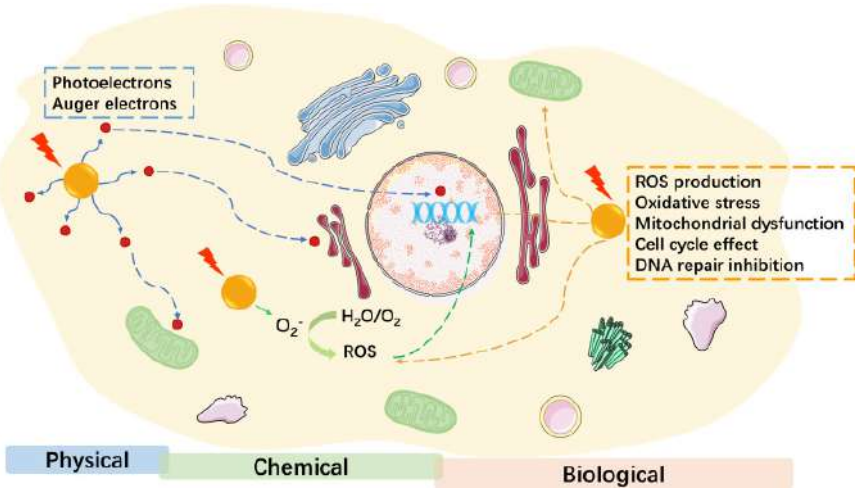

FIGURE 1.12: The potential mechanisms of GNP radiosensitization, which could be summarized as three parts: 1) physical dose enhancement, including the Compton effect and the photoelectric effect; 2) chemical contributions based on the chemical sensitization of DNA to radiation-induced damage as well as the increased generation and catalysis of radicals; 3) biological phase could be divided into Reactive Oxygen Species (ROS) production, oxidative stress, mitochondrial dysfunction, cell-cycle effect, DNA repair inhibition and other biological mechanisms (such as autophagy and endoplasmic reticulum stress). [50]

In Proton Therapy, the physical mechanism also leads to localized dose enhancement. When irradiated with protons, AuNPs serve as dose enhancers by interacting with the proton beam to increase the generation of secondary electrons.

Following the physical energy deposition, chemical mechanisms further amplify the damage. The electronically active surfaces of AuNPs act as catalysts, particularly small AuNPs (<5 nm), promoting the transfer of electrons to molecular oxygen [124][164][278]. This leads to the production of Reactive Oxygen Species (ROS), such as hydroxyl radicals and superoxide anions. The increase in ROS is closely related to the emission of Auger electrons and photons from AuNPs, as well as to the secondary radiolysis of water.

Excess ROS causes indirect damage to DNA, proteins, and lipid membranes through oxidation, which in turn triggers apoptosis or cell death [60][211][210]. The localized ionization and oxidative stress result in complex DNA lesions, including Single-Strand Breaks (SSBs) and, more critically, Double-Strand Breaks (DSBs). AuNPs have been shown to increase the frequency of DSBs, which are particularly lethal because they disrupt the continuity of genetic material and are difficult to repair [169][279][253].

In PT, the inclusion of AuNPs considerably increases the generation of ROS, resulting in higher levels of oxidative damage than PT alone. AuNPs increase the quantity of secondary electrons, which interact with water molecules to produce ROS, as shown by Lo et al. [166]. In their work, AuNP-loaded tumor cells exposed to a proton beam in the spread-out Bragg peak region produced much more ROS,

resulting in increased cytotoxicity due to mitochondrial malfunction and cellular damage.

1.6.3 Gold nanorods: synthesis and applications

Among the various morphologies of gold nanoparticles, Gold Nanorods (AuNRs) offer distinct advantages. They are typically synthesized using the seed-mediated growth method, which allows for precise control over their size and shape. This method involves first synthesizing small gold seeds and then promoting their growth in the presence of additional gold ions and a reducing agent [138].

The primary advantage of AuNRs lies in their optical versatility. Unlike spherical nanoparticles, AuNRs exhibit two distinct Surface Plasmon Resonance (LSPR) bands: a transverse band in the visible region and a longitudinal band that can be tuned to the near-infrared (NIR) region [179][97]. This NIR absorption is particularly valuable for multimodal therapies, as it allows for deep tissue penetration, enabling the combination of radiotherapy with Photothermal Therapy (PTT) [286][254][275].

Additionally, AuNRs possess a large surface area relative to their volume, making them reliable platforms for conjugating high loads of therapeutic agents or antibodies [50]. While spherical particles are often cited for efficient cellular uptake, the ability of AuNRs to be functionalized and their potential for synergistic thermal and radiation enhancement make them a strategic choice for advanced cancer treatments [255].

The integration of Gold Nanoparticles into radiotherapy and proton therapy represents a promising frontier in precision oncology. By exploiting the physical phenomena of the photoelectric effect and the Auger cascade, AuNPs can significantly increase the local dose delivered to tumors while sparing healthy tissue. However, translating these findings into clinical practice requires addressing challenges related to long-term toxicity, clearance pathways (e.g., liver accumulation), and the standardization of synthesis protocols. Future research must focus on optimizing these parameters to realize the full clinical potential of AuNR-mediated radiosensitization.

Chapter 2

Microdosimetry: principles and detectors

2.1 Microdosimetry quantities

Microdosimetry, initially developed by Keller and Rossi in the 1960s, is the technique that analyzes the deposition of radiation energy at the microscopic level to explain the different biological effectiveness of radiation with different LETs, for the same physical dose. The stochastic equivalent of the dose is the specific energy z, as discussed in section 1.3. From a microdosimetric point of view, the lineal energy y is introduced, defined as:

$$y = \frac{\epsilon}{\bar{l}}. \tag{2.1}$$

where ε is the energy imparted per event and l is the mean chord length. Lineal energy is measured in keV/μm and is considered the stochastic equivalent of LET. The average distance a particle will travel through a radiation-sensitive region is known as the mean chord length. For an isotropic uniform field, l can be calculated via the Cauchy formula:

$$l = 4\frac{V}{S} \tag{2.2}$$

where V is the volume, and S is the surface area of the radiation-sensitive volume. Since energy deposition has stochastic behavior, probability distributions must be used. A "single event" is defined as the energy deposited by particles that are statistically correlated. The distribution of the single event is defined as

$$f(y) = \frac{dF(y)}{dy} \tag{2.3}$$

where $f(y)$ is the distribution of lineal energy under the condition that at least one event has occurred at the site, and $f(y)$ is the probability of having an event with lineal energy between y and y+dy. Since microdosimetry does not take into account particles that pass through the volume without interacting, the function $f(y)$ is normalized to unity and excludes the component with y=0. The lineal energy dose distribution $D(y)$ is the fraction of absorbed dose with lineal energy less than or equal

to y. The dose probability density is:

$$d(y) = \frac{dD(y)}{dy} \tag{2.4}$$

The moments of these distributions provide important mean quantities. The first moment is the frequency mean lineal energy $\bar{y}_F$:

$$\bar{y}_F = \int_0^\infty y\, f(y)\, dy \tag{2.5}$$

The lineal energy dose distribution $d(y)$ is related to $f(y)$ by the equation:

$$d(y) = \frac{y\, f(y)}{\bar{y}_F} \tag{2.6}$$

The expectation value of d(y), commonly referred to as the dose mean lineal energy $\bar{y}_D$, is therefore calculated as the ratio of the second moment of $f(y)$ over its first moment:

$$\bar{y}_D = \int_0^\infty y\, d(y)\, dy = \int_0^\infty y^2 f(y) dy \tag{2.7}$$

For the specific energy z, mean quantities and probability distributions $f(z)$ are also defined. Despite being a stochastic variable, z can indicate the total energy transferred by multiple events.

The result of sampling the lineal energy distribution is the microdosimetric spectrum [143]. Using a solid-state microdosimeter or tissue-equivalent proportional counter (TEPC), this can be measured experimentally.

Since microdosimetry involves different radiation fields, the values of lineal energy y can cover four or five orders of magnitude. Consequently, the microdosimetric spectrum is usually represented in semi-logarithmic form: the x-axis shows y on a logarithmic scale, while the y-axis shows the function $yd(y)$ on a linear scale.

The area under the curve between two y values is proportional to the fraction of dose delivered by events that have linear energies in that specific interval. The Figure 2.1 shows an experimental microdosimetric spectrum obtained with protons.

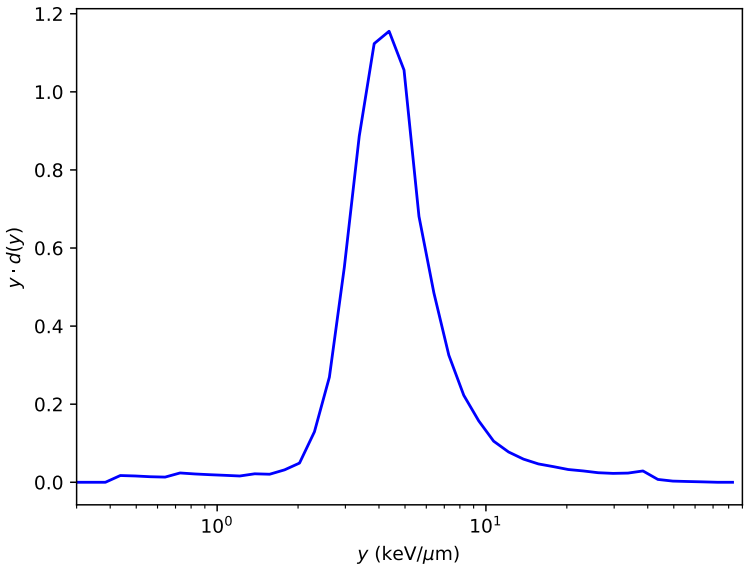

FIGURE 2.1: Microdosimetric spectra of clinical proton beam in the Bragg Peak region, measured at TIFPA using a diamond detector.

2.2 Radiobiological models based on microdosimetry

2.2.1 RBE weighting functions

Microdosimetric distribution provides information on the quality of radiation in a beam, and is useful for estimating biological effectiveness and understanding how the radiation field changes in depth within the tissue.

Menzel, Pihet, Wambersie et al. [185][214] [273][274] proposed the microdosimetric RBE-weighting function approach to compare the beam quality of various neutron and proton therapeutic installations using measured microdosimetric distributions of lineal energy. This approach evaluates the RBE by combining microdosimetric spectra of y with an experimentally generated biological weighting function, $r(y)$, for specific cell lines and endpoints, building on previous studies on proton beams [150][117].

For a population receiving a fraction of dose $d(y)dy$ corresponding to the lineal energy y, $P(y)$ is the cellular response function. The biological impact E per unit dose, or the linear α parameter, is expressed as follows:

$$\alpha = \frac{E}{D} = \int P(y)\, y\, d(y)\, dy \equiv \int r(y)\, d(y)\, dy \tag{2.8}$$

where $r(y)$ is defined as the response function. Typically, experimental measures are used to determine either $P(y)$ or $r(y)$. $r(y)$ can be rewritten as [190][201]:

$$r(y) = \sigma E \left(1 - \exp\left[-\frac{a_1 y + a_2 y^2 + a_3 y^3}{y}\right]\right) \tag{2.9}$$

where the parameters σ_E, a_1, a_2, and a_3 are independent of radiation quality and specific to the radiobiological endpoints. These parameters are experimentally found by fitting a set of different measurements of α_i or RBE_α, $i = \alpha_i/\alpha_X$, where α_X is defined as related to irradiation with 250 kVp X-ray employing multiple irradiation modalities with variable radiation quality i=1,2,3,..., N. Thus, the set of relationships that have to be fitted to the data is:

$$\mathrm{RBE}_{\alpha,i} = \int r(y)\, d_i(y)\, dy, \quad i = 1, \ldots, N \tag{2.10}$$

The solution of Equation 2.10 can be obtained with different methods, such as the iterative procedures like the Loncol [168] which iteratively updates an initial estimate function $r(y)$ to best match Equation [168]. Figure 2.2 shows Loncol's biological weighting function $r(y)$ [168].

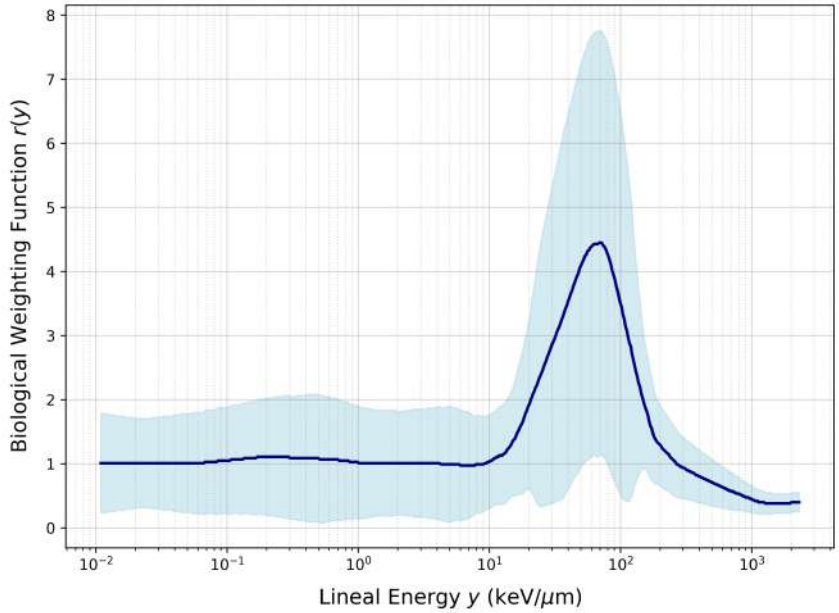

FIGURE 2.2: Loncol's biological weighting function. Figure adapted from [168].

The plot begins with a plateau corresponding to low-LET radiation (y $\leq$10 keV/μm). It then rises to reach a maximum of 70 keV/μm due to high-LET radiation. After this maximum, it becomes lower than one. This behavior can be explained by the overkill effect, where further increases in y do not produce additional biological damage. The Loncol's weighting function provides a good estimate for neutron or proton beams targeting crypt cells, but not necessarily for other beam-target combinations. The overall uncertainty of the RBE depends on the uncertainties of $r(y)$, the distributions $d(y)$, the calibration procedure of y, and the detection efficiency of the detector. The weighting function is not universal but depends on the beam, the cell line, the biological endpoint, the simulated volume, and the absorbed dose.

2.2.2 Theory of Dual Radiation Action (TDRA)

According to the theory of dual radiation action (TDRA) [148][230], the square of the specific energy z deposited in a *site* is proportional to the number of fatal lesions in a small volume of the cell nucleus following cell irradiation:

$$\varepsilon = Kz^2 \tag{2.11}$$

where the K factor expresses the average yield of lethal lesions for an imparted dose of z. The TDRA doesn't take into consideration the probability of cell repair following irradiation when predicting the biological effect. The Microdosimetric-Kinetic model (MKM) was created as a result of combining models that integrated repair kinetics and microdosimetry. By adding the quadratic proportionality to the lethal damages, the TDRA postulate is generalized in the MKM evolution [123], implying a linear-quadratic dependence of the survival probability on z.

2.2.3 The Microdosimetric Kinetic Model (MKM)

The MK model is based on the following funding assumptions [123][122][121].

The sensitive target is the cell nucleus, which is divided into N_D sub-units known as domains, similar to the TDRA sites. In general, the domains are shaped differently and fit together to fill the nucleus. Ionizing radiation can induce two types of primary lesions. **Type I** lesions correspond to directly lethal clustered DNA damage, while **type II** lesions can be repaired at rate r, or converted to irreparable lesions through a first-order process with a constant rate a, or at the second order, representing pairwise combinations, with a constant rate b.

Lesions of types I and II are limited to the domain in which they originate. Because two lesions may only interact if they are in close proximity to each other, this assumption provides a sub-nuclear correlation length among lesions. Specifically, only when two type II lesions are formed in the same domain may they merge to generate a type I lesion. The idea behind the division of a cell into sub-volumes arises because a couple of type II lesions are all likely to happen in a short time period, even for lesions that are far away in the cell nucleus. To solve this issue, the nucleus can be divided into smaller subdomains, allowing interactions to happen within a single volume, as assumed by the MKM. Choosing the right domain size is crucial to predict cell survival. Too large domains allow for interactions between far-away lesions, while too small domains limit the number of lesions within a single domain, making interactions less likely. Selecting different domains can result in varying model predictions. To reduce the model sensitivity caused by arbitrary domain selection, consider allowing interactions across domains. This idea allows for the moving of lesions between domains or pairs of lesions to interact if they are formed in adjacent domains.

The number of type I and II lesions in a domain is proportional to the specific energy (z) deposited in it. Following the MK notation $x_I^{(c,d)}(t)$ and $x_{II}^{(c,d)}(t)$ represent the

time-dependent average number of type I and type II lesions for a cell-domain (c,d) caused by an acute dose $z(c,d)$ deposited in the cell c and domain d at $t=0$. These assumptions define the following set of coupled ordinary differential equations:

$$\begin{cases} \dot{x}_I^{(c,d)} = \lambda\, \dot{z}^{(c,d)} + a\, x_{II}^{(c,d)} + b\left(x_{II}^{(c,d)}\right)^2 \\ \dot{x}_{II}^{(c,d)} = k\, \dot{z}^{(c,d)} - (a+r)\, x_{II}^{(c,d)} - 2b\left(x_{II}^{(c,d)}\right)^2 \end{cases} \tag{2.12}$$

with boundary conditions defined as:

$$\begin{cases} x_I^{(c,d)}(t=0) = \lambda\, z^{(c,d)} \\ x_{II}^{(c,d)}(t=0) = k\, z^{(c,d)} \end{cases} \tag{2.13}$$

For charged particles, the pairwise combination of type II lesions is negligible compared to the first-order process $(2b(x_{II}^{(c,d)})^2 \ll (a+r)x_{II}^{(c,d)})$[122], so the quadratic term is omitted in the calculations. Consequently, equation 2.12 simplifies to:

$$\begin{cases} \dot{x}_I^{(c,d)} = \lambda\, \dot{z}^{(c,d)} + a\, x_{II}^{(c,d)} + b\left(x_{II}^{(c,d)}\right)^2 \\ \dot{x}_{II}^{(c,d)} \simeq k\, \dot{z}^{(c,d)} - (a+r)\, x_{II}^{(c,d)} \end{cases} \tag{2.14}$$

The solution of the kinetic equations led to:

$$\begin{cases} x_I(t) = \lambda z + \int_0^t \left[akz\, e^{-(a+r)t'} + bk^2z^2\, e^{-2(a+r)t'}\right] dt', \\ x_{II}(t) = kz\, e^{-(a+r)t} \end{cases} \tag{2.15}$$

Substituting $x_{II}(t)$ solution into the kinetic equation 2.15 and integrating $x_{II}(t)$ with respect to time, it follows that:

$$x_I^{(c,d)}(t) = \lambda z^{(c,d)} + a\kappa z^{(c,d)}\left(\frac{1-e^{-(a+r)t}}{a+r}\right) + b\kappa^2\left(z^{(c,d)}\right)^2\left(\frac{1-e^{-2(a+r)t}}{2(a+r)}\right). \tag{2.16}$$

The repair kinetics in Equation 2.16 can be validated by H2AX phosphorylation mapping experiments (γ-H2AX), assuming that the total number of lesions ($x_I(t)$ + $x_{II}(t) \sim N_{DSB}(t)$) represents the number of DSBs in the DNA [175][240].

Assuming a Poisson distribution for type I lesions in the nucleus, the surviving probability for the c-th cell in the irradiated population can be calculated as:

$$S_c = \exp\left(-\sum_{d=1}^{N_D} \lim_{t\to+\infty} x_I^{(cd)}(t)\right) = \exp\left(-\sum_{d=1}^{N_D} \tilde{x}_I^{(cd)}\right) \tag{2.17}$$

2.2.4 The Monte Carlo temporal-Microdosimetric Kinetic Model

The LQM β parameter plays a crucial role in determining the biological impact of the dose rate-time. Some studies investigated its dependence on LET, but findings are contrasting. Friedrich et al. [91] reported a general decrease in β with increasing

LET, while other authors observed the opposite trend [10][9][107][284]. The behavior of this parameter as a function of LET remains controversial due to experimental uncertainties and the difficulties associated with its measurement. These uncertainties propagated into modeling, leading different models to predict different β behaviors. For example, the Local Effect Model predicts a decreasing β with increasing LET, whereas the Microdosimetric-Kinetic Model predicts a constant β. These models are widely used in treatment planning worldwide, with the Local Effect Model (LEM) applied at clinical centers such as GSI, HIT, and CNAO [55][88][155][241], while the MKM was recently introduced into clinical practice by NIRS [131]. Most models neglect the β dependence on dose rate and time structure, so they do not account for increased cell survival with protracted or fractionated doses. Consequently, modern treatment plans assume instantaneous dose delivery, and the resulting uncertainties in β lead to a related variability in RBE [174]. Previous studies by Inaniwa et al. [129][130] applied the MKM to carbon ion beams, but they neglected the β dependence on LET.

To account for an arbitrary dose–rate time structure, Manganaro et al. [174] implemented a reformulation of the MKM, known as the Monte Carlo temporal-MKM (MCt-MKM). In this thesis (Chapter 5), the MCt-MKM is applied for the first time for the prediction of the cellular survival fraction of a radionuclide, explicitly incorporating the dose–time structure of the irradiation. This model is based on a Monte Carlo approach that includes the analytic solution of the kinetic equations described above and allows for the evaluation of the temporal effects of the irradiation. The model aims to predict cell survival for ionizing radiation delivered with any dose time structure.

The solutions $x_I(t)$ and $x_{II}(t)$ need to be generalized to consider a sequence of n consecutive interactions occurring at intervals t_0, t_1,..., t_{n-1}, in which the domain absorbs z_0, z_1,..., z_{n-1}. In this case, the solution of equation 2.12 for x_{II} must be divided into n time intervals:

$$x_{II}(t) = \begin{cases} kz_0 \exp[-(a+r)(t-t_0)] \equiv x_{II}^{(0)} & t_0 < t < t_1 \\ kz_0 \exp[-(a+r)(t-t_0)] + kz_1 \exp[-(a+r)(t-t_1)] \equiv x_{II}^{(1)} & t_1 < t < t_2 \\ \vdots & \vdots \\ \sum_{i=0}^{n-2} kz_i \exp[-(a+r)(t-t_i)] \equiv x_{II}^{(n-2)} & t_{n-2} < t < t_{n-1} \\ \sum_{i=0}^{n-1} kz_i \exp[-(a+r)(t-t_i)] \equiv x_{II}^{(n-1)} & t > t_{n-1} \end{cases} \tag{2.18}$$

The integral that defines x_I (eq. 2.15) must also be split into n integrals:

$$x_I(t) = \sum_{i=0}^{n-2} \left[\lambda z_i + \int_{t_i}^{t_{i+1}} \left(a x_{II}^{(i)} + b x_{II}^{(i)^2} \right) dt \right] + \lambda z_{n-1} + \int_{t_{n-1}}^{t} \left(a x_{II}^{(n-1)} + b x_{II}^{(n-1)^2} \right) dt' \tag{2.19}$$

which can be solved in the limit $t \to \infty$:

$$x_I = \frac{\alpha_0}{N_D}\sum_{i=0}^{n-1} z_i + \frac{\beta_0}{N_D}\sum_{i=0}^{n-1} z_i^2 + \frac{\beta_0}{N_D}\sum_{i=0}^{n-2}\sum_{j=i+1}^{n-1} e^{-(a+r)(t_j-t_i)} 2 z_i z_j \tag{2.20}$$

where:

$$\begin{cases} \frac{\alpha_0}{N_D} = \lambda + \frac{ak}{a+r} \\ \frac{\beta_0}{N_D} = \frac{bk^2}{2(a+r)} \end{cases} \tag{2.21}$$

By subtracting and adding to equation 2.20 the quantity

$$\frac{\beta_0}{N_D}\sum_{i=0}^{n-2}\sum_{j=i+1}^{n-1} 2 z_i z_j \tag{2.22}$$

this leads to:

$$\tilde{x}_I^{(cd)} = \frac{\alpha_0}{N_D}\sum_{i=0}^{n_c-1} z_i^{(cd)} + \frac{\beta_0}{N_D}\left(\sum_{i=0}^{n_c-1} z_i^{(cd)}\right)^2 - 2\frac{\beta_0}{N_D}\sum_{i=0}^{n_c-2}\sum_{j=i+1}^{n_c-1}\left(1 - e^{-\frac{1}{\tau}(t_j^{(c)} - t_i^{(c)})}\right) z_i^{(cd)} z_j^{(cd)} \tag{2.23}$$

For each cell c and domain d, a microscopic local Lea-Catcheside G factor [37][159] might be defined by rewriting equation 2.23:

$$G_{cd} = 1 - \frac{2}{\left(\sum_{i=0}^{n_c-1} z_i^{(cd)}\right)^2}\sum_{i=0}^{n_c-2}\sum_{j=i+1}^{n_c-1}\left(1 - e^{-\frac{1}{\tau}(t_j^{(cd)} - t_i^{(cd)})}\right) z_i^{(cd)} z_j^{(cd)} \tag{2.24}$$

The solution of the kinetic equations for x_I became:

$$\tilde{x}_I^{(cd)} = \frac{\alpha_0}{N_D}\sum_{i=0}^{n_c-1} z_i^{(cd)} + G_{cd}\frac{\beta_0}{N_D}\left(\sum_{i=0}^{n_c-1} z_i^{(cd)}\right)^2 \tag{2.25}$$

This expression reproduces the LQ correlation between the total absorbed dose and the number of lethal events [174]. The final surviving fraction is calculated by averaging S_c across the whole cell population, and the survival probability for a single cell is calculated by replacing 2.25 in 2.17:

$$S = \langle S_c \rangle_c = \left\langle \exp\left(-\sum_{d=1}^{N_D} \tilde{x}_I^{(cd)}\right)\right\rangle_c . \tag{2.26}$$

An example of the temporal evolution of the lesions in a cell is shown in Figure 2.3.

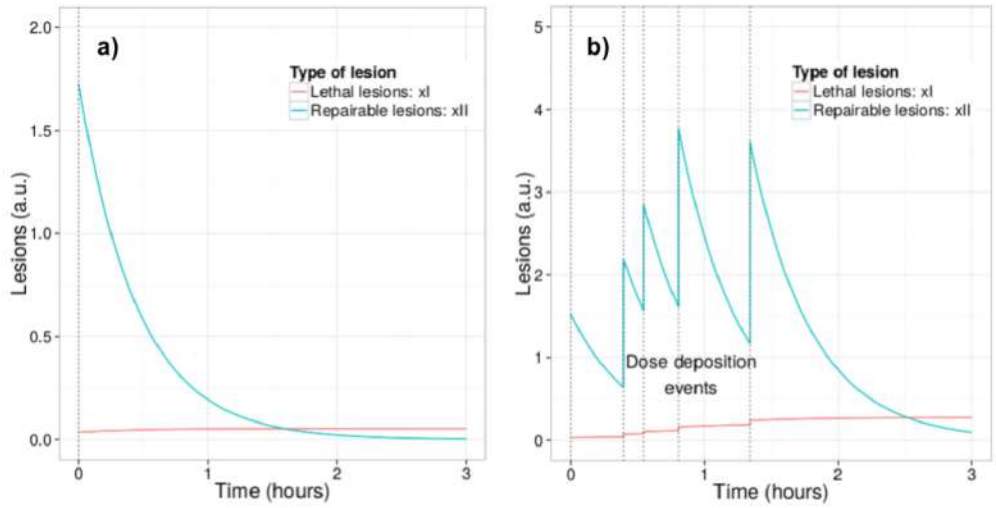

FIGURE 2.3: Time evolution of x_I(t) and x_{II}(t) damages for a single instantaneous irradiation as described by Eq. 2.16 and the x_{II}(t) solution in Eq. 2.15, respectively (A). Generalization of the temporal evolution for any time structured irradiation as described in 2.18 and 2.19. The dotted vertical lines represent the energy deposition events in the cell nucleus due to the passage of ionizing particles (B) [19].

The saturation correction

At high doses, the biological effect reaches saturation. To account for this behaviour, the empirical parameter y^* was introduced [143]. It represents the saturation-corrected dose-mean lineal energy, introduced for conditions in which excessive local energy deposition produces an overkill (saturation) effect. This correction was obtained by using an empirical saturation parameter y_0 based on the method introduced by Powers et al. [218] and then used in the TDRA [147]. Mathematically, it is expressed as:

$$y^* = \frac{y_0^2 \int_0^\infty \left(1 - exp(-y^2/y_0^2)\right) f(y)\, dy}{\int_0^\infty y f(y)\, dy} \tag{2.27}$$

where y_0 was typically fixed to 125 keV/μm. The modified MKM enables the derivation of the RBE for mammalian cells exposed to ion irradiation. For a general cell line, the surviving fraction S is expressed through a linear–quadratic function of the absorbed dose D, as shown in equation 1.21, where α is defined as:

$$\alpha = \alpha_0 + \frac{\beta}{\rho \pi r_d^2} y^* \tag{2.28}$$

α_0=0.13 Gy^{-1} is a constant that represents the initial slope of the survival fraction curve in the limit of zero LET, while β is a constant equal to 0.05 Gy^{-2}, $\rho = 1\, g/cm^3$ is the density of tissue, and r_d = 0.42 μm is the radius of a sub-cellular domain in the model. By using this formula [142]:

$$RBE_{10} = \frac{2\beta D_{10,R}}{\sqrt{\alpha^2 - 4\beta \ln(0.1)} - \alpha} \tag{2.29}$$

it can be possible to estimate the RBE_{10} for HSG cell. $D_{10,R}$ = 5.0 Gy is the 10% survival dose of 200 kVp X-rays for HSG cells [143].

Besides the models described so far, which are closely based on microdosimetric quantities and stochastic distributions, it is worth mentioning the Local Effect Model (LEM) for the full context. The Local Effect Model is a biophysical model that allows the RBE to be predicted based on physical and biological factors. It represents one of the main radiobiological approaches used for clinical treatment planning.

2.3 The Local Effect Model (LEM)

The Local Effect Model (LEM) was introduced by M. Scholz and Kraft [242][244][243]. LEM assumes that damage to a small (subcellular) volume is only dependent on the expected value of energy deposited in that sub-volume, which is independent of radiation type [141][183]. There are four versions of LEM and will be briefly discussed in the following section.

LEM I

In this version of the model, the biological effect was derived directly from the corresponding photon dose-response curve S_γ(D)[141]. For photon radiation, energy deposition is Poisson-distributed, making the distribution of lethal events in subcellular volumes Poissonian as well. Cell survival can thus be calculated as:

$$S_x = \exp(-\bar{N}_{l,x}); -\bar{N}_{l,x} = \ln(S_x) \tag{2.30}$$

From the above equation, the frequency number of lethal events within the target volume for X-rays can be calculated:

$$v_x(D) = \frac{\overline{-N_{l,x}}}{V_{\text{Nucleus}}} \tag{2.31}$$

where V_{Nucleus} is the volume of the cell nucleus. To extend this approach to other radiation fields, the microscopic patterns of energy deposition must be considered by calculating the local dose. For small volumes, the local dose is assumed to be uniform for photon radiation. In contrast, for charged particles, the dose decreases with the square of the perpendicular distance from the particle track. The average number of lethal events by considering the local density v_{ion}can then be calculated as:

$$-N_{l,x} = \int_{V_{\text{Nucleus}}} v_{\text{ion}}(d(x,y,z))\, dV \tag{2.32}$$

The event densities are equal for the same local dosage because the local dose is independent of radiation type. This is the only version of the LEM currently used in clinical practice [89][141].

LEM II

The impact of the double-strand break is also taken into consideration in the second version of the LEM [80]. This addition enhances the biological dose in areas showing very high local dose levels. The enhancement parameter η is defined as:

$$\eta = \frac{N(\text{DSB}) + N(\text{SSB} + \text{SSB}_{\text{within 25 BP}})}{N(\text{DSB})} \tag{2.33}$$

where N(DSB) is the number of double-strand breaks and N(SSB + $\text{SSB}_{\text{within 25 BP}}$) is the number of pairs of single-strand breaks occurring within 25 base pairs. So, the cellular survival fraction can be expressed as:

$$S(D) = \begin{cases} e^{-\alpha D - \beta D^2} & : D \leq D_t \\ S(D_t)e^{-s[\eta(D)D - D_t]} & : D > D_t \end{cases} \tag{2.34}$$

The two cases depend on whether or not the local dose exceeds a threshold (D_t).

LEM III

An energy-dependent track structure description based on the particle's LET was included in the third version of the LEM [79] to account for the δ-electrons released as the charged particle traverses the medium. The average energy deposited is modified to:

$$D(r) = \begin{cases} \frac{\lambda \text{LET}}{r_{\text{min}}^2} & : r < r_{\text{min}} \\ \frac{\lambda \text{LET}}{r^2} & : r_{\text{min}} \leq r \leq r_{\text{max}} \\ 0 & : r > r_{\text{max}} \end{cases} \tag{2.35}$$

where λ is the normalization constant, LET is the unrestricted linear energy transfer, r_{min} is the transition from the dose plateau within the track to the $1/r^2$ behavior outside of the track. The maximum distance a δ-electron can travel is r_{max}. The survival probability will be:

$$S(D) = \begin{cases} e^{-\alpha D - \beta D^2} & : D \leq D_t \\ e^{-(\alpha D_t + \beta D_t^2 + s_{\text{max}}(D - D_t))} & : D > D_t \end{cases} \tag{2.36}$$

where S_{max} is $\alpha + 2\beta D_t$.

LEM IV

To account for the structure of chromatin organization in the cell nucleus, LEM version IV incorporated parameters [251]. Isolated DSB (iDSB) and clustered DSB (cDSB) are two distinct kinds of double-strand breaks that were identified and treated independently. The main hypothesis of this extension is that cDSBs are more likely to cause cell death than iDSBs because, in an iDSB, the DNA is still linked at one end and can thus be repaired more easily than in a cDSB, which removes at least one segment of DNA from the loop. The clustering index (C) is defined as the ratio of the

number of cDSBs to the total number of DSBs:

$$C = \frac{N_{\text{cDSB}}}{N_{\text{iDSB}} + N_{\text{cDSB}}} \tag{2.37}$$

The number of iDSBs and cDSBs is estimated by dividing the cell nucleus into cubic sub-volumes with 540 nm sides. The DSBs within each sub-volume are determined from the local dose distribution, and iDSBs and cDSBs are then calculated based on these sub-volume DSB counts.

The predictive effectiveness of the radiobiological models already described above, from TDRA to recent MCt-MKM formulations, strictly depends on the availability of accurate physical data concerning the microscopic distribution of energy.

As noted in the previous equations, knowing the macroscopic absorbed dose D is not enough to describe the biological effects of dense ionizing radiation. It is essential instead to know the probability density of lineal energy and specific energy within the target volume.

Consequently, dedicated instrumentation is what is required to validate and apply these models clinically, as they are capable of overcoming the limitations of conventional dosimetry and measuring stochastic energy fluctuations in volumes comparable in size to cellular structures (on the order of micrometers or less).

This experimental need has long guided the historical and technological evolution of microdosimetry detectors, whose development and operating characteristics will be discussed in the next sections.

2.4 Detector for microdosimetry

The first microdosimeter was designed and built by H.H. Rossi in 1955. This detector consisted of a spherical proportional counter with plastic walls tissue equivalence (TE), filled with low-pressure TE gas. Although technological advances have led to the development of new solutions (such as solid-state detectors, SSDs, or GEM-based detectors), conventional TEPC is widely considered the gold standard for microdosimetry.

This section reviews the state of the art in microdosimetry detector technologies, with a focus on solid-state detectors. Diamond-based solid-state detectors are described in detail, as they were used in all experimental work presented in this thesis.

2.4.1 TEPC

Conventional TEPC uses a macroscopic Sensitive Volume (SV), typically between 10 and 150 mm in diameter, filled with low-pressure TE gas to simulate a biological volume (such as a cell) of micrometric dimensions. They simulate micrometric tissue volume by controlling gas pressure. If the filling gas and simulated tissue maintain the same atomic composition and atomic proportions, differences in density can be reasonably neglected. Under these physical conditions, a charged particle passing

through the detector SV interacts with the same number and type of atoms it would encounter in tissue.

A classic example is a 2.5 cm diameter SV filled with propane gas at 17 Torr, equivalent to a 1 μm spherical SV in tissue. The walls of the detector are generally made of A-150 plastic. The most common filling gases are methane-based TE gas, propane-based TE gas, and pure propane. The SV can be confined by solid TE plastic walls (solid-walled TEPC) or by well-defined electric field lines (wall-less TEPC) [209].

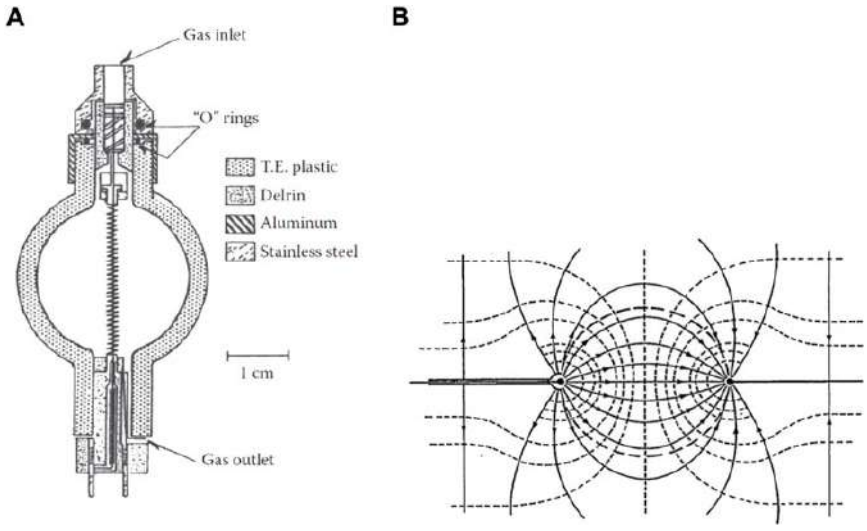

FIGURE 2.4: Comparison between solid wall and wall-less TEPCs : (A) Solid wall TEPC has a central core with anodic wire, helical grid, and chamber structure with connections for gas flow; (B) Wall-less TEPC is illustrated by a diagram highlighting the electric field lines that define the spherical collection volume [209].

There are also variants such as grid-walled and ring-walled TEPCs, where the SV is defined by guided electric field lines. The detector functions as a proportional counter by applying an electrical potential. The wall acts as a cathode, and a central wire acts as an anode. In spherical detectors, the central wire is placed from pole to pole; in cylindrical detectors, it is placed along the longitudinal axis.

The electric field and, consequently, the gas gain must be uniform and homogeneous throughout the SV to ensure a uniform response from the TEPC. In cylindrical detectors, uniformity can be achieved relatively easily using field tubes, while in spherical detectors, several measures are necessary. Gas-flow operation is often required to prevent contamination of the gas by water vapor and atmospheric gases that could permeate through the plastic wall.

TEPC has been successfully used to characterize different radiation fields and applied in various radiation therapies. It can detect the widest range of lineal energy among current microdosimetry technologies, down to a few hundred of eV μm^{-1}. However, TEPCs have significant limitations. It requires a high-voltage power supply (typically 600/800 V for a conventional proportional meter), a vacuum container and a pump, pressure control, and, in some cases, a gas flow system. Its operational complexity makes it impractical in many experimental conditions, and its portability

is moderate to poor when operating in gas flow mode. The relatively large dimensions of conventional TEPCs limit their performance when high spatial resolution is required, e.g., around the Bragg peak.

Wall effects are among the most relevant problems encountered in solid wall TEPCs. They result from the significant difference in density between the solid wall (typically A-150 plastic) and the low-pressure TE gas [14]. These effects do not alter the absorbed dose, but modify the size of the individual energy deposition event, compromising the microdosimetric spectrum. They can affect up to 10-20% of detected events and are particularly important for high-energy protons and heavy ions. Rossi [229] and [146][145] studied and suggested four main types of wall effects.

- **Delta-ray effect**: This occurs when the primary particle and its delta ray enter the cavity (due to the non-uniformity of density between the wall and the gas), depositing energy together. This is common in the presence of heavy ions passing through the detector with a dense distribution of delta rays, which can lead to an increase of $\bar{y}_F$ and $\bar{y}_D$ values.

- **Re-entry effect**: This occurs when an electron re-enters the cavity after initially passing through it on a curled track. In real microscopic cavities, the probability of this effect is low. The re-entry effect is only significant for electron energies up to 1 MeV.

- **V effect**: This is common in inelastic nuclear interactions that produce nuclear fragments outside the cavity. It occurs when several charged fragments simultaneously enter the large cavity of the counter.

- **Scattering effect**: Occurs when neutral particles (such as neutrons or photons) interact with the surrounding medium, producing more than one charged particle passing through the cavity.

In order to overcome the dimensional and spatial resolution limitations typical of conventional TEPCs, miniaturized versions have been developed. The mini-TEPC was developed to simulate smaller site sizes, down to the nanometer scale. Thanks to its small size and fast response time, the mini-TEPC can operate at flow rates of around 10^6 $cm^{-2}s^{-1}$ without significant pile-up problems. This is a major advantage over conventional TEPCs. The mini-TEPC has proven to be stable and reliable and has been widely used for microdosimetry in clinical hadron therapy beams [57][54][68][67].

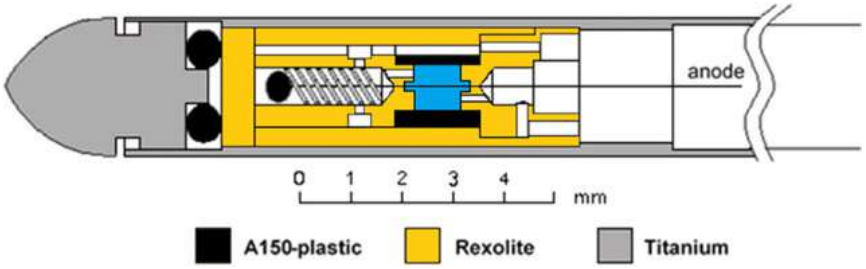

FIGURE 2.5: Scheme of mini-TEPC. Photo from [26].

Specifically, the design proposed by De Nardo et al. [68] involves the creation of a cylindrical Sensitive Volume (SV) 1 mm thick and in diameter inside an A-150 plastic cylinder. The volume is delimited by two Rexolite®inserts, which allow the SV to be defined without the aid of field tubes. The anode wire passes through the centers of the inserts through relatively large diameter holes (150 μm) to prevent melting of the insulating material caused by electron avalanches. The entire device is enclosed in a 0.23 mm aluminum cylinder to ensure electromagnetic shielding. A scheme of mini-TEPC is shown in Figure 2.5. Although the first version operated in gas flow mode, subsequent developments introduced gas-steady mode [56], modifying the ducts to improve filling procedures and cleaning from plastic degassing.

A significant improvement based on the mini-TEPC concept is represented by the Avalanche Confinement TEPC [32][45][180]. This device divides the gas volume into two distinct regions: an external drift zone and an internal multiplication region. This configuration allows an SV to be created in the drift zone free from electronic multiplication. The separation is achieved through the use of three independently polarized electrodes: a central graphite anode, a cylindrical A-150 plastic cathode, and an additional gold-plated tungsten helix (consisting of 19 turns). The helix, suitably polarized, confines the electron avalanche to a restricted region, while two field tubes support its structure, preventing distortion of the electric field. This design, equipped with thin walls for measuring high LET particles and an internal energy calibration system (^{244}Cm alpha source and solid-state detector) [30], is capable of simulating sites ranging in size from 300 nm to 25 nm. Preliminary tests with proton, helium, and carbon ion beams have shown promising results in agreement with Monte Carlo simulations [32][31][182][181]. However, systematic comparisons with reference TEPCs are still needed to evaluate the impact on the microdosimeter of particles passing through the multiplication region (approximately 20% of the total volume).

2.4.2 GEM

The Gas Electron Multiplier (GEM) was first introduced by Sauli in 1997 [238], proposing a charge amplification device to be coupled with gas detectors to improve their performance in critical conditions. Structurally, a GEM consists of a thin insulating sheet, typically 50 μm thick, coated on both sides with a metallic coating and perforated with a high density of holes (50–100 mm^{-2}) with a diameter of approximately 100 μm. The operating principle is based on the application of a potential difference between the two metal faces: the electrons generated in the gas volume above are drawn towards the holes, where the intense electric field triggers an avalanche multiplication process. The amplified charge is then transferred to the read anode for collection or further amplification.

A crucial advantage of this technology lies in the possibility of arranging multiple GEM sheets in cascade, achieving high gains with low operating voltages (e.g., 300–450 V per stage versus the 600–800 V required by conventional TEPCs). This significantly reduces the risk of electrical discharges, especially in the presence of highly ionizing particles [237]. GEM detectors are distinguished by their geometric

and electrical separation between the Sensitive Volume (SV), the multiplication region, and the readout board. This architecture provides better operational stability and flexibility in the design of the readout pattern, avoiding traditional structural constraints such as the need for a central anode wire. These characteristics make GEM detectors an affordable solution that is simple to construct and highly adaptable to a variety of experimental applications.

Early feasibility studies of this technology for microdosimetry led to the development of specialized GEM-based *mini-TEPCs*. In 2003, Farahmand proposed a multi-element device that operated in continuous gas flow conditions [83]. The structure was built from Rexolite insulating layers combined with a GEM foil, forming five cylindrical sensitive volumes. The readout system assigned a dedicated anode pixel to each sensitive volume and included additional pixels to monitor the charge produced in the inactive regions. This arrangement ensured that the entire anode structure remained at ground potential. De Nardo et al. [69] adopted a different approach, developing a mini-TEPC with 16 "wall-less" sensitive volumes—regions without physical boundaries, defined solely by the strong electric field established in the drift region. Studies on this device have shown that operating with pure propane (C_3H_8) provides better performance than using tissue-equivalent propane mixtures. In mixed neutron–photon fields, both prototypes exhibited performance comparable to that of reference TEPCs.

A major advancement in the field is represented by GEMpix, developed by the CERN Radioprotection Group. This device couples a triple-GEM structure to a Timepix quad ASIC readout system, providing more than 260,000 pixels with a pitch of 55×55 μm^2. The distinctive feature of GEMpix is its capability to simultaneously measure both the deposited energy and the arrival time for each individual pixel, enabling three-dimensional reconstruction of particle tracks with an effective spatial resolution of approximately 170 μm.

Although the device has demonstrated outstanding tracking performance in mixed proton–pion beams and has been employed to characterize clinical carbon-ion beams, certain limitations have been identified [162]. In particular, a nonlinear response has been found for low energy deposition events and dosimetric discrepancies of up to 15% compared to reference dosimeters. Currently, developments are underway to integrate the system into special water phantoms and refine the necessary software corrections. A valid alternative is provided by Thick GEMs (TGEMs) [48][49].

Unlike standard GEMs, TGEMs have thicknesses and hole diameters in the order of millimeters, characteristics that allow them to be manufactured using standard printed circuit board (PCB) technologies. Although studies on TGEM-based TEPCs have shown improved detection efficiency by up to a factor of 3 compared to conventional TEPCs [12], problems of spectral misalignment and a marked angular dependence for energetic neutrons (MeV) have been detected [13]. This evidence suggests that, despite its potential, TGEM technology requires further optimization to ensure the accuracy required in microdosimetry.

2.4.3 Solid state microdosimeter

Solid-state detectors (SSDs) represent a valid alternative to TEPCs and are attracting growing interest thanks to technological advances in materials processing and crystal growth techniques. SSDs are based on monolithic silicon or diamond microcrystals. Diodes are used as radiation detectors due to the advantageous properties of the junction formed between n-type and p-type semiconductors. When ionizing radiation passes through the semiconductor, it interacts with the atoms in the crystal, depositing energy that produces electron-hole pairs along the radiation path. The mean number of electron-hole pairs generated, $N_{e-h\text{ pairs}}$, is given by:

$$N_{e-h\text{ pairs}} = \frac{\Delta E}{W} \tag{2.38}$$

where ΔE is the total energy deposited and W is the average energy required to produce one electron-hole pair. In silicon, W is largely independent of the incident particle energy but depends on the type of radiation, with variations of a few percent for different ions.

The p-n junction is formed by thermodynamic contact between n-type and p-type regions. The excess electrons in the n-type region create a higher density of conduction electrons compared to the p-type region, leading to diffusion of electrons into the p-type material and holes into the n-type material. Electrons recombine with holes in the p-type region, leaving immobile positive charges (ionized donors), while holes leave immobile negative charges (filled acceptor sites) in the n-type region. This creates a space charge distribution that generates an electric field and defines the *depletion region*, where the concentrations of free electrons and holes are greatly reduced. If the dopant concentrations on both sides are equal, the depletion region extends symmetrically; otherwise, it extends more deeply into the less doped side. When radiation generates electron-hole pairs within the depletion region, the electric field causes them to drift toward the opposite electrodes, producing a current. The integration of this current pulse generates a voltage pulse that is processed by acquisition electronics.

Because the intrinsic electric field may be insufficient to collect all carriers before recombination or trapping, an *external reverse bias* is usually applied, which increases the electric field, widens the depletion region, and enlarges the active volume of the detector. Under reverse bias, the reverse current is relatively small, since only minority carriers move across the junction. If the voltage is sufficiently high for the depletion region to span the entire wafer thickness, the device is said to be fully depleted. Exceeding the breakdown voltage may cause irreversible damage due to a sudden surge in the reverse current. The thickness of the depletion region, d, under reverse bias can be approximated by [152]:

$$d \approx \sqrt{\frac{2\epsilon V}{eN}} \tag{2.39}$$

where ϵ is the permittivity of the semiconductor, V is the applied voltage, e is the elementary charge, and N is the dopant concentration. This active volume constitutes

the *Sensitive Volume (SV)* of the detector, in which charge collection occurs and the detector's microdosimetric response is determined. Most SSDs developed for microdosimetry are p-n or p-i-n junctions operating at or slightly above their depletion voltage. Increasing the applied voltage (beyond the breakdown voltage) increases the charge collection efficiency (CCE). The operating condition in which collection is complete (saturation region) is reached when the pulse height does not change by further increasing the bias voltage.

Despite their advantages, SSDs have specific limitations. The absence of internal electronic gain makes solid-state microdosimeters more susceptible to electronic noise, which worsens the minimum detectable energy and reduces the signal-to-noise ratio compared to detectors with gas amplification. As a consequence, the linear low-energy cut-off is degraded.

Another limitation is that the SV of SSDs is not intrinsically tissue-equivalent, meaning that accurate and complex corrections are required to achieve tissue equivalence. Moreover, many solid-state microdosimeters exhibit a peripheral region surrounding the SV with reduced charge-collection efficiency (incomplete CCE), which introduces a characteristic low-energy tail in the measured spectra (see Chapter 4).

The detector response is also not isotropic and can vary significantly with the direction of the incident radiation. Furthermore, radiation damage represents a major concern for SSDs, as it can alter the detector performance over time and compromise the reliability of microdosimetric measurements.

2.4.4 Silicon microdosimetry

Silicon-based detectors are p-n or p-i-n junctions with a depletion layer thickness (SV) between 1 and 10μm and typical sensitive areas between 10×10 and $100\times100\mu m^2$. They represent the first solid-state microdosimeters, initially studied by Dicello et al. [72]. Their micrometric size gives these sensors a fundamental operational advantage over gas proportional counters (TEPC): silicon detectors can operate at the full intensities of clinical therapeutic beams.

In contrast, TEPCs require a reduction in beam intensity to avoid saturation, making measurements more complex and less representative of actual clinical conditions. Although charge collection efficiency (CCE) is typically very high ($\sim$100%), conventional silicon devices suffer from the so-called "field funneling" effect [125]. This phenomenon consists of a temporary and local distortion of the electric field induced by the transit of high LET particles. When a particle passes through the detector, the electric field, normally confined to the depletion region, extends deep into the substrate along the particle track. This delivers a large number of charge carriers to the junction even from areas outside the defined region, preventing a rigorous definition of the Sensitive Volume (SV).

The technological solution adopted to overcome this limitation is the use of Silicon-On-Insulator (SOI) devices [222].

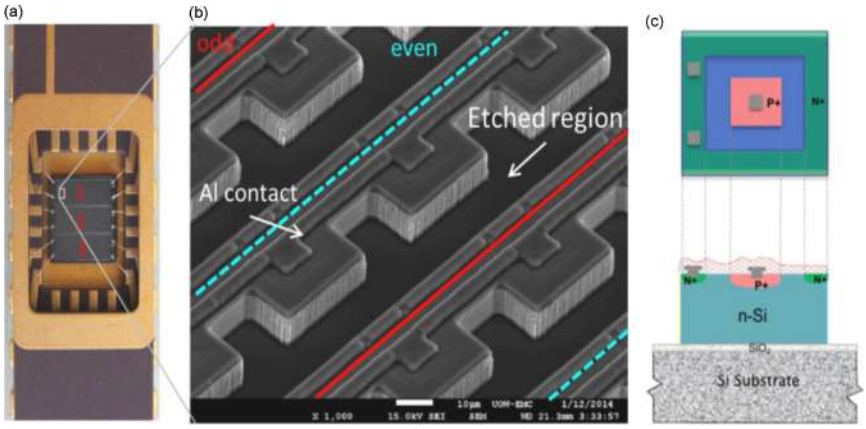

FIGURE 2.6: Bridge microdosimeter mounted on a dual-in-line package; (b) SEM image of part of the sensitive-volume array; (c) simplified topology of the n-SOI bridge microdosimeter sensitive volume [228].

This technique allows the SV to be electrically isolated, eliminating the field funneling effect and ensuring well-defined volumes. Currently, this technology is being developed by the CMRP (University of Wollongong) and the IMB-CNM (Spain).

Rosenfeld [228] described the evolution of CMRP microdosimeters into five generations of SOI arrays. The first three reduced charge sharing between adjacent SVs and diffusion collection, leading to the development of the fourth and fifth generations, which are now the reference standard.

- **4th Generation (Bridge Microdosimeter):** Designed specifically for low dose rate environments (such as aviation and space), this detector consists of a matrix of 4248 well-defined SVs, each measuring $30 \times 30 \times 10\ \mu m^3$ for a total sensitive area of $4.1 \times 3.6\ mm^2$. The SVs are made by completely etching a layer of high-resistivity n-type silicon (10 μm) on a low-resistivity support wafer. The structure is passivated by a layer of silicon oxide (SiO_2) and phosphosilicate glass. A key feature is the connection of the SVs in two independent parallel arrays, "even" and "odd" (see Figure 2.6). This configuration allows events to be distinguished: if a particle crosses two adjacent cells obliquely, the signals are read separately and not as a single erroneous event. Coupled with MicroPlus readout electronics, the "Bridge" system has been shown to measure linear energies down to 0.2 keV/μm [46], making it a viable alternative to TEPCs, also due to its low detection threshold. IBIC (Ion Beam Induced Charge) analyses have confirmed a CCE close to 100% in the sensitive volume, although a residual lateral charge collection from the connection "bridges" has been observed.

- **5th Generation (Mushroom Microdosimeter):** To overcome the remaining limitations of the previous generation, the “Mushroom” design [261] was developed using 3D technologies. The detector consists of an array of cylindrical VCs (diameter and thickness $\approx 10\ \mu m$) fabricated on a SiO_2 layer and embedded in polymethyl methacrylate (PMMA). The electrodes (n^+ columnar and p^+ ring) are fabricated using etching and gas implantation techniques. Although the agreement between measurements and simulations is good, IBIC analysis has

revealed low CCE regions within the central electrode and around the SVs, which create a linear low-energy "tail" in the measured spectrum. Design optimizations based on Monte Carlo simulations are currently underway for both space and clinical applications [262].

The technology developed by the Spanish group, described by Guardiola et al. [110], has evolved through developments based on 3D detectors.

- **Ultra-thin 3D Si detector:** The first device [82][108] consisted of a matrix of p-type and n-type columnar electrodes on SOI wafers. However, it had significant disadvantages, such as incomplete SV definition and the presence of internal dead zones caused by the electrode columns.
- **3D-cylindrical microdetector:** To improve performance, a second generation [111][86] based on quasi-toroidal trenches (internal diameters 9-25 μm) dug into the SOI wafer has been introduced (see Figure 2.7). The trenches, filled with an internal n-type electrode and insulated by SiO_2, define cylindrical SVs with a thickness between 5 and 20 μm. A central p-type electrode is created by boron implantation. The strength of this system lies in its customized front-end electronics, which include high-pass and low-pass filters. The configuration allows each cell of the matrix to be read individually (to reduce pile-up in high-fluence beams) or grouped to increase the sensitive area in low-fluence conditions. A third generation, integrated into an automated portable system for real-time clinical use, is currently being characterized.

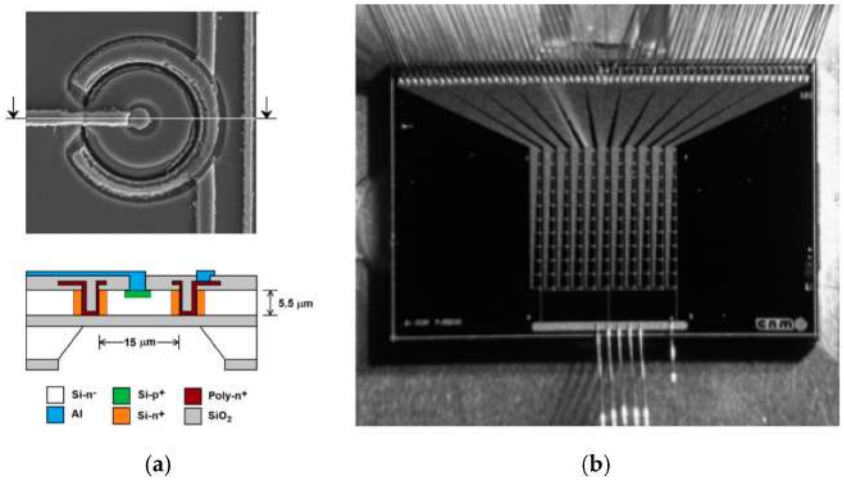

FIGURE 2.7: (a) Front view of the 3D-cylindrical unit cell of the microdosimeter. (b) Photograph of an 11×11 detector array: the upper part shows the fan-out connections to the readout electronics, while the lower part shows the connections that bring the rings around the active areas to a common ground reference [219].

Silicon microdosimeters have demonstrated excellent reliability in the characterization of therapeutic beams, providing results consistent with both reference TEPCs and Monte Carlo simulations, and withstanding clinical fluence rates without saturation.

Specifically, the Ultra-thin detector was tested with 62 MeV protons and 94.98 MeV/u ^{12}C ions, showing energy thresholds of 75 and 200 keV, respectively [100][109]. The 3D-cylindrical detector was validated in carbon pencil beams at 115.23 MeV/u at clinical rates ($5 \cdot 10^7 s^{-1} cm^{-2}$)[220]. CMRP (Bridge and Mushroom) technologies have been widely used to compare radiobiological models (RBE) and characterize heavy ion beams (from Helium to Neon) [29][160] and clinical protons [8][71][119].

2.4.5 Diamond microdosimetry

Diamond is recognized as one of the most promising alternatives to silicon for the implementation of radiation detectors [5][96]. The wide bandgap (5.5 eV) guarantees extremely low leakage currents, while the high mobility of charge carriers allows very fast response times, in the order of nanoseconds. The low dielectric constant results in minimal parasitic capacitance, thereby improving the signal-to-noise ratio. In addition to these electronic characteristics, diamond is chemically inert, has excellent thermal stability, and, crucially for dosimetry, high radiation hardness.

However, the distinctive advantage of diamond over silicon lies in its tissue equivalence (atomic number Z=6), which makes it an ideal material for radiobiological and medical physics applications, thereby reducing the need for correction factors. Improvements in homoepitaxially Chemical Vapor Deposition (CVD) growth techniques have enabled the production of high-quality single-crystal artificial diamond crystals at affordable costs. The use of CVD diamond for microdosimetry was proposed by Rollet et al. [227]. Currently, three institutes are developing diamond microdosimeters: the University of Rome Tor Vergata, the CEA–LCD Laboratory (France), and the CMRP at the University of Wollongong.

The research group at the University of Rome Tor Vergata has focused its development on the production of single-crystal detectors based on a p-i-n multilayer structure [6]. The manufacturing process begins with the deposition of a conductive layer of p-doped diamond (boron) using microwave plasma-assisted CVD on an inexpensive commercial HPHT (High Pressure High Temperature) substrate. This layer acts as a backing contact, on which an ohmic contact is made using annealed silver paint. The boron concentration is typically around $0.5 \cdot 10^{20} \mathrm{cm}^{-3}$. Subsequently, a layer of intrinsic diamond, which acts as a Sensitive Volume (SV), is grown homoepitaxially on the p layer; its thickness can vary from 1 μm to several tens of microns. Finally, a thin metal electrode is deposited by thermal evaporation on the intrinsic surface to define the sensitive area (Figure 2.8).

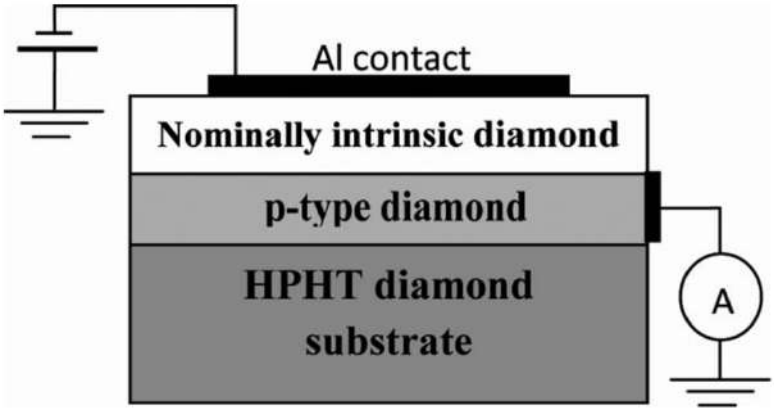

FIGURE 2.8: Structure of the CVD diamond based detector developed by the University of Roma Tor Vergata [6].

Characterization using IBIC (Ion Beam Induced Charge) technique showed very precise SV definition and 100% CCE in the sensitive region, with no evidence of external charge collection [270]. A variant of this technique, studied by Verona et al. [265], combines standard photolithography with selective CVD to define the SV with micrometric accuracy (Figure 2.9). Although IBIC analysis showed good CCE uniformity, a thin region of low efficiency was detected at the edges of the detector, responsible for a low-energy tail in the spectra. Despite this, the device demonstrated excellent linearity with respect to the LET of the incident particle in the range 100–3000 keV/μm, with a lower energy threshold (cut-off) of approximately 80 keV.

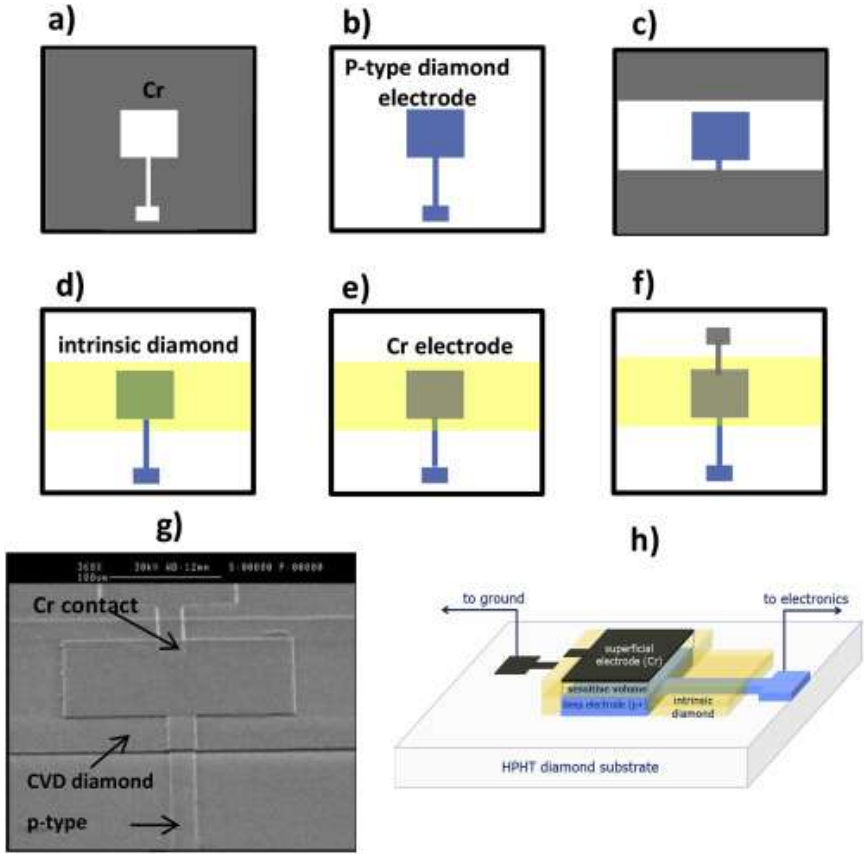

FIGURE 2.9: Main fabrication steps of the diamond-based microdosimeter: patterned Cr masks, selective growth of p-type diamond for the back electrode and intrinsic diamond for the sensitive layer, followed by deposition of the top electrode and bond pad. (g) SEM image and (h) schematic of the DBM [265].

The CEA (France) LCD laboratory has developed an alternative approach based on thin membrane processing [283]. Starting with thicker intrinsic CVD crystals (supplied by Element Six), the samples are cut and polished to thicknesses of 20/60 μm. A thin layer of p-doped diamond (boron) is grown on one side. The structure is then thinned to its final thickness (<10 μm) by deep Ar/O_2 plasma etching. In this configuration, the electrical contacts create a p-i-m junction under the doped layer (which defines the SV) and a surrounding m-i-m structure. The device operates without external bias, exploiting only the built-in potential. Tests on 4 μm prototypes showed a CCE of 100% for protons, but reduced to 80% for carbon ions, as the internal potential is not sufficient to efficiently separate the very dense electron-hole pairs created by heavy ions. Radiation hardness is excellent (estimated >500 treatments before a 1% drop in CCE), but the problem of low-energy spectral tailing due to edge effects persists.

To solve the problems of CCE and spectral distortion, a guard ring design was introduced [282].

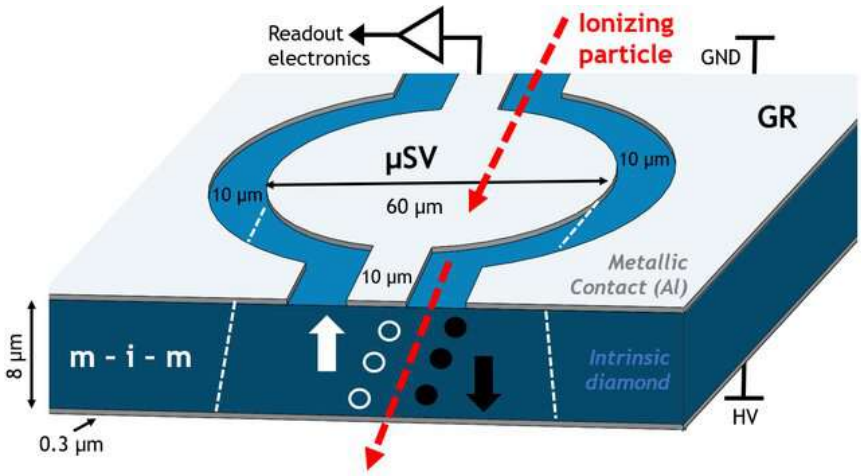

FIGURE 2.10: Scheme of the Guard-Ring diamond microdosimeter [282].

An intrinsic diamond membrane is equipped with aluminum electrodes on both sides (m-i-m structure). Using laser photolithography and wet etching, an isolation trench is created on the metal electrode, separating the collection region from the guard ring (GR), as shown in Figure 2.10. By applying an external bias, the electric field is stabilized. An 8 μm prototype with 10 μm trenches showed well-defined SVs; however, the region under the isolation trench still causes charge sharing between the electrodes. Reducing the isolation gap is the strategy currently being pursued to minimize this effect.

The CMRP has explored advanced microfabrication techniques such as laser ablation and the use of active brazing alloys (ABA) on high-purity CVD diamonds [64][65][63]. The latest development, the 3D-LES (Lateral Electrode Structure) detector, was achieved by creating isolation trenches and electrode wells using lasers, which were then filled with silver ABA. This geometry generates a lateral electric field between the two electrodes (Figure 2.11).

However, IBIC analysis has revealed critical limitations: the conductive walls of the trenches act as "virtual electrodes", creating additional electric field components that extend well below the depth of the electrodes themselves. This phenomenon degrades spatial resolution, introduces regions of low charge collection, and increases leakage current. As a result, the CMRP is now directing its research towards a hybrid approach [66], which combines layer growth (similar to the Tor Vergata technique) with laser post-processing.

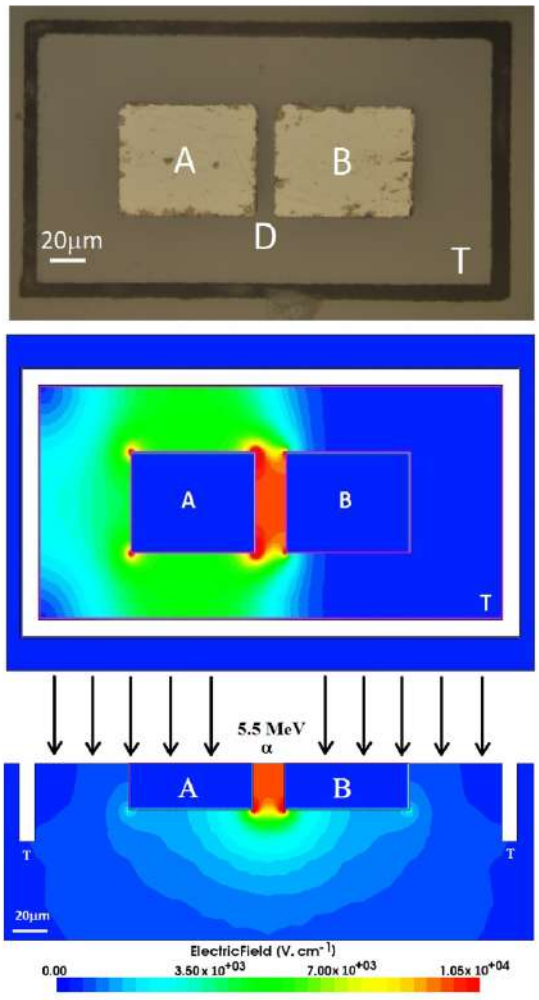

FIGURE 2.11: Top: view optical image of the device showing electrodes (A, B), the isolation trench (T), and contact separation (D). Simulations illustrate the electric field distribution (with and without the graphite-coated trench) for a 20 V bias and 500 μm substrate. The lower panel also shows the ion range of 5.5 MeV He^{2+}. Devices were fabricated with 10, 20, and 30 μm electrode separations [63].

2.4.6 Summary and conclusions

Because of its wide lineal energy range and tissue-equivalent sensitive volume, which can detect events down to a few hundred eV$\cdot\mu$m^{-1}, the Tissue Equivalent Proportional Counter (TEPC) continues to be the standard for microdosimetry, especially when characterizing new devices. However, the practicality of conventional TEPCs is limited by their complexity, which calls for high-voltage supplies, pressure and gas flow control, and frequent vacuum containment. They are also impacted by wall effects (apart from wall-less designs), and their size limits performance and spatial resolution in situations with high fluence rates or steep stopping power gradients.

Solid State Detectors (SSDs) still outperform Mini-TEPCs in terms of spatial resolution and performance at high fluence, but they do reduce size-related limitations while maintaining the majority of TEPC advantages. By separating the detection,

multiplication, and readout regions and enabling adaptation to various experimental conditions, GEM-based TEPCs simplify design and construction. Particle tracking is possible with GEMpix in particular, but its sensitive volume definition, size, and data volume make it difficult to use in clinical settings.

Even in areas with sharp stopping power gradients, like those close to the Bragg peak, micrometric sensitive volumes of SSD allow for high spatial resolution. They operate at a variety of fluence rates and are quick and adaptable. Nevertheless, because their sensitive volume is not tissue-equivalent, uncertainty-introducing correction factors are needed. Additionally, SSDs show anisotropic behavior based on radiation incidence and poor low-energy response.

Hadron therapy applications

Conventional TEPCs are not practical in hadron therapy due to high fluence rates ($\sim 10^2$ cm^{-2}s^{-1}). SSDs or mini-TEPCs are recommended, with SSDs being especially well-suited for high spatial resolution in areas like the Bragg peak that have sharp energy gradients [206].

SSD thickness must be carefully considered because too thin detectors raise the low-energy cut-off, which affects entrance-region measurements, and too thick detectors distort spectra beyond the Bragg peak. Microdosimetric results can be impacted by radiation damage, which primarily affects SSDs [209]. Although SSDs are still clinically useful with more frequent calibration, diamond-based detectors offer better radiation hardness than silicon. Uncertainties are further increased by the need for material correction, particularly in the vicinity of the Bragg peak. It is still difficult to find a single reference microdosimeter for hadron therapy [206]. By combining detectors, it is possible to exploit the advantages while mitigating the disadvantages of the described technologies.

To ensure consistency and accuracy throughout the entire dose-depth profile, an ideal system might have a thin SSD for the Bragg peak, a thicker SSD for plateau-region measurements, and a mini-TEPC for entrance-region characterization and tissue-equivalency reference [206].

Chapter 3

Monte Carlo methods and its applications

Monte Carlo methods use computational algorithms based on repeated random sampling to simulate problems and obtain numerical solutions. They are usually used in physical and mathematical situations when the solution depends on a great number of variables. The Monte Carlo method originated in the 18th century with Georges-Louis Leclerc, Comte de Buffon's "Buffon's needle" experiment. This involved randomly tossing needles on a table with parallel lines to determine the value of π [128]. Monte Carlo techniques were first introduced in the 1940s by physicists Stanislaw Ulam and John von Neumann at the Los Alamos laboratories. They used statistical methods to simulate neutron trajectories and study neutron diffusion.

"The first thoughts and attempts I made to practice were suggested by a question which occurred to me in 1946 as I was convalescing from an illness and playing solitaires. The question was what are the chances that a Canfield solitaire laid out with 52 cards will come out successfully? After spending a lot of time trying to estimate them by pure combinatorial calculations, I wondered whether a more practical method than "abstract thinking" might not be to lay it out say one hundred times and simply observe and count the number of successful plays. This was already possible to envisage with the beginning of the new era of fast computers, and I immediately thought of problems of neutron diffusion and other questions of mathematical physics, and more generally how to change processes described by certain differential equations into an equivalent form interpretable as a succession of random operations. Later I described the idea to John von Neumann, and we began to plan actual calculations." [77]

This project required a code name since it was secret. Von Neumann adopted the name Monte Carlo, referring to the Monte Carlo Casino in Monaco, where Ulam's uncle would borrow money to gamble [187]. The Monte Carlo approach thus became increasingly popular in the scientific community, particularly in nuclear physics. In 1948, Enrico Fermi, Nicholas Metropolis, and Ulam obtained Monte Carlo estimates for the eigenvalues of the Schrödinger equation.

Spencer was the first to use the Monte Carlo approach to radiation transport problems, specifically studying the impact of polarization on multiple Compton scatterings. In 1949, Kahn published a paper in which he used Monte Carlo to predict neutron fluxes from nuclear reactors. In the same year, Mayer described in a

symposium his use of one of the first digital electronics computers, the ENIAC, for neutron transport Monte Carlo calculations [114].

In parallel, Fermi developed the analog computer FERMIAC to replace ENIAC during periods of operation shutdown and used it to investigate the variation in time of neutron number [53]. Since then, Monte Carlo techniques have been used in a wide variety of fields of human knowledge, from mathematics to chemistry, economics to computer science [165]. Among these, one of the application areas that is growing most rapidly is medical radiation physics.

It is recognized that Monte Carlo (MC) simulations are the most reliable approach in order to estimate early radiobiological effects induced by ionizing radiation [73]. At the cellular and subcellular levels, energy deposition occurs through intrinsically stochastic processes that are difficult to measure experimentally and cannot be adequately described using macroscopic approaches. The Monte Carlo method allows these processes to be accurately reconstructed by modeling the physics of low-energy interactions and the geometric complexity of biological systems. The microdosimetric information thus obtained provides radiobiological models with fundamental parameters for correlating the distribution of energy deposits with the probability of biological damage induction, contributing to a more robust understanding of the effects of radiation and the improvement of therapeutic strategies.

This chapter aims to describe the overall features of the MC method, its fundamental assumptions for radiation transport applications, and the specifics of the technique as it is implemented in MC code. The chapter is structured as follows: the fundamental principles of Monte Carlo methods and the use of stochastic algorithms for solving complex problems are introduced; then, the "condensed-history" approach is described with an in-depth analysis of the Geant4 toolkit, examining its modular architecture, essential classes, and tracking hierarchy; Finally, the “track structure” approach is illustrated using the Geant4-DNA extension, which is fundamental for nanoscale modeling and the study of radiobiological effects.

3.1 Monte Carlo methods - Basic concept

Monte Carlo simulations represent a large category of statistical methods that use computational algorithms based on repeated random sampling to obtain numerical solutions to problems that do not admit analytical solutions or whose solution is difficult to calculate. The idea behind these calculations is to model the real system of interest as accurately as possible. This can be obtained by defining its input variables, generating these inputs through random sampling from appropriate Probability Density Functions (PDFs), and recording the output variables each time.

By repeating this process a sufficiently large number of times to satisfy the Law of Large Numbers (LLN), it is possible to aggregate the results obtained and derive statistically reliable estimates of the parameters of interest [232].

PDFs are fundamental because they describe the relative probability that a continuous random variable will take on a given value. The probability that the variable

will fall within a specific interval is given by the integral of the PDF over that interval. PDFs also provide the necessary a priori information about the processes to be simulated. The principle of the LLN ensures that as the number of simulated events, which are called "histories", increases, the quality of the average behavior of the output variables improves. This leads to a reduction in the associated statistical uncertainty [114].

A key element in any Monte Carlo calculation is the Random Number Generator (RNG), which is the portion of code responsible for providing a stream of seemingly unrelated numbers to mimic the stochastic nature of the process. It is important to point out that it is inherently impossible to produce truly random numbers in a computational context, as codes are based on deterministic and repeatable algorithms. Therefore, the work is carried out with "pseudo-random numbers", which appear to be random but still exhibit a specific repeatable pattern [165].

3.1.1 Sampling methods

Random numbers R, uniformly distributed in the interval, are used to sample a stochastic variable x according to its PDF $f(x)$. The PDF $f(x)$ is defined in the interval $[x_{\text{inf}},x_{\text{sup}}]$. The basis for this sampling is the Cumulative Distribution Function (CDF), $F(x)$, defined as the integral of the PDF:

$$F(x) = \int_{x_{\text{inf}}}^{x} f(\tau)\, d\tau \tag{3.1}$$

$F(x)$ gives the probability that the random variable τ is less than or equal to x. There are three main methods for performing sampling [114]:

1. **Direct sampling:** This method is applicable when it is easy to calculate the inverse of the cumulative distribution function, $F^{-1}(x)$. The sampled value x is obtained by replacing $F(x)$ with the uniform random number R and solving the equation for x: $x = F^{-1}(R)$.

2. **Rejection sampling:** When calculating the inverse of $F(x)$ is not feasible, the rejection method is used. A normalized function $f'(x)$ is defined. A uniform random number R in the interval [0,1] is sampled to calculate a value x uniformly distributed in the PDF interval. Next, a second uniform random number R_2 is sampled in the same interval. The value x is accepted as a sampled value only if R_2(x)$< f'(x)$; otherwise, it is rejected and the process is repeated. This method is valid provided that $f(x)$ is not infinite at any point.

3. **Mixed sampling:** This is used when the two previous methods are not applicable individually. It assumes that the PDF $f(x)$ can be decomposed into the product of two PDFs, $f(x)$=f_a(x)$\cdot f_b$(x), where f_a(x) acts as a rejection function. In practice, a value x is determined using direct sampling on f_a(x), and the rejection method is applied to f_b(x) with that value of x.

By defining the system of interest and the PDFs from the existing models or experimental data describing the interactions to be simulated, Monte Carlo methods

can be used to simulate physical processes. The MC technique is based on random number generation and enables the simulation of the stochastic nature of particle-matter interactions. In particular, it is used for the simulation of the transportation of radiation through matter. Monte Carlo simulations are known to be the "gold standard" for modeling radiation-matter interactions and predicting their effects [1][52][85][204][233]. Monte Carlo radiation transport codes are classified into two types based on how particles are tracked: Monte Carlo condensed-history (MCCH) codes and Monte Carlo track structure (MCTS) codes.

3.2 The condensed-history Monte Carlo approach

Monte Carlo condensed-history (MCCH) codes, also known as general-purpose MC codes, divide a particle path into discrete steps, each of which contains a significant number of collision processes. Multiple scattering theories are used to calculate particle deflection caused by elastic collisions. Stopping power values are tabulated and used to calculate energy losses. At the end of each step, both the angular changes in the particle's trajectory and the energy losses are estimated.

Condensed-history algorithms are divided into two types [11]. At the end of the step, a class I method randomly samples interactions, groups all collisions, and employs a predefined set of path lengths. The class I approach accounts for energy-loss straggling, but it no longer preserves the link between large energy deposits and the generation of secondary particles. In contrast, class II methods separate interactions into "soft" and "catastrophic" events, depending on a chosen threshold.

MCCH codes have the advantage of significantly reducing computation time while producing results accurate enough for dimensions of the order of or greater than mm. However, MCCH codes may have important limitations when dealing with very small geometries or low-energy transfers [198]. There are several MCCH codes, including MCNP [225], FLUKA [84] and Geant4 [2] [3][4].

The Geant4 simulation toolkit will be used for all Monte Carlo simulations in this thesis since it offers a several advanced particle therapy examples and is easily extensible. Moreover, it is known to scale well and includes numerous experimentally validated physics models.

3.2.1 Geant4

GEometry ANd Tracking 4 (Geant4) is an open source multithreaded C++ toolkit for simulating the passage of radiation through matter [2] [3][4]. Geant4 is implemented in C++ and uses object-oriented programming to organize its functionality into a modular class structure.

The code is divided into three main sets of modules, which can be combined to meet the specific needs of the simulation. This framework allows defining the geometry and materials of a setup, including detectors, analyzing its structure, using different physics engines to simulate interactions, visualizing and saving results, and integrating models and cross sections for an accurate description of physical

processes. These modules can be classified into three main categories, each with a specific role in the toolkit architecture. The *kernel* is responsible for initializing and managing geometry and runs, including particle tracking, propagation in electric or magnetic fields and materials, as well as enabling the simulation of physical processes. *Physics processes* represent the largest module in the toolkit and include the models and cross sections needed to accurately describe particle interactions with matter. Finally, the *interfaces* provide the user with tools for visualization, input/output, and application control, facilitating simulation management and analysis.

To define a complete simulation environment in Geant4, the user is required to instantiate three mandatory user action classes.

The **Detector Construction class** (inherits from `G4VUserDetectorConstruction`) is fundamental for describing the geometric space and materials through which the particles will propagate. The toolkit supports a number of solid geometry types, which can be combined using Boolean operations. It is also possible to import geometric descriptions generated by computer-aided design (CAD) tools. This class includes the definition of materials and their specific properties, such as density and optical properties.

The **Primary Generator Action class** (inherits from `G4VUserPrimaryGeneratorAction`) defines the "*primary generator*", which contains the initial particles of each event. Specifically, it establishes the energy and creation vertex (the point of origin) of the initial particle.

The **Physics List** (a mandatory class in the latest versions of Geant4, inherited from `G4VUserPhysicsList`) is crucial because it defines all the particles and their interactions in the simulation. Within this class, the user must define all the particles that can be generated during the simulation process. Each particle must be associated with one or more processes, represented by C++ classes that describe how and when a specific interaction occurs along the particle trajectory. One or more models can be registered for each process. A model is defined as a C++ class that implements the specific details of an interaction, such as its kinematics. Geant4 provides coherent configurations of predefined physical models, known as "Physics Lists", which are useful for specific purposes. The user can choose from these reference lists or customize one according to application requirements.

The toolkit can simulate the interaction of any particle in a wide energy spectrum, ranging from a few eV to several TeV. The physics models cover electromagnetic processes from approximately 10 eV to PeV and hadronic processes from a sub-eV scale to PeV, including decays and processes for optical photons. In addition to the required classes, there are additional user action classes (such as Run Action, Event Action, Tracking Action, and Stepping Action) that allow the user to access and handle simulation data with increasing levels of detail. In order to simulate particle transport, each particle is tracked discretely by constructing a track object, placing it

on a stack, and sequentially numbering it with a trackID. It is then moved step-by-step through the specified geometry. When a particle changes volume, undergoes an interaction, or is limited by a user-defined cut after a specific length, the step ends. The simulation is structured around four main classes [95]:

- **G4Run**: Contains a set of events that share the same geometry and physics conditions.
- **G4Event**: Represents the creation and transport of a primary particle and the transport of all its secondary particles through the defined volumes.
- **G4Track**: This is a snapshot of a single particle and its trajectory, containing information on its initial and current state. Each track is assigned a trackID and placed on a stack to be processed.
- **G4Step**: Contains information about the change in a track during propagation, including the initial and final points and differential information. Geometrically, a step is the distance between two successive interaction positions.

Particle transport is the result of the combined action of the Stepping Manager kernel, the Physics processes it invokes, and the Transportation Process, which determines the geometric limits and the next volume when a boundary is crossed. At the beginning of each step, the particle is subject to several competing processes, each with a specific relative probability (cross section) depending on the identity of the particle, its energy, and the medium. The next interaction point is sampled in terms of the "number of mean free paths (n_λ)". The mean free path (λ), or "interaction length", for a given process can be expressed as a function of the total cross section σ(Z,E):

$$\lambda(E) = \left(\sum_i [n_i \cdot \sigma(Z_i, E)] \right)^{-1} \tag{3.2}$$

where n_i is the number of atoms per unit volume of the i-th element. Since λ depends on the composition of the medium, the mean free paths n_λ, which are independent of the material traversed, are used. It influences the probability $P(l)$ of interaction along a path l for a given process ($P(l) = 1 - e^{-n_\lambda \cdot l}$) and is defined by the integral:

$$n_\lambda = \int_{x_1}^{x_2} \frac{dx}{\lambda(x)} \tag{3.3}$$

At the beginning of the step, n_λ is sampled using direct sampling to extract a random number η distributed uniformly in the range (0, 1), by setting n_λ as $n_\lambda = -log(\eta)$. The lowest value among the n_λ samples for the different processes is chosen as the actual step, thus determining the selected process.

However, the step can also be limited by geometric boundaries or user-imposed thresholds (such as energy cuts or maximum step limits). If a border crossing occurs in a new medium, the number of mean free paths is adjusted. The particle is transported along a straight line if it is neutral or if there are no electromagnetic (EM) fields;

otherwise, charged particles follow a curved line based on the equation of motion that takes into account the EM fields involved.

In addition to discrete processes, continuous phenomena such as continuous energy loss and multiple scattering also set a limit on the step size. The secondary particles generated by an interaction are also tracked. All particles are tracked until they reach a cut-off energy, below which the simulation stops, and the remaining energy is considered absorbed. The entire "cascade" of tracks constitutes a single event.

3.2.2 Physics lists for particle therapy simulations

Since one of the aims of this thesis is to simulate the interaction of particles with biological matter, the physics of interest must accurately include both electromagnetic and hadronic processes.

Nuclear interactions cause the attenuation of primary ions and build up of secondary ions, aspects that are crucial for accurate dose delivery and dosimetry [76]. Inelastic interactions are responsible for beam attenuation of the primary beam with penetration depth, and elastic interactions contribute to beam broadening. In the case of carbon ions, it was estimated with MC simulations that up to about 40% of the dose in the region between the entrance channel and the Bragg peak is delivered by fragments [41]. Thus, wrongly modeled cross sections would clearly lead to discrepancies in longitudinal and lateral dose distributions between measurements and MC simulations.

In Geant4, the user can select different models by specifying the physics list. The toolkit offers several alternatives for electromagnetic processes. The constructors G4EmStandardPhysics_option3 and option4 are often the reference for medical physics when high precision is required in standard tracking. However, for applications involving micrometric-scale geometries or low-energy interactions, users can opt for the Livermore model, which provides a detailed description of atomic shell effects and fluorescence. Similarly, the choice of models for hadronic interactions is crucial in particle therapy to correctly describe beam attenuation and secondary particle production.

EMopt3

The standard EM Opt3 Physics List includes a collection of electromagnetic (EM) processes that accurately simulate gamma and charged particle transport. Its processes include physics from 0 to 100 TeV for gammas, electrons, and positrons, up to 1 PeV for muons, and electromagnetic interactions of charged hadrons and ions from 0 to 100 TeV. All of the mentioned intervals are well beyond the energy range of interest for microdosimetry applications. The main models used in this physics list are reported for the following types of particles:

- **Photons**:

  - e^-/e^+ pair production → BetheHeitler model with the Landau-Pomeranchuk–Migdal (LPM) effect at high energies.
  - Compton scattering → Klein-Nishina model.
  - Photo-electric effect and Rayleigh scattering → the Livermore models.

- **Electrons and positrons**:
  - Multiple Coulomb scattering Urban model from 0 to 100TeV.
  - Bremsstrahlung → eBremSB model and the eBremLPM model
  - Ionization → Moller-Bhabha formulation.
  - Positron annihilation → eplus2gg model.

- **G4GenericIon(s)**:
  - Multiple Coulomb scattering Urban model
  - For alphas, Bragg ionization is performed below 7.9 MeV and BetheBloch ionization above.
  - For generic ions, Bragg is used below 2 MeV and Bethe-Bloch above.
  - Nuclear stopping model is used below 1 MeV.

EMopt4

The standard EM Opt4 Physics List combines low-energy and standard EM models. Although it is the slowest among the standard EM constructors, it provides the highest accuracy. The relevant processes are implemented using the following models [94]:

- **Photons**
  Same as EM Opt3, except for the Monash University model (G4LowEPComptonModel) used for Compton scattering below 20 MeV, and the Penelope model for pair production.

- **Electrons and positrons**
  Same as EM Opt3, except for multiple Coulomb scattering, which is treated with:
  - Goudsmit–Saunderson model from 0 to 100 MeV,
  - WentzelVI model from 100 MeV to 100 TeV,
  - single Coulomb scattering model for large-angle scattering.

  The `UseSafetyPlus` step limitation with an error–free boundary approach is adopted for multiple scattering.

- **Alpha particles and** `G4GenericIon`
  Same as EM Opt3, except that for ion ionization:
  - below 1 GeV/u the ICRU73 model (`G4IonParametrisedLossModel`) is used,
  - above 1 GeV/u the Bethe–Bloch model is applied.

Livermore

The Livermore Physics List relies on evaluated experimental data libraries, including EPDL97 for photons, EEDL for electrons, and EADL for atomic relaxation. These datasets provide cross sections and transition probabilities derived from experimental measurements, ensuring accurate modeling of electromagnetic interactions at low energies. The relevant processes are implemented using the following models [94]:

- **Photons**:
  - e^-/e^+ pair production $\rightarrow$ Implemented by the *Bethe-Heitler 5D* model below 80 GeV and the *relativistic Bethe-Heitler* model above.
  - Compton scattering $\rightarrow$ Implemented by the *Livermore* models up to 1 GeV and by the *Klein-Nishina* models at higher energies.
  - Photo-electric effect and Rayleigh scattering $\rightarrow$ Both handled by *Livermore* models.
- **Electrons**:
  - Multiple Coulomb scattering (MSC) $\rightarrow$ Handled by the *Goudsmit-Saunderson (GS)* model at low energy and by the *WentzelVI* model at higher energies. The latter is combined with the *Single Coulomb scattering* model, applied for large angle scattering.
  - Bremsstrahlung $\rightarrow$ Implemented by the *Seltzer-Berger* model below 1 GeV and by the *eBremsstrahlungRelModel* at high energies.
  - Ionization $\rightarrow$ Modelled by the *Livermore* model.
- **Other interactions**:
  - All other electromagnetic interactions (including those for positrons and hadrons/ions) are configured identically as in the `G4EmStandardPhysics_option4` constructor.

Decays

In addition to the processes already described, the EM Standard Physics Lists handle the decay of all long-lived hadrons and leptons through the `G4Decay` process, which, however does not include hadronic resonances (e.g., deltas) or heavy-flavor particles (such as D/B mesons or charmed hyperons). Radioactive nuclei are treated via the `G4RadioactiveDecay` process, which simulates α, β^+, β^-, γ emissions and electron capture, both at rest and in flight. The decay scheme is based on ENSDF nuclear data [4], which provides half-lives, level structures, branching ratios, and transition energies. If the daughter nucleus is left in an excited isomeric state, its prompt de-excitation is modeled using the `G4PhotoEvaporation` class.

Hadronic physics

Given the importance of nuclear interactions in proton therapy for describing beam attenuation and secondary particle production, a specific set of hadronic physics constructors has been selected to ensure high accuracy in the therapeutic energy range.

- **Elastic Interactions** ($\rightarrow$ `G4HadronElasticPhysicsHP`): This constructor handles the elastic scattering of hadrons.
  - **Neutrons ($<$ 20 MeV)**: Utilizes the *NeutronHP* (High Precision) elastic model, which relies on evaluated nuclear data libraries (such as ENDF/B-VII) for precise cross-sections and angular distributions.
  - **Protons and other hadrons**: Handled by standard elastic models (typically the *Barashenkov-Glauber-Gribov* or *Chips* parameterizations depending on the specific Geant4 version), valid for all energies.
- **Inelastic Interactions** ($\rightarrow$ `G4HadronPhysicsQGSP_BIC_HP`): This is the primary constructor for inelastic scattering of protons and neutrons. It adopts a multi-stage approach based on energy:
  - **High Energy ($>$ 25 GeV)**: Interactions are modelled by the *Quark-Gluon String (QGSP)* model.
  - **Intermediate Energy (20 MeV - 10 GeV)**: Handled by the *Binary Cascade (BIC)* model. This intranuclear cascade model is particularly recommended for medical applications as it accurately predicts the production of secondary neutrons and protons.
  - **Low Energy Neutrons ($<$ 20 MeV)**: Utilizes the *NeutronHP* models for inelastic scattering, capture, and fission, ensuring data-driven accuracy in the thermal and epithermal range.
- **Ion Inelastic Interactions** ($\rightarrow$ `G4IonBinaryCascadePhysics`): This constructor manages the inelastic interactions of generic ions.
  - **Light Ions (d, t, ^{3}He, α) and Generic Ions**: Modelled using the *Binary Light Ion Cascade (BIC Ion)* model. This extension of the standard Binary Cascade handles the fragmentation of the projectile and the target, which is crucial for determining the mixed radiation field in the patient.

3.3 The Monte Carlo track structure approach

As described in the previous section, MCCH codes may have important limitations with low energy transfers and small geometries. In fact, particle transport below the micrometer, which is typically the sub-cellular scale, cannot be accurately simulated due to the step limit being too large [157]. To get around these limitations, Monte Carlo track structure codes have been developed. Contrary to MCCH codes, these

codes follow both the primary and secondary particles on an event-by-event level until their energy falls below a defined cutoff threshold, which is often established by the validity of the interaction models.

Track structure simulations use random sampling to determine the particle travel distance, the type of interaction at that point, and the resulting secondary particle kinematics. To accurately model particle transport in a given medium, MCTS codes rely on total and differential cross sections that describe different particle-induced interactions. These cross sections are typically obtained from a combination of experimental measurements and theoretical calculations. Since liquid water constitutes more than 60% of the human body, most MCTS codes model the biological medium as water [188].

Some codes incorporate models which allow a more detailed study of radiation effects on biological structures, such as the DNA molecule, and can be extended to investigate interactions in medically relevant materials such as gold used in nanoparticle applications. MCTS codes provide accurate microdosimetry calculations and are able to quantitatively model DNA damage from both direct and indirect radiation effects. However, their predictions at very low energies and nanometer scales should be interpreted with caution. Nikjoo et al. [199] provided a review of the various MCTS algorithms used in radiation research.

3.3.1 Geant4-DNA

Geant4-DNA is one of numerous Monte Carlo Track Structure (MCTS) codes. The European Space Agency (ESA) first introduced the Geant4-DNA project (http://GEANT4-dna.org) in 2011. It is completely integrated into the Geant4 toolkit. With a focus on space radiation protection studies, it aimed to give the scientific community an open-access tool to assess the biological damage caused by ionizing radiation at the subcellular level [21][132][133][134]. The approach used by Geant4-DNA for evaluating DNA damage based on time evolution and stage is shown in Figure 3.1.

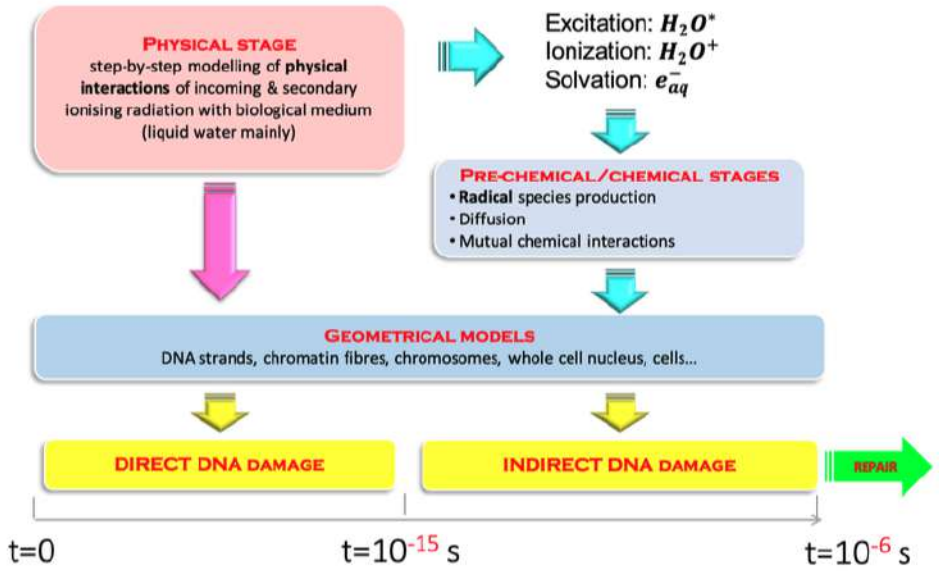

FIGURE 3.1: Geant4-DNA approach to modeling biological effects caused by ionizing radiation.

Not all stages of Geant4-DNA will be examined in detail. In this thesis, the analysis focuses on the physical stage, used to describe the interaction between the ^{99m}Tc-AuNR system and the aqueous medium (see Chapter 5).

Physical interactions are described by specific C++ "process classes", which compute the total cross section of specific physical interactions (e.g., elastic scattering, ionization, etc). A full description of the interaction products (kinematics, production of secondary particles, energy deposits, e c.) is provided as well [134]. In Geant4-DNA, these processes are fully discrete, which means they replicate all physical interactions using a step-by-step, precise tracking method without needing any condensation methodology [134].

The Geant4-DNA extension provides models for simulating, step by step, the electromagnetic interactions of charged particles with liquid water, the main component of biological systems. These particles include electrons, protons, neutral hydrogen, alpha particles, and selected light and heavy ions such as Li, Be, B, C, N, O, Si, and Fe. The processes are valid down to very low energies, close to the lowest excitation level of the water molecule (about 7.4 eV for electrons). Below these thresholds, particles are no longer tracked by DNA models and deposit their energy locally.

Unlike models of Geant4, which are limited to interactions with isolated atoms, Geant4-DNA takes into account the molecular structure of water and accurately describes both the cross sections and final states of interactions, including secondary products, energy loss, and angular deviations. The types of simulated interactions depend on the particle [21]:

- **Electrons**: elastic scattering, electronic and vibrational excitation, ionization, and molecular attack (7.4 eV - 1 MeV);

- **Protons and hydrogen atoms**: elastic scattering, electronic excitation, ionization, and electron exchange (100 eV - 100 MeV);
- **Helium and associated charge states**: elastic scattering, excitation, ionization, and charge exchange (1 keV - 400 MeV);
- **Other ions**: ionization only (0.5 MeV/u – 106 MeV/u).

A detailed description of interactions is essential for correctly reproducing energy distribution at the nanoscale, particularly for low-energy secondary electrons, which are primarily responsible for damage to DNA and subcellular structures [198]. The Geant4-DNA physics models used in this thesis are those for electrons in water and are listed in Table 3.1.

Process	**Geant4-DNA Model**
Ionization	G4DNABornIonisationModel
Excitation	G4DNABornExcitationModel
Attachment	G4DNAMeltonAttachmentModel
Vibrational excitation	G4DNASancheExcitationModel
Elastic scattering	G4DNAChampionElasticModel

TABLE 3.1: Physics models for electron interactions in water used in this thesis (Chapter 5).

One advantage of Geant4-DNA is the ability to choose between multiple physical models for the same process, allowing the impact of different theoretical descriptions on the results to be studied. This selection is easily done using physics constructors, which collect the models dedicated to each particle and type of interaction.

Chapter 4

Experimental characterization and Monte Carlo analysis of diamond detectors in hadrontherapy

As previously discussed in Section 1, microdosimetry provides physical quantities connected to RBE, such as lineal energy (y). Furthermore, it allows for a precise characterization of the stochastic interactions of radiation within sensitive volumes (SV) with micrometric dimensions close to those of a human cell. Single-crystal synthetic diamond detectors are a promising solution for dosimetry and microdosimetry due to their unique physical qualities, such as strong radiation resistance and near tissue equivalence.

These properties make them suitable for ion beam therapy. DIODE (Diamond Integrated device fOr HaDronthErapy), a three-year INFN (CSN5) project, is set within this context. Through close collaboration with Claudio Verona (University of Rome Tor Vergata) and my supervisor, Andrea Fabbri, I contributed to characterizing this new device throughout the entire duration of the project.

This project aims to develop a new detector specifically designed to simultaneously perform dosimetric and microdosimetric characterization of clinical ion beams. This would allow a fast and exhaustive beam characterization and quality assurance (QA) in hadrontherapy centres, reducing the experimental uncertainties such as those associated with the detector positioning. Dosimetric information will be used to compensate for the distortions at the lowest part of the microdosimetric spectrum due to the unavoidable electromagnetic noise.

Continuing in this field, in collaboration with Dr. Gabriele Parisi, I studied and characterized the "border effect" in diamond microdosimeters. This phenomenon distorts the deposited energy spectra, compromising the estimation of microdosimetric quantities. The second year of PhD focused on ensuring the accuracy and reliability of measurements in hadron therapy.

The methodology used in this work is described in Section 4.1. Section 4.1 provides a detailed overview of the DIODE detection system, including the geometry and electrical configuration of both the dosimeter and the microdosimeter. Subsections 4.1.2, 4.1.3, and 4.1.4 report the experimental setups adopted for IBIC characterization and for measurements with proton beams at the various facilities, while introducing the

Monte Carlo framework developed to model the border effect and its implementation in Geant4 simulations.

The results and analyses are reported in Section 4.2. Specifically, Section 4.2 presents the characterization of the border effect and its dependence on detector and irradiation parameters. Section 4.2.1 evaluates its impact on clinically relevant microdosimetric quantities. Section 4.2.2 demonstrates the dosimetric performance of DIODE in terms of linearity and depth-dose measurements, also discussing the microdosimetric spectra acquired along the Bragg curve and the associated RBE estimations.

A final summary and conclusions of the work are provided in Section 4.3.

The work presented in this chapter is based on the following peer-reviewed publications:

- Verona C, Fabbri A, Fazzi A, Bianchi L, Bianchi A, Cirrone P, Conte V, Petringa G, Raso AM, Scifoni E, Selva A, Tommasino F, Verona Rinati G, Verroi E. Experimental characterization of a diamond detection system for combined dose, LET and RBE assessment in clinical proton beams. Phys Med Biol. 2025 Sep 25. doi: 10.1088/1361-6560/ae0be8. Epub ahead of print. PMID: 40997903;
- Parisi G, Bianchi L, Couture P, Palitsin V, Fabbri A, Schettino G, Romano F, Verona C. The border effect in diamond microdosimeters and its impact on hadron therapy applications. Phys Med Biol. 2025 Jan 27;70(3). DOI: 10.1088/1361-6560/adaace. PMID: 39813791;
- C. Verona, A. Fabbri, A. Fazzi, L. Bianchi, V. Conte, G. Petringa, A. Raso, G. Verona Rinati; Development of a compact and portable diamond-based detection system for dosimetry and microdosimetry in ion beam therapy. Rev. Sci. Instrum. 1 November 2024; 95 (11): 113302. https://doi.org/10.1063/5.0235400.

4.1 DIODE device

The detectors were fabricated as a monolithic structure at the laboratories of the Industrial Engineering Department of Rome Tor Vergata University. The technological process employed microwave-enhanced chemical vapor deposition (CVD) and photolithography techniques. The configuration includes two independent active elements integrated on a single synthetic single-crystal diamond (scCVD) substrate measuring $3 \times 3 \times 0.3$ mm^3. Both components are configured as Schottky diodes with a boron-doped/intrinsic diamond/Cr structure. The boron-doped diamond layer, which acts as the back contact, has a thickness of approximately 0.4 µm. The two active elements are:

1. Dosimeter (Dos): Designed to measure the absorbed dose, it features a donut-shaped contact with a sensitive area (A_{Dos}) of approximately 3.4 mm^2 in clinical tests (or $\sim$ 4.2 mm^2 in the initial prototype) and a very thin sensitive volume (SV) thickness of approximately 0.70 ± 0.05 μm. The Dos has typically been used in unbiased mode.

2. Microdosimeter (μDos): Designed for microdosimetry, it has a circular shape with a sensitive area of 0.038 mm^2 (diameter 100 μm in the initial prototype) and an SV thickness of 6.3 ± 0.2 μm in clinical tests, although the thickness can vary between 2 and 10 μm. A bias voltage of $+20$ V (corresponding to 3 V/μm) was applied to the μDos to extend the depletion region to the entire thickness and ensure 100% CCE (Charge Collection Efficiency).

The diamond-integrated detector was micro-bonded in a Teflon-coated PCB and placed inside a hermetically sealed aluminum box connected to two readout chains. To prevent air ionization from altering the dosimetric response and assure waterproofing, the detector was enclosed in epoxy resin (2.7 mm in water equivalent thickness). The Al enclosure has dedicated front-end electrical circuits for dosimetric and microdosimetric signals, reducing noise and increasing device compactness. Figure 4.1 shows a schematic of the DIODE detector.

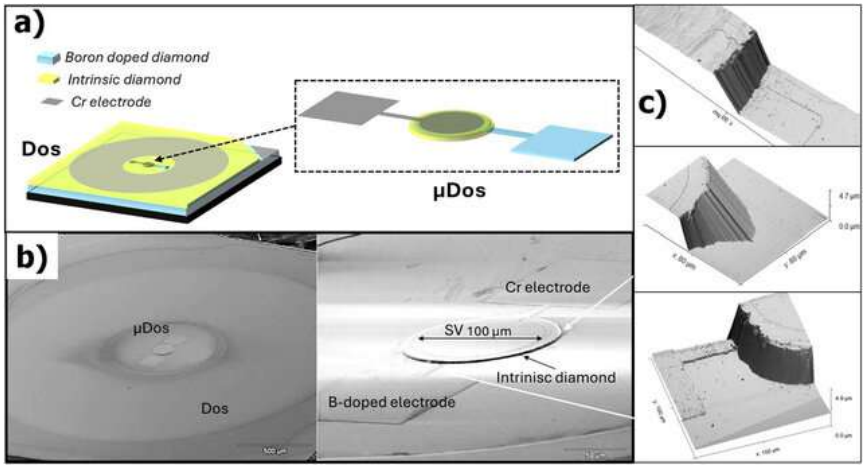

(A)

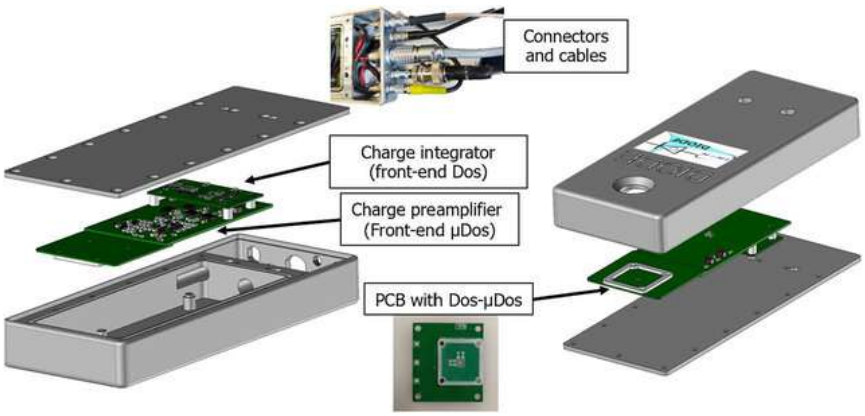

(B)

FIGURE 4.1: (A) Sketch (a) and SEM (b) picture of the Dos-μDos detector, and AFM maps (c) of the SV of the μDos device. (B) Schematic representation of the DIODE device as embedded in water-proof aluminium housing, along with the front-end electronic circuits [267].

4.1.1 Data analysis

Data analysis was a fundamental part of this PhD, involving the processing of raw data from both experiments and simulations to derive the final results for discussion. Several Python scripts were used to perform these analyses. In the case of IBIC measurements, for example, they were used to reproduce the deposited energy spectra, obtain the IBIC maps, and generate the charge collection profiles. They also processed the Geant4 simulation outputs, allowing for a direct comparison between simulated and experimental data.

These analyses proved to be fundamental for estimating the border effect, as detailed in the following sections. For all the analyses reported in this chapter, the relevant microdosimetric quantities were extracted from the energy spectrum acquired by the microdosimeter and from the simulation outputs.

As already discussed in Chapter 2, an important parameter in microdosimetry is lineal energy y. It is computed as $\epsilon_{dep}/\bar{l}$, where ϵ_{dep} is the energy deposited in the SV of the detector during a single event and $\bar{l}$ is the mean chord length within that SV. Since experimental microdosimetric spectra are referred to water (or expressed in water), it is necessary to convert the spectra in diamond using the water-equivalent mean chord length. In this specific case, a value of 20.15 μm was estimated for the μDos, as reported in [268].

The microdosimetric spectra were represented as $yd(y)$ vs y. The primary objective of this analysis is to transform raw data, typically consisting of a list of lineal energy values for each event, into microdosimetric distributions ($f(y)$ and $d(y)$). The process follows standard microdosimetric formalism. The raw data are organized in a logarithmic binning histogram, using a fixed number of bins per decade, providing uniform resolution on a logarithmic scale. To account for the variable width of the logarithmic bins (Δy_i), the counts in each bin are divided by the width of the bin itself, thus calculating the density distribution ρ_i.

This density is normalized by the total number of events ($\sum_j N_j$) to obtain the frequency distribution $f(y)$. The frequency-mean lineal energy is the mean value of $f(y)$:

$$\bar{y}_F = \sum_i y_i f_i \Delta y_i \tag{4.1}$$

The dose distribution is therefore obtained by normalizing the frequency distribution for this mean value:

$$d_i = \frac{y_i}{\bar{y}_F} f_i \tag{4.2}$$

Another relevant microdosimetric quantity is the dose-mean lineal energy, $\bar{y}_D$. This represents the mean value of the dose distribution $d(y)$ and is calculated as:

$$\bar{y}_D = \sum_i y_i d_i \Delta y_i = \sum_i y_i^2 f_i \Delta y_i \tag{4.3}$$

The DIODE detector was also used to calculate the RBE using microdosimetric data. As reported in Section 2.2, the in vitro clonogenic cell survival RBE_{10} for the V79 cell line was estimated by applying Loncol's biological weighting function, $r(y)$,

to the experimentally measured $d(y)$ spectra [168]. As reported in Chapter 2, the RBE can be calculated as the integral of the dose distribution $d(y)$ weighted by the biological function $r(y)$

$$RBE = \int r(y)d(y)dy \tag{4.4}$$

Computationally, this integral was calculated in its discrete form using Python scripts. Since the y_i bins of the experimental spectrum (stored in the y array) and the tabulated y points of the $r(y)$ function (loaded from a "weight_function" external file) do not coincide, an interpolation process was implemented. For each bin-center y of the $d(y)$ spectrum, the corresponding $r(y_i)$ value was estimated by linearly interpolating the Loncol function data. The RBE was then calculated as the discrete sum:

$$RBE = \sum_i r(y_i)d_i\Delta y_i \tag{4.5}$$

4.1.2 Characterization of diamond integrated device at LNL-INFN

The Dos-μDos detectors were preliminary tested at the Laboratori Nazionali di Legnaro (LNL)-INFN using a 1 MeV proton beam and 1 nA ions from a Van de Graaff accelerator (AN2000).

The dosimeter (or Dos) detector electronic readout circuit was designed to accurately measure the charge produced by the diamond device, which is proportionate to the dose absorbed. The current range is from a few tens of fA (the diamond dark current) to tens of nA around the Bragg peak of high LET particles. The Dos front-end used a charge integrator approach to ensure proper precision over six orders of magnitude of the input signal. The integration time is managed by an external microcontroller (8.5 $\times$3.5 $\times$6.5 cm^3), with a 16-bit A/D converter acquiring the integrator output values at the start and end of each integration period, which is delimited by two reset pulses. Using a dedicated MOS-based circuit, the capacitor may be reset quickly (<1 μs), reducing system dead-time. Moreover, a single-ended to differential output operational amplifier (commonly termed ADC driver) stage is present if the charge integrator output signal has to be driven to a remote A/D converter several meters away. When using a water phantom, this scenario is very common.

On the other hand, the μDos electronic chain consists of a charge sensitive preamplifier (CSP), followed by a spectroscopy amplifier and pulse height analyzer. The front-end electronics is a custom CSP board placed in the same chassis of the detector board, decreasing the capacitance of the electrical connections. Commercial standard modules or a small digital multi-channel analyzer (MCA) (e.g., Caen DT5770, 10 $\times$4 $\times$13 cm^3 in size) can be used to complete the remaining chain. The choice of the value of the feedback capacitance and, therefore, of the sensitivity, is crucial for the dynamic and noise performance trade-off.

A high sensitivity of about 7.7 V/pC has been chosen. The noise has been extensively characterized both under open circuit conditions and when connected to the detector board. The noise level gives an energy resolution of about 4.3 keV$_{FWHM}$ in diamonds. More info about the electronic read-out systems is reported in [267].

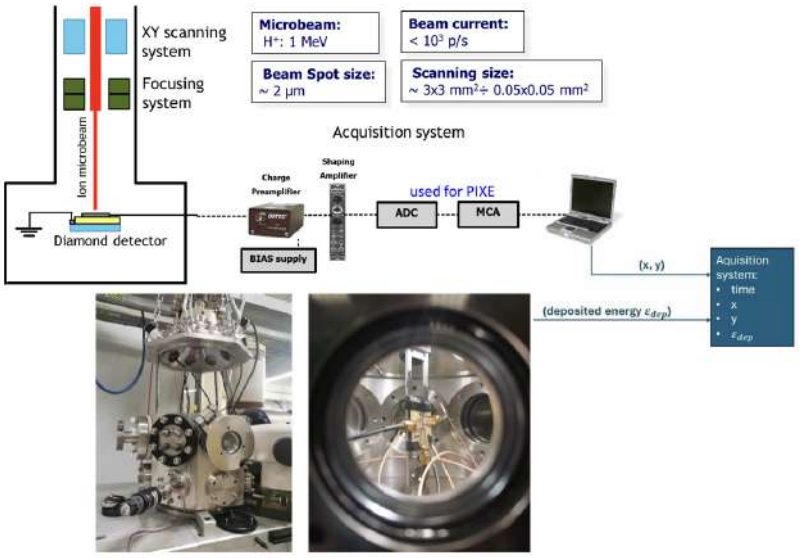

FIGURE 4.2: Experimental setup for IBIC measurements at the National Laboratories of Legnaro (LNL). Top: diagram of the microcollimator and acquisition chain. A 1 MeV microbeam of protons (spot ~ 2 μm) scans the surface of the diamond; the induced charge is processed in real time to generate CCE maps by correlating the beam position (x,y) with the deposited energy ε. Bottom left: external view of the vacuum chamber. Bottom right: detail of the diamond based microdosimeters housed inside the chamber.

As shown in Figure 4.2, the signals from both acquisition chains, as well as the beam position (x,y coordinates), were recorded in an event-by-event list format. IBIC maps were created based on the scanned area's spatial energy distribution. To calibrate the energy, a pulse generator and a thick diamond detector were bombarded with the same ion species at 100% CCE. Figure 4.3 show a large IBIC map ($\sim$3$\times$3 mm^3) of the Dos-μDos detector.

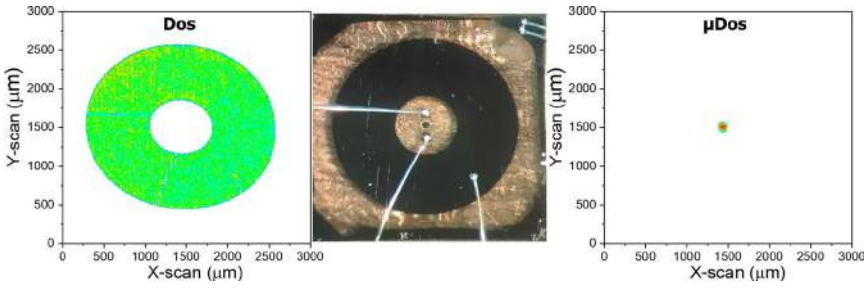

FIGURE 4.3: IBIC map of the Dos-μDos device. For visual comparison, an optical image of the device is presented.

The Dos-μDos detector IBIC map shows two separate sensitive zones with uniform sensitivities. These areas are contained inside the detectors' metallic contact areas. The drift of charge carriers in the depletion region below the Cr electrode produces a distinct current signal, while free carriers created elsewhere do not give detectable signals. To better characterize the μDos, an enlarged IBIC map (400 $\times$ 400 μm^2 in size) was acquired, as reported in Figure 4.4.

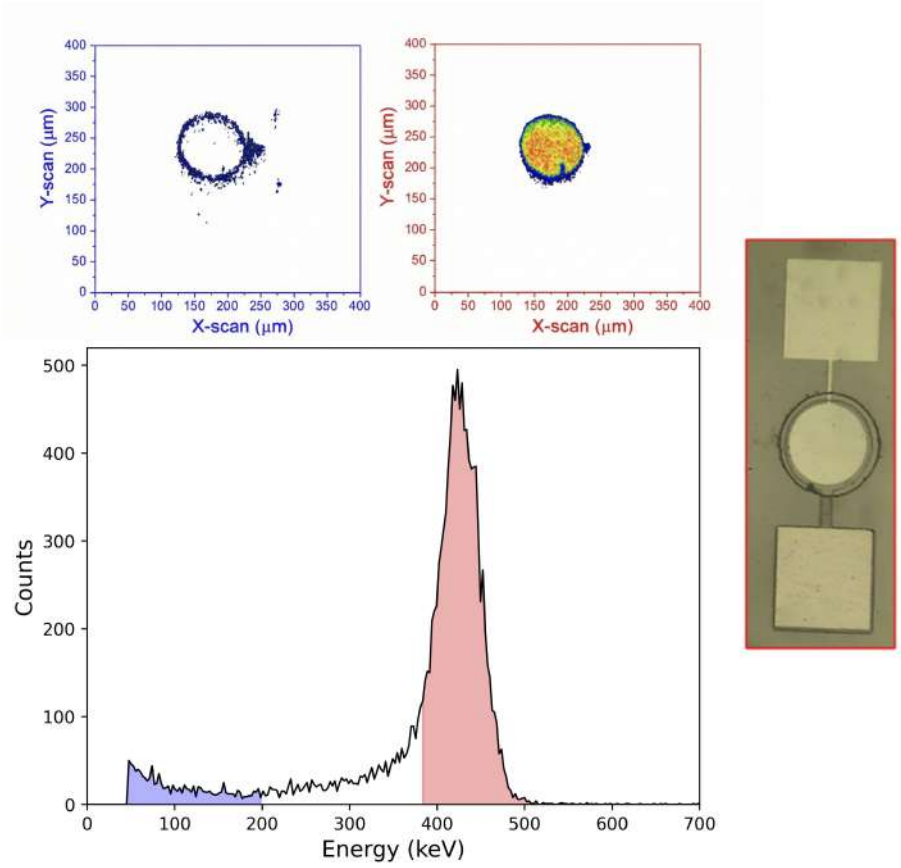

FIGURE 4.4: μDos energy spectrum for 1 MeV protons, showing two regions. Upper: Corresponding IBIC maps for the selected energy regions.

The energy spectrum was separated into two sections (red and blue) to investigate the origins of distinct contributions within the detector. Partial IBIC maps were then generated for each region, with a focus on events occurring during these energy windows. The main peak events (red region) were collected by a well-defined SV with a diameter of 100 μm. The blue region represents incomplete charge collection near the SV edge. Furthermore, a signal can be seen in a small region on the right side, only a few micrometers from the SV edge. This region corresponds to the initial part of the Cr strip connecting the bond pad. It partially overlaps the intrinsic diamond layer, which is slightly larger than the boron-doped diamond electrode (see optical image of the microdosimeter in Figure 4.4).

After characterizing the integrated diamond detectors, the DIODE prototype was tested in air with 5.47 MeV α-particles irradiation (not collimated) from a ^{241}Am source at 4 mm from the detector surface. The energy of impinging α-particles was estimated to be 5.1 MeV, considering air absorption under the given irradiation conditions. The detector surface had a fluence rate ϕ of approximately 100 particles/mm$^2\cdot s$. During testing, the output signal waveforms from both detectors were obtained using a 200 MHz PicoScope 3000E series with a 3-bit digital filter. Figure 4.5 shows typical signals from Dos and μDos detectors.

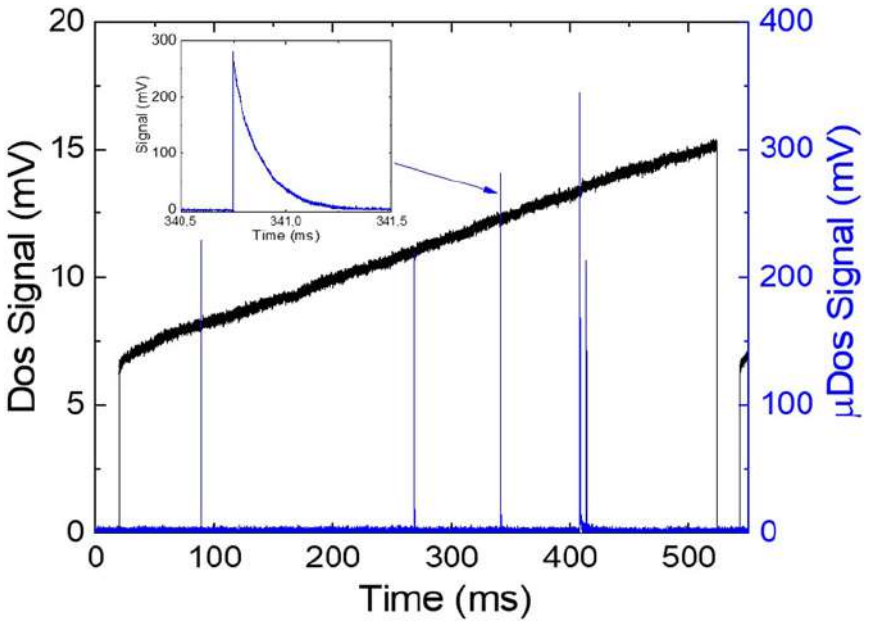

FIGURE 4.5: Signals from the Dos (black curve) and μDos (blue curve) detectors during α-particle irradiation.

The black line represents the signal coming from the charge integrator output for a 500 ms integration time. It represents the voltage across the 100 pF integrating capacitor. For the measurements shown in Figure 4.5, a reset time of 10 ms was adopted to better separate a single acquisition window, instead of the shorter usual one (0.1 ms). During the integration interval, the integrated charge shows an almost constant increase, reflecting a nearly steady detector current. The signal originates from individual α-particles, but because many of them hit the Dos detector within 500 ms (around 200) and each produces only a small amount of charge, the events merge together, appearing as a continuous growth in the integrated charge. Since the signal is sampled just after the first reset and just before the second, a difference of about 8 mV between the two samplings over a 100 pF capacitor corresponds to an integrated charge of 0.8 pC, which in turn yields a detector current of approximately 1.6 pA.

The blue line represents the μDos output signal, resulting from α particles impinging on the SV of the μDos detector. The typical δ-response of a CSP is shown in the inset of Figure 4.5. The exponential decay time constant of 130 μs arises from the continuous CSP reset through the feedback resistor. The voltage pulses shown in Figure 4.5 range from roughly 200 to 350 mV. Multiplying these amplitudes by the CSP sensitivity yields charge values of 26–45 fC. These charges can then be converted into the energy deposited in the SV25 by multiplying by the mean energy required to create an electron–hole pair in diamond (13.2 eV) and dividing by the electron charge (1.6×10^{-19} C), resulting in an energy range of 2.1–3.7 MeV.

The current generated in the SV of the Dos and the energy deposition distribution in the SV of the μDos were recorded simultaneously when the device was irradiated by α-particles. Figure 4.6(a) shows the pulse height analysis (PHA) spectrum of the diamond μDos with an SV thickness of 2.5μm, measured under α-particle irradiation.

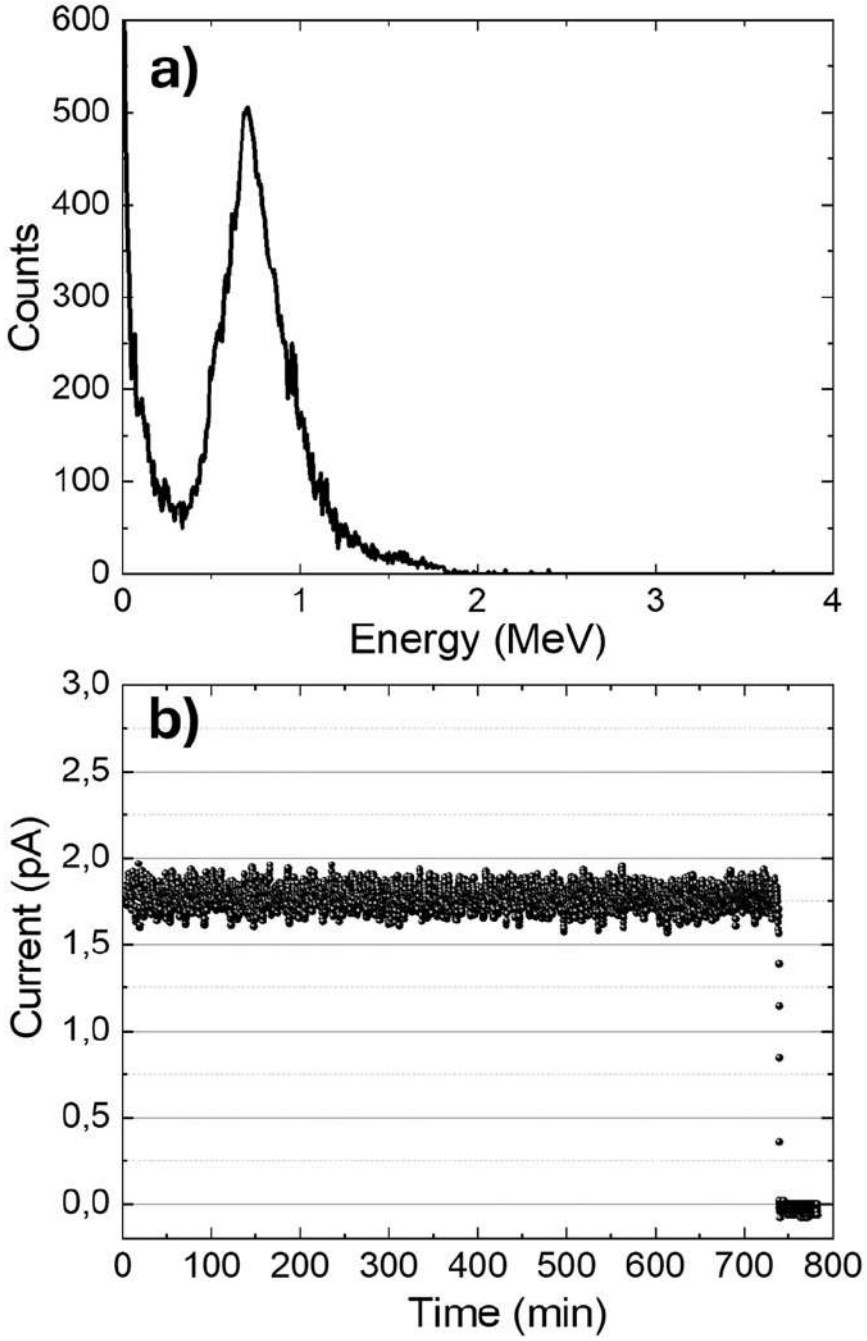

FIGURE 4.6: (a) PHA spectrum acquired by μDos and (b) Dos current over time during α-particle irradiation.

The PHA spectrum was collected over approximately 12 hours to ensure sufficient statistical accuracy. The detector response remained stable and reproducible, showing no signs of polarization effects.

Gaussian fitting of the spectrum yielded a peak energy of around 710 keV, in close agreement with the Monte Carlo simulation, confirming a 100% CCE for μDos. Events observed below 0.3 MeV are mainly attributed to edge effects, where charge collection is incomplete near the SV borders. Additionally, the absence of collimation in the alpha-particle beam contributes to these low-energy events by increasing the angular spread of the incident particles and broadening their energy distribution.

Figure 4.6(b) shows the current measured by Dos detector as a function of time. The current remained stable, showing a good signal-to-noise ratio within the pA range. The dark current was very low, around 0.1 pA, comparable to the leakage current of the electronic circuit. The measured current amplitude was approximately 1.7 ± 0.2 pA, consistent with expected values. Monte Carlo simulations estimated that a single α-particle deposited an average energy of about 285 keV in the $\sim$1 μm-thick Dos device. Considering the α-particle fluence rate, the expected current in the diamond dosimeter, calculated as

$$i = \frac{\phi E e}{A_{\mathrm{Dos}}\, 13.2},$$

was approximately 1.5 pA, matching the observed measurements. These results underline the accuracy and reliability of the DIODE device under such irradiation conditions.

4.1.3 Characterization of diamond integrated device with clinical proton beam

In order to evaluate the detector behavior under clinical conditions, the study was expanded to include measurements made using a clinical proton beam. These measurements were performed at the Trento Proton Therapy Centre (Italy), operated in collaboration with TIFPA (Trento Institute for Fundamental Physics and Applications, INFN), using a quasi-monochromatic 70 MeV proton beam on the 30° beamline [260].

The spatial profile of the proton beam at 70 MeV is Gaussian, with $\sigma \sim 6.93$ mm at the isocenter. At the isocenter, 1.25 meters from the beam exit window, the detector was aligned with a laser-based reference system. For measurements made in the distal fall-off region of the Bragg peak, the nominal beam current was increased from 10 nA to 50 nA to improve the statistics.

At each position, the DIODE detector was used to simultaneously acquire energy spectra and current. Custom software was used to record the current and total charge created in the sensitive volume (SV) of Dos, following proton irradiation. The energy-deposition distribution in the SV of the µDos was measured on an event-by-event basis, with around 3×10^6 events recorded throughout the irradiation period.

A variable number of calibrated EBT3 gafchromic films ($3 \times 3\, cm^2$, each with a known thickness of 0.355 mm water-equivalent (WE)) were placed in front of the DIODE detector to produce 23 different WE depths as reported in Table 4.1. The WE thickness of the EBT3 layers and the epoxy resin layer in front of the detector, which was 2.7 mm, were taken into consideration when estimating the overall WE depth. The uncertainty resulting from the placement and calculation of the WE thickness of the materials in front of the detector was included in the positioning error ($\pm$0.20 mm).

TABLE 4.1: Measured WE depths and associated uncertainty.

No.	Depth (mm)	No.	Depth (mm)	No.	Depth (mm)
1	3.05	9	35.71	17	39.26
2	8.38	10	36.42	18	39.62
3	11.22	11	36.78	19	39.97
4	18.68	12	37.13	20	40.33
5	23.64	13	37.49	21	40.68
6	28.97	14	37.84	22	41.04
7	34.29	15	38.20	23	41.39
8	35.00	16	38.55		

Positioning error: $\pm$0.20 mm

4.1.4 Border effect characterization at Surrey Ion Beam Center

Complementary IBIC measurements were performed at the Surrey Ion Beam Centre (UK) [245][249] to characterize the border effects in the diamond microdosimeters. The facility uses a 2 MV Tandetron from High Voltage Engineering Europe (HVEE), and an OM-150 magnetic quadrupole triplet lens from Oxford Microbeams Ltd [200].

Three diamond microdosimeters with different thicknesses were employed. They had a square sensitive area of equal size and a thickness of 2, 6, and 12 μm. While the thickness of the detectors was measured by means of an atomic force microscope, the side of their sensitive area was measured 102 μm by an optical microscope. The three detectors were fabricated by the University of Roma "Tor Vergata" based on the technology presented by Verona et al. [270][265] and discussed deeply in Chapter 2.

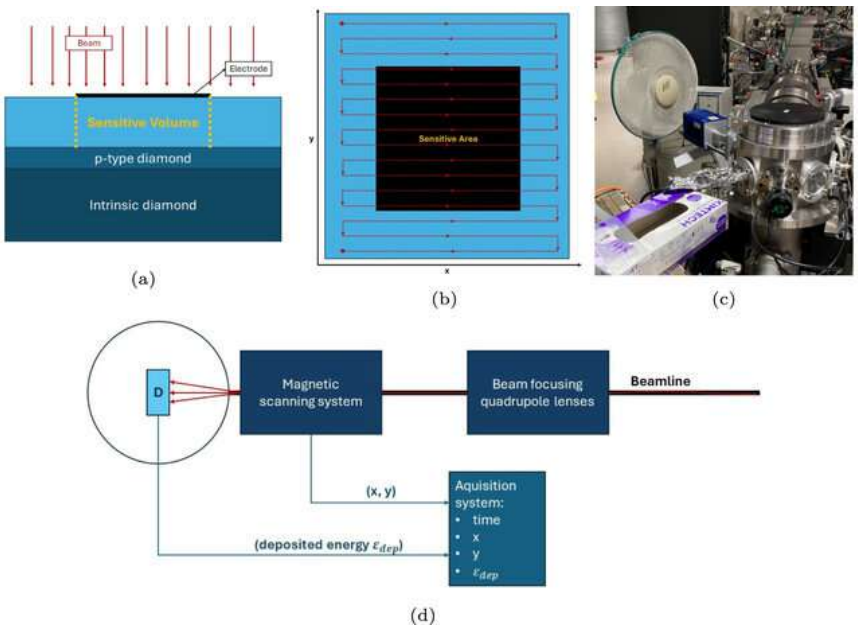

FIGURE 4.7: The figures show the detector structure, IBIC irradiation logic, experimental beamline, and experimental set-up at the Surrey Ion Beam Centre.

A schematic representation of the experimental set-up is shown in Figure 4.7 (d). The irradiation chamber is provided with a tiltable sample holder in which the

detector is fixed. A motorised system allowed for fine-tuning the detector position to place it at the beam focus point. The microdosimeter was connected to a conventional amplification chain for pulse-shape-analysis measurements.

A CAEN A1422 charge-sensitive pre-amplifier was followed by an ORTEC 671 shaping amplifier that was connected to a custom ADC-MCA (Analog to Digital Converter—Multi Channels Analyser) module to read and acquire charge-collection signals. The ADC-MCA module was coupled to a dedicated acquisition device, which read and recorded the amplitude of the scanning magnets magnetic field. The detectors were operated at bias voltages of 6, 18, and 36 V for the 2, 6, and 12 μm thick microdosimeters, respectively. Each detector was subjected separately to each radiation quality. The 'OMDAQ3' software by Oxford Microbeams Ltd (2024) was used for data collection and online analysis.

IBIC raw data, such as the deposited energy and the location (x and y coordinates) of each event, were collected and analyzed sequentially. The results were calibrated in energy using measurement sites where the nominal energy of the ion provided fell within a range less than the detector thickness. The pulse height spectra were fitted using a Gaussian function to find their peak. The peak position corresponds to the equation

$$E_{peak} = E_{beam} - E_{f.e.}, \tag{4.6}$$

where E_{beam} is the nominal energy of the ion beam and $E_{f.e.}$ is the fraction of energy deposited in the front electrode. $E_{f.e.}$ was estimated by using Geant4 toolkit.

The calibration factor was determined as $k = \frac{E_{peak}}{\mu_{peak}}$, where μ_{peak} represents the expectation value of the Gaussian fit for the peak position in the acquisition units. This procedure was used to calibrate all data in energy. To remove background electronic noise, a low-energy cut-off at 120 keV was applied to each measurement. IBIC maps were generated by attributing the average deposited energy to each map pixel, taking into account only the events that occurred at that point.

Spatial coordinates were calibrated from pixels to μm. The spatial calibration factor was computed by dividing the SV side length measured with an optical microscope by the pixel value calculated from raw IBIC data. Incomplete charge collection leads to a long tail of events at lower energy than the main peak associated with full CCE events.

To distinguish between incomplete charge collecting regions, a tail threshold was applied to each measurement. Two regions were identified: one for events collected with full CCE, and another for incomplete charge collection. Figure 4.8 illustrates the behavior described and the two regions identified. Two IBIC maps were generated based on events with deposited energy inside the selected region. This helped identify parts of the SV that had incomplete charge collection.

Monte Carlo simulation details

The Geant4 toolkit was used to perform Monte Carlo simulations [2][3][4]. As previously discussed, Monte Carlo simulations were performed to estimate the impact of the border effect distortion on the microdosimetric quantities measured by

diamond detectors under typical proton therapy conditions. Furthermore, they were used to reproduce the deposited energy spectra in the μDos.

The simulation code used was based on the Geant4 advanced example `EXP_MICRODOSIMETRY`. The detector structure, shown in Figure 4.1a, was accurately reproduced in the simulation code. The square or circular shape was simulated based on the microdosimeter used during the experimental measurement. The diamond material was modelled as solid carbon with a density of 3.51 g·cm^{-3}.

To replicate CCE profiles and the deposited energy spectrum, a scoring function was implemented to collect the energy deposition within the SV and the coordinates of the particle's impact position. For the simulations, the following Geant4 physical models were used:

- `G4EmLivermorePhysics` for electromagnetic interactions;
- `G4HadronElasticPhysicsHP` for hadronic elastic interactions;
- `G4HadronPhysicsQGSP_BIC_HP` and `G4IonBinaryCascadePhysics` for hadronic inelastic interactions.

The border effect arises when the applied electric field lines overflow outside the SV region. The thickness of the detector impacts the operational bias voltage and thus the intensity of the electric field overflow. The electric field near the boundary is not uniform, both radially and longitudinally, due to the bending of the field lines.

This study aimed to analyze the border effect and its impact on many parameters, including detector thickness, ion penetration depth, and ion atomic number (Z). Since the particle Z alters the geometrical topology of energy deposition on the nanometric scale, it is expected that it will have an impact on the charge collection by a non-uniform electric field.

The border effect could be estimated by analyzing the form of the measured CCE profiles. To achieve this, the CCE profiles were fitted by an error function:

$$f_{err} = \frac{1}{2}\left(\text{erf}\left(\frac{x-\mu}{\sigma\sqrt{2}}\right)+1\right) \tag{4.7}$$

The two free parameters of the fitted function were μ and σ. The error function, a recurring function used to describe electrical phenomena, was chosen to represent the border effect, which is caused by undesirable electrical phenomena.

Equation 4.7 defines the derivative of the error function as a Gaussian function with mean value μ and standard deviation σ. This characteristic of the error function is useful for understanding its parameters. The Gaussian peak position μ represents the highest CCE gradient, while the σ value represents the width of the border effect. The border effect was quantitatively described using the full width half maximum (FWHM) of the Gaussian derivative, which is $2\sqrt{2ln2}\sigma$. The ideal condition of no border effect is represented by $\sigma = 0$, and the larger σ, the worse the border effect. The attenuation slope is unaffected by μ, which is a positional parameter. The uncertainty of the FWHM value was calculated by propagating the uncertainty of σ. This was calculated as the variance of the parameter obtained by the fit.

The first phase of the simulation strategy was to model the border effect and simulate the experiments in order to replicate the results of the IBIC experiments. The model was validated based on the agreement between experimental IBIC data and simulated results. The border effect model was then applied to the simulated data in order to quantify the influence of the border effect in three typical proton treatment scenarios. In this regard, a comparison with an experimental measurement of a clinical proton beam provided support for the approximation of applying the border effect model to energies greater than those examined [208].

Reproducing the IBIC experiment

Mono-energetic beams with nominal energies provided in Table 4.2 were simulated to reproduce the experiments carried out at the Surrey Ion Beam Centre. Following the guidelines of the Ion Beam Center, and to account for potential experimental disturbances, the beam energy was simulated using a Gaussian distribution with a mean value equal to the nominal beam energy and a standard deviation of 1%.

Because the error function accurately described the border effect, a model based on it was developed to reproduce the border effect on simulated data. Equation 4.7 was adjusted to correctly attenuate the CCE on all sides of the SV area. The σ value, which represents the border effect, was determined by fitting the experimental IBIC data.

As the electric field lines bend towards the margins of the SV, the μ value was adjusted to begin attenuation around the nominal border at point x_b. For the border at lower x, $= x_b - \sigma$, while for the border at higher x, $\mu = x_b + \sigma$. The attenuation function $f_{att}(x, y)$ was applied to the simulated data to replicate the border effect, as follows:

$$\varepsilon_{wb} = \varepsilon f_{att}\,(x, y) \tag{4.8}$$

where ε is the simulated energy deposition, and x and y are the coordinates of the event position. The model was validated by the agreement between experimental IBIC data and the results of using the model on simulated data.

TABLE 4.2: Summary of measurement points from the IBIC experiment carried out at the Surrey Ion Beam Centre. The range values were obtained from SRIM tables [290].

Particle type	Energy (MeV)	Z	Range in diamond (μm)
Proton	1.0	1	7.9
	1.8	1	20.3
Helium	1.6	2	2.75
	2.8	2	5.3
Carbon	2.5	6	1.4
	6.0	6	2.8
Oxygen	8.0	8	2.8

Application of border effect to the microdosimetry simulation of typical proton therapy conditions

To quantify the impact of the border effect on microdosimetric quantities, the microdosimetric measurement for different typical proton therapy radiation qualities was simulated. The border effect model described in the preceding section was then correctly applied to the simulation data. Only protons were evaluated in this investigation.

The approximation of applying the border effect model to energies higher than those explored in the IBIC experiment was supported by a comparison with an experimental measurement of a clinical proton beam. The conventional microdosimetry formalism [35] was used to determine microdosimetric quantities such as frequency-mean lineal energy ($\bar{y}_F$) and dose-mean lineal energy ($\bar{y}_D$).

The simulated detector reproduced one of the detectors used for IBIC measurements with a thickness $\sim 6\mu$m, which is similar to that of the DIODE μDos. The sensitive area was equal to $102 \times 102\ \mu m^2$. A 70 MeV proton beam was simulated, with energy modeled as a Gaussian distribution with a standard deviation of 3%.

Three simulations were performed with the detector placed at different depths in water: 20, 38, and 43 mm. These indicate the three main regions of a depth-dose profile: the entrance (E), Bragg Peak (BP), and fall-off (FO). Each simulation was carried out in line with the recommendations provided by [206], gathering sufficient statistics to ensure that the uncertainty of ($\bar{y}_F$) and $\bar{y}_D$ was less than 5%. This ensured that any observed deviations were due to the border effect rather than statistical fluctuations.

To evaluate the impact of the border effect on microdosimetric quantities, variations in the values of ($\bar{y}_F$) and $\bar{y}_D$ at different depths in water were calculated. As will be discussed below, the value of σ used is that measured by the IBIC experiments for the 6 μm detector with protons at 1.8 MeV. The impact of the border effect depends on the number of events collected in the border region, compared to the total number of events measured.

These border events are those characterized by incomplete CCE. The number of events collected in a homogenous radiation field, such as an ion beam on the micrometric area of a solid-state detector, is proportional to the collecting area. The impact of the border effect was investigated as a function of the ratio between the area of the border region and the sensitive area ($R_{area} = A_{borders} / A_{detector}$). The border region area $A_{borders}$ was defined as the area of a sensitive-area contour of width σ. Hence, for a square detector with side l:

$$R_{area} = \frac{(l + 2\sigma)^2 - l^2}{l^2} = \frac{(l + 2\sigma)^2}{l^2} - 1 \tag{4.9}$$

R_{area} depends by two parameters: σ and detector size (l in this case). The relationship between the two factors was investigated individually. In one case, R_{area} varied by changing σ while keeping the detector sensitive area constant. In the other case, the sensitive area was modified while σ remained constant. This was achieved by changing the application point μ of the attenuation function.

4.2 Results and discussion

Border effect characterization

The border effect was characterized by studying the experimental IBIC maps, deposited energy spectra, and CCE profiles. The energy deposition spectrum of a mono-energetic particle beam passing through a thin detector was expected to be a Landau distribution, tending to a Gaussian. Therefore, the low-energy tail was supposed to be an experimental distortion caused by the presence of incomplete CCE regions in the detectors.

Figure 4.8a shows the deposited energy spectrum of 1 MeV proton beam by the 6 μm thick diamond detector. The orange region is the main energy deposition peak, while the blue region is the incomplete CCE tail. Figure 4.8c, 4.8b shows the two IBIC maps related to the two regions of the spectrum. As it could be observed, the microdosimeter showed a good uniformity of the CCE response at the center of the SV, which degraded at the SV borders and outwards. The *border effect* is the attenuation of CCE and manifests as a continuous flat tail in the energy deposition spectrum, at values lower than actual energy deposited by the particle.

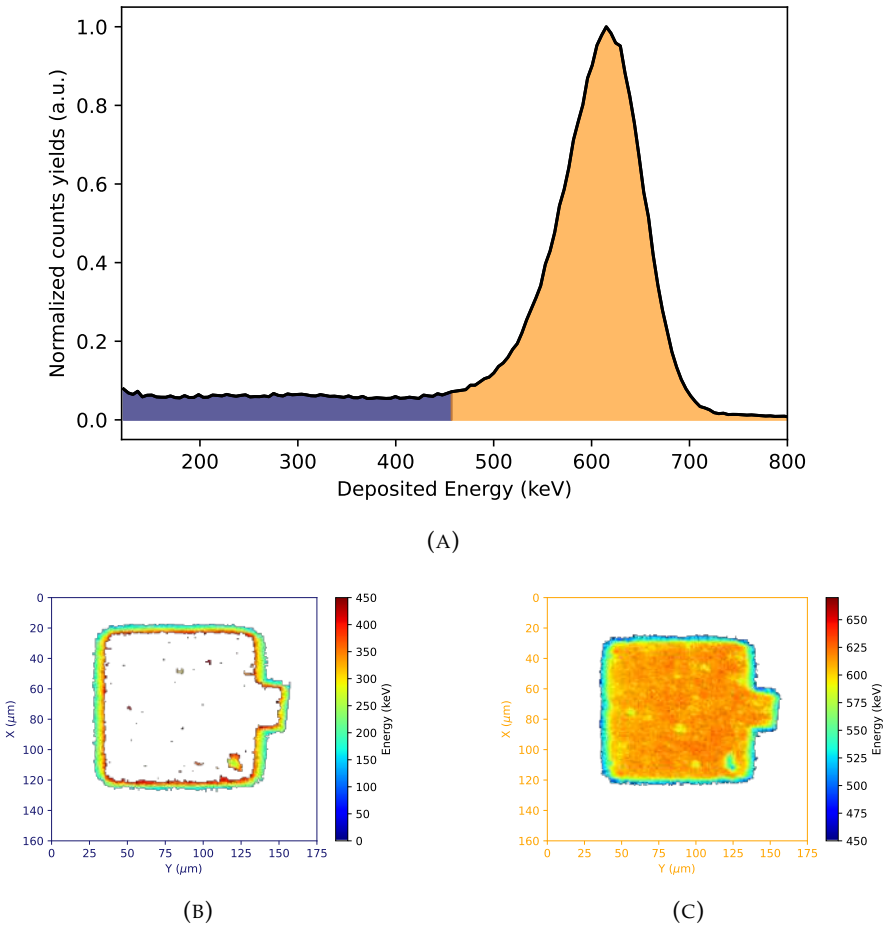

(A)

(B) (C)

FIGURE 4.8: IBIC measurement of 1 MeV proton beam by the 6 µm diamond microdosimeter: a) deposited-energy spectrum where the main peak region and the low-energy tail region were highlighted in orange and blue, respectively; (b) the IBIC map corresponding to the low-energy tail region (blue region); (c) the IBIC map corresponding to the main peak region (orange region). A low-energy noise cut-off of 120 keV was applied.

Following an error-function behavior, the CCE drastically decreased to zero as the beam moved outside the SV area. Figure 4.9a shows a good agreement between the experimental CCE profile and the profile derived by applying the border effect model to the Geant4 simulations. The σ value was obtained by fitting the results of the IBIC experiment with the equation 4.7.

The combined effect of the detector SV structural non-homogeneity, dirt particles that deposit on the electrode (as seen in Figure 4.8c at the bottom right corner of the SV) and experimental noise can be used to explain the broader peak that was observed experimentally. The simulation does not account for these effects.

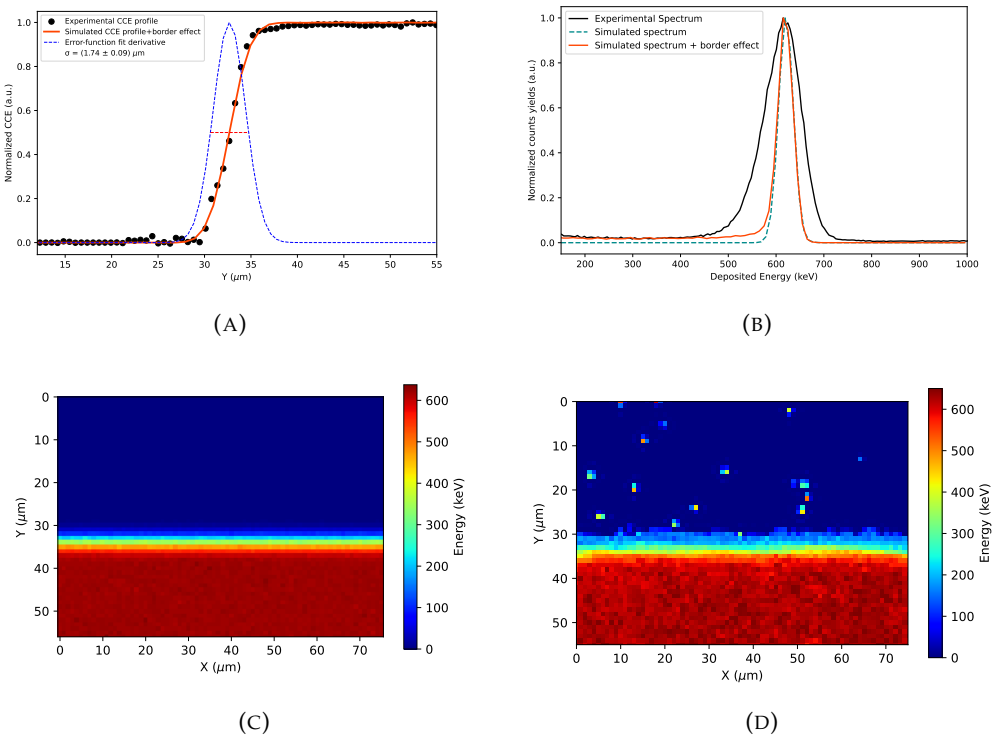

FIGURE 4.9: IBIC measurements (1 MeV protons) on the 6 μm diamond microdosimeter: (A) CCE profile of the SV border, comparing the experimental data, the error function fit derivative, and the Geant4 simulation with the border effect model. (B) Energy deposited spectrum, showing the experimental data and the Geant4 simulation with and without the model. (C) Simulated and (D) experimental CCE maps.

A quantitative analysis was performed to investigate the behavior of the border effect as a function of different physical parameters, such as SV thickness, incident particle type, and penetration depth in diamond. Figure 4.10 shows how the penetration depth in diamond and the border effect, as defined by the FWHM of the border profile derivative, are correlated. A detailed overview of the border effect behavior versus the relevant parameters examined - the detector thickness, the particle atomic number (Z), and the penetration depth in diamond (or range) - is given in Figure 4.10.

In particular, the figure distinguishes between the different particle types and SV thicknesses analyzed. As the penetration depth in diamond increased, the border effect decreased for all three SV thicknesses investigated and for all particle Z. It changes significantly at penetration depths of a few μm, whereas there is only a slight dependency at higher depths. An increased density of field lines is produced in the direction of the electrode as the electric field lines that overflow the SV bend outward.

The border effect is stronger in the first few μm of detector thickness and decreases as penetration depth increases due to fewer dense field lines. As the penetration depth increases and become larger than the detector thickness, the value of FWHM tends to stabilize, suggesting asymptotic behaviour. This could be expected since once the penetration depth becomes much larger than the detector thickness, stopping power gradients becomes increasingly milder and the LET can be reasonably considered

constant within the few μm thick detector crossed. Therefore, in this condition, the charge collection should be equally affected by the overflown inhomogeneity of the electric field.

The results indicate that the behavior can be described by a power-law or exponential function. For microdosimetric applications such as hadron therapy, where most of the particles detected have energies (and consequently penetration depths) higher than those being studied, this deduction is significant. So it is possible to estimate the border effect using the single asymptotic value of the FWHM.

However, the data provided in this study only allowed to estimate this value for protons. The FWHM value measured for protons at 1.8 MeV might be considered a reliable estimate of the asymptotic FWHM value. For helium and carbon ions, however, the maximum penetration depth studied was insufficient to be considered representative of the asymptotic value.

Further studies should be conducted to quantify the border effect FWHM at higher energies (i.e., higher penetration depths), in order to obtain a representative value for estimating the influence of the border effect in such microdosimetric applications.

TABLE 4.3: FWHM measured at the largest penetration depth.

Particles	**Energy (MeV)**	**2 µm SV**	**6 µm SV**	**12 µm SV**
^{1}H	1.8	2.3 ± 0.1	3.5 ± 0.2	5.2 ± 0.2
^{4}He	2.8	5.1 ± 0.3	6.3 ± 0.2	—
^{12}C	6.0	3.2 ± 0.3	4.6 ± 0.2	5.4 ± 0.2
^{16}O	8.0	2.4 ± 0.2	—	—

Table 4.3 shows the FWHM values measured at the maximum penetration depth used in this study for each ion. The border effect for different particle Z values also showed consistent behavior at different SV thicknesses and penetration depths. The FWHM showed an inverse proportionality to the particle Z.

This behavior could be explained by the denser but narrower ionization clusters formed by ions with higher Z values. The charge generated away from the sensitive area by a higher Z ion is less likely to be affected by the denser electric field lines found closer to the electrode (since the secondary electrons produced travel a shorter path than lighter ions).

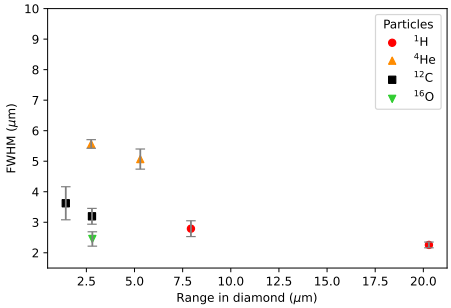

(A) SV thickness: 2μm

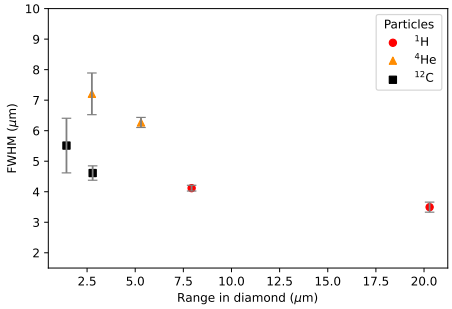

(B) SV thickness: 6μm

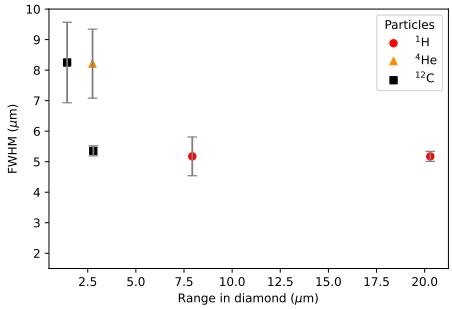

(C) SV thickness: 12μm

FIGURE 4.10: Border effect behavior as a function of penetration depth in diamond. Each of the three sub-figures shows the results for one of the three different SV thicknesses studied.

The charge created by a heavier ion near the SV border is more likely to be collected with complete CCE because secondary electrons are less likely to reach the border effect region outside the SV. It is important to note that higher Z ion beams are more difficult to focus. A worse beam focus (i.e., a larger beam size) of heavier ions could have contributed to the behavior observed. However, any contribution is expected to be minimal because each beam quality change was followed by an accurate beam focus.

As seen by comparing the three graphs in Figure 4.10, the discussed trends were consistently found at higher FWHM values in thicker detectors. This is thought to be the result of applying higher voltage to thicker detectors: the stronger the electric field, the more the field lines overflow. A lower FWHM was found when the applied bias was less than the operational voltage.

The results indicated that each of the parameters investigated influenced the border effect independently of the others. The border effect FWHM is dependent on the particular solid-state detector technology used (detector layout and materials), along with the parameters examined. While the observed behaviors are not expected to change, the FWHM absolute values shown in Figure 4.10 should be considered specific to the diamond microdosimeter technology used.

4.2.1 Impact of border effect to the microdosimetric measurement of hadron therapy radiation quality

The impact of the border effect on the microdosimetry measurement of hadron therapy typical radiation qualities was determined by simulating the microdosimetric measurement using Geant4 and applying the border effect reproduction model. A single value of the border effect FWHM could be used to replicate the border effect, as was discussed in the previous section. Because the particle energies involved in a typical hadron therapy field correspond to penetration depths significantly greater than the detector thickness, the border effect could be replicated by estimating the asymptotic value of FWHM.

This single FWHM approximation has intrinsic limits:

- The FWHM value used must be representative of the stabilized 'asymptotic' value. The higher the energy of the particle used for measurement, the more representative the FWHM is, resulting in a reduced impact of overestimation.
- Secondary fragments may have a different Z than the primary, necessitating a different FWHM and compromising approximation accuracy.
- Towards the end of the FO, the fraction of particles with range values of a few μm becomes significant. The border effect dependency against penetration depth (i.e., particle energy) cannot be ignored. The approximation is no longer valid.

For heavier ions, such as carbon ions, where the fraction of secondary fragments such as boron, helium, and hydrogen is higher, the limits mentioned are particularly relevant. The measured FWHM values would also not be indicative of the stabilized FWHM value for large penetrations. However, for protons, the FWHM measured with 1.8 MeV protons could be considered representative of the stabilized FWHM.

The application of the border effect model to Geant4 simulations was compared with an experimental measurement. The experiment was carried out at the Trento Proton Therapy Centre using a 68.8 MeV proton beam measured at a depth of 38.5 mm in water by a 6 μm diamond microdosimeter. The measurement was reproduced using Geant4 and the border effect model was applied by considering a FWHM of 3.5 μm. IBIC measurements on the 6 μm detector with 1.8 MeV protons revealed a border effect of σ = 1.48 ± 0.07 μm. Figure 4.11 shows that the simulation using the border effect model agrees well with the observed spectra, giving confidence in the single-FWHM approximation for protons.

The border effect model was applied to simulations of a nominal 70 MeV proton beam monitored by a 6 μm diamond detector at the entrance, BP, and mid FO (Figure 4.12). The figure shows the spectra produced with different FWHM values in order to show the effect of the FWHM value on the microdosimetric spectrum.

A typical low lineal energy cut-off of 1 keV μm^{-1} was applied. A low lineal energy cut-off affects the variation in $\bar{y}_F$ and $\bar{y}_D$ by reducing the low lineal energy tail caused by the border effect. Its consideration was considered fundamental to provide a reliable idea of an experimental scenario, where a low lineal energy cut-off

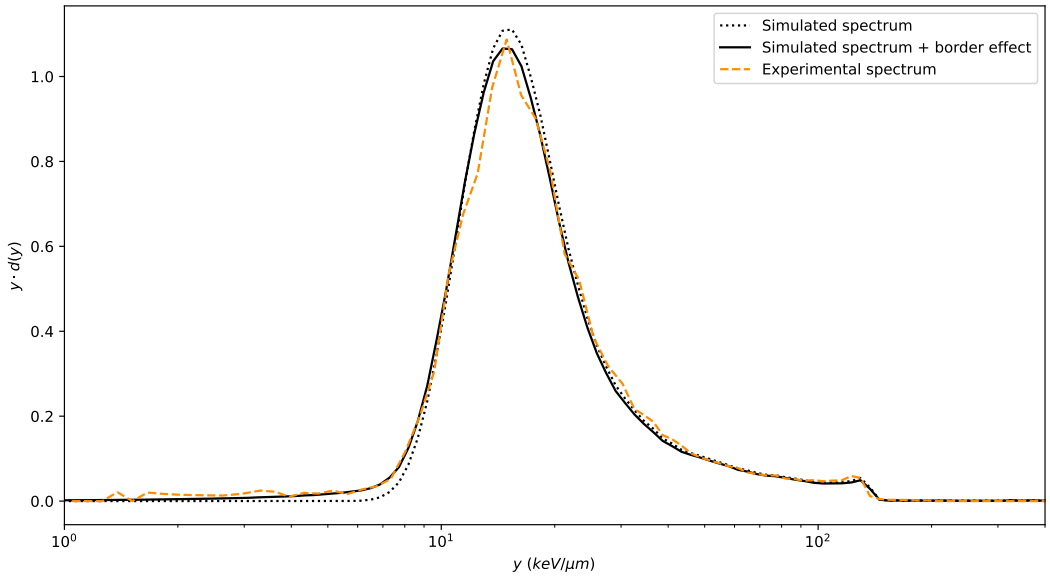

FIGURE 4.11: Comparison of experiment and Geant4 simulation using the border effect model with σ = 1.48 ± 0.07 μm. A 6 μm diamond microdosimeter was placed at 38.5 mm depth in water and irradiated by a 69 MeV proton beam.

intrinsically exists. The spectrum distortion caused by the border effect produced a shoulder at the low lineal energy side of the spectrum, while most importantly, preserving the original spectrum shape.

The border effect was expected to show differently on microdosimetric spectra (Figure 4.12) and on the deposited energy spectra of IBIC measurements (Figure 4.9b. The deposited energy spectra were shown as normalized count yield, thus proportional to a frequency distribution $f(y)$, whereas the microdosimetric spectra were reported as dose distribution $d(y) \propto yf(y)$. The frequency distribution is weighted on y, decreasing the contribution to the spectrum of low lineal energy values.

The frequency and dose mean lineal energies, $\bar{y}_F$ and $\bar{y}_D$, were calculated from the simulated spectra. This was done both with and without the use of the border effect model, to quantify the influence of the border effect. The border effect caused a negative variation by reducing the $\bar{y}_F$ and $\bar{y}_D$ values. As expected, the impact on $\bar{y}_F$ was higher than on $\bar{y}_D$.

In fact, by definition, $\bar{y}_F$ is determined by weighting the frequency distribution $f(y)$ on y, whereas $\bar{y}_D$ is determined by weighting $f(y)$ on y^2. The border effect contribution will be given a lower weight in the $\bar{y}_D$ calculation since it results in events with a lower lineal energy. The impact of the border effect on the variation of $\bar{y}_F$ and $\bar{y}_D$ was investigated as a function of $R_{\text{area}}(\sigma, l)$ (4.9) as shown in Figure 4.13.

The border effect caused variations comparable to or greater than standard experimental uncertainties, indicating distortion of measurements. Changing σ or l while keeping the other variable constant revealed an important property of the border effect. Its impact is determined by R_{area}, rather than the exact value of σ or the

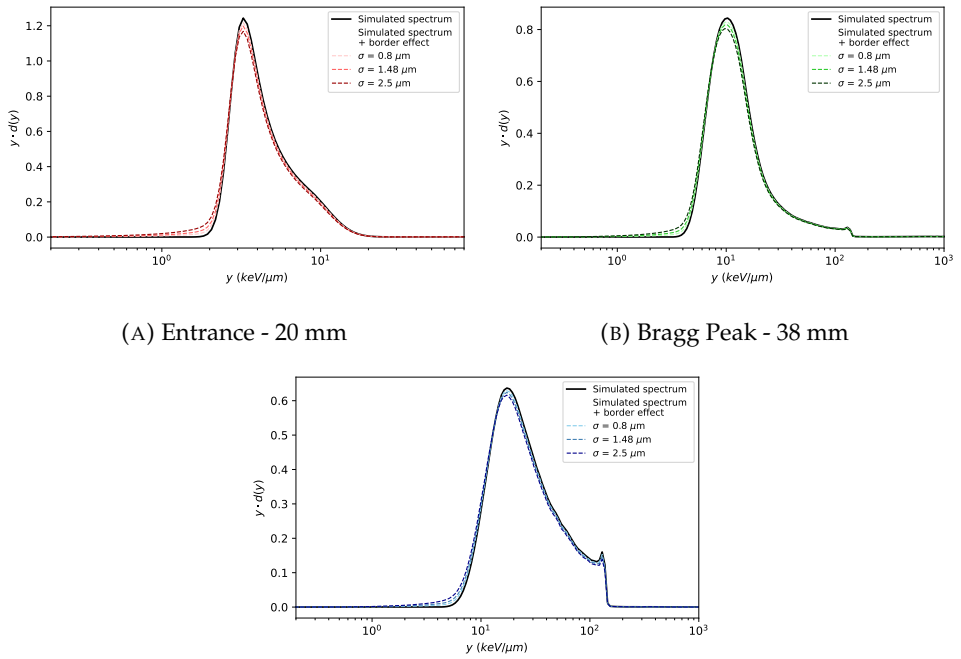

(A) Entrance - 20 mm

(B) Bragg Peak - 38 mm

(C) Fall off - 43 mm

FIGURE 4.12: Simulated microdosimetric spectra for 70 MeV protons at different depths in water. The graph compares the results obtained with and without applying the edge effect model. All spectra are reported as measured in diamond (density 3.51 g cm^{-3}), without material conversions.

geometry alone.

As a result, the curves in Figure 4.13 for the radiation quality investigated are generally applicable to any detector type and configuration. The R_{area} curve for a specific microdosimetric spectrum (i.e., radiation quality) can be calculated using Monte Carlo simulations with the proposed border effect model. Its impact can be evaluated using the R_{area} curve, given the detector geometry (i.e., the geometrical parameter l) and the value of σ (i.e., the detector type and layout, the particle energy, and its atomic number). This is true as long as the single-FWHM approximation is valid, which happens when the particle field has a mono-energetic kinetic energy spectrum or when the mean penetration depth of the particles is significantly greater than the detector thickness.

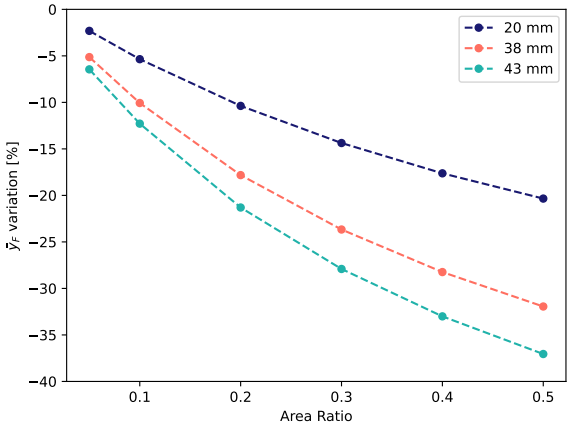

(A) $\bar{y}_F$

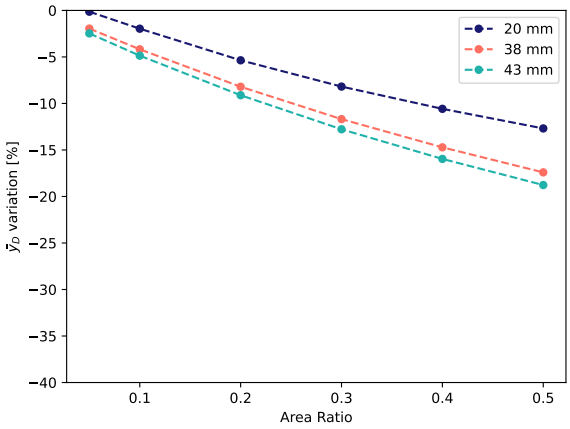

(B) $\bar{y}_D$

FIGURE 4.13: Variation of $\bar{y}_D$ $\bar{y}_F$ as a function of the area ratio R_{area}. The data refer to protons at different depths in water.

For 70 MeV protons, the mean kinetic energy at 20, 38, and 43 mm in water was roughly 47, 14, and 2 MeV, with penetration depths of 6382, 712, and 25 μm in diamond, respectively. As a result, the single-FWHM approximation can be confidently assumed to be valid. In a 6 μm diamond microdosimeter with a 102 $\times$ 102 μm^2 area and a typical experimental cut-off of 1 keVμm^{-1}, the border effect deviates $\bar{y}_F$ and $\bar{y}_D$ values by around -8% and -3% at 43 mm, respectively, assuming an FWHM of 3.5 μm ($R_{area} = 0.06$). Even with a lower stabilized FWHM, such as 3.0 μm ($R_{area} = 0.05$), the impact remains significant, down to around -6% and -2% for $\bar{y}_F$ and $\bar{y}_D$ at 43 mm.

With an FWHM of 3.5 μm, an R_{area} of 0.5 corresponds to regions of approximately 10 $\times$ 10 μm^2, similar to array microdosimeters [266]. At 43 mm, $\bar{y}_F$ and $\bar{y}_D$ showed deviations of -37% and -19%, respectively. Such significant effects underline the importance of evaluating the border effect and highlight the need to mitigate it, particularly for microdosimeter arrays and detectors with small sensitive areas.

4.2.2 Characterization of DIODE detector using clinical proton

Dosimetric characterization

The combined analysis of the temporal response, linearity, and depth dose profile (DDP) provides a complete experimental characterization. These results confirm the dosimetric reliability of the DIODE detector in clinical proton beams. The DIODE detector was tested under a quasi-monoenergetic 70 MeV proton beam at the Trento Proton Therapy Center.

Under beam-off conditions, the DIODE detector exhibited a very low dark current of less than 0.1 pA, comparable to the leakage current of the readout electronics. This ensured a good signal-to-noise ratio (SNR). The reproducibility of dose measurements was verified by means of three irradiations under identical conditions, with a variation between the measured values consistently less than 2%.

The linearity of the DIODE detector response was examined in the entry region (at a depth of approximately 3 mm WE). The charge data measured as a function of the absorbed dose (estimated using EBT3 film) up to approximately 11 Gy produced a coefficient of determination for linear regression (R^2) equal to 0.99984, demonstrating good linearity across the entire dose range investigated (Figure 4.14). The deviation from linearity of the response remained within 2%.

The sensitivity of the detector, calculated from the slope of the linear fit, was 0.60 ± 0.01 nC Gy^{-1}, a value compatible with the theoretically expected sensitivity of (0.64 ± 0.05) nC Gy^{-1}. Furthermore, the charge was measured as a function of the total number of protons incident on the μDos; again, the data showed a linear trend with a deviation from linearity within 3% [268]. These results highlight the consistency and reliability of the DIODE under proton irradiation conditions. The DDP is a comprehensive test that evaluates dose linearity, energy dependence, and detector LET.

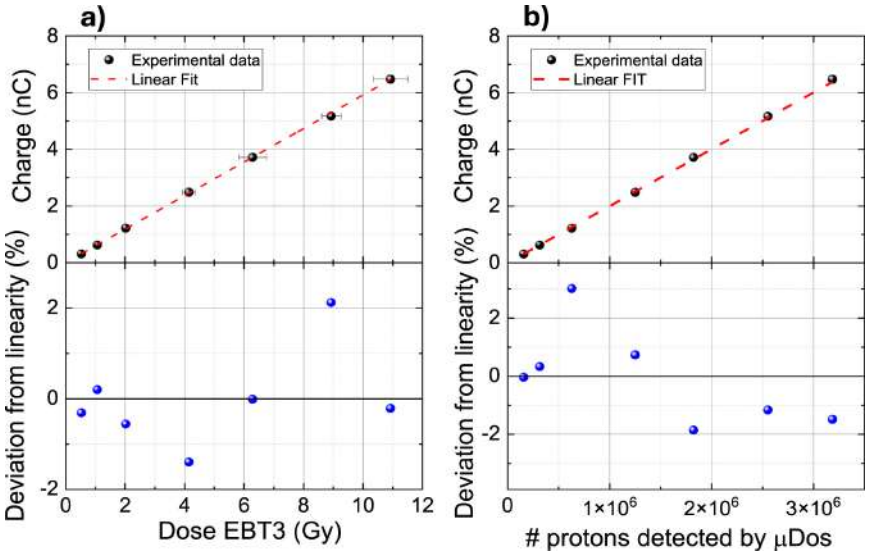

FIGURE 4.14: Linearity of the DIODE detector response at the beam entrance. (a) Upper plot: charge measured as a function of the delivered proton dose, estimated by EBT3 film. (b) Upper plot: charge measured as a function of the number of protons impinging on the μDos. In both panels, the lower plots show the percentage deviation from linearity.

The relative DDP measured with the DIODE detector (blue dots, Figure 4.15) for the 70 MeV proton beam showed reasonable agreement with the data obtained from reference detectors (EBT3 film, Giraffe) and with the Monte Carlo (MC) simulation. The MC simulation reproduced the dose profile for a proton beam with an energy of 68.8 MeV and an energy spread of approximately 600 keV. All curves are normalized to the signal at a depth of 3 mm in the entrance region of the Bragg curve. Quantitative analysis of the DDP parameters (Table 1) showed that the values calculated by DIODE are consistent with those obtained by Monte Carlo simulations. In particular, the peak/plateau ratio measured by DIODE (4.60±0.18) and that simulated in MC (4.69) agree within 2%, which is compatible with experimental uncertainties [268][260].

TABLE 4.4: Analysis parameters for the depth dose curves reported in Figure 6.

Detector	R_{90} **(mm)**	**DDF (80%–20%) (mm)**	**Peak-to-plateau ratio**
DIODE	39.5 ± 0.2	0.9 ± 0.2	4.60 ± 0.18
EBT3	39.20 ± 0.35	1.30 ± 0.35	3.98 ± 0.27
MC	39.5	1.0	4.69

The only significant discrepancy observed was in the Bragg Peak region, where EBT3 films underestimated the dose by approximately 20% and showed a lower peak/plateau ratio (3.98±0.27) due to the well-documented LET-dependent quenching of Gafchromic films [106][212]. The agreement of the DIODE DDP with MC simulations, combined with the previously demonstrated dose linearity, suggests that the DIODE detector exhibits a stable response in the investigated energy and LET range, with limited dependence on LET (from approximately 70 MeV up to the

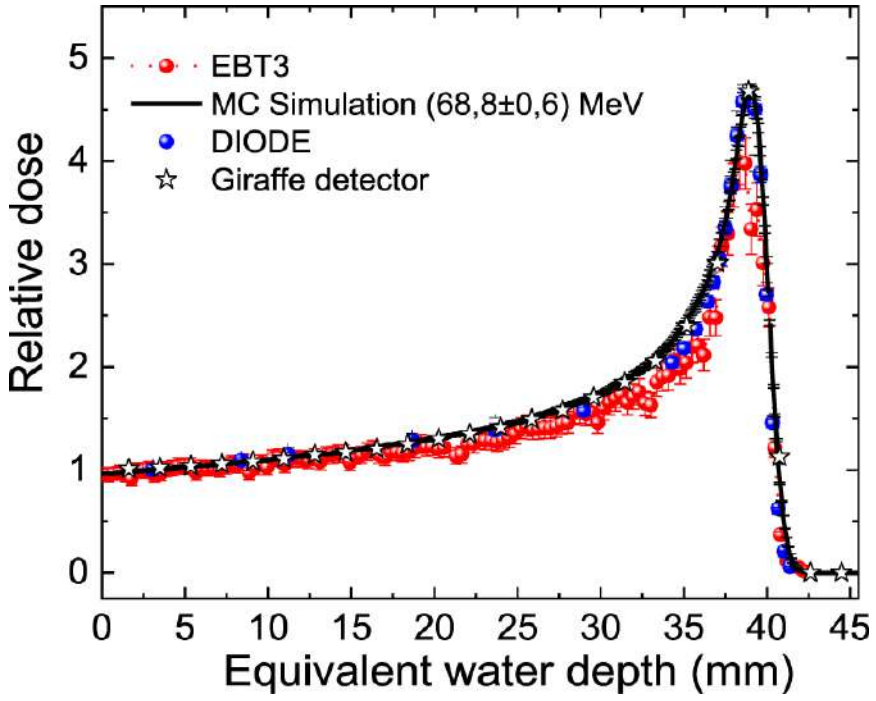

FIGURE 4.15: Central-axis depth dose curves for a 70 MeV proton beam: comparison between DIODE, EBT3 measurements, and Monte Carlo simulation.

Bragg Peak region). This favorable characteristic is attributed to the extremely thin, high-quality SV of the dosimeter [268][173].

Microdosimetric characterization

The microdosimetric spectra acquired by the DIODE detector for the different measurement positions along the proton Bragg peak are shown in Figure 4.16. The curves show a clear evolution with depth in water:

- Entry region (dark blue curves on the left): The lineal energy generated by the proton beam varies from 0.3 to 7 keV μm^{-1}.
- Proximal region (light blue and green curves): The variation is between 1 and 10 keV μm^{-1}.
- Distal region (red curves on the right): The variation ranges from 0.5 to 45 keV μm^{-1}.

It can be observed that microdosimetric distributions shift towards higher lineal energy values with increasing depth in water, reflecting the increase in LET of protons near the distal edge. This trend peaks near the Bragg region, where ionization density is at its maximum. At the far right of the spectra, the distributions drop sharply to zero. This "proton edge" represents the maximum lineal energy that a proton can deposit within the SV of the detector. For the μDos, which has an active thickness of 6.3 μm, protons deposit a maximum energy of approximately 860 keV, which corresponds to a lineal energy in water of approximately 43 keV μm^{-1}.

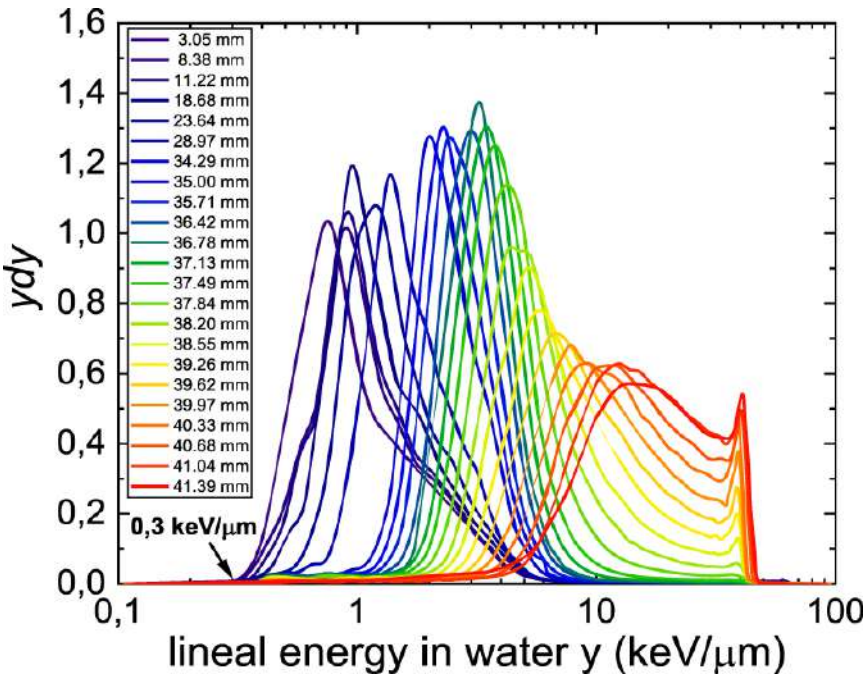

FIGURE 4.16: Microdosimetric spectra, $yd(y)$ vs y, acquired by DIODE at different water equivalent depths.

In the entrance region, where proton energy is still high and LET is low, the signal-to-noise ratio was sufficient to obtain reliable microdosimetric spectra. The spectra show a low cut-off around 0.3 keV μm^{-1}. This value corresponds to the electronic noise threshold of the detection system during irradiation and is significantly lower than the typical values reported in the literature for diamond microdosimeters, which generally approach or exceed 1 keV μm^{-1} [172][207][269]. The front-end electronic readout system is placed inside an encapsulated housing that encloses the DIODE detector, reducing electromagnetic and electronic noise. A comparison with MC simulations performed using Geant4 showed strong agreement between experimental and simulated data, both in the shape of the spectra and in the positioning of the lineal energy values.

Figure 4.17 shows the microdosimetric spectra obtained with the DIODE detector and the corresponding Geant4 simulations at four WE depths: 11.22 mm and 28.97 mm (entry region), 38.20 mm (Bragg Peak region), and 40.68 mm (fall-off region). The simulations also took into account the border effects of the SV of the μDos, estimated at 3.5 μm (see Table 4.3). A slight discrepancy occurs only at low lineal energy values, immediately before the cut-off due to noise. In MC simulations, particularly in the entrance regions, rare high lineal energy events (in the range 100–1000 keV μm^{-1}) are present. These events are caused by nuclear interactions, secondary particle production, and proton-induced fragmentation, which deposit significantly more lineal energy than the primary protons. The DIODE detector was unable to experimentally detect these high-energy events due to saturation of the electronic acquisition chain, which prevented the recording of events above 65 keV μm^{-1}. Since secondary fragments play a crucial role in defining biological effects, it is essential to optimize the electronic system (e.g., by reducing the gain) to extend

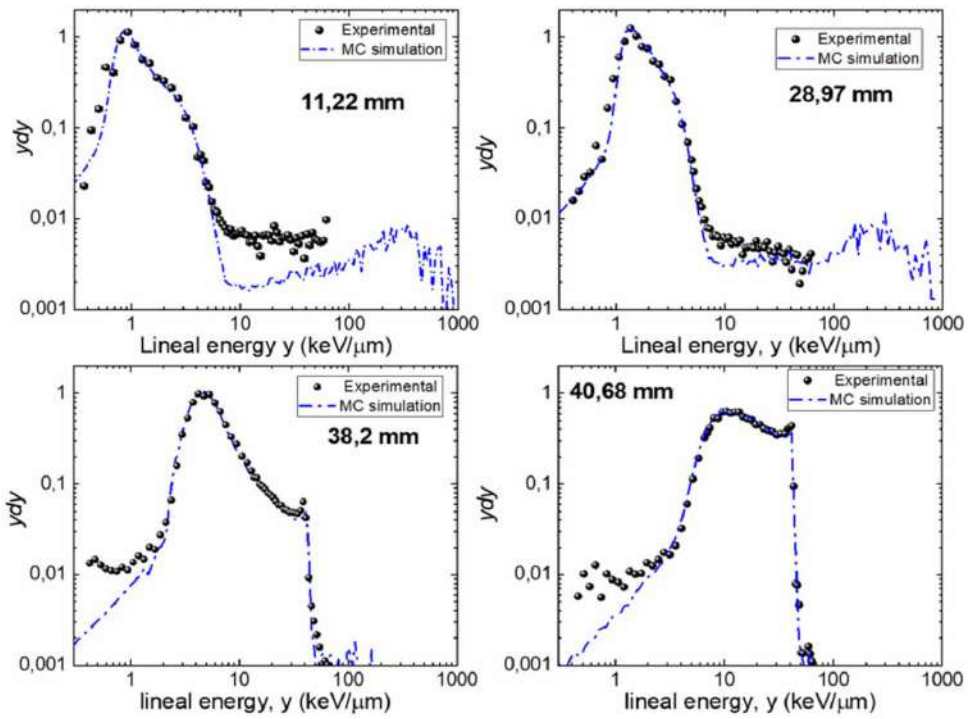

FIGURE 4.17: Experimental and simulated $yd(y)$ vs y at four water equivalent depths.

the dynamic range and ensure accurate detection of both primary protons and rare high-energy secondary fragments.

Figure 4.18(a) shows microdosimetric spectra measured with the mini-TEPC and the DIODE detector at two different water depths, i.e., entrance region (18 mm) and fall-off region (40 mm).

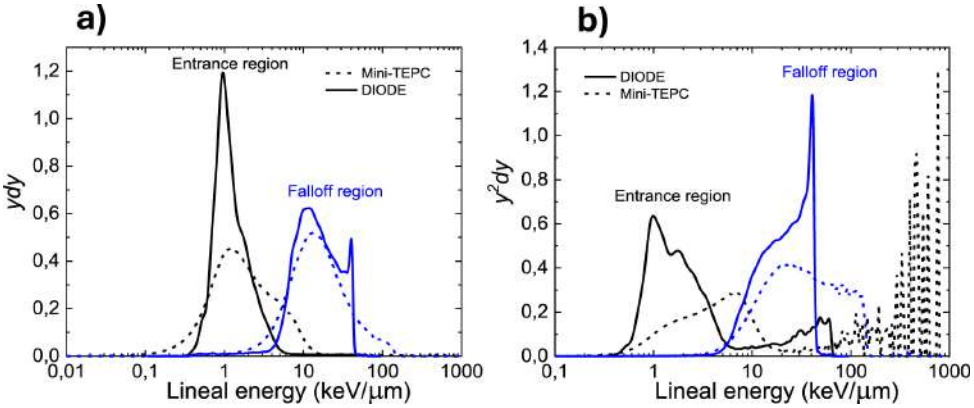

FIGURE 4.18: The $y\,d(y)$ and $\frac{y^2 d(y)}{y_D}$ regions distributions measured with the DIODE and the mini-TEPC at the entrance and falloff.

The positions of the lineal energy peak resulting from the electromagnetic interactions of primary protons are consistent between the two detectors. Differences in spectral shapes arise mainly due to variations in the geometry and Size of their SVs. The μDos, having a slab geometry, exhibits a path-length distribution of primary particles that closely resembles a Dirac delta function at its thickness. In contrast, the mini-TEPC,

with its cylindrical geometry, has a much broader distribution, peaking at the diameter size and extending into a long tail toward smaller chord lengths. Furthermore, energy-loss straggling is more pronounced in thinner SVs, contributing to the broader lineal energy spectrum observed in the mini-TEPC.

Notably, the events in the 3-10 keV μm^{-1} range in the mini-TEPC spectra are attributed to secondary δ-electrons generated outside the SV. This contribution is not observed in the μDos due to its larger SV, where electron signals are overshadowed by those of primary protons. Similar differences were observed between other solid-state microdosimeters and mini-TEPC at the CATANA beam line [23].

Due to their rarity, high lineal energy events exceeding 20 keV μm^{-1} in lineal energy are not easily distinguishable in the conventional $y\,d(y)$ representation. However, they became more apparent in the $y^2 d(y)/\bar{y}_D$ representation, employed also in other beam quality studies [24][25][57] as shown in Figure 4.18(b). In such representation, equal areas under the curve correspond to equal contributions to the dose mean lineal energy, $\bar{y}_D$. It is clearly observed in figure 4.18(b) that, in the case of the mini-TEPC, these rare fragments have a significant impact on $\bar{y}_D$ at a depth of 18 mm, increasing its overall value. Conversely, in the DIODE detector, the electronic readout chain saturation leads to a lower $\bar{y}_D$. At a depth of 40 mm (fall-off region), the contribution from high-energy deposition events other than those of primary particles becomes negligible, resulting in more consistent $\bar{y}_D$ values between the two detectors.

RBE calculation and lateral dose profile

Relative Biological Effectiveness (RBE) analysis was conducted to evaluate the variation in biological effects along the proton beam penetration and demonstrate the ability of DIODE to serve as a physical surrogate for biological dose estimation. The estimate started from the experimental distribution of the lineal energy dose, $d(y)$. The Loncol's biological weighting function, $r(y)$, was applied [168].

Although this function was originally derived for a specific biological endpoint in vivo (early intestinal intolerance), it is known to accurately reproduce RBE_{10} variations (RBE relative to a survival fraction of 10%) for clonogenic assays of different radio-resistant cell lines [70]. The calculated RBE refers to the clonogenic survival in vitro of the V79 cell line. The RBE estimate is calculated using the integral of the product of the weighting function and the lineal energy dose distribution.

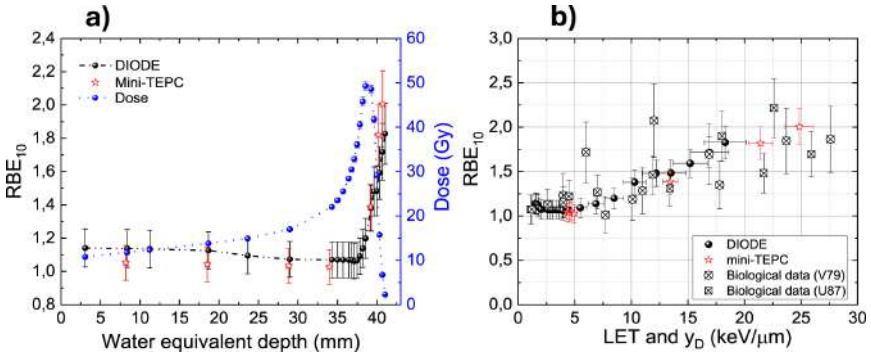

FIGURE 4.19: Comparison between the DIODE detector (filled circles) and the mini-TEPC (empty stars) for RBE estimation. (a) RBE (estimated using Loncol's function) as a function of depth in water. The right axis shows the dose calculated by DIODE. (b) RBE as a function of $\bar{y}_D$. The data from the two detectors are compared with biological data from the literature (RBE_{10} for V79 and U87) as a function of LET.

Figure 4.19(a) illustrates the profile of the estimated RBE_{10} as a function of depth in water. The RBE_{10} and dose refer to the same positions, ensuring a precise correlation between physical and biological effects. The RBE_{10} varies significantly with depth: at the beam entrance, it is approximately 1.1, increases to 1.2 at the Bragg peak, and reaches values around 1.8 in the distal falloff region. These values are in good agreement with those obtained with the reference mini-TEPC and with the RBE_{10} values reported in the literature for V79 and U89 cells. The results confirm that the RBE_{10} of protons increases with depth in water. The use of a fixed RBE value of 1.1 (as recommended by ICRU Report 78 [137]) is known to underestimate the effect of increased LET in the distal region of the clinical beam [47][202][205][203][98]. Figure 4.19(b) compares the RBE_{10} as a function of the dose mean lineal energy $\bar{y}_D$. $\bar{y}_D$ is a quantity that closely approximates the average LET in dose (LET_D) of the radiation field. The RBE values determined experimentally with DIODE show trends and values consistent with the biological data for proton RBE reported in the literature (V79 [213][221][87][18] and U87 cells [47]). The DIODE detector, providing dose and RBE estimates at the same point and simultaneously, offers rapid and valuable information for optimizing treatment protocols, especially in ion therapy, where RBE is variable.

The lateral dose profile and energy spectra were measured by moving the DIODE detector perpendicularly to the beam direction in 5 mm steps, obtaining profiles in the x-direction. The detector positioning uncertainty is estimated to be ± 1 mm. In the entrance region ($\sim$3 mm WE), the dose profiles measured by the DIODE Dos and EBT3 films show good agreement. Both detectors estimated a consistent beam FWHM (Full Width at Half Maximum) (approximately 18 mm for DIODE, 17 mm for EBT3).

Figure 4.20 (lower graph) shows that the $\bar{y}_D$ values remain almost constant along the lateral profile in the entrance region. This constancy is expected since the proton LET varies slowly at high energies.

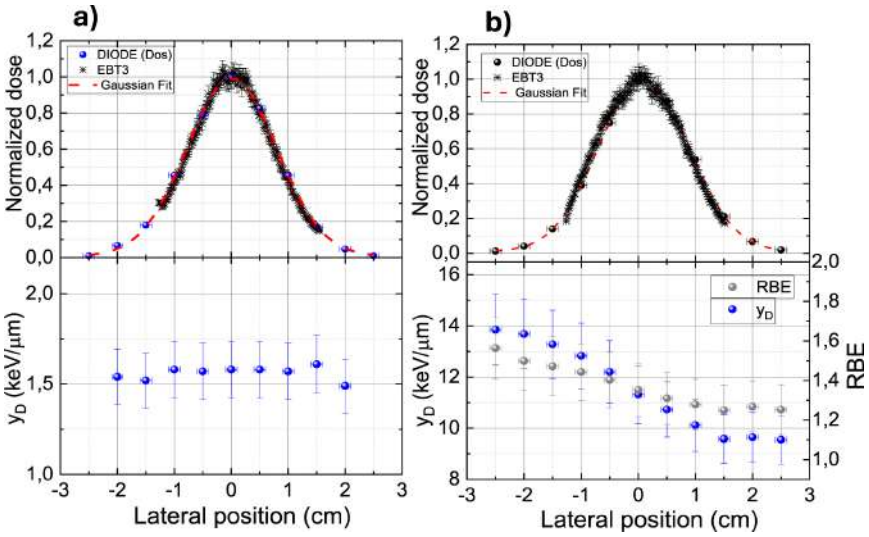

FIGURE 4.20: Comparison of lateral profiles measured by DIODE and EBT3. (a) Entrance region: normalized dose (top) and $\bar{y}_D$ (bottom). (b) Bragg peak: normalized dose (top) and $\bar{y}_D$/RBE (bottom).

The measurements were repeated at a WE depth of 39.5 mm (close to the Bragg peak). The dose profile measured by the DIODE is consistent with that obtained from the EBT3 film.

The FWHM is estimated to be approximately 20 mm for both, indicating a slight beam broadening due to Coulomb scattering. At this critical depth, radiation quality showed significant variation depending on lateral position: the $\bar{y}_D$ decreased from approximately 14 keV μm^{-1} to 9.5 keV μm^{-1}, while the RBE decreased from approximately 1.6 to 1.2 along the x-axis. The variation in $\bar{y}_D$ and RBE was attributed to a difference in the LET of protons along the lateral profile.

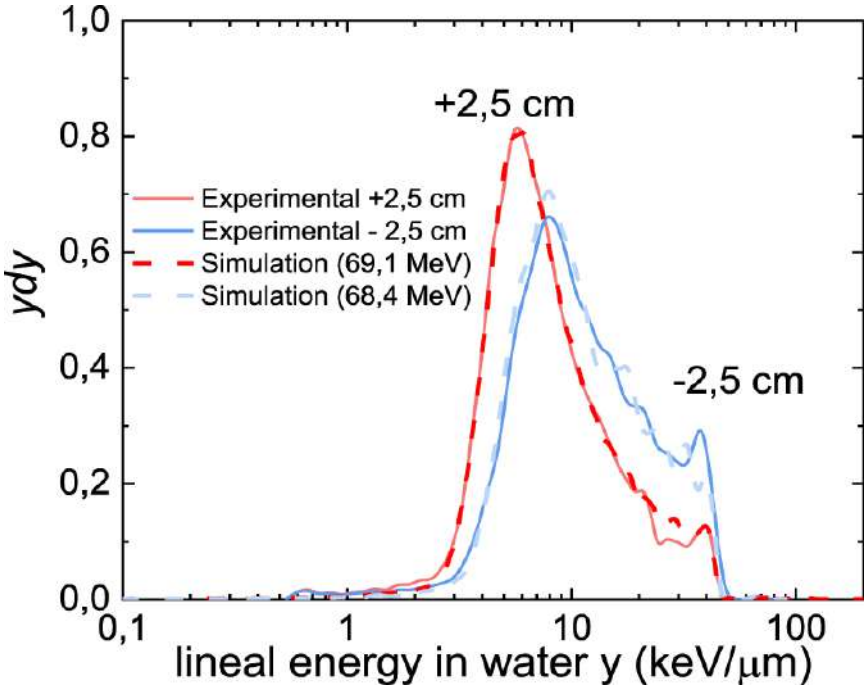

FIGURE 4.21: Comparison of experimental and simulated microdosimetric spectra measured at lateral positions ±2.5 cm.

Figure 4.21, comparing the microdosimetric spectra at ±2.5 cm lateral distance, shows a shift in lineal energy between the two positions. MC simulations and analysis of the incident proton energy, reconstructed using the EBT3 film stack, confirmed that there is an energy difference of approximately 800 keV between the two extreme lateral positions.

The estimated energy is 69.0±0.5 MeV at a positive x-coordinate and 68.2±0.8 MeV at a negative x-coordinate. Although this energy variation is not sufficient to be detected by the DIODE in the input region, it is clearly evident at the Bragg peak (where the LET varies rapidly) and highlights the importance of assessing radiation quality with high spatial resolution. Such slight effects can play a significant role in the radiobiological effectiveness of irradiated targets.

4.3 Conclusions

A novel detection system based on a synthetic single-crystal diamond, namely, DIODE, was developed to perform simultaneous dosimetric and microdosimetric characterizations of clinical ion beams to provide fast and reliable dosimetry in ion therapy centers, improving existing approaches. Characterization using the IBIC technique revealed two distinct sensitive areas confined within the metallic contact regions, underscoring the accurate spatial resolution of the device. The electronic circuits for both detectors work as expected; even in the integrated housing, the noise interferences are negligible. Dos electronic components exhibit a leakage current of about 0.1 pA, while the μDos ones achieve an energy resolution of 4.3 keV FWHM in diamonds and a high sensitivity of about 7.7 V/pC. Laboratory tests using alpha particles emitted from an ^{241}Am source in the air produced encouraging results with

a particularly good signal-to-noise ratio.

The study of the "border effect", conducted on similar diamond microdosimeters (and supported by the INFN DIODE project), addresses a critical technological challenge that affects the accuracy of microdosimetric measurements, including those of DIODE. The edge effect is due to the incomplete charge collection region that forms at the edges of the detector sensitive volume (SV). Using the IBIC (Ion Beam Induced Charge) technique, the effect was characterized as a function of detector thickness, particle atomic number (Z), and penetration depth (range). The amplitude of the border effect (measured by the FWHM of its derivative) was significantly higher for shallow penetration depths, tended to converge towards an asymptotic value when the particle range is much greater than the thickness of the SV, and was greater for thicker SVs (due to the higher applied voltage) and for particles with lower Z. The application of the border effect model with a single FWHM approximation (considered valid for high-energy protons) showed good agreement with experimental measurements of a 69 MeV proton beam measured at a depth of 38.5 mm of water. The border effect causes significant and systematic perturbations in experimental measurements of $\bar{y}_D$ and $\bar{y}_F$. The last one is the most affected quantity: for microdosimeters with small sensitive areas (such as arrays, 10×10 μm^2), deviations can reach -20% - -40%. Even for detectors with larger areas (100×100 μm^2), such as the DIODE's μDos, significant deviations are observed (approximately -5% - -10%). It is crucial to recognize, consider, and mitigate the impact of the edge effect, especially now that microdosimetry is moving toward standard protocols. On the other hand, these results suggest the possibility of implementing a correction method based on the model developed to reproduce the border effect on data from Monte Carlo simulations.

The DIODE detector was experimentally characterized under 70 MeV clinical proton beams, demonstrating its capability for simultaneous dosimetric and microdosimetric measurements. The detector exhibited very good linearity and a good agreement with reference EBT3 film dosimeter and MC simulations in both depth-dose and lateral profile measurements. The RBE values increased with depth, reaching values up to 1.8 in the distal region, consistent with mini-TEPC data, MC predictions, and published biological RBE trends for monoenergetic proton-irradiated cell lines. This supports the detector potential as a physical surrogate for biological dose estimation. However, the adopted acquisition system limited the detection of rare high-LET secondary particles, particularly in the entrance region. Optimizing the dynamic range of the acquisition chain will be essential to fully capture these contributions and improve sensitivity to the complete radiation field. Overall, the ability to provide, in a single compact device and in real time, accurate measurements of absorbed dose, and to derive LET and RBE through microdosimetric analysis, represents a significant advancement for beam quality assessment in proton therapy. These features position the DIODE detector as a promising tool for integration into biologically optimized treatment planning and advanced quality assurance protocols.

Chapter 5

Monte Carlo modeling of gold nanoparticles and radiopharmaceuticals

5.1 Introduction

The development of new theranostic systems, which combine diagnosis and treatment, presents a significant opportunity in the fight against cancer in nuclear medicine. Radiation therapy is a well-established treatment method that targets cancer cells by damaging their DNA. However, a significant challenge remains in increasing the radiation dose delivered to tumours while minimising toxicity to healthy tissues [58][156][256].

Target radiotherapy through the use of Auger electrons (AEs) has become increasingly popular for cancer treatment throughout the body [156][256]. Auger electrons, when released after nuclear decays such as electron capture or internal conversion, have very low energies (from a few eV to tens of keV) and a very short range, on the order of nanometers or micrometres [58]. As a consequence, having a high LET makes them very efficient at killing cancer cells, especially if they are close to sensitive cellular targets like DNA. Through water radiolysis, AEs can destroy DNA both directly and indirectly, also killing cancer cells by disrupting their membranes, as well as non-targeted cells via the cross-dose or bystander effect [156].

Technetium-99m radiopharmaceuticals, used for diagnosis, can also be applied in theranostic fields. Its diagnostic characteristics, combined with the therapeutic potential derived from AEs, make it a suitable choice for the development of theranostic systems, enabling monitoring and follow-up therapy. ^{99m}Tc radiopharmaceuticals might be applied in theranostic domains when conjugated to AuNRs and delivered to the DNA of tumour cells [27].

Photons and electrons emitted by ^{99m}Tc could stimulate gold nanobands, which in turn could emit Auger electrons. The interest in exploiting these mechanisms to develop a new theranostic system is the focus of the SEGNAR project carried out in collaboration with the Nuclear Medicine Unit of Policlinico Gemelli, the Department of Sciences of Roma Tre University, the National Institute for Nuclear Physics (INFN), and the Italian National Institute of Health (ISS). Given the lack of studies investigating the biological effects of ^{99m}Tc and its therapeutic impact, the

work presented in this thesis focuses on evaluating the radiobiological impact of this radionuclide.

The MCt-MK model was used to estimate the cell surviving fraction. Unlike traditional radiobiological models, which typically assume acute irradiation, this approach explicitly takes into account the time structure of dose deposition. Since the half-life of ^{99m}Tc is 6 hours, the resulting irradiation is of the protracted type. It is therefore crucial to quantify how sublethal damage repair mechanisms, characterized by time constants in the order of minutes, act during irradiation itself to reduce sublethal damage.

A further objective of the thesis is to investigate the dose enhancement induced by the presence of AuNRs. In particular, the work aims to determine whether the interactions between photons and electrons emitted by the radionuclide and the nanoparticle lead to an increase in the local dose through the emission of secondary Auger electrons and photoelectrons. Since the radiopharmaceutical is loaded onto the surface of the nanoparticle, the impact of its molecular structure on the estimation of survival curves was studied.

The radiobiological effect was also analyzed as a function of the coordination number of the ^{99m}Tc-AuNR system. Variations in this number alter the spatial distribution of the dose within the cell nucleus, leading to a transition from a homogeneous distribution to an extremely heterogeneous topology, characterized by isolated dose peaks. This analysis makes it possible to establish whether there is a synergistic effect between the radionuclide and the nanoparticle and to quantify its extent.

Overall, these results provide critical input for optimizing the design of theranostic systems. The HSG (Human Salivary Gland) cell line was selected as a reference due to its extensive experimental characterization, while the chemical-physical parameters required for Monte Carlo simulations were derived from preliminary characterization studies [27].

The methodology used in this work is described in Section 5.1. Section 5.1.1 reports the chemical-physical characterization of AuNRs, including FESEM-EDX and SR-XPS analyses to confirm the stability of the conjugation with the radiopharmaceutical. Section 5.1.2 describes the Monte Carlo simulation framework based on Geant4 and Geant4-DNA, focusing on the geometric modeling of the cell nucleus and the molecular occupancy of the radiopharmaceutical. Section 5.1.3 introduces the event reconstruction algorithm developed to isolate the dosimetric contribution of secondary particles generated by the nanoparticle from the primary source. Section 5.1.4 presents the MCt-MKM (Monte Carlo temporal - Microdosimetric Kinetic Model) model, used to estimate the cell survival fraction taking into account the temporal structure of ^{99m}Tc decay.

The results and discussion are presented in Section 5.2. A general conclusion is provided in Section 5.3.

5.1.1 AuNR characterization

As discussed in Section 2, AuNRs serve as strategic drug carriers due to their combination of inherent gold stability and biocompatibility with anisotropic morphology, which offers versatility.

Furthermore, AuNRs possess specific plasmonic properties, presenting two plasmonic peaks in the visible and/or near-infrared spectral range. Gold nanorods (AuNR) were synthesized using a seed-mediated growth protocol to obtain nanoparticles with specific aspect ratios suitable for cellular internalization [27]. From FESEM EDX studies, average sizes of 39 $\pm$ 5 nm and 11 $\pm$ 2 nm (Aspect Ratio = 3.2) were observed.

Furthermore, UV-Vis spectroscopy confirmed the nanometric size, showing two characteristic plasmonic bands at 520 nm and 680 nm (see Figure 5.1).

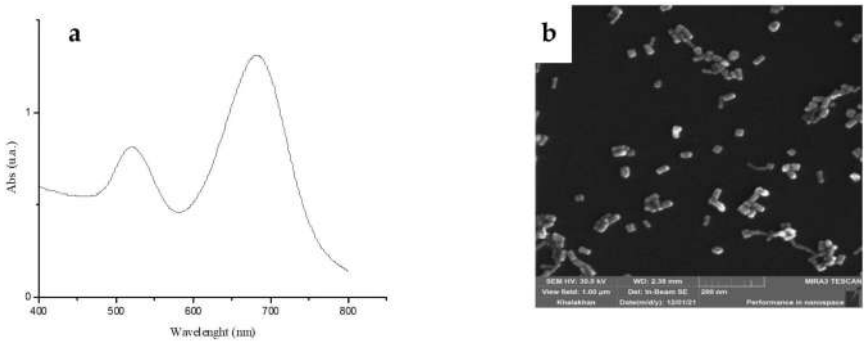

FIGURE 5.1: a) Visible spectrum in water suspension with λ_{max}= 520-680 nm. (b) FESEM-EDX image with scale bar 200 nm [27].

Loading studies were conducted to evaluate the drug loading of the long-lived ^{99}Tc-SestaMIBI complex on the AuNR surface.

The procedure involved simple contact between the radiopharmaceutical solution and the suspension of AuNRs, performed under stirring at room temperature for 24 hours. The experimental data indicated a loading efficiency of $\eta = 5 \pm 2\%$, corresponding to 0.0033 mg of drug for 1 mg of AuNRs [27].

To confirm the chemical nature and stability of the conjugation between the radiopharmaceutical and the AuNR, synchrotron radiation-induced X-ray photoelectron spectroscopy (SR-XPS) measurements were performed at the SuperESCA beamline of the Elettra synchrotron. Spectral analysis was extended to the core levels of several key elements. Analysis of the C1s and N1s levels confirmed the presence of the surfactant CTAB (Cetyltrimethylammonium bromide) on the surface of the nanorods, which is essential for their colloidal stability.

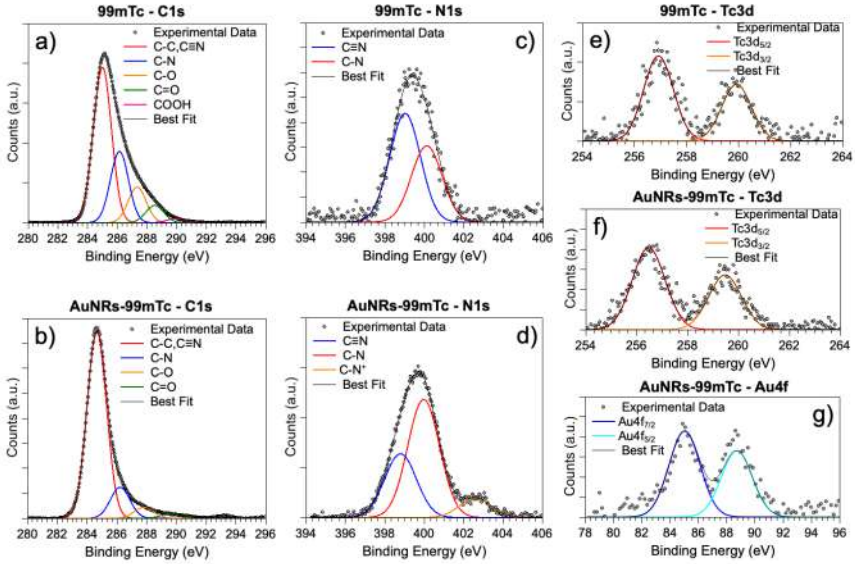

FIGURE 5.2: SR-XPS spectra: C1s (a,b), N1s (c,d) and Tc3d (e,f) of decayed and non-radioactive radiopharmaceutical ^{99}Tc and its conjugate on gold rods, AuNRs-99Tc. SR-XPS Au4f spectrum of AuNRs-99Tc (g) [27].

In particular, an increase in the intensity of the C1s component at 285.0 eV (C-C bonds) was observed, attributable to the aliphatic chains of CTAB, and the presence of specific signals attributable to its structure (such as C N). The investigation then focused on the Au4f and Tc3d orbitals.

The Au4f spectrum (Figure 5.2 g) showed a main component ($Au4f_{7/2}$) centered at a binding energy of 85.04 eV, typical of surface gold atoms interacting with ligands [27]. The analysis of the Tc3d level (the signal from the electrons in the 3d level of the ^{99}Tc atom) confirmed the presence of the technetium complex anchored on the AuNRs, maintaining its energy position and spectral peak shape compared to the free radiopharmaceutical (Figure e,f).

5.1.2 Modeling the synergistic effects of AuNR and ^{99m}Tc

Monte Carlo simulations were carried out using Geant4 and Geant4DNA [3][4] to study the radiobiological effects of ^{99m}Tc and a possible synergistic effect in ^{99m}Tc-AuNR system. The simulation code used was based on the Geant4 extended example "AuNP" [21] [133][233], appropriately modified to incorporate the radioactive decay of ^{99m}Tc.

The choice to use the AuNP example is driven by the possibility of exploiting a physics list that is already set up to include Geant4-DNA processes in gold. The simulation geometry consisted of a spherical water volume with a radius of 5 μm, representing the cell nucleus. The AuNR was modelled as a cylindrical structure with dimensions matching those observed in FESEM experimental data (see section 5.1.1). In the ^{99m}Tc-AuNR system, the ^{99m}Tc source was placed at a distance of approximately 0.7 nm from the AuNR surface. This distance was estimated based on the chemical structure of SestaMIBI radiopharmaceutical, using the Avogadro software [15][120].

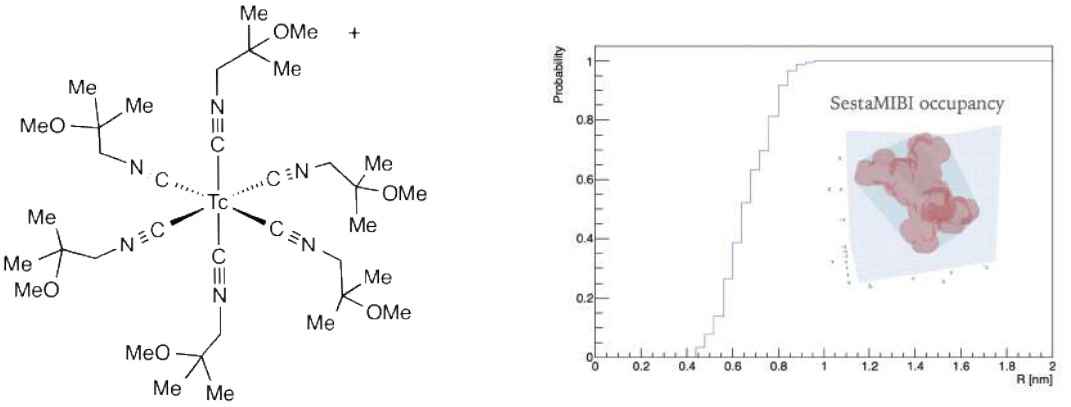

(A) (B)

FIGURE 5.3: Geometric modeling of ^{99m}Tc-Sestamibi. (A) Chemical structure. (B) Radial probability P(r) representing the occupancy profile derived from the 3D molecular mesh (inset).

To evaluate the occupancy of the radiopharmaceutical, a 3D mesh of the ^{99m}Tc-SestaMIBI molecule was generated. By importing the Simplified Molecular Input Line Entry Specification (SMILES) string of ^{99m}Tc-SestaMIBI into the Avogadro software, it was possible to export the 3D structure of the molecule (with Van der Waals spheres) as a VRML file.

Using a Python script I developed, the 3D geometry was reconstructed, allowing the structure to be managed as a mesh, in order to evaluate the geometric probability of finding DNA $P(r)$. 10^7 random points were sampled inside a 10 nm radius sphere centred on the 3D molecule centre of mass. Points inside the mesh were scored 0 (no DNA presence), and points outside were scored 1 (accessible). The fraction of accessible points was binned by radial distance to build the probability function $P(r)$.

As shown in Figure 5.3, $P(r)$ does not behave as a sharp step function. It exhibits a transition slope in the range 0.4 nm $< R <$ 1.0 nm. This gradual increase reflects the complex spatial structure of SestaMIBI. Within this radial range, the molecular volume is not uniform, and it becomes fully accessible ($P(r) = 1$) only at radial distances exceeding the maximum molecular extension ($\approx$ 1.0 nm). By weighting the energy deposited in water by ^{99m}Tc with the function $P(r)$, the occupancy of the SestaMIBI can be taken into account. The corresponding specific energy can be calculated as $z_{eff} = z(r) \cdot P(r)$. This ensures that energy depositions occurring within the molecular volume are excluded from the radiobiological analysis.

In Geant4 simulation, ^{99m}Tc was positioned within the 5 μm spherical water volume, as reported in Figure 5.4.

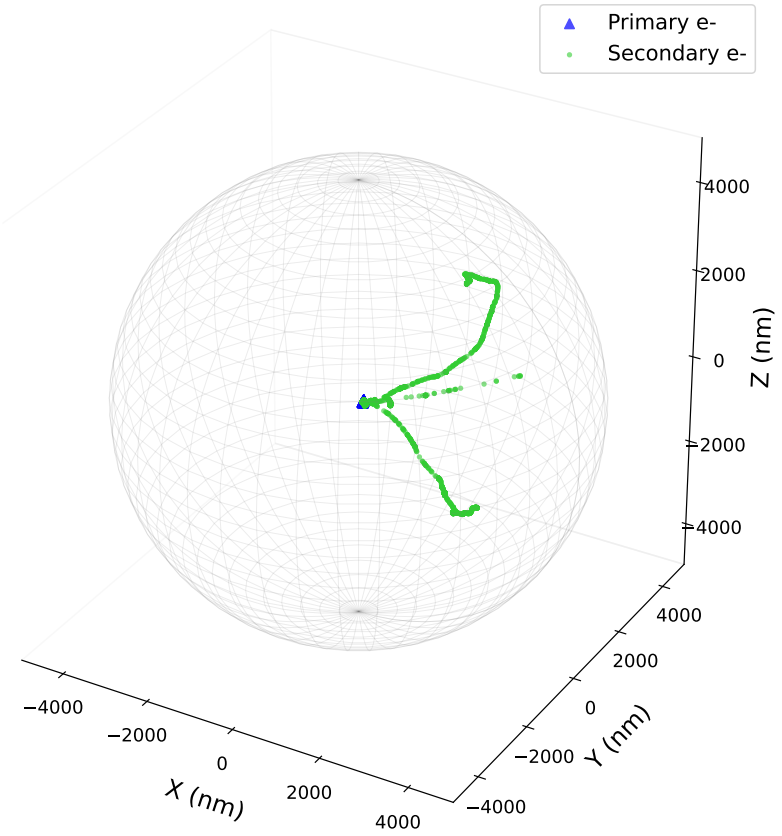

FIGURE 5.4: Simulated particle tracks for a single ^{99m}Tc decay event within the spherical cell nucleus (5 μm radius) using Geant4-DNA. The energy deposits induced by the primary electron are shown in blue, while those induced by the secondary electrons are reported in green.

The initial kinetic energy of the radionuclide was set to zero. The Geant4-DNA extension physics list was used to model the transportation and interactions of particles with the water medium. The Geant4-DNA processes `e-_G4DNAExcitation`, `e-_G4DNAAttachment`, and `e-_G4DNAVibExcitation` were included in the simulation but not recorded in the output, as the analysis focused on ionization events, which are more relevant for DNA damage.

Electrons below 8.22 eV cannot induce ionization or significant excitation [90]. The Livermore physics models were employed for electron-gold interactions, as it currently offers the best agreement with NIST data compared to the `DNA_AU_2016 model`. Future developments in the analysis will benefit from the new Geant4-DNA model for gold, which reduces the discrepancy with reference measurements and overcomes the main limitations of the current default model, allowing for more accurate simulations [217]. The production cut was set to 0.1 nm. All simulations were performed using version 11.3 of Geant4. In the Stepping Action class, all the information needed to evaluate the dose deposited in water was saved. The x, y, and z positions were saved both Pre and Post step, along with the EventID, the energy deposited, the name of the particle, the Volume Pre and Post step, as well as the energy deposition processes and particle creation processes. TrackID

and ParentID were necessary to isolate the dose contribution of gold secondaries, including Auger electrons. 10^6 primary ^{99m}Tc events were simulated. Simulation outputs were analyzed using custom codes that I developed in ROOT C++ [39] and Python.

Each ^{99m}Tc decay produces a set of spatially correlated energy depositions in the cell nucleus. Microdosimetry quantifies these energy depositions as specific energies z_i within small sub-volumes. Based on the energy depositions simulated with Geant4-DNA, the z_i values were calculated for each decay following the definition of z (see eq.1.18). The resulting microdosimetric spectrum $f(z)$ represents the probability distribution of local energy depositions.

This spectrum provides the input for the MCt-MK model, where z_i allows to determine the formation of lethal and sub-lethal lesions and thus the cell surviving fraction. The microdosimetric spectra $f(z)$ for both ^{99m}Tc and ^{99m}Tc-AuNR are shown in Figure 5.5. These spectra were calculated considering the source fixed at the center of the simulation sphere.

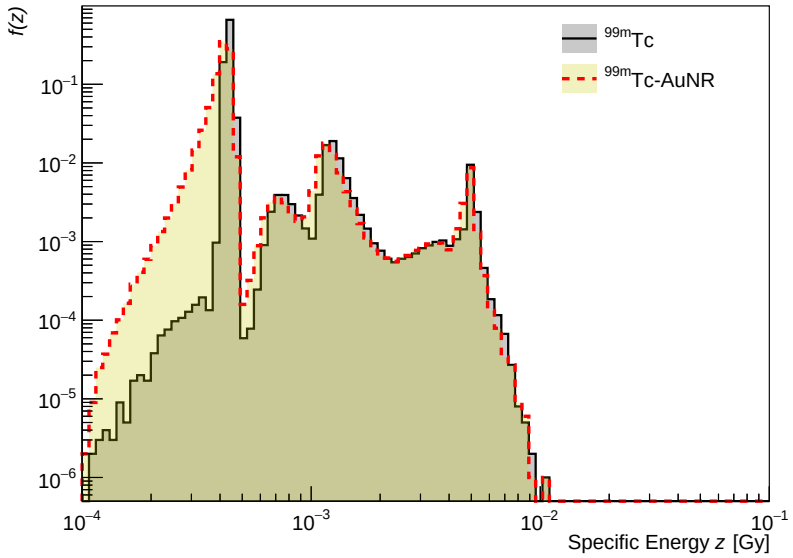

FIGURE 5.5: Comparison of simulated microdosimetric spectra $f(z)$ for ^{99m}Tc alone (black solid line) and the ^{99m}Tc-AuNR system (red dashed line) calculated for a spherical cell nucleus of 5 μm radius.

5.1.3 Radial dose profiles

To investigate the radiobiological impact of ^{99m}Tc and the potential synergistic effects of the ^{99m}Tc-AuNR system, two scenarios were simulated: one with ^{99m}Tc alone, and the other with ^{99m}Tc combined with AuNR. Both aspects are of interest, as they are not well documented in the literature.

The energy deposited in the water volume was scored in concentric spherical shells centered on the source position. A logarithmic binning scheme with 20 bins per decade was used to histogram the dose as a function of radial distance. The

radial dose profiles were normalised per decay event of ^{99m}Tc, where a decay event is defined as the complete decay from ^{99m}Tc to ^{99}Tc, including all associated emissions.

To separate the dosimetric contribution due to secondary particles generated within the gold nanoparticle from that of the primary source (decay of technetium in the surrounding medium), I developed an event reconstruction algorithm. A virtual cylindrical volume corresponding to the physical dimensions of the nanoparticle was defined to select the vertex positions of particles generated inside the nanoparticle. Within this volume, the primary escaped tracks were identified using a geometry-boundary condition: at each simulation step, the associated pre-step volume had to correspond to the nanoparticle ("NanoParticle"), while the post-step volume had to correspond to the surrounding water ("World"). This selection ensured that the particles leaving the nanoparticle could be isolated for the analysis of their energy deposition in water.

Once the particles generated inside the nanoparticles and escaping from it have been isolated, the selection was extended to the entire cascade of secondary particles generated in the surrounding medium, so as not to underestimate the local dosimetric contribution. The reconstruction logic was performed event by event using EventID, TrackID,, and ParentID information.

During the iteration, the algorithm checks whether the ParentID of the track under consideration matches the TrackID of an event already classified as an "escaped track" and belonging to that same EventID. If there is a match, the track is added to the list of particles originating from AuNR. This selection continues until convergence is achieved, i.e., until all associations have been reached. In this way, it was possible to isolate the dose contribution due to the presence of the AuNR and that of ^{99m}Tc.

5.1.4 The Monte Carlo temporal - Microdosimetric Kinetic Model

To estimate the surviving fraction of cells irradiated with ^{99m}Tc, a two-step Monte Carlo approach was used. The first step involved the use of Geant4, with the Geant4-DNA extension, to simulate the physical processes associated with the decay of ^{99m}Tc and the interactions of secondary particles in water. The simulation output was then analyzed using a second Monte Carlo step based on the MKM model. This allowed the estimation of the radiobiological damage induced by ^{99m}Tc and the evaluation of a possible synergistic effect in the ^{99m}Tc - AuNR system.

The analysis was carried out using the MCt - MKM, an original reformulation of MKM [123]. Details of the model are given in section 1.

The geometric model consists of two cubic volumes (Figure 5.6):

- **Cell nucleus volume ($V_{\mathbf{nc}}$)**: a cube with side length L_n^{cubic} whose volume has been divided into a grid of N_D smaller cubic domains with side length l. From the ratio L_n^{cubic}/L_d^{cubic}, the number of domains n per row has been estimated. The total number of domains in the cubic volume is N_D= n $\times$ n $\times$ n.

- **Simulation volume ($V_{\mathbf{sim}}$)**: The position of the source was randomized within a cubic volume with a side equal to $L_{\text{sim}} = r + L_n^{cubic}$, where r is the radius of the

Geant4 simulation sphere. This was done to include those events in which the source is located outside the cell nucleus, but part of the energy deposited by the secondary particles occurs within the latter.

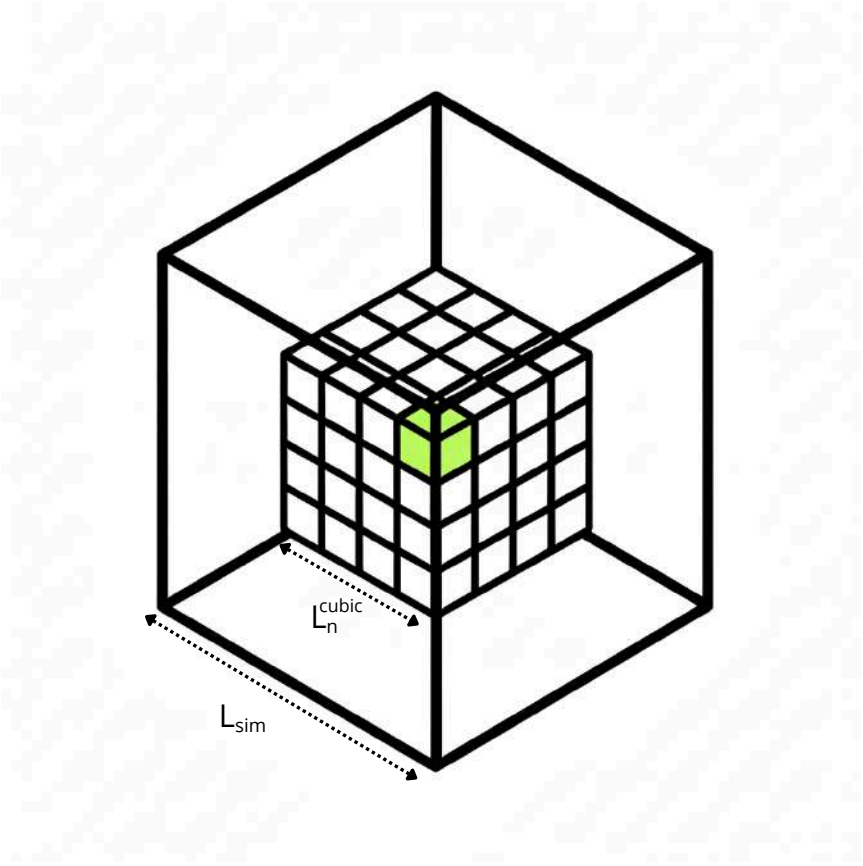

FIGURE 5.6: Schematic representation of the geometric model used in MCt-MKM. The simulation volume with side length L_{sim} contains the cubic cell nucleus, with side length L_n^{cubic}. The green subcube represents a domain with side length L_d^{cubic}.

The number of domains per nucleus used in the simulation varies in a range from 1000-2000 depending on the cell type.

The dimensions of the nucleus and domains are shown in Table 5.1 and were estimated from experimental data on HSG cell line.

TABLE 5.1: MCt-MKM parameters from [174].

Cell Line	$\alpha_0\,(\mathbf{Gy^{-1}})$	$\beta_0\,(\mathbf{Gy^{-2}})$	$R_n\,(\mu\mathbf{m})$	$R_d\,(\mu\mathbf{m})$	$L_n^{cubic}(\mu m)$	$L_d^{cubic}(\mu m)$
HSG	0.312	0.073	4.611	0.365	8.51	0.672

Based on the dimensions of the domains and cells reported in [174], the dimensions for the cubic cell nucleus geometry were estimated, assuming equal volume. In this study, the source is a ^{99m}Tc atom that decays over time. Each event corresponds to a decay.

The number of events (^{99m}Tc sources) used in the simulation was expressed as a function of concentration C (events/μm^3). Due to the lack of systematic experimental

evidence, a uniform spatial distribution of sources inside and outside the cell nucleus was assumed. For each cell simulation, a Poisson random number of events, N, was extracted from the concentration C.

A spatial position $\vec{p}_k$ was then generated by uniformly sampling the coordinates (x, y, z) within V_{sim}. Each event is associated with a random time coordinate t_i. The time coordinate is sampled randomly from a temporal PDF of the exponential decay of ^{99m}Tc, with a half-life of 6h, so that each decay event has a specific time t_i.

The production of particles from the decay of ^{99m}Tc is assumed to be instantaneous. The events were then ordered temporally in order to define a temporal sequence where if $i > j$, $t_i \geq t_j$. From the output of the Geant4 simulation, a number N of random events were selected. Each event was translated by the vector $\vec{p}_k$ and randomly rotated.

If a step belonging to that event fell within the cell nucleus volume V_{nc}, the corresponding domain was identified. Otherwise, the step was not saved. For each event, there will be an associated dose z_{event} and time t_i. After processing all selected events, the total dose z_d was calculated by summing all dose contributions z_i received from domain d.

The expected number of lethal lesions x_I^{cd} in a domain d and per cell c, which received the dose z_i^{cd}, is given by the solution of the kinetic equation discussed in Section 2.2.3:

$$\tilde{x}_I^{(cd)} = \frac{\alpha_0}{N_D} \sum_{i=0}^{n_c-1} z_i^{(cd)} + \frac{\beta_0}{N_D} \left(\sum_{i=0}^{n_c-1} z_i^{(cd)} \right)^2 - 2\frac{\beta_0}{N_D} \sum_{i=0}^{n_c-2} \sum_{j=i+1}^{n_c-1} \left(1 - e^{-\frac{1}{\tau}(t_j - t_i)} \right) z_i^{(cd)} z_j^{(cd)} \tag{5.1}$$

where n_c is the event number inside a single domain, α_0 and β_0 are the parameters of the model, and the indices i and j identify two specific and different events within the same domain. The time constant that defines the repair kinetics, τ, is equal to 23 ± 3 min, as a result of a fit to the experimental data [174][129]. To account for the repair of sublethal damage that occurs between two energy deposits, 5.1 could be rewritten using the Lea-Catcheside factor G_{cd} (see Section 2.2.3 for details):

$$\tilde{x}_I^{(cd)} = \frac{\alpha_0}{N_D} \sum_{i=0}^{n_c-1} z_i^{(cd)} + G_{cd}\frac{\beta_0}{N_D} \left(\sum_{i=0}^{n_c-1} z_i^{(cd)} \right)^2 \tag{5.2}$$

A possible synergistic effect in the ^{99m}Tc-AuNR system was also studied. It is expected that the co-location of multiple sources of ^{99m}Tc on the surface of an AuNR could produce a significant local increase in dose. From a radiobiological point of view, such a concentration of radiation sources should increase the probability of generating complex and lethal DNA damage. This effect is expected to increase with the coordination number, i.e., the number of radionuclides associated with each nanoparticle.

The Geant4 simulation was used, which takes into account the presence of the gold nanoparticle, excluding the energy depositions z_i in its volume, as it is not radiobiologically relevant. The MC procedure used is the same as described above. The selected events have been grouped into clusters containing a variable number of

events N_c around a common translation point, corresponding to the position of the AuNR.

Therefore, once the coordination number N_c was set, the total number of selected events was divided into groups of N_c events each. To introduce further geometric randomization, each event had a random rotation around this point, consistent with all events in that cluster. An example of the 3D distribution of randomly oriented ^{99m}Tc-AuNR systems is shown in Figure 5.7.

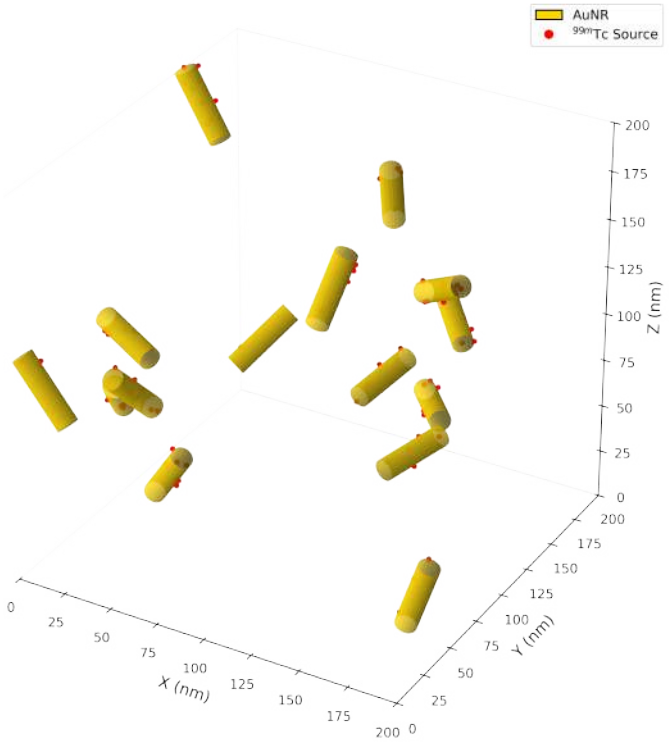

FIGURE 5.7: 3D view of randomized AuNRs (yellow cylinders) and ^{99m}Tc sources (red dots) inside the cell nucleus sub-volume. The sources were distributed near the AuNR surfaces according to the coordination number N_c.

In order to highlight the effect of the protraction of the irradiation, due to the long ^{99m}Tc half life time, two different scenarios were analyzed to study the effect of dose rate:

- **Acute irradiation**: it is assumed that the entire dose is released instantaneously at time t=0. Under this condition, the time interval between any two energy deposition events i and j is zero ($\Delta t = |t_i - t_j| \approx 0$). Consequently, the repair term associated with the exponential decay of sub-lethal lesions becomes $e^{-\Delta t/\tau} \sim 1$. This maximizes the interaction probability between sub-lethal lesions, leading to a Lea–Catcheside factor $G_{cd} = 1$.

- **Protracted irradiation**: dose is delivered follow the decay of the ^{99m}Tc (half-life of 6 hours). In this case, the non-zero time intervals between energy deposition events allow cells to partially repair sublethal damage during the irradiation itself, leading to a Lea-Catcheside factor $G_{cd} < 1$.

The simulation uses particle tracks generated using Geant4 code as input. For each domain of a cell, the time sequence of specific energy deposits at specific times is processed to analytically solve the kinetic equations (2.14). The algorithm I implemented follows the mathematical derivation of the equations 2.19,2.18.

Between two consecutive dose deposition events, the number of sublethal lesions decays due to repair processes. The code calculates this trend by implementing the solution for time intervals described by Equation 2.18, which models the sum of the residual contributions of all previous events weighted by the exponential decay factor and $e^{-(a+r)\Delta t}$. At the same time, lethal lesions x_I accumulate both through direct production at the moment of interaction and through the conversion of sub-lethal lesions. The simulation calculates this second contribution by integrating the density x_{II} over time, in accordance with the integral formulation of Equation 2.19.

The parameters used in calculating x_I and x_{II} (λ,k,a,b) are directly related to the parameters α_0 and β_0 shown in 5.1, according to the relationships in equation 2.21. The table 5.2 shows the parameters for HSG cell line used in following analyses.

TABLE 5.2: MKM parameters used in calculations [129].

$\boldsymbol{\lambda}$ [Gy^{-1}]	$\boldsymbol{k}$ [Gy^{-1}]	$\boldsymbol{a}$ [h^{-1}]	$\boldsymbol{b}$ [h^{-1}]	$\boldsymbol{\tau}$ [min]
1.934×10^{-4}	1.934×10^{-2}	0.022	0.3975	23.0

5.2 Results and discussion

Figure 5.8a shows the radial dose of ^{99m}Tc per energy deposition process. The ionization process (`e-_G4DNAIonisation`) is the dominant contributor to the dose over the entire simulation volume. The contributions of photon processes, such as `compt` (Compton effect) and `phot` (photoelectric effect), are lower by several orders of magnitude than the electron ionization process, depending on the radial distance considered.

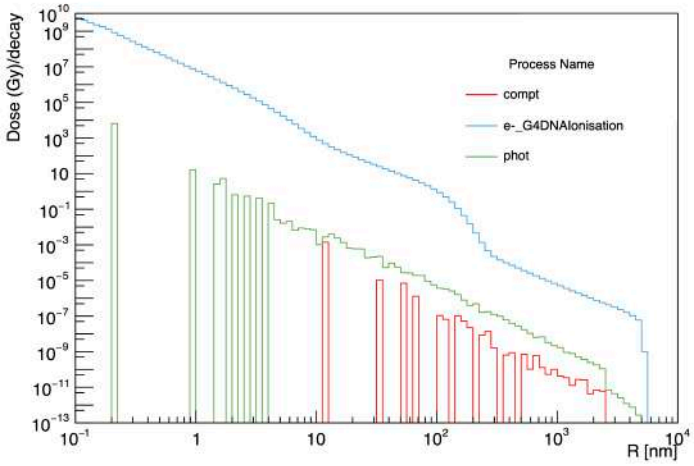

(A)

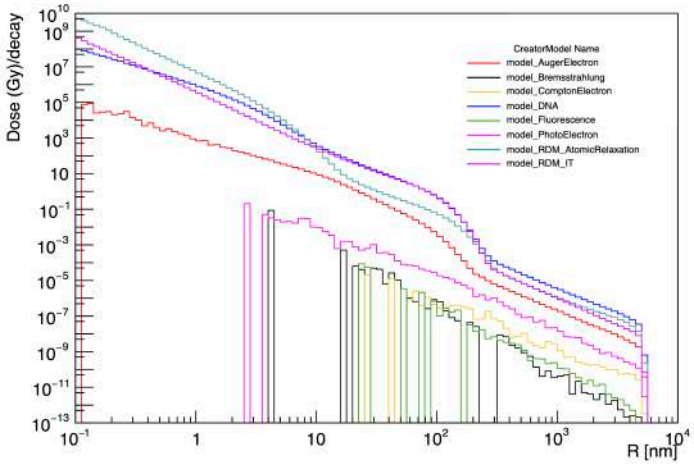

(B)

FIGURE 5.8: Radial dose distribution per ^{99m}Tc decay from a point source at $R = 0$. The total dose is decomposed by: (A) physical energy-deposition process and (B) particle creation model, which identifies the origin of the particle depositing the dose.

To explain the behavior of the radial dose profile, it is important to analyze the energy spectrum of the produced particles. Near the source (R $\sim$ 1–10 nm), a very high dose concentration is observed. This is due to the low-energy component of the Auger spectrum generated by the decay of ^{99m}Tc (`model_RDM_IT` and `model_RDM_AtomicRelaxation`). In particular, CK and M–N Auger electrons have maximum energies of about 500 eV (Figure 5.10) and a range in water of the order of a few tens of nanometers [90].

The most energetic component of internal conversion electrons (approximately 1.5–3 keV) has a range in water of approximately 100–150 nm. The bump observed in the dose profile is consistent with the contribution of L-Auger electrons, which deposit their energy in this distance range. For R > 100 nm, the dose is dominated by higher energy electrons.

As shown in Figure 5.10, ^{99m}Tc emits Auger electrons with energies between 15 and 22 keV, associated with K-LL and KLX transitions; these electrons have a range in water of the order of micrometers. In this region, the `model_DNA` and `model_AugerElectron` models also become relevant, which include the interactions of secondary electrons in water and the production of additional Auger electrons (approximately ∼500 eV) emitted by water molecules following their ionization [135].

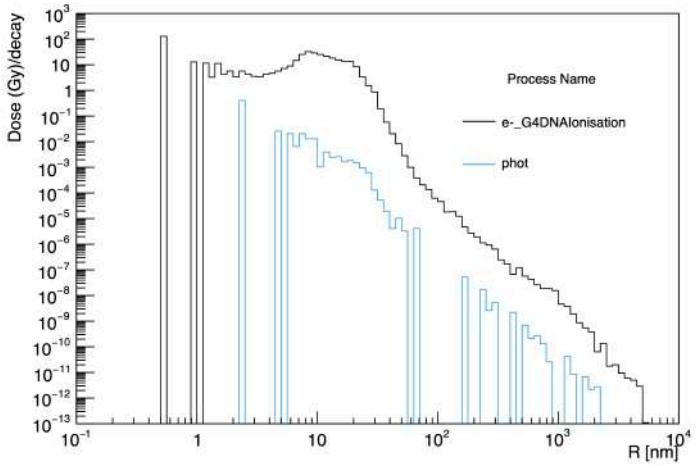

(A)

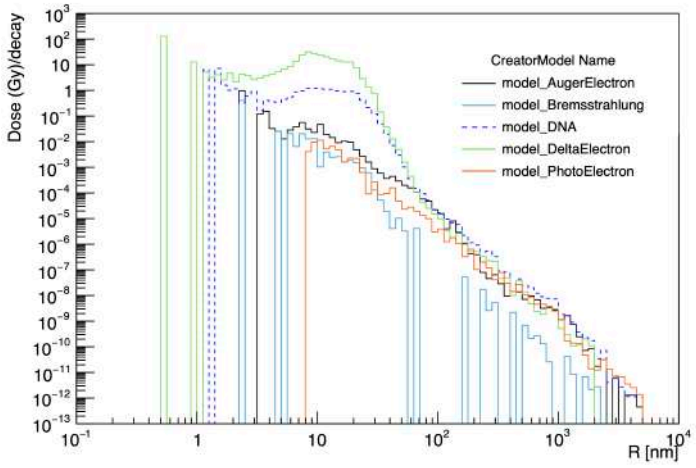

(B)

FIGURE 5.9: Radial dose profiles showing the isolated contribution of the AuNR. The total dose is decomposed in two ways: (A) by the physical interaction process leading to energy deposition; and (B) by the particle creation model, which identifies the origin of the particle depositing the dose.

Using the algorithm described above, it was possible to isolate the contribution of the dose due to the presence of the AuNR as shown in Figure 5.9. Again, the dominant process is the ionisation one (`e-_G4DNAIonisation`), followed by the photoelectric process `phot`. The peak dose deposited near the AuNR is 6-7 orders of magnitude

lower than the contribution of ^{99m}Tc alone. This depends on the photon-gold interaction cross-section and the nanoparticle size. For an incident photon of 140.5 keV, approximately 0.0005 secondary particles are produced within the AuNR.

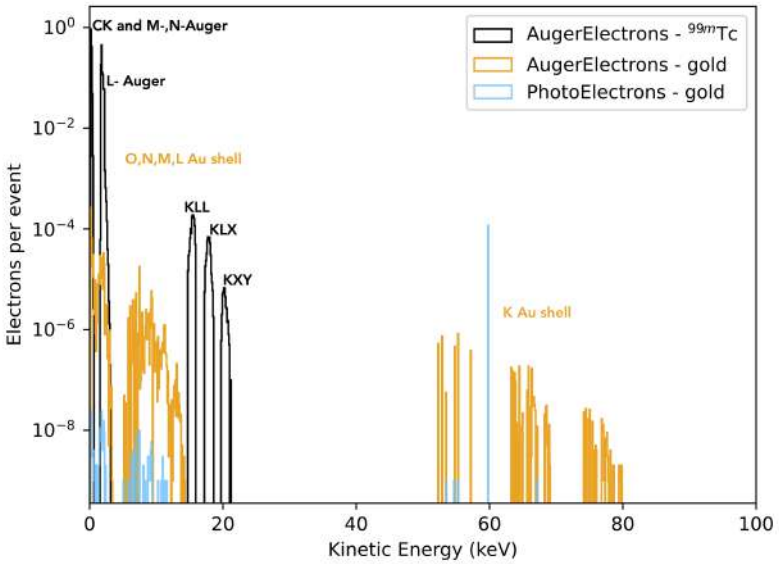

FIGURE 5.10: Simulation of Auger emission from both ^{99m}Tc and gold. The spectra are normalized per decay event (Tc-99m) and per ionization event (Au).

Delta electrons `model_DeltaElectron` deposit most of the dose, and they are subsequently followed by secondary particles produced in water `model_DNA`. Most of the events deposit near the AuNR (see the bump at R = 10-30 μm in 5.9b). As shown in figure 5.10, the electrons spectrum, which was generated from the interaction of 140.5 keV photons (characteristic of the decay of ^{99m}Tc) with AuNR, has both a low-energy component and a higher-energy component. Auger electrons from the O, N, M, and L shells produced have energies similar to those of ^{99m}Tc and have a significantly lower production rate. Auger electrons (k shells) and photoelectrons with energies between 60 and 80 keV have a greater range in water (>50 μm) and deposit less dose locally, having also a lower production rate than lower-energy Auger electrons.

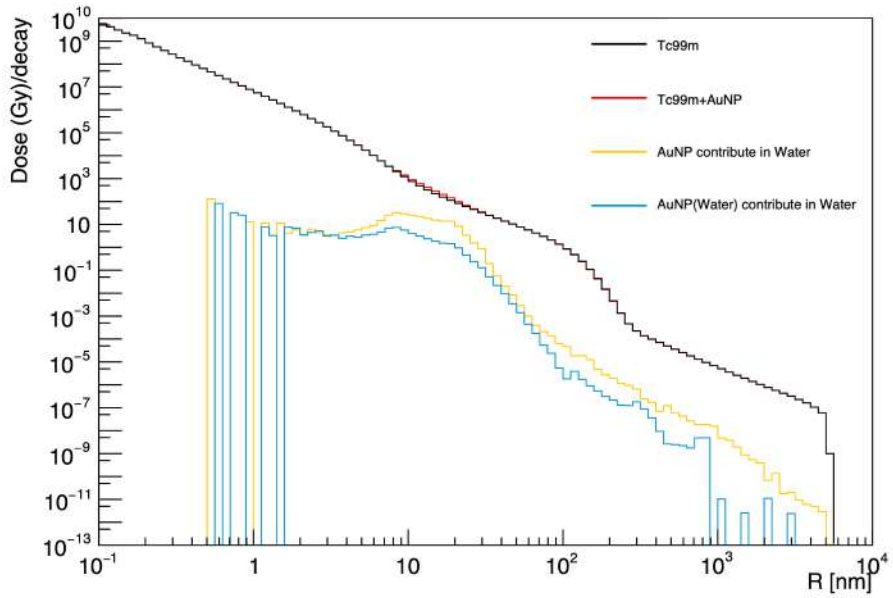

FIGURE 5.11: Radial dose profiles as a function of distance from source R. The plot compares the ^{99m}Tc + AuNR system (red line) with the radionuclide alone (black line). The yellow line shows the dose deposited only by secondary particles emitted from the AuNR, while the blue line shows the dose that would be produced by a volume of water of the same size.

The comparison between the radial dose profiles of the ^{99m}Tc alone and the ^{99m}Tc-AuNR system is reported in Figure 5.11. Given that the sensitive target (DNA) is located outside the nanoparticle, the dose that is deposited within the gold volume (visible in Figure 5.11 as the gap between the red line (^{99m}Tc-AuNR system) and the black line (^{99m}Tc) at roughly 10 nm) is irrelevant concerning biological damage. Consequently, even if the local dose peak is physically present, it will not be considered in the biological efficacy calculation. Despite the local dose intensity, the overall contribution of AuNR to the total dose is limited when compared to the energy released by the decay of ^{99m}Tc.

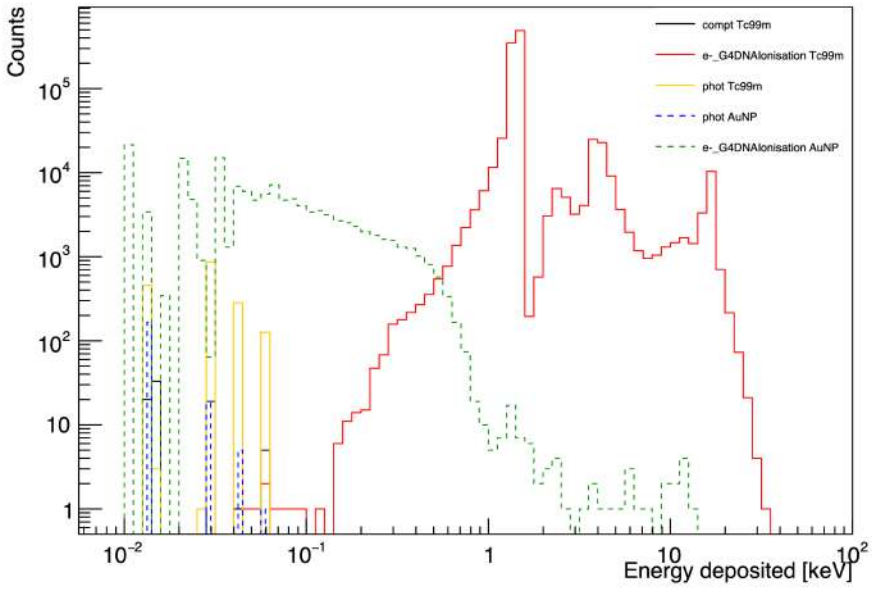

FIGURE 5.12: Energy deposited spectra for the contribution of ^{99m}Tc alone (solid line) and AuNR (dashed line) in water.

TABLE 5.3: Comparison of energy-deposition processes for AuNR and ^{99m}Tc. The column "Mean Edep" represents the mean energy deposited per event, while "Total Edep" corresponds to the cumulative energy deposited within the volume throughout the simulation, reported for each physical process.

Source	Process	Mean Edep (keV)	Total Edep (keV)
AuNR	e$^-$_G4DNAIonisation	0.080	1.09×10^4
	phot	0.016	3.10×10^0
^{99m}Tc	e$^-$_G4DNAIonisation	1.900	1.90×10^6
	phot	0.029	5.11×10^1
	compt	0.021	1.60×10^0

Confirming the marginal nature of the contribution of AuNR to the total dose, Figure 5.12 shows the energies deposited per process in the ^{99m}Tc-AuNR system. As reported in Table 5.3, for ^{99m}Tc, the dominant ionisation process deposits an average of about 2 keV per event, compared to 0.08 keV for the AuNR contribution. The energy deposited directly by ^{99m}Tc is about 170 times higher than that deposited by processes related to the presence of gold. The AuNRs contribution to the total energy absorbed by the system is negligible. Relating the irradiation dose profile to its biological effects, the following analysis evaluates survival curves using the MCt-MK model. As discussed in section 5.1.2, by weighting the energy deposited by ^{99m}Tc by the probability $P(r)$ of finding or not DNA at a radial distance r from the source, the occupancy of SestaMIBI can be integrated into the microdosimetric evaluation.

Figure 5.13 shows the mean surviving fraction $\langle S \rangle$ as a function of the mean absorbed dose $\langle D \rangle$ for the two geometric scenarios (point source vs. ^{99m}Tc-SestaMIBI). As expected, the mean surviving fractions decrease with increasing doses. The surviving fractions were calculated according to Equation (2.26) and evaluated for different ^{99m}Tc concentrations. The investigated concentration range (0.1–10.0 sources/μm^3) was chosen to represent clinically relevant concentrations. Based on the activity of ^{99m}Tc-SestaMIBI (3 GBq/mL) used in preliminary studies at Policlinico Gemelli, a local density of approximately 9 ^{99m}Tc atoms/μm^3 was estimated. As can be seen from Figure 5.13, in order to achieve a survival rate of approximately 35%, high concentrations of the order of 10 ^{99m}Tc/μm^3 are required.

The survival curves, with and without Sesta-MIBI occupancy, are comparable for the range of concentrations considered. The differences fall within the statistical uncertainties and do not lead to significant variations in the estimation of LQ model parameters (see Table 5.4). The difference in scale between the molecular volume of SestaMIBI (r ∼1–2 nm) and microdosimetric domains volume (l∼600 nm) makes the point source approximation in MCt-MKM valid, without affecting the radiobiological evaluation.

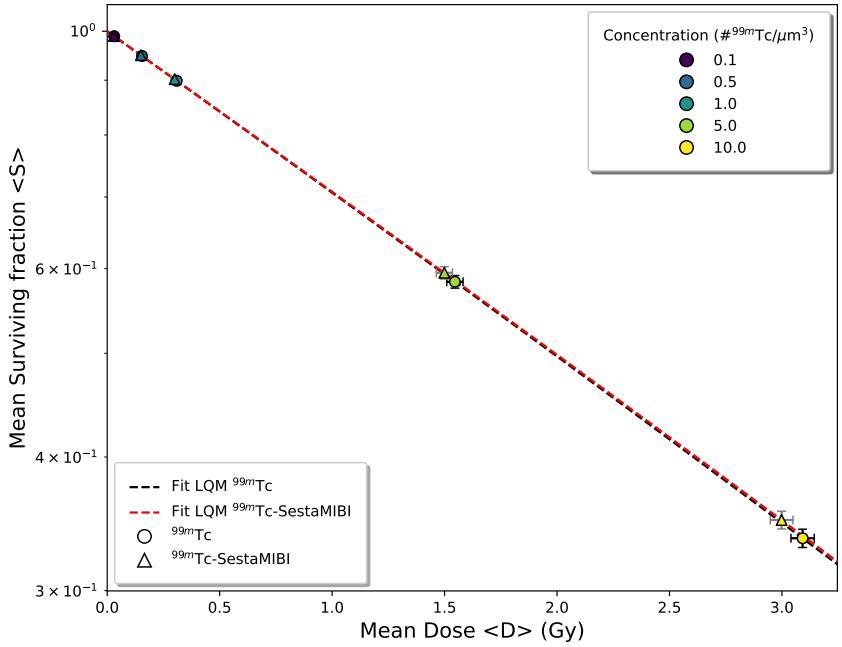

FIGURE 5.13: Comparison of the mean survival fraction $\langle S \rangle$ as a function of the mean dose $\langle D \rangle$ in the point source approximation ^{99m}Tc (circles) and 3D molecular geometry of ^{99m}Tc-SestaMIBI (triangles). Dashed lines show the Linear-Quadratic model (LQM) fit, from which α and β for (^{99m}Tc) and ^{99m}Tc SestaMIBI configurations were estimated. The mean survival fraction was calculated over a population of 10,000 cells.

Based on this validation, the point-source approximation was applied to evaluate the possible synergistic effect of ^{99m}Tc-AuNR system.

TABLE 5.4: Radiobiological parameters obtained from the Linear-Quadratic Model fit of the survival curves for the two simulated geometric configurations. The parameters α,β(for ^{99m}Tc) and α', β' (^{99m}Tc SestaMIBI) are reported with their respective standard errors.

Configuration	$\boldsymbol{\alpha}$ $[\boldsymbol{Gy^{-1}}]$	$\boldsymbol{\beta}$ $[\boldsymbol{Gy^{-2}}]$
^{99m}Tc (Point source)	0.345 ± 0.012	0.003 ± 0.005
^{99m}Tc-SestaMIBI	0.343 ± 0.013	0.003 ± 0.005

Figure 5.14 shows the 3D spatial distribution of the local dose within the cell nucleus for different coordination numbers (from 1 to 500 sources per AuNR). The maps clearly show the transition from a relatively "rough" and diffuse dose distribution (Figure A, 1 source/AuNR) to an extremely heterogeneous topology dominated by isolated peaks (Figure D, 100 sources/AuNR). The dose peaks physically represent the microdosimetric domains containing the AuNRs, while the "flat" areas represent the stochastic background of the nucleus, where the dose is lower by orders of magnitude.

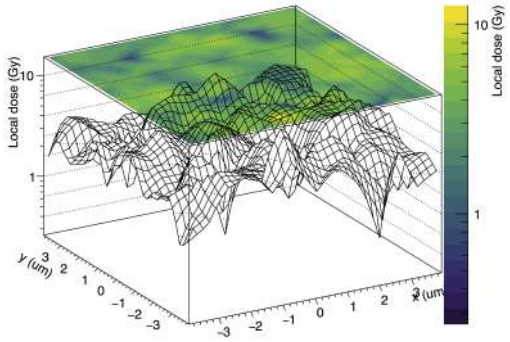

(A) 1 sources per AuNR

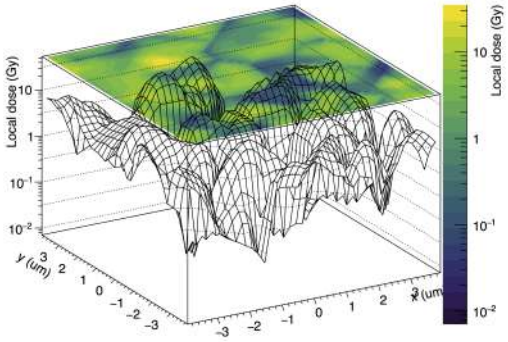

(B) 10 sources per AuNR

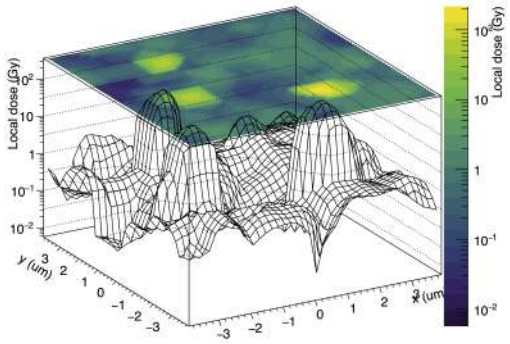

(C) 100 sources per AuNR

FIGURE 5.14: Three-dimensional representation of the spatial distribution of the local dose (z) within the simulated nuclear volume. The four figures correspond to ^{99m}Tc–AuNR coordination numbers of 1 (A), 10 (B), 100 (C). The vertical axis reports the local dose on a logarithmic scale (Gy), while the xy-plane indicates the spatial coordinates in μm. The surfaces depict the topology of energy deposition, underlining the variation between background regions and dose peaks.

As shown in Figures 5.15, the mean surviving fraction was studied as a function of the number of sources per AuNR. Despite the decreasing trend as the number of sources per AuNR increases, mean surviving fractions for 1 source/μm^3 remain > 0.6 within the statistical uncertainties.

A pronounced effect ($\langle S \rangle \approx 0.2$) emerges with high coordination numbers (500 sources/AuNR) associated with higher volumetric density (5 sources/μm^3). Explaining this behavior requires accounting for the temporal structure of the radiation. Unlike external hadron beams (e.g., protons or carbon ions), which deliver dose on timescales comparable to cellular kinetics repair, the decay of ^{99m}Tc results in a protracted dose relative to HSG cell repair times. To show the effect of the dose rate time structure, the following analyses will integrate the Lea-Catcheside factor in both the acute and protracted dose hypotheses.

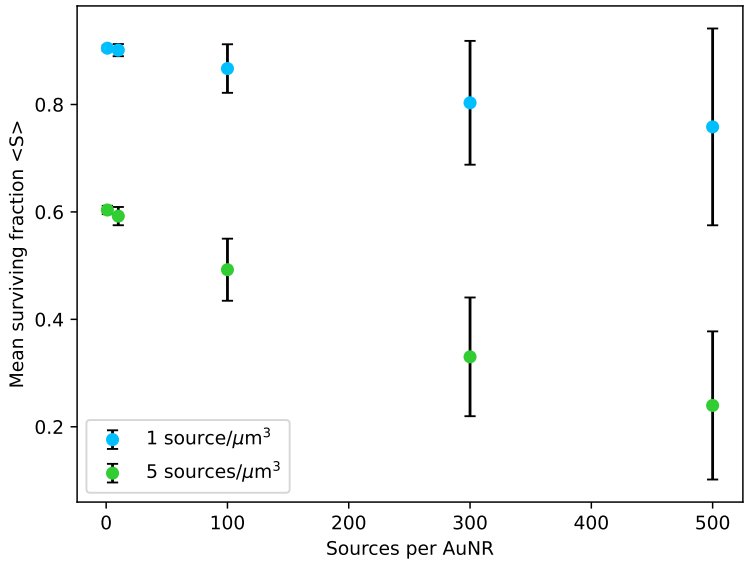

FIGURE 5.15: Mean surviving fraction $\langle S \rangle$ estimated by the MCt-MK model as a function of sources per AuNR, calculated over a population of 10,000 cells. The graph compares two source concentrations: 1 source/μm^3 (blue dots) and 5 sources/μm^3 (green dots).

Figure 5.16 compares two distinct scenarios defined by Lea-Catcheside's G factor (G_{cd}), which modulates the quadratic term βz^2 based on DNA repair kinetics. For acute irradiation ($G_{cd} = 1$), the dose is released instantaneously with respect to cell repair time. In this case, biological damage is maximised because sublethal damage is not repaired during irradiation. The case of a protracted dose regime (G_{cd}<1) represents the realistic scenario that takes into account the temporal structure of ^{99m}Tc decay. Since the dose is released over an extended period of time, cellular repair mechanisms can act during the exposure itself. The evaluation of the surviving fraction as a function of the G_{cd} factor was performed for different concentrations of ^{99m}Tc.

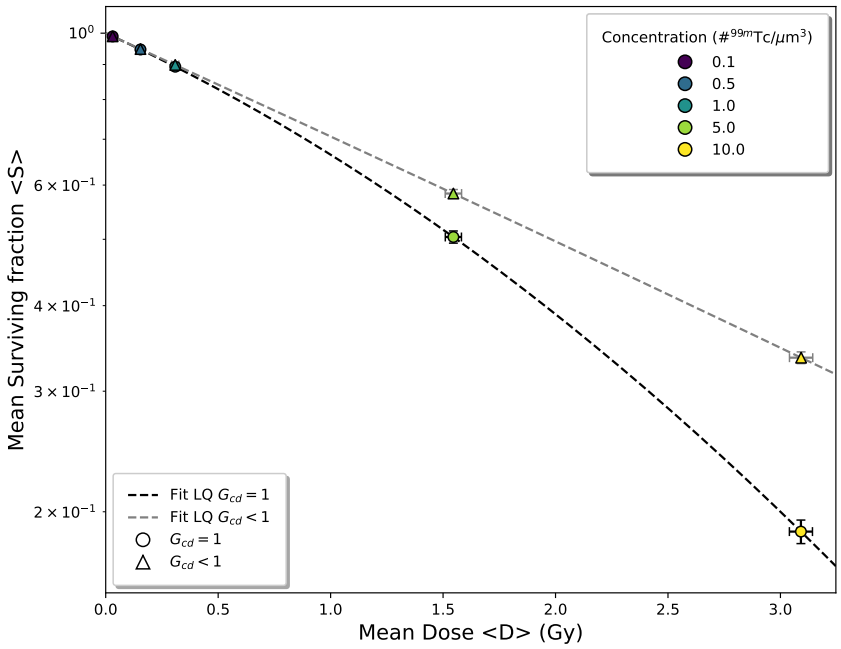

FIGURE 5.16: Mean cell-survival curves ($\langle S \rangle$) as a function of the mean absorbed dose ($\langle D \rangle$), simulated for different concentrations of ^{99m}Tc (from 0.1 to 10.0 sources/μm^3), comparing two scenarios. One corresponds to an acute irradiation with G_{cd} = 1 (circles, black line), and the other to the case G_{cd} < 1 (triangles, gray line), which accounts for the temporal structure of the decay. Dashed lines show the Linear-Quadratic model (LQM) fit, from which α, β (G_{cd} = 1) and α^*, β^* (G_{cd} < 1) were estimated.

TABLE 5.5: Radiobiological parameters obtained from the Linear-Quadratic Model fit of the survival curves for the two irradiation scenarios. Standard errors are also reported.

Irradiation	**Linear Param.** $[Gy^{-1}]$	**Quadratic Param.** $[Gy^{-2}]$
Acute ($G_{cd} = 1$)	$\alpha = 0.3446 \pm 0.0001$	$\beta = 0.0639 \pm 0.0001$
Protracted ($G_{cd} < 1$)	$\alpha^* = 0.3446 \pm 0.0001$	$\beta^* = 0.0027 \pm 0.0001$

The analysis of the LQ model fits (see equation 1.21) performed on the two curves allowed the impact of the temporal structure to be quantified. The linear parameter does not change between the two scenarios, as shown in Table 5.5, suggesting that the dose rate has no influence on the formation of lethal lesions. The quadratic term, on the other hand, shows a significant decrease, going from $\beta \approx 0.0639$ Gy^{-2} in the acute irradiation to $\beta^* \approx 0.0027$ Gy^{-2} under protracted irradiation. The dose-rate effect is quantified by this significant decrease, which results in a quasi-linear survival curve since the quadratic term in Eq. 5.2 is suppressed. From the ratio between β of G_{cd}=1 and β^* of G_{cd}<1, a macroscopic G factor of 0.04 was estimated. It is evident that cell survival is higher in the case of G_{cd}<1 for the same absorbed dose.

The temporal distribution of damage reduces the probability that two sublethal lesions will interact to form a lethal lesion. The inclusion of the time structure results in an effective reduction in the β parameter of the dose-response curve, indicating lower toxicity per unit dose compared to acute irradiation. To fully understand the reasons for the increase in survival observed in the G_{cd}<1 regime, it is necessary to analyze the temporal evolution of DNA lesions by comparing it with the acute irradiation limit $G_{cd} = 1$.

Figure 5.17 shows the temporal trend of the two types of lesions (x_I and x_{II}) for different coordination numbers (1, 10, 100 ^{99m}Tc for AuNR) for the two scenarios. In the $G_{cd} = 1$ regime (Figure 5.17), reparable lesions (x_{II}) start from a high initial value ($>$ 12 lesions/cell) and then undergo an exponential decay during the first few hours. Since the damage is concentrated at the beginning, irreparable lesions (x_{I}) rapidly reach a plateau. Increasing the coordination number (number of $^{99\mathrm{m}}$Tc per AuNR) leads to significant higher amount of irreparable or misrepaired lesions ($x_{\mathrm{I}} \approx 1.2$).

In $G_{cd} < 1$ situation, type II lesions show a peak in the first hours after irradiation, corresponding to the maximum activity of the radionuclide. However, their number decays exponentially, tending towards zero within 30-40 hours. This trend confirms that during the half-life of ^{99m}Tc ($T_{1/2}$=6 h), the cell's repair mechanisms are active and manage to remove most of the sublethal damage before it can interact to become lethal. On the other hand, type I lesions show a progressive accumulation reaching a plateau when the source activity is decayed.

Notably, an increase in coordination number does not significantly alter the kinetics of the repairable lesions. This behavior is consistent with the kinetic equation (Eq. 2.14), in which the production of x_{II} lesions depends linearly on the dose rate ($\propto k\dot{z}$).

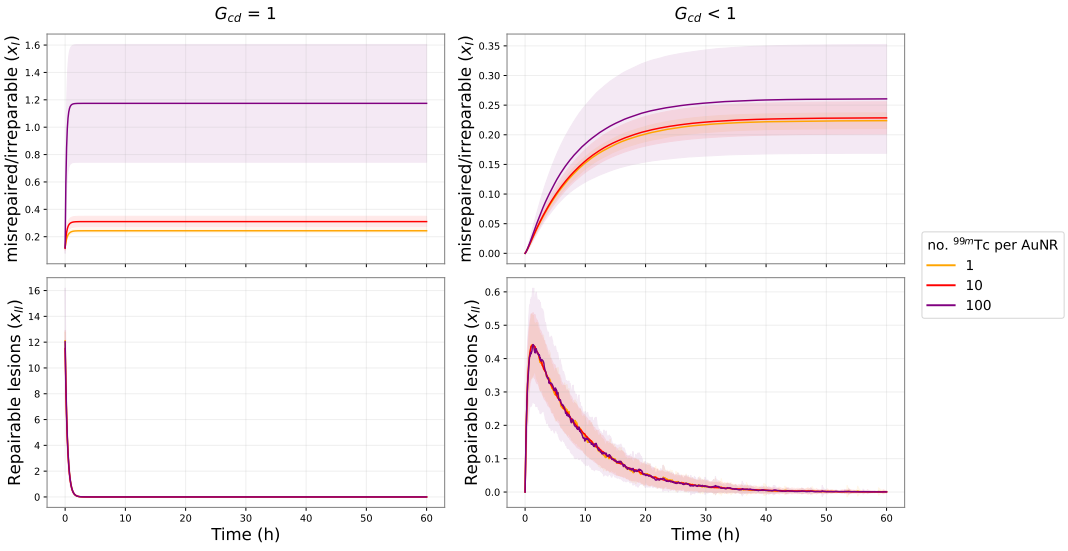

FIGURE 5.17: Temporal evolution of irreparable/misrepaired (x_I) and reparable (x_{II}) lesions simulated with the MCt-MKM model for different coordination numbers. Figures on the left show the case of acute irradiation ($G_{cd} = 1$), while those on the right correspond to a protracted irradiation ($G_{cd} < 1$).

Figure 5.18 presents a combined analysis correlating the dose absorbed by the domain (X-axis) with the number of decays occurring within it (upper graph) and the corresponding G factor (lower graph). From the simulated data set, the cells with the highest deposited dose per domain were randomly extracted for the three coordination numbers.

The domains receiving high doses (> 20 Gy) correspond to the higher coordination (e.g., the green dots at 100 decays correspond to the "100 Tc/AuNR" group). This confirms that the high-dose domains are exclusively those containing clustered sources. On the contrary, the majority of domains have zero or very few decays. The dose they receive (< 5 Gy) is much lower due to particles passing from neighbouring domains.

Figure 5.18 shows that domains with high doses also have extremely low G values. Since the dose in these domains is generated by local ^{99m}Tc decays, the energy rate deposition follows the decay law of ^{99m}Tc. This means that even if the dose is locally very high, it will be released over a long time range.

This time range is long enough for DNA repair mechanisms to intervene between one ionisation event and another, reducing the probability of synergistic damage combination (quadratic behaviour as a function of dose) between different ^{99m}Tc decays.

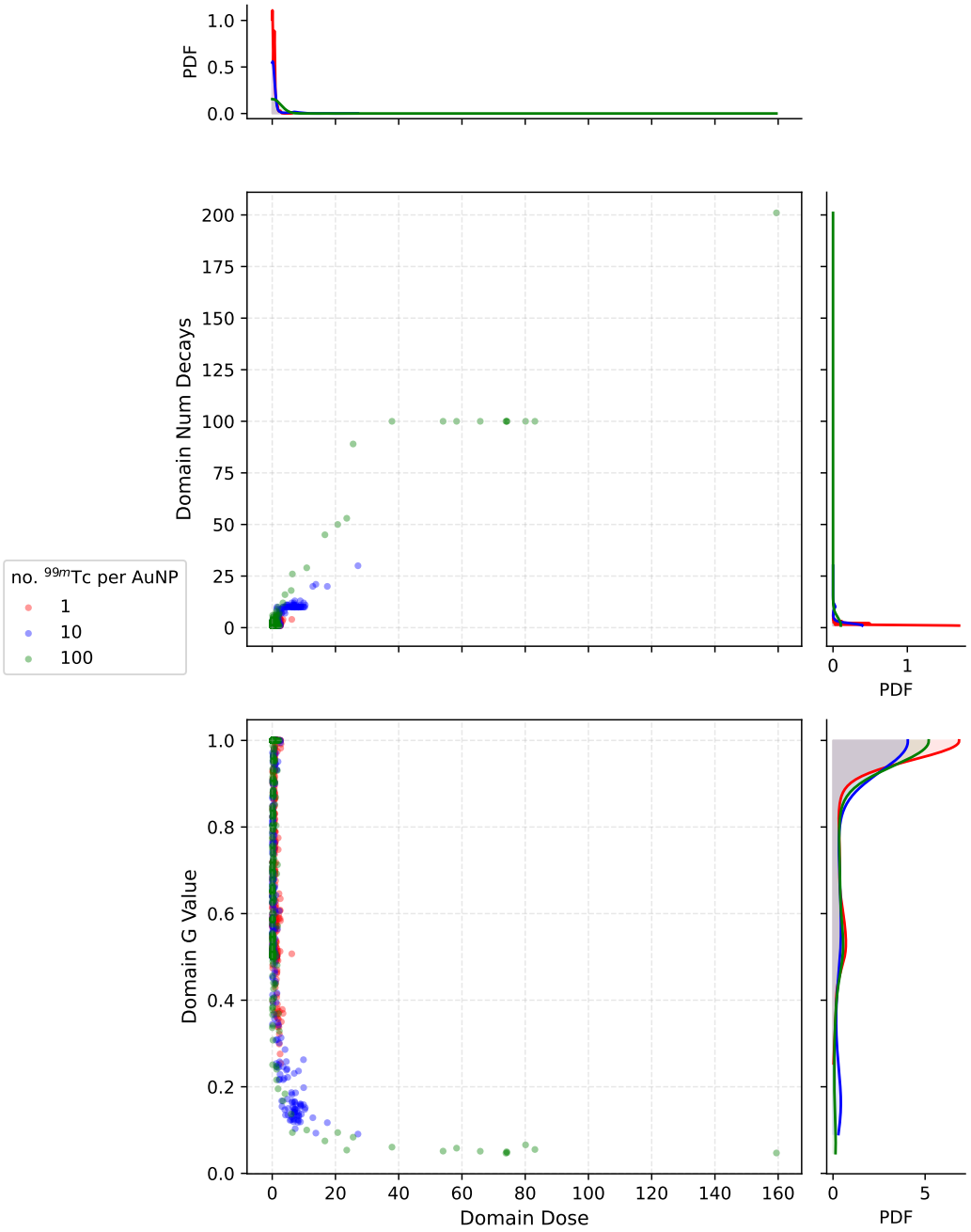

FIGURE 5.18: Combined analysis of the number of decays and the G-factor per domain as a function of the domain dose. (Upper Figure): Scatter plot of the number of decays occurring within each domain. (Lower Figure): Scatter plot of the Lea–Catcheside G-factor. Colors indicate the different coordination numbers (1, 10, 100 ^{99m}Tc/AuNR). The side and top Figures show the probability density functions (PDFs) of the respective variables.

When analysing the dose mean values μ_{dose} and its standard deviations σ_{dose}, an increase in dose heterogeneity can be observed as the coordination number rises. For one ^{99m}Tc per AuNR, the dose distribution is relatively homogeneous. Conversely, at 100 ^{99m}Tc per AuNR, the standard deviation on the dose is ~ 9.40. This indicates that the variance is driven by a few high-dose domains as opposed to a larger low-dose

Coordination number	Cell ID	$\mu_{\mathbf{dose}}$	$\sigma_{\mathbf{dose}}$	$\mu_{G_{cd}}$	$\sigma_{G_{cd}}$
1	500	0.5274	0.5541	0.9094	0.1759
10	942	0.8176	2.2586	0.8524	0.2686
100	67	1.3124	9.3995	0.8918	0.2174

TABLE 5.6: Mean (μ) and standard deviation (σ) of the probability density functions for domain dose and G-value.

background. Interestingly, the overall mean G factor $\mu_{G_{cd}}$ remains constant across the cells. That confirms that volumetrically, most of the core is in the stochastic background at this G value. The effect of G <0.2 is purely local, confined to the points where the dose varies the most.

It should be noted that, in domains with small volumes and high ionization density (local dose > 100 Gy), a saturation effect (overkill) may be possible. Once the biological target (DNA) within a domain reaches lethal damage, subsequent dose deposition does not further increase the cell killing probability. Currently, the MCt-MKM does not explicitly model this saturation effect. Future developments of the model should integrate a saturation correction factor to avoid potential overestimations of the biological effects of radiations.

5.3 Conclusions

This work aimed to investigate the potential radiobiological enhancement of a theranostic system based on ^{99m}Tc and AuNRs using a Monte Carlo approach, which involved Geant4 simulation. The study focused on the characterization of energy deposition at the nanoscale, evaluating also the biological effect by accounting for the temporal structure of radionuclide decay.

The analysis of radial dose profiles revealed that dose deposition is dominated by the direct emission of Auger and internal conversion electrons from ^{99m}Tc. Although the presence of AuNRs generates a local dose enhancement near the nanoparticle, due to the emission of photoelectrons and low-energy Auger electrons, the contribution is 6-7 orders of magnitude lower than that of the radionuclide alone. Quantitative analysis of the total deposited energy confirmed that the dose enhancement provided by AuNR is minimal compared to the dose released by ^{99m}Tc decay. Furthermore, ^{99m}Tc-SestaMIBI occupancy has a negligible impact on the evaluation of the biological effect induced by ^{99m}Tc.

The radiobiological analysis performed through MCt-MKM underlined the critical role of the dose rate time structure. The comparison between acute (G_{cd}=1) and protracted (G_{cd}<1) irradiation scenarios demonstrated that by neglecting the temporal decay of ^{99m}Tc ($T_{1/2}$=6 h), the biological damage can be significantly overestimated. HSG cellular repair mechanisms effectively repair sublethal lesions (x_{II}) during the protracted irradiation, reducing the formation of lethal lesions.

Investigation of a possible synergistic effect in ^{99m}Tc-AuNR system showed that by increasing the number of ^{99m}Tc sources per AuNR, a spatial heterogeneity in dose distribution can be found. However, even in domains where high doses are received

due to high coordination numbers, the local Lea-Catcheside G-factor remains low. This confirms that the slow dose rate allows DNA repair to minimize the synergistic effect. It should be noted that the low G-values observed in high-dose domains might also reflect a saturation effect (overkill), where the biological target (DNA) is lethally damaged by the events, leaving subsequent depositions ineffective.

Despite the limited AuNR dose enhancement, these results do not reduce the therapeutic potential of this combined system. AuNRs should not be viewed as dose enhancers, but as carriers. Their ability to be functionalized and selectively accumulate in tumor cells allows for the transport of the ^{99m}Tc radionuclide directly inside the cell or close to the nucleus. In this way, the short-range dose of ^{99m}Tc is deposited within the target volume, maximizing the therapeutic index while minimizing healthy tissue exposure. The combination of source localization and local high-LET dose deposition confirms the validity of this approach in the theranostic framework.

In conclusion, for the specific configuration and cell line investigated, the therapeutic efficacy relies on the high-LET Auger electrons emitted by ^{99m}Tc, carried by the AuNRs. MCt-MKM proved to be a solid model for predicting survival fractions in scenarios characterized by complex temporal dose structures, providing a framework for future optimisation of radiopharmaceutical-based therapies.

Chapter 6

Conclusions and future works

This PhD thesis explored the crucial role of microdosimetry in optimizing modern radiotherapy treatments, with a focus on hadron therapy and targeted radionuclide therapy. This work has demonstrated how understanding energy deposition at the micro and nanometer scale is fundamental to overcoming the limitations of conventional dosimetric models, enabling the development of more accurate radiobiological models and reliable predictions for treatment planning and outcomes.

Integrating experimental and Monte Carlo modeling approaches, the work focused on the characterization of DIODE, a novel detector for ion beam therapy, and the study of the radiobiological effects of innovative theranostic systems based on radionuclides and gold nanoparticles.

The validation of the DIODE detector in proton therapy has confirmed that the use of single-crystal synthetic diamond detectors is a reliable solution for the simultaneous dosimetric and microdosimetric evaluation of clinical proton beams. The detector exhibited very good linearity, minimal LET dependence, and good agreement with the reference EBT3 film dosimeter and MC simulations in both depth-dose and lateral profile measurements. Microdosimetric analysis confirmed the detector ability to resolve lineal energy variations and support model-based RBE assessment along the proton beam, supporting its use as a physical surrogate for biological dose.

One critical challenge in solid-state microdosimetry is the so-called "border effect," which can impact measurement accuracy. The border effect in diamond microdosimeter was characterized and studied as a function of detector thickness, particle atomic number, and particle range, and a model was developed and validated to reproduce the border effect in Monte Carlo simulations. The results showed significant variations of up to 40% in $\bar{y}_F$ and 20% in $\bar{y}_D$ values.

One of the future improvements on the DIODE detector is optimizing the range of the acquisition chain to fully capture the rare high LET secondary particles. This will lead to an improvement in sensitivity to the complete radiation field. Future tests on clinical beams using other ion beams, such as carbon or helium ions, are in progress to further validate the performance of the DIODE system.

On the other hand, the concept behind the SEGNAR project could open new perspectives in theranostics, serving as a proof of concept for a conjugated AuNRs – radiopharmaceutical system for diagnosis and therapy. ^{99m}Tc was selected as the radionuclide to be combined with AuNRs due to its imaging-friendly characteristics, potential theranostic use, and the limited number of studies in the literature on ^{99m}Tc-AuNRs.

Studying the radiobiological effect of ^{99m}Tc is one of the goals of this thesis. Thanks to Monte Carlo simulations with Geant4-DNA, it was possible to estimate the surviving fractions for this radionuclide, taking into account the protracted dose structure due to its mean lifetime of several hours.

The results show that the fundamental role of nanoparticles does not lie in dose enhancement, but rather in their function as carriers capable of positioning the radionuclide close to the cell nucleus. This localization is essential for exploiting the high LET of Auger electrons, allowing a diagnostic radionuclide already in clinical use to be used in a therapeutic context. The study of a possible synergistic effect through the coordination number can provide initial indications on the concentration of ^{99m}Tc–AuNRs to be used to achieve lethal surviving fractions for the cancer cell. The co-location of multiple sources of ^{99m}Tc on the surface of an AuNR could produce a significant local increase in dose and an increase of the probability of generating complex and lethal DNA damage. This effect increases with the coordination number. However, the slow dose rate allows DNA repair to minimize the synergistic effect. A possible saturation effect (overkill) may occur in domains with small volumes and high dose density. The integration of the temporal structure of irradiation through the MCt-MKM model has shown that neglecting dose protraction would lead to an overestimation of biological damage.

Currently, the MCt-MKM does not explicitly include this saturation effect. Future developments of the model should integrate it to avoid potential overestimations of the biological effects of the irradiation. It will be crucial to work toward experimental validation of SEGNAR results through in vitro biological studies.

The work carried out in this thesis represents a significant advance in the quality assurance of proton therapy and targeted radionuclide therapy.

The ability of DIODE to provide accurate measurements of absorbed dose and to derive LET and RBE through microdosimetric analysis represents a significant advancement for beam quality assessment in proton therapy. The device will allow more accurate and reliable dosimetry for Treatment Planning System (TPS) commissioning and treatment plan verification. It will also contribute to reducing uncertainties in radiobiological calculations performed by the TPS and to improving their robustness. Finally, the positive outcomes of this research may lead to the definition of a new standard for the use of solid-state microdosimeters in hadrontherapy.

The theranostic system under study with a ^{99m}Tc-based radiopharmaceutical could be, in the future, converted and used with other toxic radiopharmaceuticals using specially designed nanomaterials. This allows the creation of a self-referential system in which the nanostructures suitably functionalized for a specific target and a specific radiopharmaceutical will work in a synergistic mode, opening up new perspectives in theranostics. Further developments will see this theranostic system refined through functionalization with a modified TAT peptide to allow targeted transport of the radiopharmaceutical (AuNRs-TAT-^{99m}Tc-SestaMIBI) into the nucleus of the tumor cell.

Bibliography

[1] S. Agosteo et al. "Monte Carlo and microdosimetry in particle radiotherapy". In: *Monte Carlo in Heavy Charged Particle Therapy*. 2023, pp. 120–134. DOI: 10.1201/9781003023920-9. URL: https://doi.org/10.1201/9781003023920-9.

[2] S. et al. Agostinelli. "Geant4 – a simulation toolkit". In: *Nuclear Instruments and Methods in Physics Research Section A* 506.3 (2003), pp. 250–303. DOI: 10.1016/S0168-9002(03)01368-8.

[3] J. et al. Allison. "Geant4 developments and applications". In: *IEEE Transactions on Nuclear Science* 53.1 (2006), pp. 270–278. DOI: 10.1109/TNS.2006.869826.

[4] J. et al. Allison. "Recent developments in Geant4". In: *Nuclear Instruments and Methods in Physics Research Section A* 835 (2016), pp. 186–225. ISSN: 0168-9002. DOI: 10.1016/j.nima.2016.06.125. URL: https://www.sciencedirect.com/science/article/pii/S0168900216306957.

[5] S. Almaviva and et al. "Extreme UV single crystal diamond Schottky photodiode in planar and transverse configuration". In: *Diamond and Related Materials* 19.1 (2010), pp. 78–82. ISSN: 0925-9635. DOI: 10.1016/j.diamond.2009.11.007.

[6] S. Almaviva et al. "Chemical vapor deposition diamond based multilayered radiation detector: Physical analysis of detection properties". In: *Journal of Applied Physics* 107.1 (Jan. 2010), p. 014511. ISSN: 0021-8979. DOI: 10.1063/1.3275501. eprint: https://pubs.aip.org/aip/jap/article-pdf/doi/10.1063/1.3275501/13649977/014511_1_online.pdf. URL: https://doi.org/10.1063/1.3275501.

[7] E. Amato et al. "Internal Radiation Dosimetry: Models and Applications". In: *12 Chapters on Nuclear Medicine*. Ed. by A. Gholamrezanezhad. InTech, 2011. Chap. 2, pp. 25–46. URL: https://www.intechopen.com/chapters/25566.

[8] S. E. Anderson and et al. "Microdosimetric measurements of a clinical proton beam with micrometer-sized solid-state detector". In: *Medical Physics* 44.11 (2017), pp. 6029–6037. ISSN: 2473-4209. DOI: 10.1002/mp.12583. URL: https://www.ncbi.nlm.nih.gov/pubmed/28905399.

[9] K. Ando et al. "Biological gain of carbon-ion radiotherapy for the early response of tumor growth delay and against early response of skin reaction in mice". In: *Journal of Radiation Research* 46 (2005), pp. 51–57.

[10] K. Ando et al. "Mouse skin reactions following fractionated irradiation with carbon ions". In: *International Journal of Radiation Biology* 74 (1998), pp. 129–138.

[11] P. Andreo. "Monte Carlo techniques in medical radiation physics". In: *Physics in Medicine and Biology* 36.7 (July 1991). Erratum in: Phys Med Biol. 1992 Oct;37(10):2031–2032, pp. 861–920. DOI: 10.1088/0031-9155/36/7/001.

[12] Z. Anjomani and et al. "Development of a multi-element microdosimetric detector based on a thick gas electron multiplier". In: *Nuclear Instruments and Methods in Physics Research Section A: Accelerators, Spectrometers, Detectors and Associated Equipment* 847 (2017), pp. 117–124. ISSN: 0168-9002. DOI: 10.1016/j.nima.2016.11.051.

[13] Z. Anjomani and et al. "Monte Carlo design study for thick gas electron multiplier-based multi-element microdosimetric detector". In: *Nuclear Instruments and Methods in Physics Research Section A: Accelerators, Spectrometers, Detectors and Associated Equipment* 757 (2014), pp. 67–74. ISSN: 0168-9002. DOI: 10.1016/j.nima.2014.04.063.

[14] Anon. *Microdosimetry. ICRU report 36*. International Commission on Radiation Units and Measurements., Jan. 2025.

[15] *Avogadro: an open-source molecular builder and visualization tool*. http://avogadro.cc/. Version 1.2.0. 2025.

[16] Sarah Baatout, ed. *Radiobiology Textbook*. Springer, 2023, pp. XXVII–667. ISBN: 978-3-031-18809-1. DOI: 10.1007/978-3-031-18810-7.

[17] D. L. Bailey et al. *Nuclear Medicine Physics: A Handbook for Teachers and Students*. Endorsed by AAPM, AFOMP, ACPSEM, EFOMP, FAMPO, WFNMB. Vienna: International Atomic Energy Agency, 2014.

[18] F. Belli et al. "RBE-LET relationships for cell inactivation and mutation induced by low energy protons in V79 cells: further results at the LNL facility". In: *International Journal of Radiation Biology* 74.4 (1998), pp. 501–509. DOI: 10.1080/095530098141375.

[19] V. E. Bellinzona et al. "Linking Microdosimetric Measurements to Biological Effectiveness in Ion Beam Therapy: A Review of Theoretical Aspects of MKM and Other Models". In: *Frontiers in Physics* 8 (2021), p. 578492. DOI: 10.3389/fphy.2020.578492.

[20] K. T. Bennett et al. "Large-scale production of ^{119m}Te and ^{119}Sb for radiopharmaceutical applications". In: *ACS Central Science* 5 (2019), pp. 494–505. DOI: 10.1021/acscentsci.8b00869.

[21] M.A. Bernal et al. "Track structure modeling in liquid water: A review of the Geant4-DNA very low energy extension of the Geant4 Monte Carlo simulation toolkit". In: *Physica Medica* 31.8 (2015), pp. 861–874. DOI: 10.1016/j.ejmp.2015.10.087.

[22] P. Bernhardt et al. "Low-energy electron emitters for targeted radiotherapy of small tumours". In: *Acta Oncologica* 40 (2001), pp. 602–608. DOI: 10.1080/028418601750444141.

[23] A Bianchi et al. "Microdosimetry of a 62-MeV clinical proton beam with five detectors". In: *Radiation Protection Dosimetry* 199.15-16 (Oct. 2023), pp. 1968–1972.

[24] A. Bianchi et al. "TOPAS simulations of the response of a mini-TEPC: benchmark with experimental data". In: *Physics in Medicine and Biology* 68.3 (2023). DOI: 10.1088/1361-6560/acabfe.

[25] Anna Bianchi et al. "Microdosimetry with a mini-TEPC in the spread-out Bragg peak of 148 MeV protons". In: *Radiation Physics and Chemistry* 202 (2023), p. 110567. ISSN: 0969-806X. DOI: https://doi.org/10.1016/j.radphyschem.2022.110567. URL: https://www.sciencedirect.com/science/article/pii/S0969806X2200603X.

[26] Anna Bianchi et al. "TOPAS simulations of the response of a mini-TEPC: benchmark with experimental data". In: *Physics in Medicine & Biology* 68 (Jan. 2023). DOI: 10.1088/1361-6560/acabfe.

[27] L. Binelli et al. "Gold Nanorods as Radiopharmaceutical Carriers: Preparation and Preliminary Radiobiological In Vitro Tests". In: *Nanomaterials* 13.13 (2023), p. 1898. DOI: 10.3390/nano13131898.

[28] L. Bodei et al. "Radionuclide therapy with iodine-125 and other Auger-electron-emitting radionuclides: experimental models and clinical applications". In: *Cancer Biotherapy & Radiopharmaceuticals* 18 (2003), pp. 861–877. DOI: 10.1089/108497803322702833.

[29] D. Bolst and et al. "Validation of Geant4 for silicon microdosimetry in heavy ion therapy". In: *Physics in Medicine and Biology* 65.4 (2020), p. 045014. ISSN: 1361-6560. DOI: 10.1088/1361-6560/ab586a. URL: https://www.ncbi.nlm.nih.gov/pubmed/31739291.

[30] D. Bortot and et al. "A miniaturized alpha spectrometer for the calibration of an avalanche-confinement TEPC". In: *Radiation Measurements* 106 (2017), pp. 531–537. ISSN: 1350-4487. DOI: 10.1016/j.radmeas.2017.01.015.

[31] D. Bortot and et al. "A nano-microdosimetric characterization of a therapeutic carbon ion beam at CNAO". In: *Radiation Physics and Chemistry* 170 (2020). ISSN: 0969-806X. DOI: 10.1016/j.radphyschem.2019.108674.

[32] D. Bortot and et al. "A novel avalanche-confinement TEPC for microdosimetry at nanometric level". In: *Radiation Measurements* 103 (2017), pp. 1–12. ISSN: 1350-4487. DOI: 10.1016/j.radmeas.2017.06.012.

[33] Adrie J. J. Bos. "Fundamentals of Radiation Dosimetry". In: *AIP Conference Proceedings* 1345.1 (2011), pp. 5–23. DOI: 10.1063/1.3576156.

[34] C. Andrew Boswell and Martin W. Brechbiel. "Auger Electrons: Lethal, Low Energy, and Coming Soon to a Tumor Cell Nucleus Near You". In: *Journal of Nuclear Medicine* 46.12 (2005), pp. 1946–1947. ISSN: 0161-5505. eprint: https://jnm.snmjournals.org/content/46/12/1946.full.pdf. URL: https://jnm.snmjournals.org/content/46/12/1946.

[35] L. A. Braby et al. "ICRU Report 98, Stochastic Nature of Radiation Interactions: Microdosimetry". In: *Journal of the ICRU* 23.1 (2023), pp. 1–168. DOI: 10.1177/14736691231211380.

[36] D. J. Brenner. "The linear-quadratic model is an appropriate methodology for determining isoeffective doses at large doses per fraction". In: *Seminars in Radiation Oncology* 18.4 (Oct. 2008), pp. 234–239. DOI: 10.1016/j.semradonc.2008.04.004.

[37] D. J. Brenner et al. "The Linear-Quadratic Model and Most Other Common Radiobiological Models Result in Similar Predictions of Time-Dose Relationships". In: *Radiation Research* 150.1 (1998), pp. 83–91. ISSN: 00337587, 19385404. URL: http://www.jstor.org/stable/3579648 (visited on 10/30/2025).

[38] Scott H. Britz-Cunningham and S. James Adelstein. "Molecular Targeting with Radionuclides: State of the Science". In: *Journal of Nuclear Medicine* 44.12 (2003), pp. 1945–1961. ISSN: 0161-5505. eprint: https://jnm.snmjournals.org/content/44/12/1945.full.pdf. URL: https://jnm.snmjournals.org/content/44/12/1945.

[39] R. Brun and F. Rademakers. "ROOT – An Object Oriented Data Analysis Framework". In: *Nuclear Instruments and Methods in Physics Research Section A* 389 (1997). Proceedings AIHENP'96 Workshop, Lausanne, Sep. 1996, pp. 81–86.

[40] Brian J Burkett et al. "A review of theranostics: perspectives on emerging approaches and clinical advancements". In: *Radiology: Imaging Cancer* 5.4 (2023), e220157.

[41] T. T. Böhlen et al. "Benchmarking nuclear models of FLUKA and GEANT4 for hadron therapy". In: *Physics in Medicine and Biology* 55.19 (2010), pp. 5833–5847. DOI: 10.1088/0031-9155/55/19/014.

[42] Cancer Research UK. *Cancer statistics for the UK: Survival*. https://www.cancerresearchuk.org/health-professional/cancer-statistics/survival. Accessed: 2025-12-17. 2025.

[43] Giorgio Giuseppe Carbone et al. "Exploring the Potential of Gold Nanoparticles in Proton Therapy: Mechanisms, Advances, and Clinical Horizons". In: *Pharmaceutics* 17.2 (2025). ISSN: 1999-4923. DOI: 10.3390/pharmaceutics17020176. URL: https://www.mdpi.com/1999-4923/17/2/176.

[44] E. Casals et al. "Hardening of the Nanoparticle–Protein Corona in Metal (Au, Ag) and Oxide (Fe_3O_4, CoO, and CeO_2) Nanoparticles". In: *Small* 7 (2011), pp. 3479–3486. DOI: 10.1002/smll.201101318.

[45] V. Cesari and et al. "Nanodosimetric measurements with an avalanche confinement TEPC". In: *Radiation Protection Dosimetry* 99.1-4 (2002), pp. 337–342. ISSN: 0144-8420. DOI: 10.1093/oxfordjournals.rpd.a006796. URL: https://www.ncbi.nlm.nih.gov/pubmed/12194318.

[46] L. Chartier and et al. "New silicon microdosimetry probes for RBE and biological dose studies using stationary and movable targets in 12C ion therapy". In: *Journal of Physics: Conference Series* 777 (2017). ISSN: 1742-6588, 1742-6596. DOI: 10.1088/1742-6596/777/1/012019.

[47] Pankaj Chaudhary et al. "Relative Biological Effectiveness Variation Along Monoenergetic and Modulated Bragg Peaks of a 62-MeV Therapeutic Proton Beam: A Preclinical Assessment". In: *International Journal of Radiation Oncology, Biology, Physics* 90.1 (2014), pp. 27–35.

[48] R. Chechik and et al. "Thick GEM-like hole multipliers: properties and possible applications". In: *Nuclear Instruments and Methods in Physics Research Section A: Accelerators, Spectrometers, Detectors and Associated Equipment* 535.1-2 (2004), pp. 303–308. ISSN: 0168-9002. DOI: 10.1016/j.nima.2004.07.138.

[49] R. Chechik, A. Breskin, and C. Shalem. "Thick GEM-like multipliers—a simple solution for large area UV-RICH detectors". In: *Nuclear Instruments and Methods in Physics Research Section A: Accelerators, Spectrometers, Detectors and Associated Equipment* 553.1-2 (2005), pp. 35–40. ISSN: 0168-9002. DOI: 10.1016/j.nima.2005.08.003.

[50] Y. Chen et al. "Gold Nanoparticles as Radiosensitizers in Cancer Radiotherapy". In: *International Journal of Nanomedicine* 15 (2020), pp. 9407–9430. DOI: 10.2147/IJN.S272902.

[51] D. B. Chithrani, S. Jelveh, F. Jalali, et al. "Gold nanoparticles as radiation sensitizers in cancer therapy". In: *Radiation Research* 173.6 (2010), pp. 719–728.

[52] G. Cirrone and G. Petringa. *Monte Carlo in Heavy Charged Particle Therapy*. 2023. DOI: 10.1201/9781003023920. URL: https://doi.org/10.1201/9781003023920.

[53] F. Coccetti. "The Fermiac or Fermi's Trolley". In: *Il Nuovo Cimento C* 39.2 (2016). DOI: 10.1393/ncc/i2016-16296-7.

[54] P. Colautti and et al. "Microdosimetric Study at the CNAO Active-Scanning Carbon-Ion Beam". In: *Radiation Protection Dosimetry* 180.1-4 (2018), pp. 157–161. ISSN: 1742-3406. DOI: 10.1093/rpd/ncx217. URL: https://www.ncbi.nlm.nih.gov/pubmed/29087524.

[55] Stephanie E. Combs et al. "Treatment of pediatric patients and young adults with particle therapy at the Heidelberg Ion Therapy Center (HIT): establishment of workflow and initial clinical data". In: *Radiation Oncology* 7.1 (2012), p. 170. DOI: 10.1186/1748-717X-7-170.

[56] V. Conte and et al. "Microdosimetry at the CATANA 62 MeV proton beam with a sealed miniaturized TEPC". In: *Physica Medica* 64 (2019), pp. 114–122. ISSN: 1724-191X. DOI: 10.1016/j.ejmp.2019.06.011. URL: https://www.ncbi.nlm.nih.gov/pubmed/31515010.

[57] V. Conte and et al. "Microdosimetry of a therapeutic proton beam with a mini-TEPC and a MicroPlus-Bridge detector for RBE assessment". In: *Physics in Medicine and Biology* (2020). ISSN: 1361-6560. DOI: 10.1088/1361-6560/abc368. URL: https://www.ncbi.nlm.nih.gov/pubmed/33086208.

[58] Bart Cornelissen and Katherine A. Vallis. "Targeting the nucleus: an overview of Auger-electron radionuclide therapy". In: *Current Drug Discovery Technologies* 7.4 (2010), pp. 263–279. DOI: 10.2174/157016310793360657.

[59] G. Coutrakon et al. "A prototype beam delivery system for the proton medical accelerator at Loma Linda". In: *Medical Physics* 18.6 (1991), pp. 1093–1099. DOI: 10.1118/1.596617.

[60] L. Cui et al. "Radiosensitization by gold nanoparticles: will they ever make it to the clinic?" In: *Radiotherapy and Oncology* 124.3 (2017), pp. 344–356. DOI: 10.1016/j.radonc.2017.07.007.

[61] R. G. Dale et al. "Practical methods for compensating for missed treatment days in radiotherapy, with particular reference to head and neck schedules". In: *Clinical Oncology* 14.5 (2002), pp. 382–393. DOI: 10.1053/clon.2002.0111.

[62] A. Dash, M. R. Pillai, and Jr. Knapp F. F. "Production of ^{177}Lu for targeted radionuclide therapy: available options". In: *Nuclear Medicine and Molecular Imaging* 49 (2015), pp. 85–107. DOI: 10.1007/s13139-014-0315-z.

[63] J. A. Davis and et al. "A 3D lateral electrode structure for diamond based microdosimetry". In: *Applied Physics Letters* 110.1 (2017). ISSN: 0003-6951. DOI: 10.1063/1.4973628.

[64] J. A. Davis and et al. "Characterization of a Novel Diamond-Based Microdosimeter Prototype for Radioprotection Applications in Space Environments". In: *IEEE Transactions on Nuclear Science* 59.6 (2012), pp. 3110–3116. ISSN: 0018-9499. DOI: 10.1109/tns.2012.2218131.

[65] J. A. Davis and et al. "Characterization of an Alternative Diamond Based Microdosimeter Prototype". In: *IEEE Transactions on Nuclear Science* 61.6 (2014), pp. 3479–3484. ISSN: 0018-9499. DOI: 10.1109/tns.2014.2354433.

[66] J. A. Davis and et al. "Evolution of Diamond based Microdosimetry". In: *Journal of Physics: Conference Series* 1154 (2019). ISSN: 1742-6588. DOI: 10.1088/1742-6596/1154/1/012007.

[67] L. De Nardo and et al. "Microdosimetric characterisation of a therapeutic proton beam used for conjunctival melanoma treatments". In: *Radiation Measurements* 45.10 (2010), pp. 1387–1390. ISSN: 1350-4487. DOI: 10.1016/j.radmeas.2010.05.034.

[68] L. De Nardo and et al. "Mini-TEPCs for radiation therapy". In: *Radiation Protection Dosimetry* 108.4 (2004), pp. 345–352. ISSN: 0144-8420. DOI: 10.1093/rpd/nch023. URL: https://www.ncbi.nlm.nih.gov/pubmed/15103064.

[69] L. De Nardo and M. Farahmand. "Operation of gas electron multiplier (GEM) with propane gas at low pressure and comparison with tissue-equivalent gas mixtures". In: *Nuclear Instruments and Methods in Physics Research Section A: Accelerators, Spectrometers, Detectors and Associated Equipment* 819 (2016), pp. 154–162. ISSN: 0168-9002. DOI: 10.1016/j.nima.2016.02.096.

[70] Laura De Nardo et al. "Microdosimetric Assessment of Nice Therapeutic Proton Beam Biological Quality". In: *Physica Medica: European Journal of Medical Physics* XX.2 (2004), pp. 1–8. URL: https://digital.casalini.it/10.1400/19291.

[71] E. Debrot and et al. "SOI microdosimetry and modified MKM for evaluation of relative biological effectiveness for a passive proton therapy radiation field". In: *Physics in Medicine and Biology* 63.23 (2018), p. 235007. ISSN: 1361-6560. DOI: 10.1088/1361-6560/aaec2f. URL: https://www.ncbi.nlm.nih.gov/pubmed/30468682.

[72] J. F. Dicello and et al. "A Comparison of Microdosimetric Measurements with Spherical Proportional Counters and Solid-State Detectors". In: *Radiation Research* 82.3 (1980). ISSN: 0033-7587. DOI: 10.2307/3575311.

[73] M. Dingfelder. "Track-Structure Simulations for Charged Particles". In: *Health Physics* 103.5 (Nov. 2012), pp. 590–595. DOI: 10.1097/HP.0b013e3182621292.

[74] Manjit Dosanjh et al. "Multidisciplinary Collaboration and Novel Technological Advances in Hadron Therapy". In: *Technology in Cancer Research & Treatment* 24 (2025). PMID: 39895029, p. 15330338241311859. DOI: 10.1177/15330338241311859. eprint: https://doi.org/10.1177/15330338241311859. URL: https://doi.org/10.1177/15330338241311859.

[75] M. Durante and J. S. Loeffler. "Charged particles in radiation oncology". In: *Nature Reviews Clinical Oncology* 7.1 (2010), pp. 37–43. DOI: 10.1038/nrclinonc.2009.183.

[76] Marco Durante and Harald Paganetti. "Nuclear physics in particle therapy: a review". In: *Reports on Progress in Physics* 79.9 (2016), p. 096702. DOI: 10.1088/0034-4885/79/9/096702. URL: https://doi.org/10.1088/0034-4885/79/9/096702.

[77] Roger Eckhardt. "Stan Ulam, John von Neumann, and the Monte Carlo Method". In: *Los Alamos Science* (1987). Special Issue, Los Alamos National Laboratory, LA-UR-88-9067, pp. 131–141.

[78] Ameer L. Elaimy et al. "History and Overview of Proton Therapy". In: *Proton Therapy - Current Status and Future Directions*. Ed. by Thomas J. FitzGerald and Maryann Bishop-Jodoin. London: IntechOpen, 2021. Chap. 1. DOI: 10.5772/intechopen.95959. URL: https://doi.org/10.5772/intechopen.95959.

[79] Thilo Elsässer, Michael Krämer, and Michael Scholz. "Accuracy of the Local Effect Model for the prediction of biologic effects of carbon ion beams in vitro and in vivo". In: *International Journal of Radiation Oncology*Biology*Physics* 71.3 (2008), pp. 866–872. DOI: 10.1016/j.ijrobp.2008.02.037.

[80] Th. Elsässer and M. Scholz. "Improvement of the local effect model (LEM)—implications of clustered DNA damage". In: *Radiation Protection Dosimetry* 122.1-4 (Dec. 2006), pp. 475–477. ISSN: 0144-8420. DOI: 10.1093/rpd/ncl521. eprint: https://academic.oup.com/rpd/article-pdf/122/1-4/475/9582463/ncl521.pdf. URL: https://doi.org/10.1093/rpd/ncl521.

[81] D. Ersahin, I. Doddamane, and D. Cheng. "Targeted radionuclide therapy". In: *Cancers* 3.4 (2011), pp. 3838–3855. DOI: 10.3390/cancers3043838.

[82] S. Esteban. "Development of Advanced Silicon Sensors for Neutron Detection and Microdosimetry". PhD thesis. PhD Thesis, 2016.

[83] M. Farahmand and et al. "Design of a new tissue-equivalent proportional counter based on a gas electron multiplier". In: *Nuclear Instruments and Methods in Physics Research Section A: Accelerators, Spectrometers, Detectors and Associated Equipment* 509.1-3 (2003), pp. 262–267. ISSN: 0168-9002. DOI: 10.1016/s0168-9002(03)01636-x.

[84] A. Ferrari et al. *FLUKA: A Multi-Particle Transport Code*. Tech. rep. SLAC-R-773. Menlo Park, CA, United States: SLAC National Accelerator Laboratory, 2005. DOI: 10.2172/877507. URL: https://www.osti.gov/biblio/877507.

[85] V. Ferrero et al. "Targeted dose enhancement in radiotherapy for breast cancer using gold nanoparticles, part 1: A radiobiological model study". In: *Medical Physics* 44.5 (May 2017), pp. 1983–1992. DOI: 10.1002/mp.12180.

[86] C. Fleta and et al. "3D cylindrical silicon microdosimeters: fabrication, simulation and charge collection study". In: *Journal of Instrumentation* 10.10 (2015), P10001. ISSN: 1748-0221. DOI: 10.1088/1748-0221/10/10/p10001.

[87] M. Folkard. "Inactivation of V79 cells by low-energy protons, deuterons and helium-3 ions". In: *International Journal of Radiation Biology* 69.6 (1996), pp. 729–738. DOI: 10.1080/095530096145472.

[88] P. Fossati et al. "Dose prescription in carbon ion radiotherapy: a planning study to compare NIRS and LEM approaches with a clinically-oriented strategy". In: *Physics in Medicine and Biology* 57.22 (2012), pp. 7543–7554. DOI: 10.1088/0031-9155/57/22/7543.

[89] Piero Fossati et al. "Radiobiological issues in prospective carbon ion therapy trials". In: *Medical Physics* 45.11 (2018), e1096–e1110. DOI: 10.1002/mp.12506.

[90] Z. Francis et al. "Molecular scale track structure simulations in liquid water using the Geant4-DNA Monte-Carlo processes". In: *Applied Radiation and Isotopes* 69.1 (2011), pp. 220–226. DOI: 10.1016/j.apradiso.2010.08.011.

[91] T. Friedrich et al. "Systematic analysis of RBE and related quantities using a database of cell survival experiments with ion beam irradiation". In: *Journal of Radiation Research* 54 (2012), pp. 494–514.

[92] S. Ftániková and R. Böhm. "Monte Carlo Calculations of Energy Deposition in DNA for Auger Emitters". In: *Radiation Protection Dosimetry* 92.4 (Dec. 2000), pp. 269–278. ISSN: 0144-8420. DOI: 10.1093/oxfordjournals.rpd.a033292. eprint: https://academic.oup.com/rpd/article-pdf/92/4/269/9932390/269.pdf. URL: https://doi.org/10.1093/oxfordjournals.rpd.a033292.

[93] Karuna Ganesh and Joan Massagué. "Targeting metastatic cancer". In: *Nature medicine* 27.1 (2021), pp. 34–44.

[94] Geant4 Collaboration. *Geant4 Guide for Physics Lists*. Version 11.4. Last accessed: 2025-12-11. 2024. URL: https://geant4-userdoc.web.cern.ch/UsersGuides/PhysicsListGuide/html/index.html.

[95] *Geant4 Physics Reference Manual*. Revision 9.0: Geant4 Release 11.3. Geant4 Collaboration. Dec. 2024. URL: https://geant4.web.cern.ch/.

[96] G. Gervino and et al. "Dosimetry with diamond detectors". In: *Nuclear Instruments and Methods in Physics Research Section A: Accelerators, Spectrometers, Detectors and Associated Equipment* 617.1-3 (2010), pp. 230–231. ISSN: 0168-9002. DOI: 10.1016/j.nima.2009.09.103.

[97] S. K. Ghosh et al. "Solvent and Ligand Effects on the Localized Surface Plasmon Resonance (LSPR) of Gold Colloids". In: *Journal of Physical Chemistry B* 108 (2004), pp. 13963–13971. DOI: 10.1021/jp048296p.

[98] G. Giovannini, T. Böhlen, G. Cabal, et al. "Variable RBE in proton therapy: comparison of different model predictions and their influence on clinical-like scenarios". In: *Radiation Oncology* 11 (2016), p. 68. DOI: 10.1186/s13014-016-0642-6.

[99] S. J. Goldsmith. "Targeted radionuclide therapy: A historical and personal review". In: *Seminars in Nuclear Medicine* 50 (2020), pp. 87–97. DOI: 10.1053/j.semnuclmed.2019.07.006.

[100] F. Gomez and et al. "Measurement of carbon ion microdosimetric distributions with ultrathin 3D silicon diodes". In: *Physics in Medicine and Biology* 61.11 (2016), pp. 4036–4047. ISSN: 1361-6560. DOI: 10.1088/0031-9155/61/11/4036. URL: https://www.ncbi.nlm.nih.gov/pubmed/27163881.

[101] Bernard Gottschalk. *Radiotherapy Proton Interactions in Matter*. 2018. arXiv: 1804.00022 [physics.med-ph]. URL: https://arxiv.org/abs/1804.00022.

[102] N. Gracheva et al. "Production and characterization of no-carrier-added ^{161}Tb as an alternative to the clinically-applied ^{177}Lu for radionuclide therapy". In: *EJNMMI Radiopharmacy and Chemistry* 4 (2019), p. 12. DOI: 10.1186/s41181-019-0063-6.

[103] GL Griffiths et al. "Cytotoxicity with Auger electron-emitting radionuclides delivered by antibodies". In: *Int J Cancer* 81.6 (1999), pp. 985–992. DOI: 10.1002/(sici)1097-0215(19990611)81:6<985::aid-ijc23>3.0.co;2-w.

[104] J. Grudzinski et al. "CLR ^{125}Auger electrons for the targeted radiotherapy of triple-negative breast cancer". In: *Cancer Biotherapy & Radiopharmaceuticals* 33 (2018), pp. 87–95. DOI: 10.1089/cbr.2017.2376.

[105] J. Grünberg et al. "Anti-L1CAM radioimmunotherapy is more effective with the radiolanthanide ^{161}Tb compared to ^{177}Lu in an ovarian cancer model". In: *European Journal of Nuclear Medicine and Molecular Imaging* 41 (2014), pp. 1907–1915. DOI: 10.1007/s00259-014-2798-3.

[106] F. Guan, X. Wang, M. Yang, et al. "Dosimetric response of Gafchromic™ EBT-XD film to therapeutic protons". In: *Precision Radiation Oncology* 7 (2023), pp. 15–26. DOI: 10.1002/pro6.1187.

[107] F. Guan et al. "Spatial mapping of the biologic effectiveness of scanned particle beams: towards biologically optimized particle therapy". In: *Scientific Reports* 5 (2015), p. 9850. DOI: 10.1038/srep09850.

[108] C. Guardiola. "Novel Silicon Sensors for Neutron Detection". PhD thesis. PhD Thesis, 2012.

[109] C. Guardiola and et al. "Preliminary microdosimetric measurements with ultra-thin 3D silicon detectors of a 62 MeV proton beam". In: *Journal of Instrumentation* 10.01 (2015), P01008. ISSN: 1748-0221. DOI: 10.1088/1748-0221/10/01/p01008.

[110] C. Guardiola and et al. "Silicon 3D Microdetectors for Microdosimetry in Hadron Therapy". In: *Micromachines (Basel)* 11.12 (2020). ISSN: 2072-666X. DOI: 10.3390/mi11121053. URL: https://www.ncbi.nlm.nih.gov/pubmed/33260634.

[111] C. Guardiola and et al. "Silicon-based three-dimensional microstructures for radiation dosimetry in hadrontherapy". In: *Applied Physics Letters* 107.2 (2015). ISSN: 0003-6951. DOI: 10.1063/1.4926962.

[112] S. V. Gudkov et al. "Targeted Radionuclide Therapy of Human Tumors". In: *International Journal of Molecular Sciences* 17.1 (2015), p. 33. DOI: 10.3390/ijms17010033.

[113] Z. Guo, S. Zhu, Y. Yong, et al. "Synthesis of BSA-coated BiOI@Bi_2S_3 semiconductor heterojunction nanoparticles and their applications for radio/photodynamic/phototherm synergistic therapy of tumor". In: *Advanced Materials* 29.44 (2017), p. 1704136. DOI: 10.1002/adma.201704136.

[114] G Sgouros H. Zaidi. *Therapeutic Applications of Monte Carlo Calculations in Nuclear Medicine (Series in Medical Physics and Biomedical Engineering)*. 1st ed. Taylor & Francis, 2002. ISBN: 0750308168; 9780750308168. URL: libgen.li/file.php?md5=2c4a7dfc4b6d0c3ecc58790b0135257a.

[115] P Häfliger et al. "Induction of DNA-double-strand breaks by auger electrons from 99mTc complexes with DNA-binding ligands". In: *Chembiochem* 6.2 (2005), pp. 414–421. DOI: 10.1002/cbic.200400210.

[116] E. J. Hall and A. J. Giaccia. *Radiobiology for the Radiologist*. 7th ed. Philadelphia: Lippincott Williams & Wilkins, 2011.

[117] E. J. Hall et al. "The Relative Biological Effectiveness of 160 MeV Protons–II. Biological Data and Their Interpretation in Terms of Microdosimetry". In: *International Journal of Radiation Oncology Biology Physics* 4.11–12 (1978), pp. 1009–1013. DOI: 10.1016/0360-3016(78)90013-5.

[118] S. Haller et al. "Contribution of Auger/conversion electrons to renal side effects after radionuclide therapy: preclinical comparison of ^{161}Tb-folate and ^{177}Lu-folate". In: *EJNMMI Research* 6 (2016), p. 13. DOI: 10.1186/s13550-016-0171-1.

[119] S. Han and et al. "Study on the RBE estimation for carbon beam scanning irradiation using a solid-state microdosimeter". In: *Medical Physics* 47.2 (2020), pp. 363–370. ISSN: 2473-4209. DOI: 10.1002/mp.13924. URL: https://www.ncbi.nlm.nih.gov/pubmed/31732963.

[120] Marcus D. Hanwell et al. "Avogadro: An advanced semantic chemical editor, visualization, and analysis platform". In: *Journal of Cheminformatics* 4.1 (2012), p. 17. DOI: 10.1186/1758-2946-4-17.

[121] R. B. Hawkins. "A Microdosimetric-Kinetic Theory of the Dependence of the RBE for Cell Death on LET". In: *Medical Physics* 25.7 (1998), pp. 1157–1170. DOI: 10.1118/1.598307.

[122] Robert B. Hawkins. "A microdosimetric-kinetic model of cell death from exposure to ionizing radiation of any LET, with experimental and clinical applications". In: *International Journal of Radiation Biology* 69.6 (1996), pp. 739–755.

[123] Roland B. Hawkins. "A Statistical Theory of Cell Killing by Radiation of Varying Linear Energy Transfer". In: *Radiation Research* 140.3 (1994). Accessed 17 Oct. 2025, pp. 366–374. DOI: 10.2307/3579114. URL: https://doi.org/10.2307/3579114.

[124] S. Her, D. A. Jaffray, and C. Allen. "Gold nanoparticles for applications in cancer radiotherapy: mechanisms and recent advancements". In: *Advanced Drug Delivery Reviews* 109 (2017), pp. 84–101. DOI: 10.1016/j.addr.2015.12.012.

[125] C. M. Hsieh, P. C. Murley, and R. R. O'Brien. "A field-funneling effect on the collection of alpha-particle-generated carriers in silicon devices". In: *IEEE Electron Device Letters* 2.4 (1981), pp. 103–105. ISSN: 0741-3106. DOI: 10.1109/edl.1981.25357.

[126] D. M. V. Huizing et al. "Dosimetry methods and clinical applications in peptide receptor radionuclide therapy for neuroendocrine tumours: a literature review". In: *EJNMMI Research* 8.1 (2018), p. 89. DOI: 10.1186/s13550-018-0443-z. URL: https://doi.org/10.1186/s13550-018-0443-z.

[127] J L Humm and D E Charlton. "A new calculational method to assess the therapeutic potential of Auger electron emission". In: *International Journal of Radiation Oncology, Biology and Physics; (USA)* 17:2 (Aug. 1989). ISSN: ISSN 0360-3016. DOI: 10.1016/0360-3016(89)90450-1. URL: https://www.osti.gov/biblio/5669985.

[128] Chi-Ok Hwang et al. "Buffon's Needle Algorithm to Estimate π". In: *Applied Mathematics* 08 (Jan. 2017), pp. 275–279. DOI: 10.4236/am.2017.83022.

[129] T. Inaniwa et al. "Effects of Dose-Delivery Time Structure on Biological Effectiveness for Therapeutic Carbon-Ion Beams Evaluated with Microdosimetric Kinetic Model". In: *Radiation Research* 180.1 (2013). Epub 2013 Jun 14, pp. 44–59. DOI: 10.1667/RR3178.1. URL: https://doi.org/10.1667/RR3178.1.

[130] Taku Inaniwa et al. "Effects of beam interruption time on tumor control probability in single-fractionated carbon-ion radiotherapy for non-small cell lung cancer". In: *Physics in Medicine and Biology* 60.10 (2015), pp. 4105–4121. DOI: 10.1088/0031-9155/60/10/4105.

[131] Taku Inaniwa et al. "Treatment planning for a scanned carbon beam with a modified microdosimetric kinetic model". In: *Physics in Medicine and Biology* 55.22 (2010), pp. 6721–6737. DOI: 10.1088/0031-9155/55/22/008.

[132] S. Incerti et al. "Geant4-DNA example applications for track structure simulations in liquid water: A report from the Geant4-DNA Project". In: *Medical Physics* (June 2018). Epub ahead of print. DOI: 10.1002/mp.13048.

[133] S. Incerti et al. "GEANT4 very low energy cross section models with experimental data in water". In: *Medical Physics* 37.9 (2010), pp. 4692–4708. DOI: 10.1118/1.3476457.

[134] S. Incerti et al. "The Geant4-DNA project". In: (Oct. 2009). DOI: 10.1142/S1793962310000122.

[135] L. Inhester et al. "Auger spectrum of a water molecule after single and double core ionization". In: *The Journal of Chemical Physics* 136.14 (Apr. 2012), p. 144304. ISSN: 0021-9606. DOI: 10.1063/1.3700233. eprint: https://pubs.aip.org/aip/jcp/article-pdf/doi/10.1063/1.3700233/15451343/144304_1_online.pdf. URL: https://doi.org/10.1063/1.3700233.

[136] International Atomic Energy Agency (IAEA). *Relative Biological Effectiveness in Ion Beam Therapy*. Technical Reports Series No. 461. Accessed: 2025-11-09. Vienna: International Atomic Energy Agency, 2008. URL: https://www-pub.iaea.org/MTCD/Publications/PDF/trs461_web.pdf.

[137] International Commission on Radiation Units and Measurements (ICRU). *Prescribing, Recording, and Reporting Proton-Beam Therapy*. Tech. rep. Report 78. Bethesda, MD, USA: International Commission on Radiation Units and Measurements, 2007.

[138] N. R. Jana, L. Gearheart, and C. J. Murphy. "Evidence for Seed-Mediated Nucleation in the Chemical Reduction of Gold Salts to Gold Nanoparticles". In: *Chemistry of Materials* 13 (2001), pp. 2313–2322. DOI: 10.1021/cm000914x.

[139] A. I. Jensen et al. "A solid support generator of the Auger electron emitter rhodium-103m from [^{103}Pd]palladium". In: *Applied Radiation and Isotopes* 156 (2020), p. 108985. DOI: 10.1016/j.apradiso.2019.108985.

[140] Lars Jødal. "Beta emitters and radiation protection". In: *Acta Oncologica* 48.2 (2009), pp. 308–313. DOI: 10.1080/02841860802245163.

[141] Christian P. Karger and Peter Peschke. "RBE and related modeling in carbon-ion therapy". In: *Physics in Medicine and Biology* 63.1 (2018), 01TR02. DOI: 10.1088/1361-6560/aa9102.

[142] Yuki Kase et al. "Microdosimetric approach to NIRS-defined biological dose measurement for carbon-ion treatment beam". In: *Journal of Radiation Research* 52.1 (2011), pp. 59–68.

[143] Yuki Kase et al. "Microdosimetric Measurements and Estimation of Human Cell Survival for Heavy-Ion Beams". In: *Radiation Research* 166.4 (2006), pp. 629–638. DOI: 10.1667/RR0536.1. URL: https://doi.org/10.1667/RR0536.1.

[144] Amin I. Kassis. "The Amazing World of Auger Electrons". In: *International Journal of Radiation Biology* 80.11-12 (2004). PMID: 15764386, pp. 789–803. DOI: 10.1080/09553000400017663. eprint: https://doi.org/10.1080/09553000400017663. URL: https://doi.org/10.1080/09553000400017663.

[145] A. M. Kellerer. "An assessment of wall effects in microdosimetric measurements". In: *Radiation Research* 47 (1971), p. 377. DOI: https://doi.org/10.2307/3573244.

[146] A. M. Kellerer. "Event simultaneity in cavities. Theory of the distortions of energy deposition in proportional counters". In: *Radiation Research* 48 (1971), p. 216. DOI: https://doi.org/10.2307/3573307.

[147] A. M. Kellerer and H. H. Rossi. "A generalized formulation of dual radiation action". In: *Radiation Research* 75.3 (1978), pp. 471–488.

[148] Albrecht M. Kellerer and Harald H. Rossi. "The theory of dual radiation action". In: *Current Topics in Radiation Research Quarterly* 8.2 (1972), pp. 85–158.

[149] J. H. Kim et al. "Phase II trial of anti-epidermal growth factor receptor radioimmunotherapy in the treatment of anaplastic astrocytoma". In: *Journal of Radiation Oncology* 2 (2013), pp. 7–13. DOI: 10.1007/s13566-012-0071-6.

[150] P. J. Kliauga et al. "The Relative Biological Effectiveness of 160 MeV Protons. I. Microdosimetry". In: *International Journal of Radiation Oncology Biology Physics* 4.11–12 (1978), pp. 1001–1008. DOI: 10.1016/0360-3016(78)90012-3.

[151] F. F. Knapp and A. Dash. *Radiopharmaceuticals for Therapy*. New Delhi: Springer, 2016.

[152] Glenn F. Knoll. *Radiation Detection and Measurement*. 3rd ed. John Wiley & Sons, 1999. ISBN: 9780471073383.

[153] K. Kobayashi et al. "Enhancement of radiation effect by heavy elements". In: *Mutation Research* 704.1–3 (2010), pp. 123–131. DOI: 10.1016/j.mrrev.2010.01.002.

[154] A. Kolstad et al. "LYMRIT 37-01: A phase I/II study of ^{177}Lu-lilotomab satetraxetan (Betalutin) antibody-radionuclide-conjugate (ARC) for the treatment of relapsed non-Hodgkin's lymphoma (NHL) – Analysis with 6-month follow-up". In: *Blood* 132 (2018), p. 2879. DOI: 10.1182/blood-2018-99-110555.

[155] Michael Krämer and Michael Scholz. "Treatment planning for heavy-ion radiotherapy: calculation and optimization of biologically effective dose". In: *Physics in Medicine and Biology* 45.11 (2000), pp. 3319–3330. DOI: 10.1088/0031-9155/45/11/314.

[156] Alan Ku et al. "Auger electrons for cancer therapy – a review". In: *EJNMMI Radiopharmacy and Chemistry* 4.1 (2019), p. 27. DOI: 10.1186/s41181-019-0075-2.

[157] P Lazarakis et al. "Investigation of Track Structure and Condensed History physics models for applications in radiation dosimetry on a micro and nano scale in Geant4". In: *Biomedical Physics & Engineering Express* 4 (Feb. 2018). DOI: 10.1088/2057-1976/aaa6aa.

[158] D. E. Lea. *Actions of Radiation on Living Cells*. London: Cambridge University Press, 1946.

[159] D. E. Lea and D. G. Catcheside. "The mechanism of the induction by radiation of chromosome aberrations in *Tradescantia*". In: *Journal of Genetics* 44 (1942), pp. 216–245. DOI: 10.1007/BF02982830. URL: https://doi.org/10.1007/BF02982830.

[160] S. H. Lee and et al. "Estimating the biological effects of helium, carbon, oxygen, and neon ion beams using 3D silicon microdosimeters". In: *Physics in Medicine and Biology* 66.4 (2021), p. 045017. ISSN: 1361-6560. DOI: 10.1088/1361-6560/abd66f. URL: https://www.ncbi.nlm.nih.gov/pubmed/33361575.

[161] S. Lehenberger et al. "The low-energy β^- and electron emitter ^{161}Tb as an alternative to ^{177}Lu for targeted radionuclide therapy". In: *Nuclear Medicine and Biology* 38 (2011), pp. 917–924. DOI: 10.1016/j.nucmedbio.2011.02.007.

[162] J. Leidner and et al. "3D energy deposition measurements with the GEMPix detector in a water phantom for hadron therapy". In: *Journal of Instrumentation* 13.08 (2018), P08009. ISSN: 1748-0221. DOI: 10.1088/1748-0221/13/08/p08009.

[163] J. Linam and L. X. Yang. "Recent developments in radiosensitization". In: *Anticancer Research* 35.5 (2015), pp. 2479–2485.

[164] K. Liu et al. "Protein-directed gold nanoparticles with excellent catalytic activity for 4-nitrophenol reduction". In: *Materials Science and Engineering C: Materials for Biological Applications* 78 (2017), pp. 429–434. DOI: 10.1016/j.msec.2017.04.052.

[165] Michael Ljungberg, Sven-Erik Strand, and Michael A. King, eds. *Monte Carlo Calculations in Nuclear Medicine: Applications in Diagnostic Imaging*. 2nd ed. Series in Nuclear Medicine and Biomedical Engineering. Boca Raton: CRC Press, 2012. ISBN: 9780429151163. DOI: 10.1201/b13073. URL: https://www.taylorfrancis.com/books/edit/10.1201/b13073/monte-carlo-calculations-nuclear-medicine-michael-ljungberg-sven-erik-strand-michael-king.

[166] C.-Y. Lo et al. "Gold-Nanoparticles-Enhanced Production of Reactive Oxygen Species in Cells at Spread-Out Bragg Peak under Proton Beam Radiation". In: *ACS Omega* 8 (2023), pp. 17922–17931. DOI: 10.1021/acsomega.3c01025.

[167] A. J. Lomax. "Intensity modulated proton therapy and its sensitivity to treatment uncertainties 2: the potential effects of inter-fraction and inter-field motions". In: *Physics in Medicine and Biology* 53.4 (2008), pp. 1043–1056. DOI: 10.1088/0031-9155/53/4/015.

[168] T. Loncol et al. "Radiobiological Effectiveness of Radiation Beams with Broad LET Spectra: Microdosimetric Analysis Using Biological Weighting Functions". In: *Radiation Protection Dosimetry* 52.1-4 (1994), pp. 347–352. DOI: 10.1093/oxfordjournals.rpd.a082212.

[169] Y. Lorat et al. "Focused Ion Microbeam Irradiation Induces Clustering of DNA Double-Strand Breaks in Heterochromatin Visualized by Nanoscale-Resolution Electron Microscopy". In: *International Journal of Molecular Sciences* 22 (2021), p. 7638. DOI: 10.3390/ijms22147638.

[170] N. Ma, Y. W. Jiang, X. Zhang, et al. "Enhanced radiosensitization of gold nanospikes via hyperthermia in combined cancer radiation and photothermal therapy". In: *ACS Applied Materials & Interfaces* 8.42 (2016), pp. 28480–28494. DOI: 10.1021/acsami.6b10132.

[171] N. Ma, F. G. Wu, X. Zhang, et al. "Shape-dependent radiosensitization effect of gold nanostructures in cancer radiotherapy: comparison of gold nanoparticles, nanospikes, and nanorods". In: *ACS Applied Materials & Interfaces* 9.15 (2017), pp. 13037–13048.

[172] G. Magrin et al. "Microdosimetric characterization of clinical carbon-ion beams using synthetic diamond detectors and spectral conversion methods". In: *Medical Physics* 47 (2020), pp. 713–721. DOI: 10.1002/mp.13926.

[173] A. K. Mandapaka et al. "Evaluation of the dosimetric properties of a synthetic single crystal diamond detector in high energy clinical proton beams". In: *Medical Physics* 40.12 (2013), p. 121702. DOI: 10.1118/1.4828777.

[174] L. Manganaro et al. "A Monte Carlo approach to the microdosimetric kinetic model to account for dose rate time structure effects in ion beam therapy with application in treatment planning simulations". In: *Medical Physics* 44.4 (2017), pp. 1577–1589. DOI: 10.1002/mp.12133.

[175] Luca G. Mariotti et al. "Use of the γ-H2AX Assay to Investigate DNA Repair Dynamics Following Multiple Radiation Exposures". In: *PLOS ONE* 8 (Nov. 2013). DOI: 10.1371/journal.pone.0079541. URL: https://doi.org/10.1371/journal.pone.0079541.

[176] M. P. Martinov, E. M. Fletcher, and R. M. Thomson. "Multiscale Monte Carlo simulations of gold nanoparticle dose-enhanced radiotherapy II: Cellular dose enhancement within macroscopic tumor models". In: *Medical Physics* 50 (2023), pp. 5842–5852. DOI: 10.1002/mp.16807.

[177] T. Mastren et al. "Separation of ^{103}Ru from a proton irradiated thorium matrix: A potential source of Auger therapy radionuclide ^{103m}Rh". In: *PLoS One* 12 (2017), e0190308. DOI: 10.1371/journal.pone.0190308.

[178] Hiroaki Matsubara et al. "Comparison of passive and scanning irradiation methods for carbon-ion radiotherapy for breast cancer". In: *Journal of Radiation Research* 59.5 (July 2018), pp. 625–631. ISSN: 0449-3060. DOI: 10.1093/jrr/rry052. eprint: https://academic.oup.com/jrr/article-pdf/59/5/625/26357653/rry052.pdf. URL: https://doi.org/10.1093/jrr/rry052.

[179] K. M. Mayer and J. H. Hafner. "Localized Surface Plasmon Resonance Sensors". In: *Chemical Reviews* 111 (2011), pp. 3828–3857. DOI: 10.1021/cr100313v.

[180] D. Mazzucconi and et al. "An Avalanche Confinement TEPC as Connecting Bridge from Micro to Nanodosimetry". In: *Journal of Physics: Conference Series* 1662 (2020). ISSN: 1742-6588, 1742-6596. DOI: 10.1088/1742-6596/1662/1/012023.

[181] D. Mazzucconi and et al. "Microdosimetry at Nanometric Scale with an Avalanche-Confinement TEPC: Response against a Helium Ion Beam". In: *Radiation Protection Dosimetry* 183.1-2 (2019), pp. 177–181. ISSN: 1742-3406. DOI: 10.1093/rpd/ncy230. URL: https://www.ncbi.nlm.nih.gov/pubmed/30535177.

[182] D. Mazzucconi and et al. "Nano-microdosimetric investigation at the therapeutic proton irradiation line of CATANA". In: *Radiation Measurements* 123 (2019), pp. 26–33. ISSN: 1350-4487. DOI: 10.1016/j.radmeas.2019.02.012.

[183] Stephen J. McMahon and Kevin M. Prise. "Mechanistic Modelling of Radiation Responses". In: *Cancers* 11.2 (2019). ISSN: 2072-6694. DOI: 10.3390/cancers11020205. URL: https://www.mdpi.com/2072-6694/11/2/205.

[184] Stephen Joseph McMahon. "The linear quadratic model: usage, interpretation and challenges". In: *Physics in Medicine & Biology* 64.1 (2018), 01TR01. DOI: 10.1088/1361-6560/aaf26a. URL: https://doi.org/10.1088/1361-6560/aaf26a.

[185] H. G. Menzel, P. Pihet, and A. Wambersie. "Microdosimetric Specification of Radiation Quality in Neutron Radiation Therapy". In: *International Journal of Radiation Biology* 57.4 (1990), pp. 865–883. DOI: 10.1080/09553009014550991.

[186] A. Mesbahi. "A review on gold nanoparticles radiosensitization effect in radiation therapy of cancer". In: *Reports of Practical Oncology and Radiotherapy* 15.6 (2010), pp. 176–180. DOI: 10.1016/j.rpor.2010.09.001.

[187] Nicholas Metropolis. "The Beginning of the Monte Carlo Method". In: *Los Alamos Science* (1987). Special Issue, Los Alamos National Laboratory, LA-UR-88-9067, pp. 125–131.

[188] H.H. Mitchell et al. "THE CHEMICAL COMPOSITION OF THE ADULT HUMAN BODY AND ITS BEARING ON THE BIOCHEMISTRY OF GROWTH". In: *Journal of Biological Chemistry* 158.3 (1945), pp. 625–637. ISSN: 0021-9258. DOI: https://doi.org/10.1016/S0021-9258(19)51339-4. URL: https://www.sciencedirect.com/science/article/pii/S0021925819513394.

[189] F. Morschhauser et al. "^{90}Yttrium-ibritumomab tiuxetan consolidation of first remission in advanced-stage follicular non-Hodgkin lymphoma: updated results after a median follow-up of 7.3 years from the international, randomized, phase III First-Line Indolent Trial". In: *Journal of Clinical Oncology* 31 (2013), pp. 1977–1983. DOI: 10.1200/jco.2012.45.6400.

[190] K. Morstin, V. P. Bond, and J. W. Baum. "Probabilistic Approach to Obtain Hit-Size Effectiveness Functions Which Relate Microdosimetry and Radiobiology". In: *Radiation Research* 120.3 (1989), pp. 383–402.

[191] C. Müller et al. "A unique matched quadruplet of terbium radioisotopes for PET and SPECT and for α- and β^- radionuclide therapy: an in vivo proof-of-concept study with a new receptor-targeted folate derivative". In: *Journal of Nuclear Medicine* 53 (2012), pp. 1951–1959. DOI: 10.2967/jnumed.112.107540.

[192] C. Müller et al. "Direct in vitro and in vivo comparison of ^{161}Tb and ^{177}Lu using a tumour-targeting folate conjugate". In: *European Journal of Nuclear Medicine and Molecular Imaging* 41 (2014), pp. 476–485. DOI: 10.1007/s00259-013-2563-z.

[193] C. Müller et al. "Terbium-161 for PSMA-targeted radionuclide therapy of prostate cancer". In: *European Journal of Nuclear Medicine and Molecular Imaging* 46 (2019), pp. 1919–1930. DOI: 10.1007/s00259-019-04345-0.

[194] N. M. S. Nagi, Y. A. M. Khair, and A. M. E. Abdalla. "Capacity of gold nanoparticles in cancer radiotherapy". In: *Japanese Journal of Radiology* 35.10 (2017), pp. 555–561.

[195] National Nuclear Data Center. *Interactive Chart of Nuclides*. https://www.nndc.bnl.gov/nudat2/. Visited: 01/10/2025.

[196] Wayne D Newhauser and Rui Zhang. "The physics of proton therapy". In: *Physics in Medicine & Biology* 60.8 (2015), R155. DOI: 10.1088/0031-9155/60/8/R155. URL: https://doi.org/10.1088/0031-9155/60/8/R155.

[197] Wilfred Ngwa, Rishi Kumar, Srinivas Sridhar, et al. "Targeted radiotherapy with gold nanoparticles: current status and future perspectives". In: *Nanomedicine (Lond)* 9.7 (2014), pp. 1063–1082. DOI: 10.2217/nnm.14.55.

[198] H. Nikjoo et al. "Radiation track, DNA damage and response–a review". In: *Reports on Progress in Physics* 79.11 (2016), p. 116601. DOI: 10.1088/0034-4885/79/11/116601.

[199] H. Nikjoo et al. "Track-structure codes in radiation research". In: *Radiation Measurements* 41.9 (2006). Space Radiation Transport, Shielding, and Risk Assessment Models, pp. 1052–1074. ISSN: 1350-4487. DOI: https://doi.org/10.1016/j.radmeas.2006.02.001. URL: https://www.sciencedirect.com/science/article/pii/S1350448706001338.

[200] Oxford Microbeams Ltd. *OMDAQ-3*. 2024. DOI: 10.13140/RG.2.1.1948.0807. URL: https://doi.org/10.13140/RG.2.1.1948.0807.

[201] H. Paganetti et al. "Calculation of Relative Biological Effectiveness for Proton Beams Using Biological Weighting Functions". In: *International Journal of Radiation Oncology Biology Physics* 37.3 (1997), pp. 719–729.

[202] H. Paganetti et al. "NRG Oncology White Paper on the Relative Biological Effectiveness in Proton Therapy". In: *International Journal of Radiation Oncology, Biology, Physics* 121.1 (2025), pp. 202–217. DOI: 10.1016/j.ijrobp.2024.07.2152.

[203] H. Paganetti et al. "Report of the AAPM TG-256 on the relative biological effectiveness of proton beams in radiation therapy". In: *Medical Physics* 46 (2019), e53–e78. DOI: 10.1002/mp.13390.

[204] Hans Paganetti. "Range uncertainties in proton therapy and the role of Monte Carlo simulations". In: *Physics in Medicine and Biology* 57 (2012), R99–R117. DOI: 10.1088/0031-9155/57/11/R99.

[205] Harald Paganetti. "Relative biological effectiveness (RBE) values for proton beam therapy: Variations as a function of biological endpoint, dose, and linear energy transfer". In: *Physics in Medicine and Biology* 59.22 (2014), R419–R472. DOI: 10.1088/0031-9155/59/22/R419.

[206] G. Parisi, G. Schettino, and F. Romano. "A systematic study of the contribution of counting statistics to the final lineal energy uncertainty in microdosimetry". In: *Physics in Medicine & Biology* 67.15 (2022). DOI: 10.1088/1361-6560/ac79fb.

[207] G. Parisi et al. "On the microdosimetric characterisation of the radiation quality of a carbon-ion beam and the effect of the target volume thickness". In: *Physics in Medicine and Biology* 69.24 (2024). DOI: 10.1088/1361-6560/ad965e.

[208] G. Parisi et al. "The border effect in diamond microdosimeters and its impact on hadron therapy applications". In: *Physics in Medicine & Biology* 70.3 (2025). DOI: 10.1088/1361-6560/adaace.

[209] Gabriele Parisi, Francesco Romano, and Giuseppe Schettino. "Microdosimetry for hadron therapy: A state of the art of detection technology". In: *Frontiers in Physics* 10 (2022). ISSN: 2296-424X. DOI: 10.3389/fphy.2022.1035956. URL: https://www.frontiersin.org/articles/10.3389/fphy.2022.1035956.

[210] I. S. Pateras, S. Havaki, X. Nikitopoulou, et al. "The DNA damage response and immune signaling alliance: is it good or bad? Nature decides when and where". In: *Pharmacology & Therapeutics* 154 (2015), pp. 36–56. DOI: 10.1016/j.pharmthera.2015.06.011.

[211] T. Paunesku et al. "Radiosensitization and nanoparticles". In: *Cancer Treatment Research*. Vol. 166. Springer, 2015, pp. 151–171.

[212] L. A. Perles et al. "LET dependence of the response of EBT2 films in proton dosimetry modeled as a bimolecular chemical reaction". In: *Physics in Medicine and Biology* 58.23 (2013), pp. 8477–8491. DOI: 10.1088/0031-9155/58/23/8477.

[213] A. Perris et al. "Biological Effectiveness of Low Energy Protons. I. Survival of Chinese Hamster Cells". In: *International Journal of Radiation Biology and Related Studies in Physics, Chemistry and Medicine* 50.6 (1986), pp. 1093–1101. DOI: 10.1080/09553008614551481.

[214] P. Pihet et al. "Biological Weighting Function for RBE Specification of Neutron Therapy Beams. Intercomparison of 9 European Centres". In: *Radiation Protection Dosimetry* 31.1–4 (1990), pp. 437–442. DOI: 10.1093/rpd/31.1-4.437.

[215] E.B. Podgorsak, ed. *Radiation Oncology Physics: A Handbook for Teachers and Students*. Accessed: 2025-11-09. Vienna: International Atomic Energy Agency (IAEA), 2005. ISBN: 92-0-107304-6. URL: https://www.iaea.org/publications/7086/radiation-oncology-physics.

[216] Ervin B. Podgoršak. *Radiation Physics for Medical Physicists*. Third. Switzerland: Springer, 2016.

[217] Ioannis Polopetrakis et al. "New Geant4-DNA physics model for electron track-structure simulations in gold nanoparticles". In: *Physics in Medicine & Biology* 70 (Aug. 2025). DOI: 10.1088/1361-6560/adf40c.

[218] E. L. Powers, J. T. Lyman, and C. A. Tobias. "Some effects of accelerated charged particles on bacterial spores". In: *International Journal of Radiation Biology* 14.4 (1968), pp. 313–330.

[219] J. Prieto-Pena et al. "Microdosimetric Spectra Measurements on a Clinical Carbon Beam at Nominal Therapeutic Fluence Rate With Silicon Cylindrical Microdosimeters". In: *IEEE Transactions on Nuclear Science* 66.7 (2019), pp. 1840–1847. DOI: 10.1109/TNS.2019.2921453.

[220] Juan Prieto-Pena and et al. "Microdosimetric Spectra Measurements on a Clinical Carbon Beam at Nominal Therapeutic Fluence Rate With Silicon Cylindrical Microdosimeters". In: *IEEE Transactions on Nuclear Science* 66.7 (2019), pp. 1840–1847. ISSN: 0018-9499. DOI: 10.1109/tns.2019.2921453.

[221] K. M. Prise et al. "The Irradiation of V79 Mammalian Cells by Protons with Energies below 2 MeV. Part II. Measurement of Oxygen Enhancement Ratios and DNA Damage". In: *International Journal of Radiation Biology* 58.2 (1990), pp. 261–277. DOI: 10.1080/09553009014551611.

[222] D. A. Prokopovich and et al. "SOI microdosimetry for mixed field radiation protection". In: *Radiation Measurements* 43.2-6 (2008), pp. 1054–1058. ISSN: 1350-4487. DOI: 10.1016/j.radmeas.2007.12.036.

[223] International Commission on Radiological Protection. *Nuclear decay data for dosimetric calculations. ICRP Publication 107*. ICRP, 2008, pp. 7–96. DOI: 10.1016/j.icrp.2008.10.004.

[224] H. Rathke et al. "Dosimetry estimate and initial clinical experience with ^{90}Y-PSMA-617". In: *Journal of Nuclear Medicine* 60 (2019), pp. 806–811. DOI: 10.2967/jnumed.118.218917.

[225] Michael Evan Rising and et al. *MCNP® Code Version 6.3.1 Release Notes*. Tech. rep. Los Alamos National Laboratory, Apr. 2025. DOI: 10.2172/2563101. URL: https://doi.org/10.2172/2563101.

[226] W. Rogowski et al. "Long-term efficacy of ^{90}Y-DOTATATE in patients with nonresectable pancreatic and small bowel neuroendocrine neoplasms". In: *Future Oncology* 12 (2016), pp. 1877–1885. DOI: 10.2217/fon-2016-0031.

[227] S. Rollet and et al. "A Novel Microdosimeter Based Upon Artificial Single Crystal Diamond". In: *IEEE Transactions on Nuclear Science* 59.5 (2012), pp. 2409–2415. ISSN: 0018-9499. DOI: 10.1109/Tns.2012.2209677.

[228] Anatoly B. Rosenfeld. "Novel detectors for silicon based microdosimetry, their concepts and applications". In: *Nuclear Instruments and Methods in Physics Research Section A: Accelerators, Spectrometers, Detectors and Associated Equipment* 809 (2016), pp. 156–170. ISSN: 0168-9002. DOI: 10.1016/j.nima.2015.08.059.

[229] H. H. Rossi. *Energy Distribution in the Absorption of Radiation*. 1st. Vol. 11. Advances in Biological and Medical Physics. New York: Academic Press, 1967, p. 58. DOI: 10.1016/b978-1-4832-3107-5.50006-6.

[230] Harald H. Rossi and Albrecht M. Kellerer. "Radiation Carcinogenesis at Low Doses". In: *Science* 175.4018 (1972), pp. 200–202. DOI: 10.1126/science.175.4018.200. eprint: https://www.science.org/doi/pdf/10.1126/science.175.4018.200. URL: https://www.science.org/doi/abs/10.1126/science.175.4018.200.

[231] Harald H. Rossi and Marco Zaider. "Microdosimetry and Its Applications". In: 1995. URL: https://api.semanticscholar.org/CorpusID:177579612.

[232] Alessandro Rotondi, Paolo Pedroni, and Alessandra Pievatolo. *Probabilità, Statistica e Simulazione*. 3rd ed. Collana di Statistica e Probabilità Applicata. Milan: Springer, 2012. ISBN: 978-88-470-2364-2. DOI: 10.1007/978-88-470-2364-2. URL: https://link.springer.com/book/10.1007/978-88-470-2364-2.

[233] D. Sakata et al. "Electron track structure simulations in a gold nanoparticle using Geant4-DNA". In: *Physica Medica* 63 (July 2019), pp. 98–104. DOI: 10.1016/j.ejmp.2019.05.023.

[234] R. Salem et al. "Technical aspects of radioembolization with ^{90}Y microspheres". In: *Techniques in Vascular and Interventional Radiology* 10 (2007), pp. 12–29. DOI: 10.1053/j.tvir.2007.08.001.

[235] P. B. Santhosh, J. Genova, and H. Chamati. "Green Synthesis of Gold Nanoparticles: An Eco-Friendly Approach". In: *Chemistry* 4 (2022), pp. 345–369. DOI: 0.3390/chemistry4020026.

[236] Alexis M. Sanwick and Ivis F. Chaple. "Radiocobalt theranostic applications: current landscape, challenges, and future directions". In: *Frontiers in Nuclear Medicine* 5 (2025), p. 1663748. ISSN: 2673-8880. DOI: 10.3389/fnume.2025.1663748. URL: https://www.frontiersin.org/journals/nuclear-medicine/articles/10.3389/fnume.2025.1663748.

[237] F. Sauli. "Development and applications of gas electron multiplier detectors". In: *Nuclear Instruments and Methods in Physics Research Section A: Accelerators, Spectrometers, Detectors and Associated Equipment* 505.1-2 (2003), pp. 195–198. ISSN: 0168-9002. DOI: 10.1016/s0168-9002(03)01050-7.

[238] F. Sauli. "GEM: A new concept for electron amplification in gas detectors". In: *Nuclear Instruments and Methods in Physics Research Section A: Accelerators, Spectrometers, Detectors and Associated Equipment* 386 (1997), pp. 531–534.

[239] Dieter Schardt, Thilo Elsässer, and Daniela Schulz-Ertner. "Heavy-ion tumor therapy: Physical and radiobiological benefits". In: *Rev. Mod. Phys.* 82 (1 2010), pp. 383–425. DOI: 10.1103/RevModPhys.82.383. URL: https://link.aps.org/doi/10.1103/RevModPhys.82.383.

[240] G. Schettino et al. "Spatiotemporal investigations of DNA damage repair using microbeams". In: *Radiation Protection Dosimetry* 143.2-4 (Dec. 2010), pp. 340–343.

[241] Ingmar Schlampp et al. "Temporal lobe reactions after radiotherapy with carbon ions: Incidence and estimation of the relative biological effectiveness by the Local Effect Model". In: *International Journal of Radiation Oncology*Biology*Physics* 80.3 (2011), pp. 815–823. DOI: 10.1016/j.ijrobp.2010.03.001.

[242] Michael Scholz and Gerhard Kraft. "Calculation of heavy ion inactivation probabilities based on track structure, X-ray sensitivity and target size". In: *Radiation Protection Dosimetry* 52.1-4 (1994), pp. 29–34.

[243] Michael Scholz and Gerhard Kraft. "The physical and radiobiological basis of the Local Effect Model: A response to the commentary by R. Katz". In: *Radiation Research* 161.5 (2004), pp. 612–620.

[244] Michael Scholz and Gerhard Kraft. "Track structure and the calculation of biological effects of heavy charged particles". In: *Advances in Space Research* 18.1 (1996), pp. 5–14.

[245] P.J Sellin et al. "Digital IBIC—new spectroscopic modalities for ion-beam-induced charge imaging". In: *Nuclear Instruments and Methods in Physics Research Section A: Accelerators, Spectrometers, Detectors and Associated Equipment* 521.2 (2004), pp. 600–607. ISSN: 0168-9002. DOI: https://doi.org/10.1016/j.nima.2003.11.248. URL: https://www.sciencedirect.com/science/article/pii/S0168900203031036.

[246] R. G. Selwyn et al. "A new internal pair production branching ratio of ^{90}Y: the development of a non-destructive assay for ^{90}Y and ^{90}Sr". In: *Applied Radiation and Isotopes* 65 (2007), pp. 318–327. DOI: 10.1016/j.apradiso.2006.08.009.

[247] George Sgouros et al. "Radiopharmaceutical therapy in cancer: clinical advances and challenges". In: *Nature Reviews Drug Discovery* 19.9 (2020), pp. 589–608. DOI: 10.1038/s41573-020-0073-9. URL: https://doi.org/10.1038/s41573-020-0073-9.

[248] S. Shrestha et al. "Gold nanoparticles for radiation enhancement in vivo". In: *Jacobs Journal of Radiation Oncology* 3.1 (2016), p. 026.

[249] A. Simon et al. "The new Surrey ion beam analysis facility". In: *Nuclear Instruments and Methods in Physics Research Section B: Beam Interactions with Materials and Atoms* 219-220 (2004). Proceedings of the Sixteenth International Conference on Ion Beam Analysis, pp. 405–409. ISSN: 0168-583X. DOI: https://doi.org/10.1016/j.nimb.2004.01.091. URL: https://www.sciencedirect.com/science/article/pii/S0168583X04001193.

[250] G. Skarnemark et al. "Production of ^{103m}Rh for cancer therapy". In: *Journal of Radioanalytical and Nuclear Chemistry* 280 (2009), pp. 371–373. DOI: 10.1007/s10967-009-0529-1.

[251] Robert D. Stewart et al. "A comparison of mechanism-inspired models for particle relative biological effectiveness (RBE)". In: *Medical Physics* 45.11 (2018), e925–e952. DOI: 10.1002/mp.13207.

[252] J. Strosberg et al. "Phase 3 trial of ^{177}Lu-dotatate for midgut neuroendocrine tumors". In: *New England Journal of Medicine* 376 (2017), pp. 125–135. DOI: 10.1056/NEJMoa1607427.

[253] M. Su et al. "Enhanced Single-Strand Breaks of a Nucleic Acid by Gold Nanoparticles under X-ray Irradiation". In: *Journal of Physical Chemistry Letters* 14 (2023), pp. 1214–1221. DOI: 10.1021/acs.jpclett.2c03885.

[254] M. Sun et al. "Thermally Triggered in Situ Assembly of Gold Nanoparticles for Cancer Multimodal Imaging and Photothermal Therapy". In: *ACS Applied Materials & Interfaces* 9 (2017), pp. 10453–10460. DOI: 10.1021/acsami.7b00766.

[255] W. Sung et al. "Dependence of gold nanoparticle radiosensitization on cell geometry". In: *Nanoscale* 9 (2017), pp. 5843–5853. DOI: 10.1039/c7nr00906c.

[256] A. A. Tavares and J. M. Tavares. "(99m)Tc Auger electrons for targeted tumour therapy: a review". In: *International Journal of Radiation Biology* 86.4 (2010), pp. 261–270. DOI: 10.3109/09553000903564083.

[257] Sara Tegami et al. "LET Monitoring Using Liquid Ionization Chambers". In: *International Journal of Medical Physics, Clinical Engineering and Radiation Oncology* 6 (May 2017), pp. 197–207. DOI: 10.4236/ijmpcero.2017.62018.

[258] H. Thisgaard and M. Jensen. "^{119}Sb – a potent Auger emitter for targeted radionuclide therapy". In: *Medical Physics* 35 (2008), pp. 3839–3846. DOI: 10.1118/1.2963993.

[259] H. Thisgaard and M. Jensen. "Production of the Auger emitter ^{119}Sb for targeted radionuclide therapy using a small PET-cyclotron". In: *Applied Radiation and Isotopes* 67 (2009), pp. 34–38. DOI: 10.1016/j.apradiso.2008.09.003.

[260] F. Tommasino et al. "Proton beam characterization in the experimental room of the Trento Proton Therapy facility". In: *Nuclear Instruments and Methods in Physics Research Section A: Accelerators, Spectrometers, Detectors and Associated Equipment* 869 (2017), pp. 15–20. ISSN: 0168-9002. DOI: https://doi.org/10.1016/j.nima.2017.06.017. URL: https://www.sciencedirect.com/science/article/pii/S0168900217306654.

[261] Linh T. Tran and et al. "3D Radiation Detectors: Charge Collection Characterisation and Applicability of Technology for Microdosimetry". In: *IEEE Transactions on Nuclear Science* 61.4 (2014), pp. 1537–1543. ISSN: 0018-9499. DOI: 10.1109/tns.2014.2301729.

[262] Linh T. Tran and et al. "A Novel Silicon Microdosimeter Using 3D Sensitive Volumes: Modeling the Response in Neutron Fields Typical of Aviation". In: *IEEE Transactions on Nuclear Science* 61.4 (2014), pp. 1552–1557. ISSN: 0018-9499. DOI: 10.1109/tns.2014.2298461.

[263] P. Unak. "Targeted Tumor Radiotherapy". In: *Brazilian Archives of Biology and Technology* 45 (2002), pp. 97–110. DOI: 10.1590/S1516-89132002000500014. URL: http://dx.doi.org/10.1590/S1516-89132002000500014.

[264] H. Uusijärvi et al. "Electron- and positron-emitting radiolanthanides for therapy: aspects of dosimetry and production". In: *Journal of Nuclear Medicine* 47 (2006), pp. 807–814.

[265] C. Verona and et al. "Toward the use of single crystal diamond based detector for ion-beam therapy microdosimetry". In: *Radiation Measurements* 110 (2018), pp. 25–31. ISSN: 1350-4487. DOI: 10.1016/j.radmeas.2018.02.001.

[266] C. Verona et al. "Development and Fabrication of Microdosimeter Arrays Based on Single-Crystal Diamond Schottky Diodes". In: *Physica Status Solidi (A)* 221 (2024), p. 2300987. DOI: 10.1002/pssa.202300987.

[267] C. Verona et al. "Development of a compact and portable diamond-based detection system for dosimetry and microdosimetry in ion beam therapy". In: *Review of Scientific Instruments* 95.11 (Nov. 2024), p. 113302. ISSN: 0034-6748. DOI: 10.1063/5.0235400. eprint: https://pubs.aip.org/aip/rsi/article-pdf/doi/10.1063/5.0235400/20250473/113302_1_5.0235400.pdf. URL: https://doi.org/10.1063/5.0235400.

[268] C. Verona et al. "Experimental characterization of a diamond detection system for combined dose, LET and RBE assessment in clinical proton beams". In: *Physics in Medicine & Biology* 70.20 (2025). DOI: 10.1088/1361-6560/ae0be8.

[269] C. Verona et al. "Microdosimetric measurements of a monoenergetic and modulated Bragg Peaks of 62 MeV therapeutic proton beam with a synthetic single crystal diamond microdosimeter". In: *Medical Physics* 47 (2020), pp. 5791–5801. DOI: 10.1002/mp.14466.

[270] C. Verona et al. "Spectroscopic properties and radiation damage investigation of a diamond based Schottky diode for ion-beam therapy microdosimetry". In: *Journal of Applied Physics* 118.18 (Nov. 2015), p. 184503. ISSN: 0021-8979. DOI: 10.1063/1.4935525. eprint: https://pubs.aip.org/aip/jap/article-pdf/doi/10.1063/1.4935525/15171250/184503_1_online.pdf. URL: https://doi.org/10.1063/1.4935525.

[271] S. Vinjamuri et al. "Peptide receptor radionuclide therapy with ^{90}Y-DOTATATE/^{90}Y-DOTATOC in patients with progressive metastatic neuroendocrine tumours: assessment of response, survival and toxicity". In: *British Journal of Cancer* 108 (2013), pp. 1440–1448. DOI: 10.1038/bjc.2013.103.

[272] P. M. Walker and J. J. Carroll. "Nuclear isomers: recipes from the past and ingredients for the future". In: *Nuclear Physics News* 17.2 (2007). See p. 116, pp. 11–15. DOI: 10.1080/10506890701404206.

[273] A. Wambersie. "Contribution of Microdosimetry to the Specification of Neutron Beam Quality for the Choice of the 'Clinical RBE' in Fast Neutron Therapy". In: *Radiation Protection Dosimetry* 52.1–4 (1994), pp. 453–460. DOI: 10.1093/oxfordjournals.rpd.a082233.

[274] A. Wambersie, P. Pihet, and H. G. Menzel. "The Role of Microdosimetry in Radiotherapy". In: *Radiation Protection Dosimetry* 31.1–4 (1990), pp. 421–432. DOI: 10.1093/rpd/31.1-4.421.

[275] R. Wang et al. "Biomimetic Upconversion Nanoparticles and Gold Nanoparticles for Novel Simultaneous Dual-Modal Imaging-Guided Photothermal Therapy of Cancer". In: *Cancers* 12 (2020), p. 3136. DOI: 10.3390/cancers12113136.

[276] J.F. Ward. "DNA Damage Produced by Ionizing Radiation in Mammalian Cells: Identities, Mechanisms of Formation, and Reparability". In: ed. by Waldo E. Cohn and Kivie Moldave. Vol. 35. Progress in Nucleic Acid Research and Molecular Biology. Academic Press, 1988, pp. 95–125. DOI: https://doi.org/10.1016/S0079-6603(08)60611-X. URL: https://www.sciencedirect.com/science/article/pii/S007966030860611X.

[277] R. R. Wilson. "Radiological Use of Fast Protons". In: *Radiology* 47.5 (Nov. 1946), pp. 487–491. DOI: 10.1148/47.5.487.

[278] X. Yao et al. "Chemical radiosensitivity of DNA induced by gold nanoparticles". In: *Journal of Biomedical Nanotechnology* 11.3 (2015), pp. 478–485. DOI: 10.1166/jbn.2015.1922.

[279] A. Yokoya and Y. Obata. "Core level ionization or excitation and Auger relaxation induce clustered DNA damage". In: *The Enzymes*. Vol. 51. Amsterdam, The Netherlands: Elsevier, 2022, pp. 79–100. ISBN: 978-0-323-99397-5.

[280] Y. Yong, X. Cheng, T. Bao, et al. "Tungsten sulfide quantum dots as multifunctional nanotheranostics for in vivo dual-modal image-guided photothermal/radiotherapy synergistic therapy". In: *ACS Nano* 9.12 (2015), pp. 12451–12463. DOI: 10.1021/acsnano.5b05825.

[281] A. A. Zade et al. "^{90}Y microsphere therapy: does ^{90}Y PET/CT imaging obviate the need for ^{90}Y Bremsstrahlung SPECT/CT imaging?" In: *Nuclear Medicine Communications* 34.10 (2013), pp. 1090–1096. DOI: 10.1097/MNM.0b013e328364aa4b.

[282] I. A. Zahradnik and et al. "A diamond guard ring microdosimeter for ion beam therapy". In: *Review of Scientific Instruments* 91.5 (2020), p. 054102. ISSN: 1089-7623. DOI: 10.1063/5.0002403. URL: https://www.ncbi.nlm.nih.gov/pubmed/32486707.

[283] Izabella A. Zahradnik and et al. "scCVD Diamond Membrane based Microdosimeter for Hadron Therapy". In: *physica status solidi (a)* 215.22 (2018). ISSN: 1862-6300. DOI: 10.1002/pssa.201800383.

[284] M. Zaider. "The variation of β with radiation quality in the α/β model". In: *Radiation Research* 141 (1995), pp. 228–230.

[285] Cary Zeitlin and Chiara La Tessa. "The Role of Nuclear Fragmentation in Particle Therapy and Space Radiation Protection". In: *Frontiers in Oncology* Volume 6 - 2016 (2016). ISSN: 2234-943X. DOI: 10.3389/fonc.2016.00065. URL: https://www.frontiersin.org/journals/oncology/articles/10.3389/fonc.2016.00065.

[286] Y. Zeng et al. "Lipid-AuNPs@PDA Nanohybrid for MRI/CT Imaging and Photothermal Therapy of Hepatocellular Carcinoma". In: *ACS Applied Materials & Interfaces* 6 (2014), pp. 14266–14277. DOI: 10.1021/am503866x.

[287] J. Zhang et al. "From bench to bedside—The Bad Berka experience with first-in-human studies". In: *Seminars in Nuclear Medicine* 49 (2019), pp. 422–437. DOI: 10.1053/j.semnuclmed.2019.06.002.

[288] X. D. Zhang, D. Wu, X. Shen, et al. "Size-dependent radiosensitization of PEG-coated gold nanoparticles for cancer radiation therapy". In: *Biomaterials* 33.27 (2012), pp. 6408–6419. DOI: 10.1016/j.biomaterials.2012.05.047.

[289] Y. Zhao, D. Sultan, and Y. Liu. "Biodistribution, Excretion, and Toxicity of Nanoparticles". In: *Theranostic Bionanomaterials*. Amsterdam, The Netherlands: Elsevier, 2019, pp. 27–53. ISBN: 978-0-12-815341-3.

[290] James F. Ziegler, M.D. Ziegler, and J.P. Biersack. "SRIM – The stopping and range of ions in matter (2010)". In: *Nuclear Instruments and Methods in Physics Research Section B: Beam Interactions with Materials and Atoms* 268.11 (2010). 19th International Conference on Ion Beam Analysis, pp. 1818–1823. ISSN: 0168-583X. DOI: https://doi.org/10.1016/j.nimb.2010.02.091. URL: https://www.sciencedirect.com/science/article/pii/S0168583X10001862.